INVESTIGATING THE FUNCTION AND REGULATION OF THE NEURONAL CEROID LIPOFUSCINOSIS PROTEIN CLN7 USING *DROSOPHILA MELANOGASTER*

by

KYLE JOHN CONNOLLY

A thesis submitted to the University of Birmingham for the degree of

DOCTOR OF PHILOSOPHY

Institute of Cancer and Genomic Sciences

College of Medical and Dental Sciences

University of Birmingham

September 2019

Abstract

The neuronal ceroid lipofuscinoses (NCLs) are inherited lysosomal disorders that manifest in neurodegeneration, mainly affecting children. Such early pathology is suggestive of a role in neurodevelopment. However the roles of NCL genes within the nervous system are not well understood. Mutations to CLN7 were only discovered to cause NCL in 2007. Currently, few models exist to investigate the function of CLN7 at the molecular level. Here, I used a *Drosophila* model to accelerate our understanding of CLN7 function. Using an unbiased lipidomic analysis, I characterised a novel defect in sphingolipid metabolism resembling a block in sphingolipid degradation. Defects in sphingolipid degradation are characteristic of the sphingolipidoses, and pathological accumulations of sphingolipids are associated with age-related conditions, such as Alzheimer's and Parkinson's diseases. In addition, I established a proximity labelling tool for investigation of the CLN7 interactome *in vitro* and *in vivo*. Initial labelling *in vitro* identified several cytoskeletal proteins that function at the *Drosophila* neuromuscular junction (NMJ), where Cln7 is known to reside *in vivo*. Finally, I characterised a reduction in TORC1 activity in Cln7 mutant flies and cells. Interestingly, the *Drosophila* insulin receptor substrate, chico, was also identified by proximity labelling, suggesting a role for Cln7 in insulin signalling.

Acknowledgements

I would like to thank my supervisor Richard Tuxworth for his continued support and guidance (and patience!) over the past 4 years. Thank you for the coffees when a pick-me-up is on the cards, or a beer when there's nothing else for it!

Also, huge thanks to everyone in the lab for making my time in Birmingham so enjoyable, both in the lab and out. Thank you for the coffee breaks, the impromptu pub trips, and for the endless stream of goodies in the office.

Special thanks to Matt for our coffee and cake trips and our deep and meaningfuls where I'm sure you just aim to troll me. To Niki for "Fishy Friday!", or the occasional time you decide to try a jacket potato, again. Thanks to Char and James for, well, my drinking habit. It seems an obligatory part of the process. And to Chloe and Dan who I can always rely on for a pizza night in, unless there's chicken out, of course.

And of course, thanks to my family for always supporting me throughout my studies, especially through my write-up.

Contents

List of Figures

List of Tables

List of Abbreviations

Abbreviation	Meaning
4E-BP1	4E binding proteins
AD	Alzheimer's disease
ADP	Adenosine diphosphate
AGE	Agarose gel electrophoresis
ALG	Apoptosis-linked gene
ALR	Autophagic lysosome reformation
AMP	Adenosine monophosphate
AMPK	5'-AMP-activated protein kinase
APP	Amyloid precursor protein
Arf	ADP-ribosylation factor
Arl	Arf-like
ATG	Autophagy-related gene
ATP	Adenosine triphosphate
AV	Autophagic vesicle
Aβ	Amyloid-beta
BLOC-1	Biogenesis of lysosome-related organelles complex 1
BORC	BLOC-1-related complex
BSA	Bovine serum albumin
CHMP	Charged multivesicular body protein
CLEAR	Coordinated lysosomal expression and regulation
Cln7	Ceroid lipofuscinosis, neuronal 7
CMA	Chaperone-mediated autophagy
CRISPR	Clustered regularly interspaced short palindromic repeats
DLG	Discs large
DMSO	Dimethyl sulfoxide
DNA	Deoxyribose nucleic acid

ECL	Enhanced chemiluminescence
EEA1	Early endosomal antigen 1
EF	Enrichment factor
EGF	Epidermal growth factor
ER	Endoplasmic reticulum
ERMES	ER-mitochondria encounter structure
ESCRT	Endosomal sorting complex required for transport
FBS	Foetal bovine serum
FLCN	Folliculin
FVCln7	FLAG-Venus-Cln7
GAP	GTPase activating protein
GDP	Guanosine diphosphate
GEF	Guanine nucleotide exchange factor
GFP	Green fluorescent protein
GGA	Golgi-localised, γ-ear-containing, Arf-binding
GTP	Guanosine triphosphate
HOPS	Homotypic fusion and vacuole protein sorting
HPLC	High performance liquid chromatography
HRP	Horseradish peroxidase
ICC	Immunocytochemistry
IF	Immunofluorescence
IGF	Insulin-like growth factor
IHC	Immunohistochemistry
IIS	Insulin/IGF signalling
InR	Insulin receptor
IP	Immunoprecipitation
IUBMB	International Union of Biochemistry and Molecular Biology
IUPAC	International Union of Pure and Applied Chemists
LAMP	Lysosome-associated membrane protein

LMSD	LIPID MAPS Structure Database
LSD	Lysosomal storage disorder
M6P	Mannose-6-phosphate
MEF	Mouse embryonic fibroblast
MFS	Major facilitator superfamily
MFSD8	MFS domain-containing protein 8
MiT/TFE	Microphthalmia transcription factor
MPR	M6P receptor
mRNA	Messenger RNA
MS	Mass spectrometry
MS/MS	Tandem mass spectrometry
MVB	Multivesicular body
NCL	Neuronal ceroid lipofuscinosis
NMJ	Neuromuscular junction
NP-40	Nonidet P-40
NVJ	Nuclear ER-vacuole junction
ORP1L	Oxysterol-binding protein-related protein 1L
PACS1	Phosphofurin acidic cluster sorting protein 1
PCR	Polymerase chain reaction
PD	Parkinson’s disease
PI3K	Phosphoinositol-3-kinase
PSD	Post-synaptic density
PVDF	Polyvinylidene fluoride
Rheb	Ras homologue enriched in brain
RILP	Rab7-interacting lysosomal protein
RNA	Ribonucleic acid
RNAi	RNA interference
RTK	Receptor tyrosine kinase
S6K	S6 kinase

SA	Streptavidin
SAP	Sphingolipid activator protein
SDS	Sodium dodecyl sulphate
SMA(LP)	Styrene maleic acid (lipid particle)
SNAP25	Synaptosome-associated protein of 25 kDa
SREBP	Sterol responsive element binding protein
SSR	Sub-synaptic reticulum
TAG	Triacylglyceride
TAP	Tandem affinity purification
TFEB	Transcription factor EB
TGN	*Trans*-Golgi network
TIP47	Tail-interacting protein of 47 kDa
TOR(C)	Target of rapamycin (complex)
TOS	TOR signalling
TRPML	Transient receptor potential cation channel, mucolipin
TSC	Tuberous sclerosis complex
UPLC	Ultra performance liquid chromatography
VAMP	Vesicle-associated membrane protein
v-ATPase	Vacuolar ATPase
vCLAMP	Vacuole and mitochondria patch
VPS	Vacuolar protein sorting
α-KG	α-ketoglutarate

1 INTRODUCTION

1.1 Lysosome biogenesis and maturation

1.1.1 *Overview of lysosomes*

Lysosomes and lysosome-like organelles are degradative organelles found in all eukaryotic cells. In higher eukaryotes, cells can contain hundreds of lysosomes ranging from 0.1 µm to 1 µm in diameter, while yeast and plant cells contain single large lysosome-like vacuoles that can reach several micrometres across (1). Lysosomes express a mixture of ~60 digestive hydrolases including proteases, lipases, nucleases, glycosidases, acid phosphatases and sulfatases (1, 2). The activation of these hydrolases requires an acidic pH of between 4.5 and 5.0, which is generated and maintained by the pumping of protons by the vacuolar H^+-ATPase (v-ATPase). These features were characterised shortly after the discovery of lysosomes in 1955 (3), and as such the cellular role for lysosomes was initially viewed from a luminal perspective; that is, the internal degradation of macromolecules. However, as research develops our understanding of lysosomal function, lysosomes are better described as biologically active membranes, with roles in cellular energy and nutrient sensing, anabolic or catabolic decision making, oxidative and hypoxic stress responses, plasma membrane repair, antigen presentation, in addition to the well-known role in autophagy and its derivatives (1, 2, 4). Lysosomal membrane proteins interface between cytosolic and luminal compartments that operate as platforms for these specialised functions. Strikingly, lysosome-associated membrane protein 1 (LAMP1) and LAMP2 account for 80% of lysosomal membrane protein content and form the luminal glycocalyx, which protects against autodigestion by internal hydrolases (1). The remainder constitute machinery that perform the many roles for

lysosomes as a spatially and metabolically dynamic organelle. In the following sections, I outline the pathways that govern lysosome biogenesis and maturation, and describe the machinery that facilitate and regulate core lysosomal processes.

1.1.2 *The endocytic pathway*

Lysosomes are terminal organelles in the endocytic pathway. Cargo from the extracellular environment is internalised via various endocytic mechanisms, for example by clathrin or caveolin-mediated endocytosis or phagocytosis (5). Several models have been proposed whereby endocytic vesicles can directly mature into or fuse with lysosomes to facilitate cargo degradation (6). In general, cargo is shuttled from the cell periphery toward the centre via a series of fusion events. Endocytic vesicles fuse with peripheral early endosomes enriched in Rab5 and PI(3)P (7, 8). Homotypic fusion of early endosomes can be split into two parts; docking and membrane fusion. Endosome docking requires the Rab5 effector endosomal antigen 1 (EEA1), which is recruited to early endosomes in a Rab5 and PI(3)P-dependent manner (9, 10). Docking is enhanced by additional Rab5 effectors Rabaptin-5/5β and Rabex-5 which promote Rab5 activation and the recruitment of phosphoinositol-3 kinases (PI3K) such as VPS34 (9, 11, 12). Membrane fusion is then mediated by interactions between soluble *N*-ethylmaleimide-sensitive factor (NSF) attachment protein receptors (SNAREs) expressed on target (t-SNAREs) and vesicular (v-SNAREs) membranes (13). Multiple fusion events concentrate cargo within growing endosomal compartments that mature by gradual acidification of the lumen, Rab conversion from Rab5 to Rab7 (7) and phosphoinositide conversion from PI(3)P to PI(3,5)P_2 (14). These biochemical changes facilitate fundamental maturation processes including the centripetal trafficking of

endosomes, protein sorting, budding of intraluminal vesicles and the delivery and activation of lysosomal hydrolases.

1.1.3 *Endolysosome acidification*

The acidity of endolysosomal compartments is established and maintained by the v-ATPase (15). V-ATPase uses energy from ATP hydrolysis to pump H^+ into luminal compartments. The pumping of protons is paired with an intricate balance of Na^+, K^+, Ca^{2+}, and Cl^- influx and efflux, which cooperate to partially dissipate the rapidly generated electrical potential to prevent self-limitation of the v-ATPase (15-18). Together, the movement of ion species establishes a luminal pH of between 4.5 to 5.0 and a resting membrane potential of between -40 to -20 mV that are fundamental for the function of lysosomal hydrolases and transporters (1, 2, 19). Many metabolite efflux channels function as H^+/metabolite symporters, using the H^+ gradient to drive metabolite export, which also helps to regulate lysosome acidity. Indeed, over-acidification of lysosomes has been observed when H^+/metabolite symporters are mutated (20). Conversely, reduction of the proton motive force by inhibition of v-ATPase reduces lysosomal export of amino acids through H^+/amino acid symporters (21). Thus, sufficient acidification is required not only for hydrolase function but also to drive nutrient export for recycling.

1.1.4 *Phosphoinositide conversion*

The recruitment of several early and late endosomal complexes is facilitated by proteins with domains that specifically bind PI(3)P or PI(3,5)P_2, respectively. Thus, the early

generation of PI(3)P and subsequent conversion to PI(3,5)P_2 are essential to endosomal function and have been strategically co-opted to ensure proper chronology of endosomal processes. GTP-bound Rab5 recruits both VPS34 and p85α-p110β PI3Ks that are responsible for generating PI(3)P on early endosomal membranes (22). PI(3)P recruits EEA1 for endosome docking during homotypic fusion, ESCRT-0-I-II for ubiquitinated cargo clustering during MVB formation, and the retomer complex for retrograde endosome-to-TGN transport (9, 10, 23-26).

PI(3,5)P_2 is an agonist for the Ca^{2+} channel TRPML1 and both are required for Ca^{2+}-dependent endolysosomal processes, including centripetal trafficking during endosome maturation and for lysosome fusion and fission which regulate lysosome size (27, 28). Both PI(3)P and PI(3,5)P_2 are also required at different stages during maturation for proper protein sorting within lysosome-related compartments and the formation of multivesicular bodies (MVBs) (14). PIKfyve is a PI(3)P 5-kinase that associates with early endosomes and catalyses the conversion of PI(3)P to PI(3,5)P_2 (14). The balance between PI(3)P and PI(3,5)P_2 is regulated by PIKfyve activators Vac7 and Vac14 and the PI(3,5)P_2 5-phosphatase FIG4 (29-31). Critically, defects in endolysosomal phosphoinositide regulation manifest in variants of Charcot-Marie-Tooth disorder and have been identified in a subset of amyotrophic lateral sclerosis patients (32-34).

1.1.5 *Generation of MVBs*

MVBs are formed by intraluminal budding of the limiting membrane of late endosomes. The MVB pathway is highly conserved and requires the assembly of class E vacuolar protein sorting (VPS) proteins into five distinct complexes, called endosomal sorting

complex required for transport (ESCRT)-0 -I -II and -III and the VPS4 complex (35, 36). ESCRT-0 is recruited to the surface of early endosomes through an interaction between PI(3)P and the FYVE domain of HRS (Figure 1.1) (23). Once associated with early endosomes, ESCRT-0 binds multiple ubiquitinated proteins and recruits ESCRT-I, which in turn recruits ESCRT-II (37, 38). Additional ubiquitinated proteins are bound by ESCRT-I and ESCRT-II (39). The GLUE domain of VPS36 within ESCRT-II simultaneously binds VPS28 of ESCRT-I, ubiquitinated cargo and PI(3)P, stabilising the ESCRT-0-I-II-ubiqutinated cargo complex on early endosomes (24).

Endosomal membrane invagination is dependent on the assembly of ESCRT-0-I-II, but requires ESCRT-III to release intraluminal vesicles (40). The formation of membrane buds by ESCRT-0-I-II conveniently couples ubiquitinated cargo to budding vesicles to facilitate efficient transfer of cargo. To release nascent vesicles, VPS25 of ESCRT-II activates the ESCRT-III subunit charged multivesicular body protein 6 (CHMP6) (41). CHMP6 nucleates the homo-polymerisation of CHMP4 in filamentous spiral structures that extend down the vesicle stalk and sequesters ubiquitinated cargo from ESCRT-0-I-II (42). CHMP3 is recruited by $PI(3,5)P_2$ to late endosomes and caps the CHMP4 filament (43, 44). Additional ESCRT-III subunits assemble at the filament cap and provide a scaffold for the VPS4 complex (45). VPS4 is an AAA-ATPase that transduces the energy from ATP hydrolysis into mechanical force to disassemble the CHMP4 filament, thereby driving membrane scission and releasing intraluminal vesicles (46). Through this mechanism, the ESCRT machinery exposes membrane-associated cargo from both cytosolic and luminal sides to lysosomal hydrolases for degradation. The ESCRT machinery also have roles in other processes that require membrane scission, including cytokinesis (47), plasma membrane repair (48, 49), neuronal pruning (50) and virus release (51, 52).

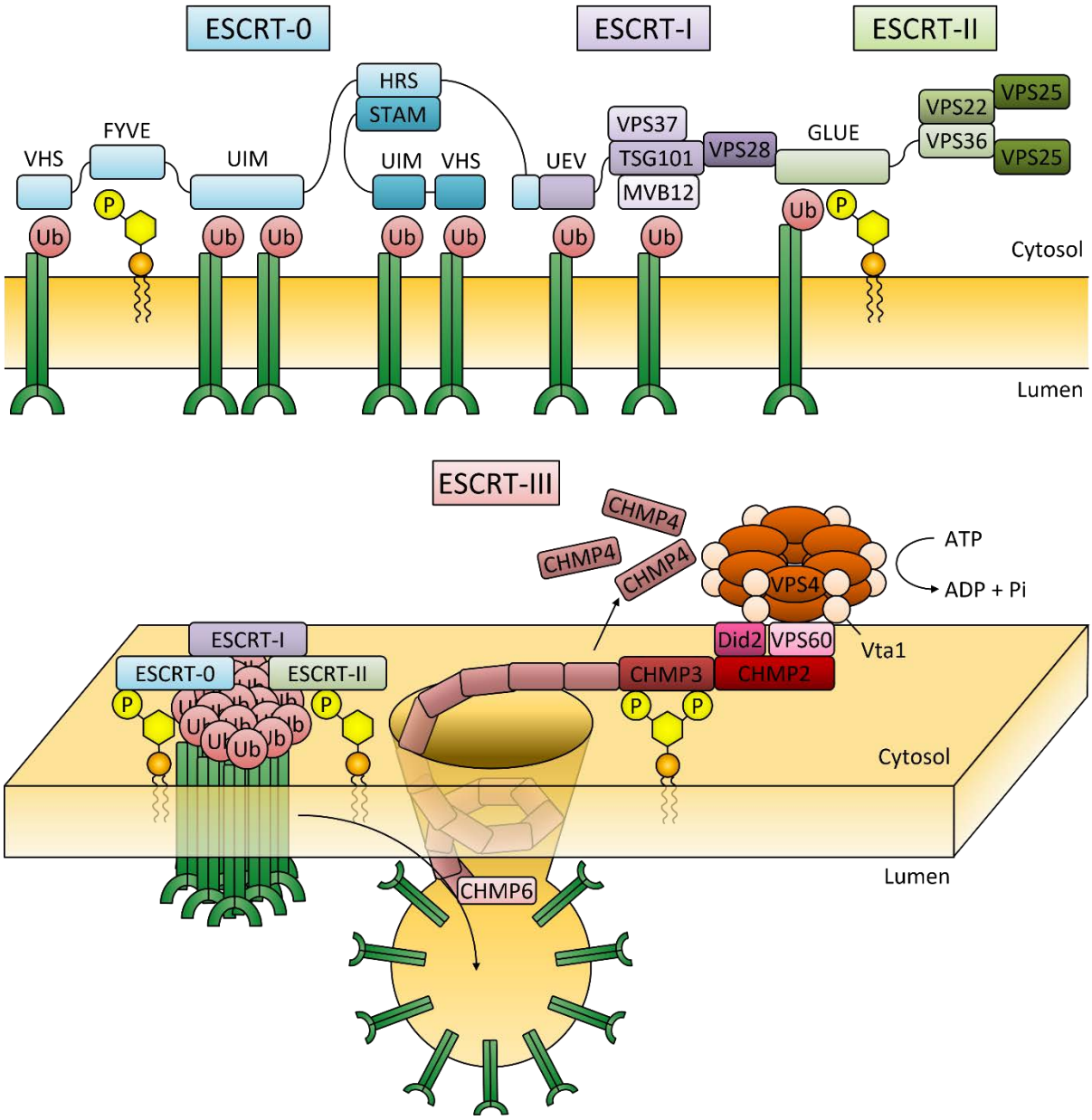

Figure 1.1. Sorting of ubiquitinated proteins and formation of MVBs by ESCRTs.

ESCRT-0 initiates MVB formation by binding PI(3)P on early endosomes and recruiting ESCRT-I and ESCRT-II. Ubiquitinated proteins are clustered by the ESCRT-0, ESCRT-I and ESCRT-II complexes. ESCRT-II also binds PI(3)P, likely stabilising the ESCRT-ubiquitin-cargo complex on early endosomes. ESCRT-II recruits the ESCRT-III subunit CHMP6, which nucleates CHMP4 homo-polymerisation. CHMP4 filaments sequester cargo and drive inward membrane budding, forming spiral filaments which extent down the vesicle stalk. CHMP4 filaments are capped by CHMP3 which binds the late endosome phosphoinositide PI(3,5)P_2. CHMP2 recruits the VPS4 complex which converts energy into mechanical force to disassemble the CHMP4 filament, resulting in membrane scission and vesicle release.

1.1.6 *Delivery of lysosomal proteins*

Lysosomal proteins are co-translationally translocated into the secretory pathway for their delivery to lysosomes. Most soluble proteins destined for the lysosome, such as hydrolases, are tagged with mannose-6-phosphate (M6P) within the *cis*-Golgi and bind to M6P protein receptors (MPRs) within the *trans*-Golgi network (TGN) (6). In addition, MPR-independent protein sorting by VPS10-domain receptors, namely sortilin and sortilin-related receptor SorLA, contributes to the delivery of some lysosomal proteins, such as sphingolipid activator proteins (SAPs), acid sphingomyelinase and cathepsins D and H (53-57). The cytoplasmic tails of these receptors are bound by Golgi-localised, γ-ear-containing, ADP-ribosylation factor (Arf)-binding proteins (GGAs) (58-60). GGAs then bind the clathrin adaptor proteins AP-1 and AP-2 to cluster cargo-loaded receptors into clathrin-coated transport vesicles (58). Mammalian GGA1 and GGA2 also interact with the Rabaptin-5-Rabex-5 complex, suggesting that GGAs may be involved in Rab5-dependent fusion of TGN-derived vesicles with endosomes (61).

In contrast, the delivery of newly synthesised membrane proteins to lysosomes is independent of MPRs. Instead, most lysosomal membrane proteins contain cytosolic tyrosine (NPXY or (G)YXXϕ, where X is any amino acid and ϕ is a hydrophobic amino acid) or dileucine (EXXXLL) motifs that determine their delivery to lysosomes (62). Proteins with GYXXϕ or EXXXLL motifs are bound by AP-3 or GGAs, respectively, that sort membrane proteins into clathrin-coated vesicles for direct trafficking to lysosomes (63, 64). In addition, YXXϕ signals that lack a glycine residue redirect membrane proteins to the plasma membrane and are subsequently trafficked to lysosomes via the endocytic pathway (65, 66). Thus, membrane proteins may be transported directly or indirectly via the plasma membrane (67, 68). To some

extent, indirect trafficking may compensate for saturation of or escape from direct routes. Indeed, AP-3 is required for direct trafficking of LAMP1, LAMP2, CD63, however the steady-state distribution of these proteins remains lysosomal (67, 69, 70).

Proteins that are delivered to endosomes but are not destined for degradation, such as MPRs, are sorted into multi-branching tubules for recycling back to the plasma membrane or the TGN (71). In yeast, retrograde recycling requires the pentameric complex containing Vps5, Vps17, Vps26, Vps29 and Vps35, collectively called the retromer (72). Humans possess Vps5 orthologues sorting nexin 1 (SNX1) and SNX2, Vps26 orthologues VPS26A and VPS26B, and orthologous VPS29 and VPS35 proteins, but not Vps17 (73). Retrieval of several membrane proteins, including MPRs, from endosomes is dependent on the retromer (54, 74-76). Additional components of the retrograde pathway have also been characterised, including phosphofurin acidic cluster sorting protein 1 (PACS1)-epsinR-AP1 and tail-interacting protein of 47 kDa (TIP47)-Rab9-p40 (77-81).

Interestingly, the recruitment of retromer to endosomal membranes and subsequent protein sorting is coupled to endosomal maturation. Rab5-PI3K-dependent generation of PI(3)P on early endosomal membranes recruits SNX1 and SNX2, which in turn recruit remaining retromer subunits (25, 26). Rab7 is then required to stabilise the retromer on endosomal membranes (25). This temporally-defined mechanism ensures that retromer functions downstream of TGN-to-endosome delivery of lysosomal proteins, establishing a cycle of lysosome protein delivery to maturing endosomes and retrograde recycling of TGN membrane and receptors.

1.2 Lysosomal function

1.2.1 *Lysosomal positioning*

1.2.1.1 Anterograde and retrograde trafficking

Lysosomes are spatially dynamic organelles that can change cellular positioning by switching directionality along microtubules via opposing plus end and minus end transport by kinesin and dynein, respectively (Figure 1.2) (82, 83). The biogenesis of lysosome-related organelles complex 1 (BLOC-1)-related complex (BORC) recruits the small GTPase Arf-like protein 8 (Arl8) to late endosomes and lysosomes, which in turn recruits SKIP (84). SKIP links the BORC-Arl8 complex to kinesins which mediate anterograde transport of lysosomes to the cell periphery (84). On the other hand, centripetal trafficking toward the perinuclear microtubule-organising centre is regulated by Rab7 and its effector Rab7-interacting lysosomal protein (RILP). RILP recruits the $p150^{Glued}$ subunit of the dynactin protein complex to late endosomes, facilitating retrograde transport by dyneins (85).

1.2.1.2 Regulation of lysosome positioning by nutrients

Interestingly, lysosomal processes can be regulated by their positioning within cells. Lysosomes favour perinuclear distribution in response to starvation, whereas nutrient recovery promotes localisation of lysosomes to the cell periphery (86, 87). This nutrient-dependent re-distribution of lysosomes was shown to depend on changes to intracellular pH, although how and where intracellular pH changes are induced is unclear. Re-distribution of lysosomes by modulating kinesin and Arl8 expression was accompanied by changes to TORC1 activity absent changes to nutrients, with greater activity observed at the cell periphery.

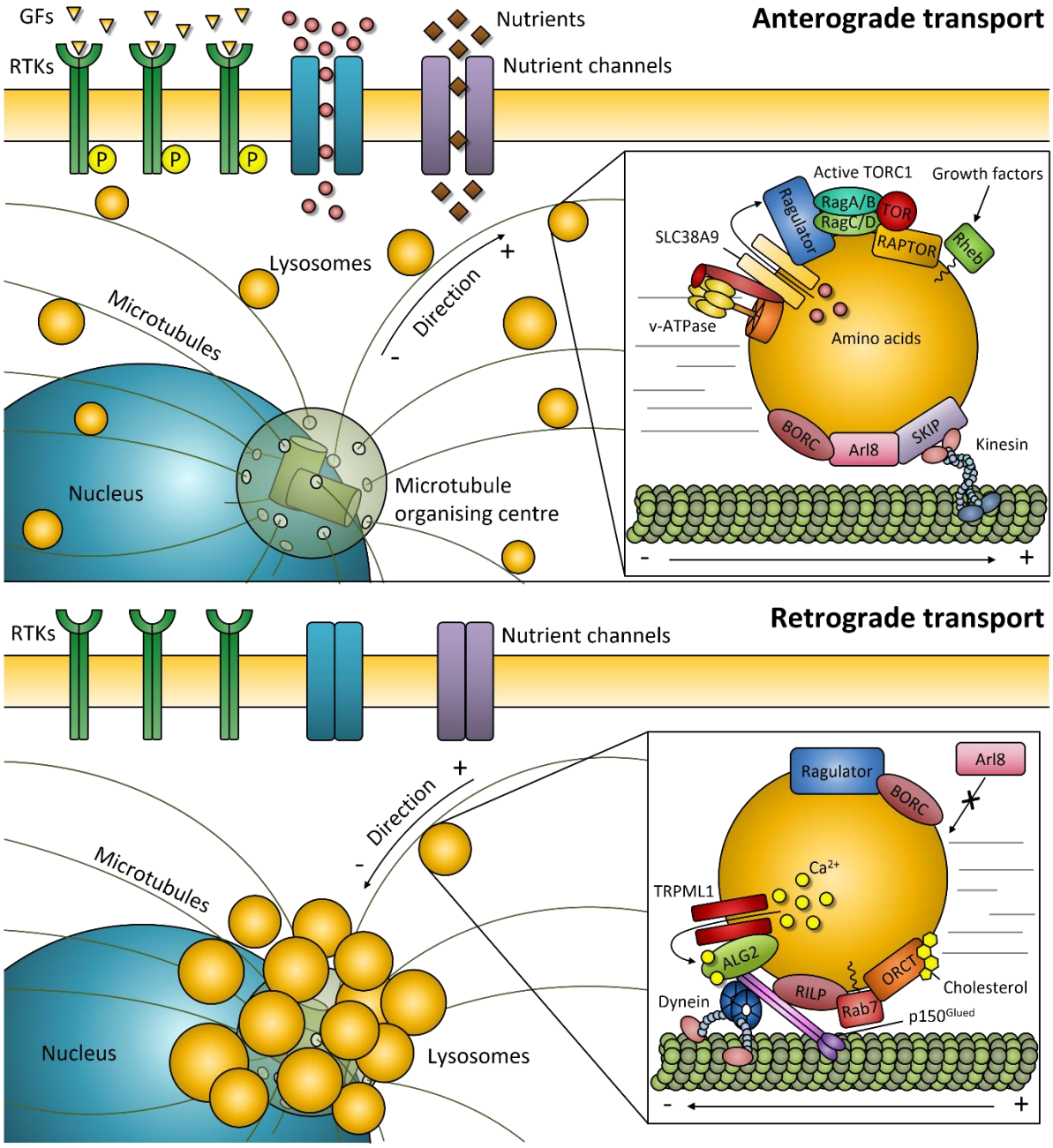

Figure 1.2. Controlling lysosome positioning by regulating transport along microtubules.

Lysosomes are trafficked to the cell periphery or perinuclear area by kinesin or dynein-mediated transport, respectively. Machinery on the surface of lysosomes regulate the association with these motor proteins. Growth factors and nutrient sufficiency stimulate anterograde transport by activating the TORC1 complex and promoting association with kinesins via BORC-Arl8-SKIP. In contrast, Ca2+ efflux and elevated cholesterol promote retrograde transport by dyneins through TRMPL1-ALG2 and ORCT-Rab7-RILP, respectively, while starvation inhibits kinesin transport by association of Ragulator with BORC.

Recent studies have shown that several factors involved in nutrient sensing and TORC1 recruitment to lysosomes, including LAMTOR2, SLC38A9 and folliculin (FLCN), regulate lysosomal positioning in response to growth factors and amino acid availability by modulating anterograde and retrograde mechanisms, likely simultaneously (87-89). During amino acid deprivation, LAMTOR2 binds to BORC and negatively regulates Arl8-dependent anterograde transport (87, 88). Amino acid recovery triggers disassembly of LAMTOR2-BORC, which requires SLC38A9, and promotes peripheral movement of lysosomes, presumably by promoting Arl8 recruitment by BORC (87). Similar de-stabilisation of LAMTOR2-BORC and peripheral migration of lysosomes was observed in response to epidermal growth factor (EGF) (88). On the other hand, FLCN/FNIP is required for perinuclear clustering of lysosomes in response to amino acid starvation (89). Interestingly, FLCN/FNIP-dependent clustering of lysosomes was suggested to depend on membrane contacts between separate Rab34-RILP- and LAMP1-positive perinuclear compartments, rather than by directly promoting Rab7-dependent retrograde transport (89).

1.2.1.3 The role of cholesterol in retrograde transport

Cholesterol-sensing machinery within late-endosomal membranes has been shown to modulate their distribution. Retrograde transport by Rab7-RILP-p150^{Glued} requires activation of the oxysterol-binding protein-related protein 1L (ORP1L) which functions as a cholesterol-sensitive switch (90). Under cholesterol-rich conditions, binding of cholesterol to ORP1L induces a conformational change that stabilises the Rab7-RILP-p150^{Glued} complex, whereas cholesterol depletion promotes the displacement of p150^{Glued} by interactions between ORP1L

and the ER protein VAP-A/B (90). In this way, cholesterol accumulation within late endosomes promotes retrograde transport to the cell centre, with a more disperse distribution when cholesterol is depleted (90).

1.2.1.4 Ca^{2+}-dependent retrograde transport

Lysosomal Ca^{2+} efflux also plays an important role in regulating lysosomal distribution. Transient inhibition of the Ca^{2+} channel TRPML1 prevented starvation- and alkalisation-induced migration of lysosomes to the perinuclear region (91). Conversely, increased Ca^{2+} efflux through TRPML1 was sufficient to drive lysosomal migration to the cell centre. Ca^{2+} efflux through TRPML1 is potentially sensed by forming Ca^{2+}-dependent interactions with apoptosis-linked gene 2 (ALG2), which is required for TRPML-dependent retrograde transport. This mechanism was dependent on dynein motors but independent of the Rab7-RILP-ORP1L pathway (91).

1.2.2 *Lysosome exocytosis*

The mechanism for lysosome exocytosis requires a sequence of Ca^{2+}-independent and Ca^{2+}-dependent processes. Firstly, lysosomes translocate from the perinuclear region toward the cell periphery in a Ca^{2+}-independent manner. Next, local increases in intracellular Ca^{2+} at the plasma membrane triggers exocytosis of peripherally positioned lysosomes (92). Ca^{2+} export from lysosomes by TRPML1 is critical for the docking of lysosomes at the plasma membrane (93, 94). Upon fusion, lysosomes release their contents into the extracellular space.

Vesicular compartments from all cell types may be secreted by either constitutive or Ca^{2+}-dependent exocytosis. In general, exocytosis is mediated by interactions between t-SNAREs and v-SNAREs (13). In neurons, neurotransmitter release from synaptic vesicles requires interactions between v-SNARE synaptobrevin/vesicle-associated membrane protein 2 (VAMP2) and t-SNAREs syntaxin-1 and synaptosome-associated protein of 25 kDa (SNAP25) (95). In contrast, lysosomal exocytosis machinery consist of the v-SNARE VAMP7 and t-SNAREs syntaxin-4 and SNAP23 (96, 97). Thus distinct SNARE complexes mediate fusion events between different compartments (98). Indeed, the expression of dominant negative SNAREs selectively inhibit fusion events between subsets of compartments, rather than a generalised block to exocytosis (96, 98). By extrapolation, this specificity argues that exocytosis of specific compartments may be spatially and temporally regulated by differential expression and localisation of cognate SNAREs. Indeed, lysosomal exocytosis occurs at basolateral membranes and not apical membranes within polarised epithelial cells, which is facilitated by restricted expression of syntaxin-4 at the basolateral membrane (99).

Ca^{2+}-dependent exocytosis requires additional components called synaptotagmins. Synaptotagmins contain two cytosolic Ca^{2+}-binding C2 domains and bind phospholipids in response to Ca^{2+}, thereby functioning as calcium sensors during membrane fusion (100). Synaptotagmin VII is specific to lysosomes and is required for fusion of lysosomes within the plasma membrane (101). Interestingly, synaptotagmins may also inhibit spontaneous Ca^{2+}-independent fusion events, which would establish an inducible system that only engages in response to specific cues (102).

Secretory lysosomes have been described as major contributors to plasma membrane repair, phagocytosis and neurite outgrowth in response to varied stresses (93, 101, 103, 104). In particular, activation of transcription factor EB (TFEB) promotes the peripheral movement of lysosomes and upregulates TRPML1 expression, which together enhances lysosome exocytosis (105). Critically, the increased secretion of lysosomal content by TFEB facilitated the clearance of pathological accumulations in *in vitro* and *in vivo* models of lysosomal storage disorder (105). Thus, enhancing lysosome exocytosis may be an effective strategy in the treatment of disorders that exhibit storage of lysosomal substrates.

1.2.3 *Lysosomes as signalling hubs*

1.2.3.1 The mechanistic target of rapamycin

The mechanistic target of rapamycin (mTOR) functions as a master growth regulator that interprets cues from extracellular and intracellular environments to switch between anabolic and catabolic states (4). mTOR forms two distinct complexes; the best characterised is mTOR complex 1 (mTORC1), composed of the serine/threonine kinase mTOR in complex with regulatory subunits Raptor, Deptor, mLst8 and PRAS40. By contrast, Raptor and PRAS40 subunits are swapped for Rictor and mSin1 in mTORC2, however the function and regulation of mTORC2 are much less characterised. mTORC1 operates strategically as a nutrient sensor on the surface of lysosomes, organelles that function as nutrient recyclers. In this way, mTORC1 is acutely sensitive to dynamic changes in energetic state and is a key regulator of adaptive lysosomal responses such as biogenesis, repositioning, autophagy and reformation (4, 106, 107).

Pathways that regulate mTORC1 can be imagined as two separable arms that govern the recruitment of mTORC1 to lysosomal membranes and its subsequent activation (Figure 1.3). Firstly, mTORC1 recruitment is regulated by the Ragulator, a pentameric complex of subunits LAMTOR1-5 (108-110). Lipidation of LAMTOR1 anchors the Ragulator to lysosomes (111), which then recruits a heterodimer of RagA/B and RagC/D GTPases (RagA is functionally redundant with RagB, as is RagC with RagD) that exist in opposite nucleotide binding states (108, 109, 112). In their active state, GTP-RagA/B and GDP-RagC/D recruit mTORC1 by binding Raptor during amino acid sufficiency (112, 113).

Growth factors are potent activators of mTORC1. Classically, binding of a growth factor to a receptor tyrosine kinase (RTK) triggers a signalling cascade via PI3K-Akt-Rheb. PI3K generates PI(3,4,5)P_3 at the plasma membrane, which in turn recruits and activates Akt (114). Akt then phosphorylates and thereby inhibits tuberous sclerosis complex 2 (TSC2) (115-117), which, in complex with TSC1 and TBC1D7, functions as a Rheb GTPase activating protein (GAP) at the lysosomal surface (118). The dissociation of the TSC complex from lysosomes relieves the inhibition of Rheb (115), which then interacts with and activates mTORC1 (119, 120). Raptor recognises TOR signalling (TOS) motifs on substrates and recruits them for phosphorylation by mTORC1 (121, 122). Downstream effects of mTORC1 activation include boosting translation by activating S6 kinases (S6Ks) (123-126) and inhibiting 4E-binding proteins (4E-BPs) (122, 127, 128), promoting lipid synthesis by activating sterol responsive element binding proteins 1 and 2 (SREBP1/2) and repressing lipin 1 (129-131), promoting nucleotide synthesis (132-135), downregulation of autophagy by inhibiting ULK1 (136, 137) and downregulation of lysosome biogenesis by repressing TFEB (138-141).

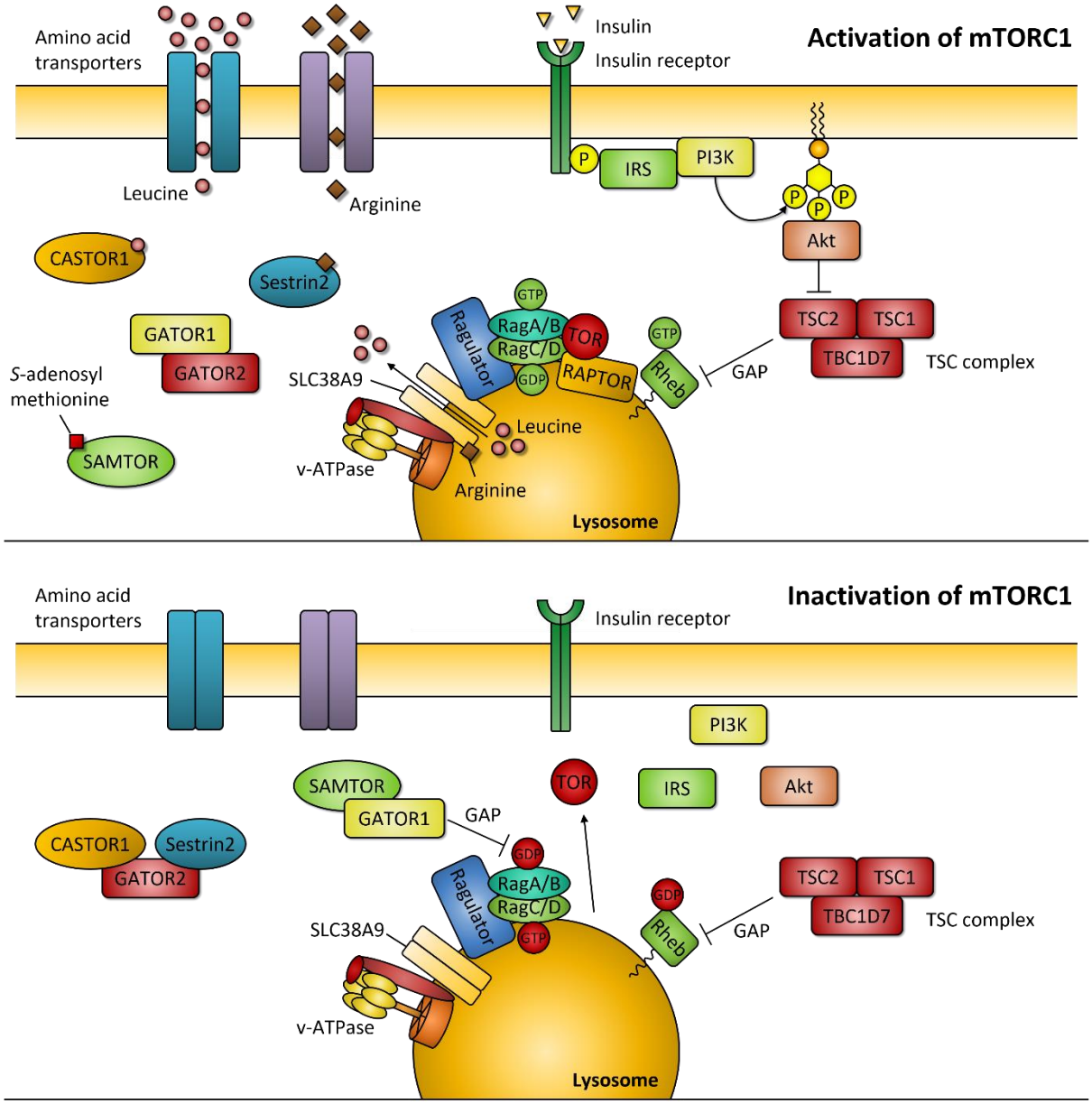

Figure 1.3. Molecular machinery for the recruitment and activation of mTORC1 and engagement with cytosolic and luminal amino acid sensing pathways.

mTORC1 is recruited to the lysosomal membrane by the GTP-RagA/B:GDP-RagC/D heterodimer, anchored on lysosomes by the Ragulator complex. mTORC1 is then activated by growth factor signalling via the PI3K-Akt-Rheb pathway. The nucleotide binding state of the Rag-GTPases is regulated by amino acid sensing pathways, including leucine-sensing CASTOR1, arginine-sensing Sestrin2 and *S*-adenosylmethionine-sensing SAMTOR. Under amino acid restriction, CASTOR1 and Sestrin2 sequester GATOR2 from GATOR1, which functions as a GAP for RagA/B. The GAP activity of GATOR1 is enhanced by the of binding SAMTOR. These events cooperate to convert the nucleotide binding state of Rag-GTPases, triggering the dissociation of mTORC1 from lysosomes. In addition, lysosomal arginine is sensed by SLC38A9, which exports hydrophobic amino acids, including leucine, in the presence of lysosomal arginine.

1.2.3.2 Amino acid sensing

The recruitment of mTORC1 to lysosomes is highly dependent on amino acid sufficiency, which is sensed by lysosomes via cytosolic and luminal mechanisms (Figure 1.3) (142, 143). The cytosolic pathway mainly involves modulating the GATOR1-GATOR2 regulatory complex in response to cytosolic arginine and leucine. GATOR1 functions as a RagA/B GAP, whereas GATOR2 interacts with and inhibits GATOR1 (144, 145). In other words, GATOR1 is inhibitory whereas GATOR2 is stimulatory to mTORC1 recruitment by Rag GTPases. CASTOR1 and Sestrin2 both operate by binding and inhibiting GATOR2 during low amino acid supply (146-150). During amino acid sufficiency, leucine-bound CASTOR1 and arginine-bound Sestrin2 dissociate from GATOR2 (147-151). Leucyl-tRNA synthetase (LRS) also functions as a RagC/D-GAP to cooperate with the RagA/B GEF activity of GATOR2 during leucine sufficiency (152, 153). Recently, the *S*-adenosylmethionine sensor upstream of mTORC1 (SAMTOR) was identified as a binding partner to GATOR1 during methionine starvation (154). Binding to SAMTOR promoted the inhibitory function of GATOR1, which was disrupted by re-supply of methionine and its endogenous conversion to SAM.

In addition the Rag-dependent mechanisms described above, cytosolic glutamine is required for Rag-independent recruitment of mTORC1 by Arf1 (155, 156). However, there is conflicting evidence surrounding whether this Rag-independent mechanism requires glutaminolysis to convert glutamine to the citric acid cycle intermediate α-ketoglutarate (α-KG). This discrepancy may be due to differences in the use of cell-impermeable α-KG versus cell-permeable α-KG derivatives, in addition to the lack of distinction between Rag-dependent and -independent mechanisms prior to the discovery of Arf1 in glutamine sensing (155-158).

The best characterised mechanism for luminal amino acid sensing is arginine sensing by the amino acid transporter SLC38A9. The binding of luminal arginine, liberated by protein degradation, to SLC38A9 triggers a conformational change that opens the channel for the export of hydrophobic amino acids (159-166). In addition, arginine-bound SLC38A9 functions as a RagA/B GEF via a mechanism that is independent of the Ragulator (159). Interestingly, exported leucine by SLC38A9 in response to luminal arginine may engage with cytosolic leucine-sensing machinery and thus may be required for mTORC1 re-activation after short-term starvation (165).

Intraluminal leucine may also be sensed by tumour suppressor FLCN, however the exact mechanism is unclear. During amino acid starvation, FLCN is recruited from the cytosol to lysosomes and promotes the retention of lysosomal leucine by inhibiting the leucine efflux channel PAT1 (167). While this seems counter-intuitive, other groups have also observed that FLCN is recruited to lysosomes by FNIP1/2 during amino acid starvation, after which FLCN interacts with inactive GDP-RagA/B and shows RagC/D GAP activity (168, 169). All groups observed that loss of FLCN reduced mTORC1 re-activation in response to amino acids, suggesting that FLCN does function with amino acid sensing machinery, however further research is needed to determine how the retention of lysosomal leucine during starvation signals to re-activate mTORC1.

1.2.3.3 Sensing cellular energy

Amino acids are potent activators of mTORC1, however they are not the only indicators of anabolic resources. Sensing amino acid concentration signals material sufficiency, but growth is also energetically demanding. Accordingly, lysosomes also evaluate cellular energy

by recruiting machinery that monitor the AMP:ATP ratio. The 5'-AMP-activated protein kinase (AMPK) is a heterotrimer of α kinase and regulatory β and γ subunits that activate or repress the kinase domain in AMP- or ATP-bound states, respectively (170). Interestingly, AMPK is recruited to and activated at lysosomal membranes by the Ragulator-axin-LKB1 complex during depletion of fructose-1,6-bisphosphate, a glycolysis intermediate (171-173). This mechanism can occur independent of changes to AMP:ATP ratio, but AMPK binding to LKB1 is strengthened in an AMP-bound state (172, 173). Active AMPK phosphorylates and activates TSC2, which inhibits Rheb and therefore prevents mTORC1 activation (174, 175). Thus, reduced glycolytic flux due to glucose depletion and a reduction in cellular energy, leading to a high AMP:ATP ratio, engages AMPK with a lysosomal energy sensor to inhibit mTORC1 activation. Together, energy sensing and amino acid sensing mechanisms cooperate to regulate both recruitment and activation arms of the mTORC1 signalling pathway.

1.2.3.4 Transcriptional control

Lysosome biogenesis is controlled by the microphthalmia transcription factor (MiT/TFE) family of transcription factors (107). Of this family, TFEB and TFE3 promote lysosomal function and autophagy by upregulating genes within the coordinated lysosomal expression and regulation (CLEAR) element network (138, 176). These include sets lysosomal and non-lysosomal genes, such as those that encode hydrolases (cathepsins A, B, D and F), membrane proteins (LAMP1, CD63, MPR), channels (TRPML1, ClC-7, CLN3), v-ATPase subunits, and proteins with roles in autophagy (Rab7, RagC, p62, LC3) (138, 176). In nutrient-replete conditions, TFEB is recruited to lysosomes by active GTP-RagA/B:GDP-RagC/D heterodimers and is phosphorylated by mTORC1 and ERK2, which promotes the binding of 14-3-3 to TFEB

and retains TFEB within the cytosol (140, 141, 177). During starvation, TFEB is dephosphorylated and dissociates from 14-3-3, promoting the translocation of TFEB to the nucleus to promote transcription of CLEAR genes (140, 178). Accordingly, upregulation of TFEB enhanced the biogenesis of autophagosomes and accelerated the degradation of long-lived proteins, consistent with an increase in autophagic flux, in addition to increased lysosome exocytosis (105, 178).

1.2.4 *Autophagy*

1.2.4.1 Overview

There are three main types of autophagy; macroautophagy (usually simply called autophagy), microautophagy and chaperone-mediated autophagy (CMA). Elements of macroautophagy and microautophagy involve selective or non-selective mechanisms that harvest cargo for degradation (179). Non-selective autophagy is triggered by starvation to recycle bulk cytoplasm, primarily by macroautophagy. Macroautophagy is the process by which expanding double-membrane structures (phagophores) sequester large cytosolic fractions to be delivered to lysosomes for degradation (Figure 1.4) (180). Microautophagy, on the other hand, is performed directly by late endosomes and lysosomes, whereby membrane protrusions or invaginations capture small quantities of proximal cytosolic material (181). As such, the formation of MVBs may be considered as both selective and non-selective forms of microautophagy. CMA is selective by definition and involves the delivery of proteins with a KFERQ motif by Hsc70 to the lysosomal membrane protein LAMP-2A (182). Binding to LAMP-2A triggers LAMP-2A multimerisation that facilitate substrate translocation into lysosomes called autophagy from now on) are the best characterised.

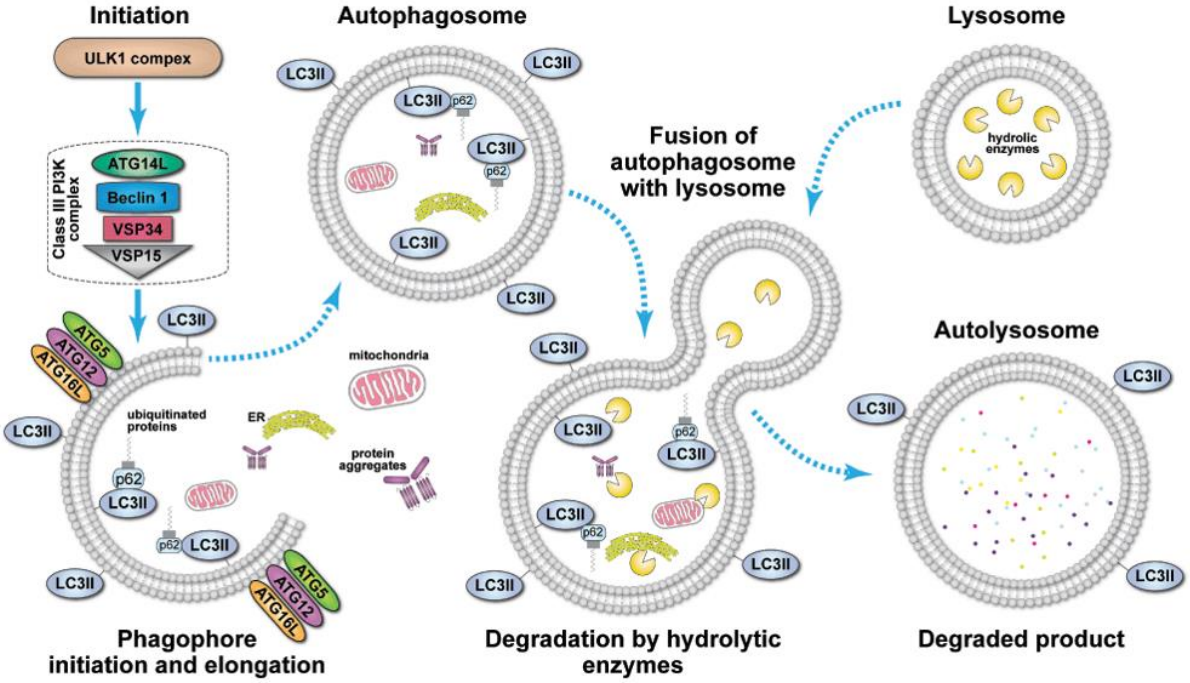

Figure 1.4. The generation of autophagosomes and fusion with lysosomes during macroautophagy.

Macroautophagy is initiated by the ULK1 complex recruiting the class III PI3K complex to the ER to generate PI(3)P-rich domains on omegasomes from which nascent phagophores nucleate. The ATG12 and LC3 ubiquitin-like systems cooperate to insert LC3-II into the limiting membrane of expanding phagophores. As phagophores expand, bulk cytosolic material and organelles are sequestered for degradation. Lysosomes then fuse with sealed autophagosomes to deliver lysosomal hydrolases to facilitate the degradation of autophagic cargo. Figure obtained from (183).

1.2.4.2 Generation of autophagosomes

The core autophagy machinery is composed of conserved autophagy-related (ATG) protein complexes and systems (179, 180, 184). In mammals, these are the ULK1/2 complex (ULK1/2-ATG13-RB1CC1/FIP200-ATG101) (136, 185-187), the ATG9 system (ATG2-ATG9-WIPI1/2) (188), the class III PI3K complex (PIK3C3-PIK3R4-BECN1-Ambra1-ATG14) (189) and the two ubiquitin-like conjugation systems LC3 (ATG3-ATG4A-D-ATG7-LC3-GABARAP) (190-192) and ATG12 (ATG5-ATG7-ATG10-ATG12-ATG16L1). To initiate autophagy, the ULK1/2 complex localises to the ER and recruits the class III PI3K complex to generate PI(3)P-rich domains within the ER, called omegasomes (193, 194). Nascent phagophores nucleate and expand using omegasomes as structural foundations (195). Phagophore membrane is suggested to be donated by several sources, including ER, Golgi, endosomes, plasma membrane, mitochondria, ATG9 vesicles and the omegasome itself (193, 196-201).

The ubiquitin-like conjugation systems engage with expanding phagophores. Firstly, ATG7 (E1-like) activates ATG10 (E2-like) which conjugates ATG12 (ubiquitin-like) to ATG5 (E3-like) (202, 203). Secondly, LC3 (ubiquitin-like) is cleaved by ATG4 to generate LC3-I, which is then transferred from ATG7 to ATG3 (E2-like) (202, 203). With both systems primed, ATG5-ATG12 interacts with ATG16L1 which together stimulate ATG3 to conjugate LC3 with phosphatidylethanolamine (PE), forming LC3-II (204-206). This anchors LC3-II to the limiting membrane of expanding phagophores, and as such the decoration of LC3-II is considered a signature for phagophores and nascent autophagosomes (closed phagophores). LC3-II is required for membrane tethering and hemifusion on autophagosomal membranes, which may be important for the incorporation of membrane from donor structures on expanding phagophores (207). Finally, ESCRT machinery and the VPS4 AAA-ATPase translocate to open

phagophore spheroids, where they facilitate phagophore closure by membrane scission (208-210).

Selective autophagy of specific targets is mediated by autophagy receptors that associate with what becomes the inner autophagic membrane. These targets include protein aggregates (aggrephagy), mitochondria (mitophagy), peroxisomes (pexophagy), ribosomes (ribophagy), ER (reticulophagy), lipid droplets (lipophagy) and intracellular pathogens (xenophagy) (211). Little is known about several of these pathways, however mitophagy is the best understood. Depolarisation of mitochondrial membranes activates the PINK1-Parkin axis that generates multiple poly-ubiquitin tracts on the surface of mitochondria (212-216). p62, in addition to other receptors with ubiquitin-binding domains, binds polyubiquitinated cargo and associates with LC3-II, targeting damaged mitochondria for degradation (212, 217-219). p62 is a major autophagy receptor and its accumulation within AVs is widely used as a marker of impaired AV maturation.

1.2.4.3 Maturation of autophagic vesicles

Autophagic vesicles (AVs) may be subdivided into three types, relating to their maturation: nascent autophagosomes, or initial AVs (AVi); amphisomes, or intermediate AVs (AVi/d), and; autolysosomes, or degradative AVs (AVd) (180). Maturation is determined by multiple rounds of fusion events between AVs and compartments at various stages of the endocytic pathway. The homotypic fusion and vacuole protein sorting (HOPS) complex is recruited to AVs by LC3-II to tether neighbouring compartments, which facilitates the assembly of SNARE complexes for membrane fusion (220-222). AVis are pre-fusion compartments and can be identified as closed double-membrane structures that are positive

for LC3-II but lack lysosomal hydrolases or membrane proteins. AVi/ds are derived by fusion of AVis with early or late endosomes. Thus AVi/ds may possess markers of varying stages of endosome maturation and therefore may themselves perform endosome-like functions, such as MVB formation, but importantly still lack hydrolases. Distinguishing features of these intermediates include a single limiting membrane with little internal degradation. AVds may be generated by fusion of degradative late endosomes or lysosomes with AVi/ds, or with AVis directly. This step delivers hydrolases for the degradation of internal cargo.

1.2.4.4 Regulation of autophagy

Under nutrient-rich conditions, mTORC1 phosphorylates ULK1 and ATG13 which inhibits the ULK1 complex (136, 137, 223). In addition, mTORC1 phosphorylates UVRAG and promotes its interaction with Rubicon, which negatively regulates the class III PI3K and the HOPS complexes, blocking both autophagy initiation and AV maturation (224). Conversely, AMPK phosphorylates and activates ULK1 during glucose depletion (137). Thus mTORC1 and AMPK facilitate switching between inhibitory and stimulatory states, respectively, to regulate autophagy. In addition to regulation via signalling molecules, autophagy may be regulated by the physical positioning of lysosomes and AVs within the cell. As described in the previous section on lysosome positioning, endosomes, lysosomes and AVs (likely AVi/ds that have inherited endosomal features) are bi-directionally motile compartments that traffic along microtubules by plus-end kinesin and minus-end dynein transport. In response to starvation, these compartments traffic to the perinuclear region to promote collisions between compartments (225). Finally, inactivation of mTORC1 during starvation promotes TFEB translocation to the nucleus to upregulate lysosomal genes within the CLEAR network.

Amongst these are genes that participate at several stages from initiation to maturation, including LC3, p62, BCLN1, UVRAG and Rab7 (138, 176).

1.2.4.5 Autophagic lysosome reformation

To maintain lysosome size and number in equilibrium, fusion must be balanced with fission. As such, lysosomes are regenerated by a process called autophagic lysosome reformation (ALR) (226, 227). Nutrients liberated by autophagy are sensed by autolysosomes and facilitate the reactivation of mTORC1 during short-term starvation (228). The reactivation of mTORC1 then signals the termination of autophagy and stimulates ALR (228). Interestingly, sugar export by spinster is required for mTORC1 reactivation to initiate ALR, with accumulation of enlarged autolysosomes lacking tubules seen in *spin* mutants (20). ALR begins with conversion of PI(4)P to PI(4,5)P_2 by PIP5K1B, which recruits the clathrin adaptor AP-2 to stimulate tubulation (229). Kinesins associate with nascent buds and effectively stretch tubules by plus-end transport (230). A second wave of PI(4,5)P_2 generation is facilitated at tubule tips by PIP5K1A which is required for tubule fission (229). The mechanism for fission is not yet characterised, but seems to require the recruitment of dynamin-1/2 (229). These nascent structures, called protolysosomes, re-enter the lysosome maturation pathway to facilitate re-acidification and replenish lysosomal hydrolases.

1.2.5 *Lysosomal contact with cellular membranes*

1.2.5.1 Overview of membrane contact sites

The occurrence of interorganelle membrane contact sites has long been observed but remain relatively under-characterised. These contact sites are suggested to have roles in the non-vesicular exchange of membrane lipids, proteins and ions between organelles (231). To this end, nuclear ER-vacuole junctions (NVJs) and vacuole and mitochondria patches (vCLAMPs) have been described (232). NVJs are established by tight interactions via the vacuolar protein Vac8 and the perinuclear ER protein Nvj1 (233, 234) and are sites of piecemeal microautophagy whereby perinuclear cargo is engulfed within vacuolar invaginations for degradation (235). NVJs are also implicated in the transfer of ceramides, sphingolipids, GPI anchors and phosphoinositides that require the synthesis of very-long-chain fatty acids within the ER (235).

1.2.5.2 Regulation of vCLAMPs

Lysosome-like organelles and mitochondria reciprocally regulate one another. For example, loss of cardiolipin synthesis in mitochondria limits vacuolar adaptation to high temperatures in yeast, causing vacuolar swelling and defective acidification (236). On the other hand, an age-related decline in vacuolar acidity causes mitochondrial dysfunction by promoting mitochondrial depolarisation and fragmentation (237). In yeast, the ER-mitochondria encounter structures (ERMES) complex tethers mitochondria to the ER and facilitates mitochondrial fission. ERMES and vCLAMPs contact mitochondria in equilibrium, whereby vCLAMP contact sites expand to compensate for deletion of ERMES components (238).

Vps39 is critical for vCLAMP formation, tethering vacuoles to mitochondria through interactions with the vacuolar Rab7 homolog Ypt7 and the outer mitochondrial membrane protein TOM40 (239). The formation of vCLAMPs by Vps39 is independent of its role in the HOPS complex (232, 239). Furthermore, the formation of vCLAMPs is inhibited by phosphorylation of VPS39 in response to respiratory growth conditions (232), while vCLAMPs are critical for cell survival during caloric restriction (239). Vps13 has also been observed to re-distribute between vCLAMPs or NVJs in response to changing metabolic states, suggesting that the formation and expansion of membrane contact sites are adaptations to metabolic flux (240, 241).

Due to the compensatory expansion of vCLAMPs when ERMES is blocked, it was initially reported that dual-deletion of MMM1 (ERMES) with Vps39, Vps13, Mcp1 or Mcp2 (vCLAMPs) is synthetic lethal (238, 240, 242). However a more recent study separated the HOPS and vCLAMP function of Vps39 and found that lethality was due to disrupted compensation by HOPS and not vCLAMPs (239). Moreover, rescue of ERMES-deficiency phenotypes, and thus vCLAMP expansion, by the Vps13-Mcp1 pathway required intact HOPS but not vCLAMP function of Vps39 (239, 240, 243). Therefore Ypt7-Vps39-Tom40 and Vps13-Mcp1 pathways participate at functionally distinct vCLAMPs (239).

1.2.5.3 Membrane contact sites in human disease

Curiously, proteins of the ERMES complex are not conserved in mammals. However, humans encode four VPS13 proteins (VPS13A-D) (244) and mutations to each cause non-overlapping neurodegenerative disorders; chorea-acanthocytosis with Huntington-like neurological phenotypes (VPS13A) (245, 246), Cohen syndrome with developmental delay and

intellectual disability (VPS13B) (247), early-onset autosomal recessive Parkinsonism (VPS13C) (248) and ataxia with spasticity (VPS13D) (249, 250). In yeast, Vps13 is required for the structural integrity of mitochondria and loss of Vps13 decreases lifespan and increases mitophagic flux (241). This is consistent with VPS13 mutations in humans, with reports of reduced membrane potential, altered morphology, reduced respiration and/or enhanced mitophagy when VPS13A, C or D are mutated (248, 250-252).

Surprisingly, VPS13 isoforms show differential cellular distribution, with VPS13A localising to mitochondria whereas VPS13B localises to the Golgi and VPS13C and D reside within endolysosomal structures (252-255). Furthermore, despite the reported localisation of VPS13A to mitochondria, the *Dictyostelium discoideum* VPS13A homolog, TipC, is required early in autophagosome formation and loss of VPS13A in humans reduces autophagic flux and causes MVB accumulation (251, 256, 257). Nonetheless, multiple lipid-binding domains within VPS13 proteins coordinate pairwise, or perhaps even ternary tethering between lysosomes, mitochondria, lipid droplets and the perinuclear ER (253). This suggests that VPS13 proteins may be critical for the clustering of organelles for non-vesicular lipid transport, autophagy and mitochondrial turnover by mitophagy. It is clear that more extensive characterisation of the machinery and conditions that regulate interorganellar contacts, and particularly their role in mammalian systems, will be key to elucidating the roles of individual disease-associated genes in the interplay between lysosomes and other organelles.

1.3 Lysosomes and neurodegeneration

1.3.1 *Alzheimer's Disease*

Alzheimer's disease (AD) is the most common form of dementia characterised by a decline in cognitive function including memory, language and behaviour (258). The presence of extracellular plaques of amyloid-β (Aβ) fibrils and intracellular tau tangles are pathological hallmarks of AD, however it is thought that smaller, soluble Aβ oligomers are the toxic species and that their generation correlates better with disease progression (259). Amyloidogenic processing of the amyloid precursor protein (APP) to generate Aβ partially occurs within the endocytic pathway (260). APP is trafficked through the secretory pathway to the plasma membrane and is endocytosed for degradation within lysosomes, or is recycled back to the plasma membrane in association with the retromer complex (261, 262). The α-secretase ADAM10 (a disintegrin and metalloproteinase domain-containing protein 10) is expressed at the plasma membrane and facilitates non-amyloidogenic processing of APP (263). In contrast, the β-secretase β-site APP cleaving enzyme (BACE) cycles between the plasma membrane and early endosomes and its cleavage activity is enhanced at acidic pH (264, 265). Also, the γ-secretase presenilin 2 (PSEN-2) resides within late endosomes and lysosomes, whereas PSEN-1 localises to the plasma membrane (266). The localisation of BACE and PSEN-2 to early and late endosomes, respectively, facilitates the sequential processing of APP to release Aβ within the lumen of late endosomes (267). Thus, the cellular distribution of APP is a key determinant in whether it is processed via amyloidogenic or non-amyloidogenic pathways. APP that is not cleaved by β or γ-secretases is ubiquitinated and sorted into MVBs for degradation within lysosomes (268). Interestingly, transcriptional upregulation of lysosomal function by TFEB

facilitates the degradation of APP by lysosomes which reduces Aβ production by as much as 50% in an APP^{Swe}/PSEN-$1^{\Delta E9}$ mouse model of familial AD (269).

Enlargement of Rab5-positive endosomes is the earliest phenotype that has been described in sporadic and familial AD pathology, occurring decades before the onset of dementia and even before birth in Down syndrome patients, who almost always develop AD due to triplication of *APP* on chromosome 21 (270, 271). Interestingly, endosome enlargement is concomitant with initial increases in intracellular soluble Aβ (272). Increases in the expression and activity of several lysosomal hydrolases, including cathepsins B and D and glycosidases, have been reported at pre-symptomatic stages, suggestive of a compensatory upregulation of lysosomal function (273-275).

There are also genetic links between lysosomes and AD. (276). The accumulation of $A\beta_{42}$ within MVBs is enhanced in mice expressing the Swedish APP variant (KM670/671NL, APP^{Swe}) (276). This accumulation of $A\beta_{42}$ was shown to impair receptor sorting and degradation within MVBs (276). Six-month-old mice expressing APP with both Swedish and Indiana mutations (Indiana: V717F, $APP^{Swe/Ind}$) have enlarged autolysosomes that accumulate LC3-II and lipids, and show impaired degradation in hippocampal neurons (277, 278). Mutations to PSEN-2 significantly increase the $A\beta_{42/40}$ ratio within late endosomes and lysosomes, by as much as > 50-fold with N141I PSEN-2 (266). The aggregation of both $A\beta_{40}$ and $A\beta_{42}$ is favoured at acidic pH, and while $A\beta_{40}$ aggregation occurs after a long lag phase, the lag time for $A\beta_{42}$ aggregation is significantly shorter (279, 280). As such, small increases in the $A\beta_{42/40}$ ratio decreases the length of the lag phase by a significant margin (281).

Interestingly, APP expression is increased in the brains of *Npc1*$^{-/-}$ mice and the levels of $A\beta_{40}$ and $A\beta_{42}$ are elevated in the cerebral spinal fluid of NPC patients (282, 283). There is evidence to suggest that the accumulation of cholesterol in NPC and of sphingolipids in Niemann-Pick types A and B (NPA/B), Tay-Sachs and Sandhoff diseases stabilises APP within lipid rafts, which favours amyloidogenic processing and increases Aβ production (284, 285). In addition, neurofibrillary tangles (NFTs) containing paired helical filament tau (PHFtau) are a hallmark of AD, but are also observed in NPC patients (270, 286, 287). Also, the phosphatidylinositol binding clathrin assembly protein (PICALM) was identified as a risk factor for AD (288). PICALM has putative roles the formation and degradation of autophagosomes and has been shown to co-localise with phosphorylated tau in AD, suggesting that PICALM may be required for the autophagic clearance of pathological tau accumulations (289, 290). Lastly, mutations to CLN11 have also been identified in a subset of AD cases, although CLN11 is more commonly associated with frontotemporal dementia and individuals can sometimes present with phenotypes that are indistinguishable from AD (291).

1.3.2 *Parkinson's Disease*

After Alzheimer's disease, Parkinson's disease (PD) is the second-most common form of neurodegeneration in humans (292). PD is characterised by a progressive decline in motor function with symptoms including tremor, bradykinesia, muscular rigidity and difficulties with speech (292). Genetic causes of early-onset PD include mutations to α-synuclein, leucine-rich repeat kinase 2 (LRRK2), Parkin, PINK1 and DJ1 (293). A major route for α-synuclein turnover is by lysosomes via autophagy and CMA, however A30P and A53T α-synuclein mutants, known

to cause familial PD, evade the CMA pathway (294). In sporadic cases, aggregates of α-synuclein have been observed to accumulate within structures containing LAMP1 and cathespin D-positive structures, suggestive of impaired clearance within lysosomes (295). The exact role for LRRK2 is not well understood, but it is thought to regulate autophagy through interactions with several Rab GTPases to regulate lysosome positioning (296). G2019S and R1441C LRRK2 mutations cause autosomal dominant PD (297).

Mutations in several genes associated with lysosomal storage disorders also cause or increase the risk of early-onset PD (298). These include mutations to glucocerebrosidase (Gaucher), sphingomyelin phosphodiesterase 1 (Niemann-Pick type A/B), Niemann-Pick type C1 protein, α-galacosidase (Fabry) acid β-galactosidase (GM1 gangliosidosis), α/β-subunits of β-hexosaminidase (Tay-Sachs and Sandhoff, respectively) and CLN12/ATP13A2/PARK9 (NCL12) (293). Parkinsonism is also a clinical manifestation of NCL2 and NCL10 (299, 300). Intriguingly, many of these proteins participate in the sphingolipid degradation pathway within lysosomes, highlighting a possible role for defective sphingolipid metabolism in the aetiology of PD. Indeed, α-synuclein deposits have been seen in the brains of several patients suffering from different sphingolipidoses (301). CLN12 has also been suggested to suppress α-synuclein toxicity (302, 303). Together, these observations suggest there may be overlaps between α-synucleinopathy and lysosomal storage disorders, particularly sphingolipidosis.

1.3.3 *Frontotemporal dementia*

Frontotemporal dementia (FTD) is used to classify a group of diseases that cause neurodegeneration with the frontal and temporal lobes, and together represent the third-

most common form of dementia after Alzheimer's disease and demetia with Lewy bodies (304). Patients with FTD present with a progressive decline in behaviour and language (304). Interestingly, heterozygous mutations in NCL genes have been linked to FTD. Heterozygous mutations to *CLN11* is the leading cause of early-onset FTD and account for 10% of all FTD cases (305-307). Storage of lipofuscin was observed in the retina and cortical neurons from *CLN11*-variant FTD patients, including those lacking clinical diagnosis of NCL (306). Reduced cathepsin D activity was also detected in fibroblasts from *CLN11*-variant FTD patients, suggesting that lysosomal function is impaired (306). Heterozygous mutations to *CLN7* were found to increase the risk of developing FTD (308). Enlarged lysosomes were detected in both sporadic and *CLN7*-variant FTD (308). Furthermore, the proteolytic activity of lysosomes was significantly reduced in fibroblasts from *CLN7*-variant FTD patients. This corresponded with an increased number of LC3 punctae, suggestive of a block in autophagosome maturation. However, the contribution of sporadic FTD to reduced lysosomal proteolysis and autophagic flux was not tested (308). Finally, a recent report found heterozygous mutations in *CLN13* in two cases of FTD, however further research is needed to conclude whether *CLN13* is a risk factor for FTD (309).

1.3.4 *Lysosomal storage disorder*

The lysosomal storage disorders (LSDs) are a group of > 70 inherited disorders with primary defects in lysosomal function (310). It is estimated that LSDs combined account for 1:5,000 live births that frequently lead to death in childhood (311). Often defects in lysosomal hydrolases, these disorders lead to the accumulation of undegraded storage material within

lysosomes. However, mutations in transporters are also known to cause LSD, such as the Niemann-Pick C1 protein in NPC and TRPML in mucolipidosis type IV. The build-up of storage material within lysosomes then leads to secondary blocks in general lysosomal function, particularly in autophagy (312-315). Interestingly, many of these disorders manifest neurological phenotypes in childhood and progress with neurodegeneration (311). However, the LSDs are too broad a set of disorders to describe each in detail here. Therefore, for the purposes of this thesis, I will focus on the neuronal ceroid lipofuscinoses.

1.3.4.1 Neuronal ceroid lipofuscinoses

The neuronal ceroid lipofuscinoses (NCLs), or Batten disease, are a group of monogenic, autosomal recessive disorders caused by mutations to ceroid lipofuscinosis, neuronal (CLN) proteins (316). These diseases are characterised by the accumulation of autofluorescent storage material within lysosomes and neurodegeneration, particularly in the cerebral and cerebellar cortices and the retina. Storage material typically contains a mixture of subunit c of the mitochondrial ATP synthase (SCMAS) and saposins, in addition to polysaccharides, glycoproteins, glycolipids, lipoproteins, phospholipids, and metal ions (317, 318). Originally, the NCLs were categorised according to the age of onset into congenital, infantile (INCL), late infantile (LINCL), juvenile (JNCL) and adult-onset (ANCL) diseases. While these descriptions infer severity, heterogeneity in clinical manifestations amongst gene variants from NCL to NCL meant that an onset-based nomenclature did not accurately define each disease. Instead, the NCLs are now named according to the causative gene, for example

a mutation in CLN1 causes CLN1 disease, or NCL1. Variants of each NCL may then be sub-divided by age of onset.

The CLN proteins are mainly lysosomal, including enzymes (CLN1, CLN2, CLN10, CLN13), membrane proteins (CLN3, CLN7, CLN12), and a soluble protein (CLN5), but also include ER membrane proteins (CLN6, CLN8), cytosolic proteins (CLN4, CLN14) and a secreted protein (CLN11) (318). Although functions for some of these proteins have been described, how loss of each protein individually causes NCL, and the molecular commonalities between the NCLs, are not well understood.

1.3.4.2 Soluble lysosomal CLN proteins

CLN1 encodes the lysosomal hydrolase palmitoyl protein thioesterase 1 (PPT1), which hydrolyses *S*-acylated proteins. Thus, CLN1 is likely required for the turnover of a cohort of membrane-associated proteins, with candidates including heterotrimeric G proteins and small GTPases. Extralysosomal CLN1 localises to axons and the presynaptic area in developing neurons within the retina and hippocampus (319). In addition, CLN1 expression through development matches synaptogenesis, peaking at young adulthood (320). These observations suggest a role for CLN1 in neuronal function and development. Indeed, a role for CLN1 in the cycling of synaptic vesicle exocytosis and endocytosis has been described (321, 322).

CLN2 encodes tripeptidyl-peptidase 1 (TPP1) and is the causative gene for autosomal recessive spinocerebellar ataxia 7 (SCAR7) (323). CLN2 is a serine protease that cleaves N-terminal tripeptides, however not much is known about its substrates. There are conflicting

accounts on whether CLN2$^{-/-}$ causes a defect in autophagosome maturation, which may be due to differences in the cell models used (324-326).

CLN5 is an extensively *N*-glycosylated, soluble lysosomal protein lacking hydrolase activity (327). CLN5 has been shown to interact with cation-independent MPRs and sortilin, and is required for Rab7-dependent recruitment of the retromer subunit Vps26 to endosomes (328). These observations suggest a role for CLN5 in protein sorting and vesicle trafficking between endosomal and TGN compartments.

CLN10 encodes the aspartic protease cathepsin D and is associated with most severe NCL described to date, with congenital onset and an expected survival of hours to days (329, 330). CLN10 is synthesised as an inactive preproenzyme that undergoes two cleavage events within lysosomes to generate mature enzyme, composed of two fragments linked by a disulphide bond (331). As a major lysosomal protease, CLN10 is central to protein turnover by autophagy, and as such loss of CLN10 is predictably associated with reduced autophagic clearance and accumulation of AVs (332, 333).

Mutations to a second cathepsin, the cysteine protease cathepsin F, also causes NCL, identifying cathepsin F as CLN13 (334, 335). Aside from its capacity as a lysosomal protease, not much is known about the role of CLN13 in NCL.

1.3.4.3 Lysosomal membrane CLN proteins

CLN3 is a multi-span transmembrane protein with 5-6 predicted transmembrane domains. Several distinct functions have been proposed in the literature. Firstly, CLN3 is implicated in protein sorting within secretory and endosome-lysosome networks, including

the delivery of hydrolases to lysosomes (336-338). In yeast, loss of the CLN3 orthologue Btn1p increases erroneous secretion of the hydrolase carboxypeptidase Y (337). In mammals, trafficking by proteins at least via the cation-independent MPR pathway is perturbed by reduced exit from the TGN (338). In addition, CLN3 binds galactosylceramide and sulfatides within lipid rafts and is proposed to possess palmitoyl desaturase activity, which may function to cluster acylated proteins, for example small GTPases, within lipid rafts (339, 340). CLN3 is also a putative member of the equilibrative nucleoside transporter family, suggesting that CLN3 may be an ion-coupled nucleoside exporter to recycle lysosomally-degraded polynucleotides. Lastly, disrupted autophagic clearance, sensitisation to oxidative stress and a general low-level accumulation of gangliosides have been reported in $CLN3^{-/-}$ models, which together may contribute to pathology (341-343).

CLN12/ATP13A2 is a lysosomal P_5 ATPase with a putative role in protection from Mn^{2+} toxicity (344). Originally described as a cause of autosomal recessive parkinsonism with dementia, homozygous mutations to CLN12 were later redefined as the cause of JNCL (345, 346). NCL12 patient-derived fibroblasts and primary neurons present several lysosomal phenotypes, including impaired acidification, enlarged lysosomes, reduced cathepsin activity, accumulation of autophagic vesicles and elevated LC3-II (303, 347).

CLN7, or major facilitator superfamily domain-containing 8 (MFSD8), is a putative lysosomal solute transporter. The function of CLN7 is described extensively in section 1.4.

1.3.4.4 Non-lysosomal CLN proteins

CLN4/cysteine-string protein α (CSPα) is a cytosolic chaperone protein that is peripherally associated with synaptic vesicle membranes (348). CLN4 has been shown to complex with Hsc70 and SGT, and interact with SNAP-25 and dynamin 1 at synaptic vesicles, suggesting a role for CLN4 in SNARE assembly during synaptic vesicle exocytosis (349-352).

CLN6 encodes a transmembrane protein that localises to the ER. Little is known about the function of CLN6 due to a lack of characterised protein homologs. Evidence suggests that *CLN6*$^{-/-}$ (*nclf*) mice exhibit an age-dependent decline in autophagic clearance associated with an accumulation of autophagosomes, presumably due to a block in AV maturation (353).

CLN8 is a membrane protein that, due to its KKXX ER-retrieval motif, predominantly localises to the ER and, to a lesser extent, the ER-Golgi intermediate compartment (ERGIC) (354). Mutations to CLN8 are associated with epilepsy with mental retardation (EPMR), in addition to NCL8 (355). CLN8 contains a so-called TRAM-LAG1-CLN8 (TLC) domain with a predicted role in ceramide biosynthesis based on homology to two other resident ER proteins, TRAM and LAG1 (356). Interestingly, a general depletion of several sphingolipids, including sphingomyelin, ceramide and galactosylceramide, in CLN8$^{-/-}$ MEFs and NCL8 patients have been reported (357-359).

Heterozygous mutations to progranulin were originally known to cause FTD, however phenotypes that resembled NCL were later observed in patients with homozygous mutations (360). Thus, progranulin was named CLN11. CLN11 is a secreted protein with growth factor-like properties, however the pathways it activates are ill-defined (361-363). As such, not much is known about the role of CLN11 in NCL.

Finally, *CLN14* encodes the cytosolic protein potassium channel tetramerisation domain-containing protein 7 (KCTD7) (364). Homozygous mutations in CLN14 are also associated with progressive myoclonic epilepsy (PME) with ataxia, possibly as a clinical manifestation of NCL14 (365-367). A role for CLN14 in the hyperpolarisation of neural membranes has been described, but how CLN14 function is linked to NCL is unknown (368).

1.4 CLN7 disease

1.4.1 *Disease presentation and histopathology*

NCL7 was characterised as a distinct form of vLINCL in 2007, with homozygous mutations in 9 consanguineous families mapping to *MFSD8/CLN7* (369). Nearly 40 mutations to CLN7 have since been identified, ~60% of which are missense, in addition to nonsense, frameshifts and splice defects (Figure 1.5) (370-372). NCL7 typically becomes symptomatic between the ages of 2-6 years, and commonly progresses with developmental regression, cognitive retardation, speech impairment, retinal dystrophy, ataxia, myoclonus, epileptic seizures and premature death (373-376). CLN7 expression is ubiquitous but very low in most tissues, with increased expression within the nervous system. In mouse retinae, CLN7 colocalises with post-synaptic density protein 95 (PSD-95) in the outer plexiform layer, which, in photoreceptors, corresponds to expression in pre-synaptic terminals (373, 377, 378). In mouse and rat brains, CLN7 is predominantly neuronal with highest expression in Purkinje and granule cells within the cerebellum, and in cornu ammonis 1 (CA1), CA3 and the dentate gyrus within the hippocampus (379, 380). Consistent with this, post-mortem analysis of NCL7 patients revealed an early, large scale reduction in granule neurons followed by later elimination of Purkinje cells within the cerebellar cortex (379). Significant accumulation of autofluorescent material was observed in the cell bodies of cerebral cortical neurons (376). In addition, the cerebellar cortex exhibited significant microglial activation and macrophages were shown to concentrate around strongly autofluorescent pyramidal neurons within the hippocampus, demonstrating widespread engagement of immune cells to clear degenerating neurons (379).

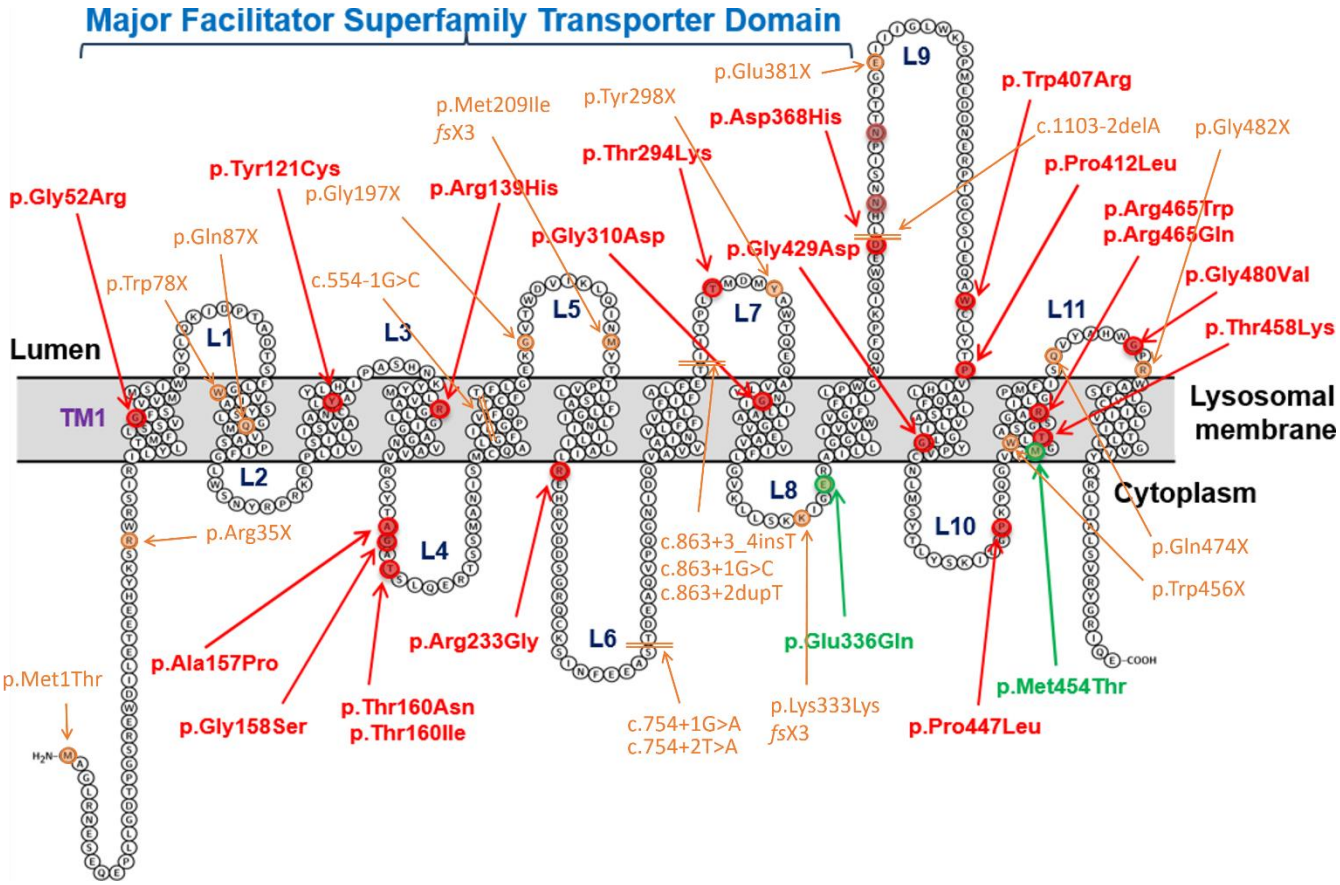

Figure 1.5. Map of disease-causing mutations to CLN7.

The location of missense, nonsense and frameshift mutations and splice defects are shown relative to the predicted topology of CLN7. The figure was adapted from (373). Loops 1-11 are designated L1-L11. In red and green are missense mutations annotated by (373), with known CLN7 disease mutations in red and mutations leading to nonsyndromic eye disease in green. Brown circles show the position of N-glycosylated Asn residues. Additional annotations were added in orange to illustrate nonsense mutations, frameshifts and splice defects that also cause CLN7 disease.

1.4.2 *Models of CLN7 disease*

1.4.2.1 Mice

Two mouse models of NCL7 have been established (380, 381). The first was generated by insertion of *lacZ*- and *neo*-cassettes spanning introns 1 and 2 of *CLN7* (*MFSD8*$^{tm1a/tm1a}$). This disruption did not completely abolish CLN7 expression, but did reduce expression to residual amounts as determined by Western blot. Thus, *MFSD8*$^{tm1a/tm1a}$ mice are hypomorphic. By 10 months of age, autofluorescent material was detected in Purkinje and granule cells of the cerebellum and in the CA3 region of the hippocampus, however this was not accompanied by detectable cell loss. At this age, *MFSD8*$^{tm1a/tm1a}$ mice also presented with moderate neuroinflammation and retinal degeneration. These phenotypes will almost certainly worsen with age, but 10 month old *MFSD*$^{tm1a/tm1a}$ mice at least resemble NCL7 in humans, perhaps with milder/slower phenotype development that could be useful to distinguish the timing of molecular events through disease progression.

The second mouse model (*MFSD8*$^{tm1d/tm1d}$, referred to here as *CLN7*$^{-/-}$) was derived from *MFSD8*$^{tm1a/tm1a}$ mice by Flp and Cre recombination to remove *lacZ* and *neo*-cassettes, deleting exon 2 in the process (381). The expected product of this deletion is a 95% truncated protein with no transmembrane domains (CLN7:p.E23F *fs*X16), therefore predicted to lack any CLN7 function. Disease progression was far more severe in these mice, with 50% mortality at 33 weeks and no survivors past 44 weeks, in contrast to no mortality reported in 10 month old *MFSD8*$^{tm1a/tm1a}$ mice. In addition, *CLN7*$^{-/-}$ mice presented with clasping phenotype, myoclonus and hindleg paralysis that were absent in *MFSD8*$^{tm1a/tm1a}$ mice. Rapid thinning of the retina and outer nuclear layer was seen between 0.5-2 month old *CLN7*$^{-/-}$ mice, which continued to decline at a slower rate until 4 months (382). By 3 months, autofluorescence was

detected in the cerebellum, cerebral cortex, hippocampus, thalamus and olfactory bulb, which intensified with age. This corresponded with increased storage of SCMAS and saposin D within brain homogenates, which are known to accumulate in NCL7 patients. Astrogliosis was observed in the hippocampus, cerebral cortex and thalamus, with onset at 5 months and became progressively worse with age. This *CLN7*$^{-/-}$ model therefore rapidly develops more severe NCL7-like phenotypes than their *MFSD8*$^{tm1a/tm1a}$ precursors, probably due differences in CLN7 activity, with likely no activity in the *CLN7*$^{-/-}$ model compared to a loosely-defined reduction in *MFSD8*$^{tm1a/tm1a}$ mice.

1.4.2.2 Cell-based models

Two cell-based models were derived from *CLN7*$^{-/-}$ mice for more detailed investigation of the cell biology of disease. Firstly, day 12.5 mouse embryonic fibroblasts (MEFs) were immortalised by transducing the SV40 large T antigen (381, 383). Secondly, postnatal day 4 mouse granule neuron progenitor cells (GNPCs) were isolated from cerebella and immortalised by transducing with temperature-sensitive SV40 large T antigen (tsA58/U19) (384). Both cell lines were established from very young tissues. While fibroblasts may be sufficient for describing general lysosomal phenotypes, GNPCs are a more attractive model to study NCL7. Granule neurons are among the most severely affected cells within the brains of NCL7 patients, with almost complete elimination during early stages (379). Thus the cell biology and lysosomal phenotypes within *CLN7*$^{-/-}$ GNPCs would likely correlate more closely with disease-relevant tissues *in vivo*. To this end, it would also be of benefit to establish an *in vitro* model of *CLN7*$^{-/-}$ photoreceptors, as another early target in NCL7 pathology.

1.4.2.3 Dogs

A spontaneous mutation to *CLN7* was reported in a Chinese Crested (385). At 1.5 years old, the dog presented with blindness and behavioural changes, which over a few weeks progressed with ataxia and cognitive decline. Post-mortem analysis found substantial storage of autofluorescent material in Purkinje cells and the granule cell layer of the cerebellum, and within cerebral cortical neurons. Moderate astrogliosis was detected within the cerebellar medulla. The authors subsequently discovered the individual was homozygous for the *CLN7:c.843delT* mutation, predicted to encode CLN7:p.F282L *fs*X13 lacking 5 C-terminal transmembrane domains.

A family of Chihuahuas harbouring mutations to CLN7, including two affected dogs, has also been described (386). Both dogs presented with visual decline and behavioural changes at 1-1.5 years old and were ataxic at age 2. MRI scans revealed significant atrophy of the cerebellum. Histopathological analysis during autopsy found autofluorescent storage material within neurons and astrocytes of the cerebral cortex, hippocampus, thalamus and cerebellum. Significant reductions in Purkinje and granule cell densities were seen, in addition to a population of shrunken Purkinje cells that were degenerating. Ganglion cell number within the retina was also reduced. Affected dogs were found to be homozygous for the same CLN7:p.F282L *fs*X13 mutation that was described in the Chinese Crested (385). Since these observations were reported, 5 additional unrelated Chihuahuas with similar clinical manifestations were reported homozygous for the same mutation (387, 388).

1.4.2.4 Non-human primates

Recently, spontaneous NCL7 was characterised in Japanese macaques (389). Affected individuals presented with significantly reduced cerebral and cerebellar volumes, particularly within grey matter. Autofluorescent storage material was present in cerebellar and cerebral tissue sections and a significant loss of neurons within granule and Purkinje cell layers was observed. In addition, progressive degeneration of retinal structure and function was tracked in one individual, which coincided with an accumulation of lipofuscin within the retina. Together, these phenotypes closely resemble several features of NCL7 in humans, providing a close model that may be valuable in the development and evaluation of therapeutic strategies.

1.4.3 *Cell biology and biochemistry*

Human CLN7 is a 518 amino acid protein predicted to fold as a 12-span membrane protein with cytosolic N- and C-termini (369, 379). CLN7 contains an N-terminal canonical dileucine motif and three YXXϕ tyrosine-based motifs (two at the C-terminus), all of which are present at the cytosolic side, which predict that CLN7 is trafficked to lysosomes (379, 390). Indeed, CLN7 colocalises with LysoTracker and LAMP1 punctae but not EEA1, corresponding to late endosomes and/or lysosomes, in a manner mostly dependent on the N-terminal dileucine motif (369, 379, 390, 391). CLN7 is post-translationally modified by *N*-glycosylation within the ER at N371 and N376 in a luminal loop between transmembrane domains 9 and 10 (379, 390). In addition, CLN7 has two putative cleavage sites for lysosomal cysteine proteases that flank these *N*-glycosylation sites (391). Two disease-causing mutations (T294K and P412L)

promoted cleavage, but this was not common to other selected mutants (391). Thus it cannot be distinguished whether increased cleavage itself causes disease in T294K and P412L mutants, or whether this is secondary to other loss-of-function mechanisms. In fact, most mutations are considered to be complete loss of function due to the consistent clinical presentation across variants, including large truncations and frameshifts. One notable exception is the substitution A157P, which presents with a delayed, JNCL phenotype.

Increases in LC3-II, p62 and ubiquitin were detected in total brain homogenates from 10 month old *CLN7*$^{-/-}$ mice. Furthermore, aggregates of p62 and ubiquitin were observed in the cerebellum, cerebral cortex, hippocampus and thalamus of *CLN7*$^{-/-}$ mice but not in controls. In addition, LAMP1-positive late endosomes and lysosomes were 30% larger in *CLN7*$^{-/-}$ cerebellar cells, whereas their number was unchanged (384). Together, these observations are suggestive of a defect in the maturation of autophagosomes or fusion with lysosomes (381). These accumulations coincided with increases in the transcription and lysosomal maturation of cathepsins B, D and Z, which suggest that lysosomal function is at least transcriptionally upregulated. In contrast, no accumulation of p62 or LC3-II were observed in *CLN7*$^{-/-}$ GNPCs. Furthermore, a general depletion of lysosomal proteins was observed in both *CLN7*$^{-/-}$ MEFs and GNPCs (383, 384). These included glycosidases (Siae, Aga, Gns), peptidases (Prcp, Cpq, Dpp7), lipidases (NAAA, $LPLA_2$) and an oxidase (Pcyox1), in addition to two NCL proteins (CLN5, cathepsin D/CLN10) and two proteins with unknown function (Npc2, Epdr1) (383). On the other hand, cathepsins S and K and prosaposin were upregulated (383). Inconsistencies in observations between models may be the result of comparisons between tissues of different age, whereby the brains of 10 month old *CLN7*$^{-/-}$ mice have degenerated significantly, compared to the much younger cell lines that are free of

storage material, autophagy defects and neuroinflammation. Thus, the depletion of lysosomal proteins is likely an early event, whereas transcriptional upregulation of cathepsins may be a compensatory response to a cycle of accumulating storage material and defective autophagy.

1.4.4 *Using Drosophila to model NCL*

CLN7 disease manifests early in human life, at ages 2-6 years old, presenting with developmental regression and severe neurodegeneration within cerebral and cerebellar cortices and the visual system. Such early pathology is suggestive of a fundamental role for CLN7 in neurodevelopment. To investigate this, a *Drosophila* model of NCL7 was recently established by our lab. *Drosophila* have been used to model several other forms of NCL (392, 393). A study into the evolution of CLN proteins revealed that *Drosophila* express orthologues of CLN1, CLN3, CLN7, CLN10 (Table 1.1) (394). More recently, an orthologue for CLN4 has been identified (395).

The accumulation of storage material and autofluorescent inclusions were also observed in the brains of *Drosophila* lacking *Ppt1/Cln1* (396), however there have been no reports of these accumulations in *Drosophila* lacking *Cln3*. Nonetheless, there is evidence of a conserved function for Cln3 in the oxidative stress response within the nervous system, which correlates with progressive oxidative damage in *Cln3*$^{-/-}$ mice and oxidative damage is known to cause lipofuscin accumulation and lysosomal dysfunction (342, 397-399). The accumulation of abnormal endo-membrane structures, another feature of NCLs, were seen in a *Drosophila* model of CLN4 disease (395). However, this was achieved by expression of gain of function mutants of human CLN4. Mutations to Drosophila *csp/Cln4* recapitulated abnormal protein

Table 1.1. The conservation of *CLN* genes and phenotype presentation in *Drosophila* models of NCL.

Human gene	Age of onset	Drosophila gene	Localisation/Function	*Drosophila* NCL phenotype	Reference
PPT1/ CLN1	Infantile	*Ppt1/Cln1*	Lysosomal palmitoyl hydrolase	Accumulation of storage material and lipofuscin.	(396)
CLN3	Juvenile	*Cln3*	Lysosomal transporter, oxidative stress response	None	(342, 398)
DNAJC5/ CLN4	Adult	*csp/Cln4*	Cytosolic chaperone protein, protein sorting	Accumulation of storage material when mutant *hCLN4* is expressed.	(395)
MFSD8/ CLN7	Late infantile	*Cln7*	Lysosomal transporter, function investigated here	Defects within the visual system and in locomotion. No lipofuscin observed.	(400)
CTSD/ CLN10	Congenital	*cathD/Cln10*	Lysosomal aspartic protease	Accumulation of lipofuscin.	(401)
TPP1/ CLN2	Late infantile	_____	Lysosomal serine protease	_____	
CLN5	Late infantile	_____	Lysosomal protein	_____	
CLN6	Late infantile	_____	ER membrane protein	_____	
CLN8	Late infantile	_____	ER membrane protein	_____	
GRN/ CLN11	Adult	_____	Secreted growth factor-like protein	_____	
ATP13A2/ CLN12	Juvenile	_____	Lysosomal ATPase, protection from Mn^{2+} toxicity	_____	
CTSF/ CLN13	Adult	_____	Lysosomal aspartic protease	_____	
KCTD7/ CLN14	Infantile	_____	Cytosolic protein, membrane hyperpolarisation	_____	

oligomerisation and accumulation within axons and neuronal somata of larval brains seen when hCLN4 mutants are expressed in *Drosophila*. It was not reported whether mutant dCSP/Cln4 expression causes the accumulation of abnormal endo-membrane structures.

Flies lacking *cathD/Cln10*, linked to the most severe form of NCL, were surprisingly viable and did not have a reduced lifespan (401). Nonetheless, autofluorescent material was shown to accumulate within neuronal cell bodies throughout the brain, which is a key feature of NCLs. However autofluorescence could only be detected in 15 day old adult flies (25 day post-hatch) at the earliest. This is in contrast to the relatively much earlier onset of pathology (congenital) during mammalian development, however in absolute terms, as soon as 25 days may be considered very rapid progression, but instead that *Drosophila* do not have a sufficiently long lifespan to develop more severe phenotypes. Therefore, *Drosophila* may not recapitulate the severity of NCL pathology the same way that mammalian models do, however this is not the reason for using *Drosophila* models. Instead, the strength of using *Drosophila* to model NCL is in the investigation of conserved genetic interactions, protein function and molecular mechanisms of CLN proteins during very early stages of the disease that underpin the severe neurological defects in mammals.

1.4.5 *Preliminary data*

Using a fluorescent CRISPR knock-in reporter (FLAG-Venus-Cln7), Cln7 expression was detected in photoreceptors, surface glia of the blood-brain barrier, and at the neuromuscular junction (NMJ) post-synaptic density (PSD) (402). Unpublished data found that deletion of Cln7 (*Cln7*^{84D}) caused synapses to under-develop at the NMJ via a mechanism originating from

the post-synaptic compartment. As a result of this, locomotion is impaired in wandering L_3 larvae, which may resemble ataxia in mammals. However, the mechanism underpinning these defects is not understood. Known regulators of synapse development include autophagy within the pre-synaptic compartment, and BMP signalling from the post-synaptic compartment, but both mechanisms were shown to be unperturbed in *Cln7*^{84D} flies. Defects within the visual system were also identified in *Cln7*^{84D} larvae. Under normal conditions, larvae respond aversively to light by burying into food to escape predation (403). However this evasive response was significantly reduced in *Cln7*^{84D} early third-instar larvae. This suggests that the role of Cln7 in the visual system may be conserved from mammals to *Drosophila*.

In addition to neurological phenotypes, *Cln7*^{84D} flies presented with a set of curious phenotypes, including *Cln7*^{84D} flies developing into visibly larger adults than wild-type controls, with enlarged wings that result from increased cell size and not cell number. *Cln7*^{84D} flies also survived longer than controls in starvation and oxidative stress resistance assays. While these phenotypes were unexpected in a model of a severe life-limiting disorder, they suggest that Cln7 may have a role in co-ordinating lysosomal responses to exogenous stresses. As such, potential regulation of TORC1 is an attractive possibility, as TORC1 functions at the surface of lysosomes and is a central regulator of several lysosomal functions in response to varied internal and external inputs.

1.5 Aims

Given that little is known about the function of CLN7, my research had two key aims. First, I investigated a role for Cln7 in the regulation of TORC1 signalling. To do this, I exploited the overgrowth phenotype of *Cln7*^{84D} flies to establish a phenotype modifier screen. This allowed me to investigate how *Cln7*^{84D} flies responded to dietary and genetic manipulations. Second, I aimed to characterise protein-protein interactions with Cln7 to investigate additional pathways that Cln7 may regulate and be regulated by. Here, I combined standard affinity purification methods with recently developed proximity labelling tools to capture and identify interacting proteins. For proximity labelling, I developed tools for *in vitro* and *in vivo* labelling of the Cln7 interactome, and established a set of *in silico* criteria for the filtering of hits. Together, these investigations utilised complementary approaches to elucidate putative roles for Cln7 in lysosomal biology and neurodevelopment.

2 MATERIALS AND METHODS

2.1 Solutions, reagents and equipment

All standard laboratory reagents were purchased from Sigma, unless stated otherwise. All media, buffers, oligos, plasmids and antibodies are listed in Tables 2.1-2.8. Oligos were synthesised by Eurofins Genomics. Plasmids were obtained from the Drosophila Gateway Vector Collection (DGRC). Manufacturers of specialist laboratory equipment and commercial buffers and kits are stated in-text.

2.2 Multiple sequence alignments

FASTA sequences, accession codes and transporter classification and IDs were obtained from the Transporter Classification DataBase (TCDB, www.tcdb.org). Distinct sequences allocated a common TCDB ID were annotated alphabetically in sequence. Human CLN7 was used for sequence alignments unless stated otherwise. CLN7 homologues were identified in non-human species using blastp searches against the human CLN7 sequence. Multiple sequence alignments were performed by simultaneously running several alignment tools made available by EMBL-EBI to reduce bias and identify consensus relationships. Where possible, alignments were performed over the maximum number of iterations (5 for Clustal Omega, 100 for MAFFT) to produce robust alignments. The relationships between aligned sequences were then estimated by Simple Phylogeny. Phylogenetic trees were visualised and exported using the open source software FigTree.

2.3 *Drosophila melanogaster* husbandry

Drosophila lines were procured from the Bloomington Stock Centre (University of Indiana) unless stated otherwise. Flies were maintained on standard food at low density at 18 °C and were flipped into fresh food every two weeks. Stock expansion and crosses were performed on semi-defined food at 25 °C. Crosses that generated genotypes for experiments were transferred to either 35 mm or 60 mm diameter egg-laying chambers (Kisker) on grape juice plates smeared with yeast paste to encourage egg laying. Females were allowed 24 h to lay eggs before the plates were replaced. Plates were incubated a further 24 h for larvae to hatch. L_1 larvae were then selected and developed on experimental foods at 25 °C.

Culture media was prepared according to recipes listed in Table 2.1. Foods containing inhibitors were prepared in the same way as SY food, with the addition of the appropriate amount of drug once the food had cooled to ≤ 60 °C. Inhibitors were dissolved in 100% ethanol and the total amount of ethanol added was equalised to 5% (v/v) across all drug concentrations including a control containing no drug.

2.4 Crossing schemes and generation of genetic stocks

All genetic stocks are listed in Table 2.9. Virgin females for crossing were collected twice a day when switching flies between day-time 8 h, 25 °C and night-time 16 h, 18 °C incubations. All adults were flipped from bottles before starting a virgin collection regime. As a general rule, experimental crosses between males and virgin females were performed using a ♂ > ♀ preference order of w^{1118} > $Cln7^{84D}$ > *RNAi* > *UAS* > *Gal4* lines. Transgenic lines were generated by the University of Cambridge Fly Facility, by microinjection of transgenes into

w^{1118} embryos for *P*-element transgenesis. Injectees were crossed to double-balanced *w*$^{-}$ flies and transgenic insertions were mapped by following *w*$^{+}$. A representative crossing scheme is shown in Figure 2.1, illustrating how transgenes were mapped and homozygous stocks were generated.

2.5 Measuring fly mass

Flies were crossed in egg-laying chambers at a female:male ratio of 3:1 to balance the number of eggs laid with population density. One hundred L_1 larvae were transferred from grape juice plates to vials containing 5 ml of experimental food per experiment to keep larva density consistent between vials. Flies were developed to adulthood at 25 °C and were massed one day post-eclosion to allow all adults to emerge and their mass to equilibrate. The adults were then separated by gender and split into at least 3 groups in cohorts of up to 10 flies per group. Group masses were taken and the mean mass per fly was calculated for each group.

2.6 Timing adult fly eclosion

One hundred L_1 larvae were developed on experimental food as described in section 2.5. The time at which larvae were placed in each vial was regarded time zero, and vials were placed immediately at 25 °C. Vials were monitored 1-2 times daily and the number of eclosed adults per vial were recorded with the date and time. Vials where no adults had emerged were still recorded at all times observed between experiment start and end points. The experiment ended when all flies from the most delayed experiment had emerged.

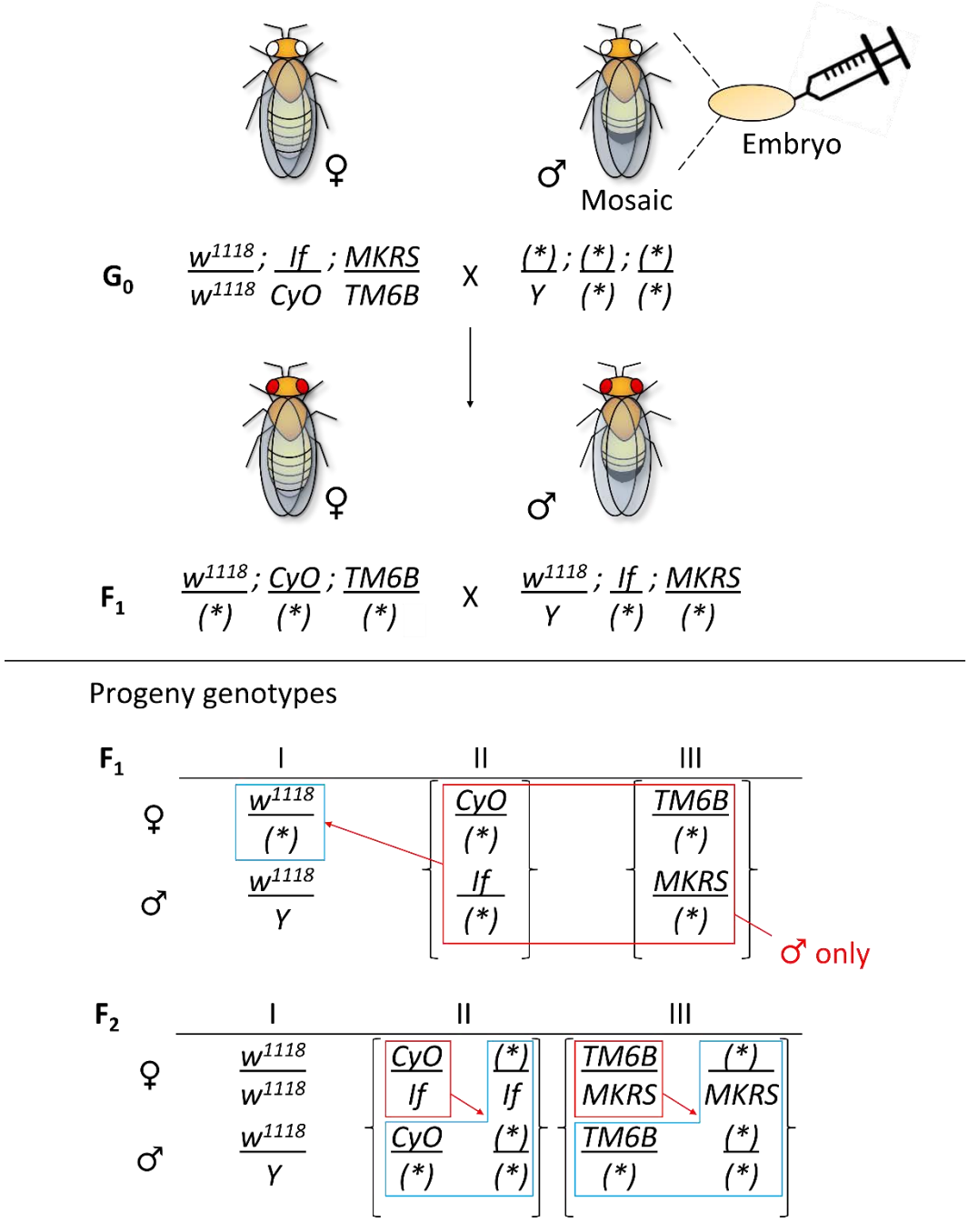

Figure 2.1. Crossing scheme for mapping transgenes.

Crosses between selected genotypes are given at the top. Underneath are Punnet squares mapping the possible genotypes of the progeny of each cross. In this example, transgenes carry a w^+ marker. An asterisk denotes a transgenic allele. An asterisk in parentheses represents a possible transgenic insertion. Curly brackets represent sets of genotypes possible in both males and females. If all progeny with genotypes highlighted in red boxes lack the transgene marker, transgenes may be mapped to genotypes in siblings marked by corresponding blue boxes.

2.7 Total glyceride assay

To quantify fat storage in adult flies, L_1 larvae from *w*^{1118} and *Cln7*^{84D} flies were selected and developed on SY food as described above. Three replicate samples of 10 flies for both genders were collected and washed in PBS to remove traces of food and their masses were recorded. Samples were then frozen at -80 °C. Total glyceride content was quantified using the Colorimetric Triglyceride Assay Kit (Cayman chemical). For sample preparation, flies were mechanically homogenised in 100 µl NP-40 substitute assay reagent with 1X protease inhibitors (Calbiochem) using a micro pestle. Homogenates were centrifuged at 10,000 x g for 10 min at 4 °C and the supernatants were transferred to fresh tubes. Glyceride concentration was then quantified according to manufacturer instructions, using a plate reader to measure absorbance at 540 nm. Protein concentration was measured in parallel with Pierce 660 nm Protein Assay Reagent (Thermo Scientific) using BSA standards.

2.8 Unbiased lipidomic analysis of *Drosophila melanogaster*

w^{1118} and *Cln7*^{84D} flies were expanded into bottles and developed on SY food. Female adult flies were collected into 1.5 ml eppendorf tubes in eight groups of approximately 100 flies per group, and the total mass was recorded. The flies were then frozen at -80 °C ahead of lipid extraction and analysis, performed by the Phenome Centre, University of Birmingham according to their standard protocol as follows.

2.8.1 *Sample preparation*

Samples of 90-200 mg of flies were transferred to Precylles tubes (Precellys, CK14, Stretton Scientific) and were homogenised in 500 µl of ice-cold isopropanol:acetonitrile (75:25 (% v/v); LCMS grade, HiPerSolv, VWR) per 90 mg of sample in a bead homogeniser (Precellys 24, Stretton Scientific) at 2 x 10 s bursts at 6,400 rpm, room temperature. Blank samples were prepared in the same way in the absence of *Drosophila melanogaster*. Samples were incubated on ice for 10 min, vortexed for 20 s and incubated a further 5 min to allow the extraction of lipids. Samples were then centrifuged at 20,000 x g for 20 min at 4 °C and 100 µl of the supernatant was loaded into HPLC vials (VI-04-12-02RVG 300µl Plastic, Chromatography Direct, UK). A sample for quality control (QC) was prepared by pooling 80 µl from each supernatant.

2.8.2 *Ultra performance liquid chromatography-mass spectrometry (UPLC-MS)*

Samples were analysed on a Hypersil GOLD C_{18} column (100 x 2.1 mm, 1.9 µm; Thermo Fisher Scientific, MA, USA). Mobile phase A consisted of 10 mM ammonium formate and 0.1% formic acid in 60% acetonitrile/water and mobile phase B consisted of 10 mM ammonium formate and 0.1% formic acid in 90% propan-2-ol/water. Flow rate was set for 0.40 $mL.min^{-1}$ with the following gradient: *t*=0.0, 20% B; *t*=0.5, 20% B, *t*=8.5, 100% B; *t*=9.5, 100% B; *t*=11.5, 20% B; *t*=14.0, 20% B, all changes were linear with curve = 5. The column temperature was set to 55 °C and the injection volume was 2 µL. Data were acquired in positive and negative ionisation modes separately within the mass range of 150-2000 *m/z* at resolution 70,000 (FWHM at *m/z* 200). Ion source parameters were set as follows: Sheath gas

= 50 arbitrary units, Aux gas = 13 arbitrary units, Sweep gas = 3 arbitrary units, Spray Voltage = 3.5 kV, Capillary temperature = 263 °C, Aux gas heater temperature = 425 °C. Data dependent MS^2 in 'Discovery mode' was used for the MS/MS spectra acquisition using following settings: resolution = 17,500 (FWHM at *m/z* 200); Isolation width = 3.0 *m/z*; stepped normalised collision energies (stepped NCE) = 20, 50, 80%. Spectra were acquired in three different mass ranges: 200 – 400 *m/z*; 400 – 700 *m/z*; 700 – 1500 *m/z*.

A Thermo ExactiveTune 2.8 SP1 build 2806 was used as an instrument control software and data were acquired in profile mode. Quality control (QC) samples were analysed as the first ten injections and then two QC samples at the end of the analytical batch. Two blank samples were analysed, the first as the 6^{th} injection and then at the end of each batch.

2.8.3 *Raw data processing and metabolite annotation*

Raw data acquired were converted from the instrument-specific format to the mzML file format applying the open access ProteoWizard software (404). Deconvolution was performed with XCMS software according to the following settings of min peak width = 6; max peak width = 30; ppm = 14; mzdiff = 0.001; gapInit = 0.4; gapExtend = 2.4; bw = 0.25; mzwid = 0.01 (405). Metabolite features were defined as unique *m/z*-retention time pairs, and were tabulated against sample ID. Features within a 5 ppm mass error and a retention time range of 2 s were grouped for molecular formula and metabolite matching. Spectra peak areas were included for each feature as a measure of abundance. Metabolites were assigned putative annotations using the PUTMEDID-LCMS workflows operating in the Taverna workflow environment (406). In some instances multiple metabolites share the same accurate *m/z* and

therefore cannot be distinguished. In these cases features were given multiple annotations. Conversely, a single metabolite may exist in multiple states, for example in distinct protonation states or as sodiated salts. All molecules were annotated according to guidelines for reporting of chemical analysis results, specifically to Metabolomics Standards Initiative level 2 (407).

2.8.4 *QC filtering and multivariate data analysis*

For each metabolite feature detected QC samples 1-8 were removed and the relative standard deviation (RSD) and percentage detection rate were calculated. Metabolite features with a RSD > 30% and a percentage detection rate < 60% were deleted from the dataset. Missing values in the data were replaced by values applying k nearest neighbour (kNN) missing value imputation followed by normalisation to sample total peak area, glog transformation and Pareto scaling prior to data analysis. Principal Components Analysis (PCA) was then performed in the web-based software MetaboAnalyst (408) to assess the technical variability (measured by the replicate analysis of a pooled QC sample) and biological variability as part of the quality control process. Areas under the Receiver Operator Curves (AUROC) were calculated.

2.8.5 *Univariate data analysis*

Data were normalised to sample total peak area. No missing value imputation, scaling or glog transformation was performed prior to data analysis. Metabolite fold changes between genotype pairs and Mann-Whitney U tests were calculated using the web-based

software MetaboAnalyst (408) and exported to Microsoft Excel for further analysis. Features with p values above 0.005 or with fold changes within ± 50% (0.66 to 1.5 fold) were excluded from analysis.

2.8.6 *Metabolite classification*

Metabolites were organised into structurally-related groups according to the online LIPID MAPS Structure Database (LMSD, www.lipidmaps.org). Structures published by the LSMD are systematically named according to guidelines provided by the International Union of Pure and Applied Chemists and the International Union of Biochemistry and Molecular Biology (IUPAC-IUBMB) Commission on Biochemical Nomenclature. Using these rules, metabolites were grouped into eight broad categories: fatty acyls, glycerolipids, glycerophospholipids, sphingolipids, sterol lipids, prenol lipids, saccharolipids and polyketides (409, 410). Within each category, lipids can be further subdivided into main and sub classes. Here, lipids were grouped into categories and main classes only. Metabolite features that were assigned multiple annotations spanning more than one category or class were placed in miscellaneous “mixed” groups. Lipids that did not fit any classification were classed as “others”. (Note, the terms “category” and “class” used here in the context of lipids are not synonymous and refer to broad and specific groupings, respectively).

2.9 Cloning

2.9.1 *Polymerase chain reaction (PCR)*

Diagnostic and cloning PCRs were performed using GoTaq G2 Flexi (Promega) and Phusion High-Fidelity PCR (Thermo) kits, respectively. Standard PCR mixtures contained 1X commercial buffer, 200 µM dNTP mix, 1.5 mM $MgCl_2$, 0.5 µM forward and reverse primers, 1-10 ng template DNA and 0.02 U/µl DNA Polymerase. Reactions were performed in a 96 well Tetrad 2 Peltier Thermal Cycler (BioRad) with an initial denaturation at 98 °C for 1 min, then 30 cycles of denaturation at 98 °C for 5 s followed by annealing plus extension at 72 °C for 30 s/kb, and concluded with a 10 min final extension at 72 °C. Reactions were analysed by agarose gel electrophoresis (AGE) to verify target amplification and product size.

2.9.2 *Transformation and plasmid preparation*

Plasmid DNA was incubated with 50 µl α-Select Gold Competent Cells (Bioline) on ice for 30 min. Cells were then heat-shocked at 42 °C for 30 s and recovered on ice for 2 min before adding 0.5 ml of super optimal broth with catabolite repression (S.O.C.) media. Cells were then incubated at 37 °C for 1 h in an orbital shaker. Cultures were spread on lysogeny broth (LB)-agar plates containing appropriate antibiotic and incubated overnight at 37 °C. Single colonies were selected for inoculation of PCR mixtures and selective LB. Inoculated cultures were incubated at 37 °C for 16 h with orbital rotation. Colony PCR was performed using external forward and internal reverse primers to check insert presence, size and directionality. Glycerol stocks were prepared from cultures validated by colony PCR by pelleting 1 ml of cell suspension at 12,000 x g for 1 min and resuspending the cells in 1 ml LB

with 15% v/v glycerol. The remaining culture was processed using GenElute plasmid preparation kits (Sigma) with elution in ddH_2O. Plasmids and glycerol stocks were stored at -20 °C and -80 °C, respectively.

2.9.3 *Gateway cloning*

Primers were designed to amplify the open reading frame (ORF) from target cDNA templates. Relative to ORF directionality, forward primers included a 5'-CACC motif for compatibility with TOPO cloning, and included the ATG start codon. Reverse primers excluded the stop codon. Respective inclusion and exclusion of ATG codon and stop codons ensured universal entry clone compatibility with the Gateway vectors containing N- or C-terminal tags. Products of the correct size were isolated and recovered from gels using the Wizard SV Gel and PCR Clean-Up System (Promega). To generate an APEX2-Cln7 fusion, N-terminal APEX2 and C-terminal Cln7 fragments were generated with complementary 15 bp overhangs, encoding a GGSGG linker. Purified fragments were then mixed with external primers for cloning by overlap extension PCR.

Products were cloned into pENTR using the pENTR/D-TOPO Cloning Kit (Thermo). Reactions were incubated for 5 min at room temperature before proceeding to transformation and plasmid preparation, as above. Transformants were selected for kanamycin resistance. Entry clones were verified by Sanger sequencing performed by Source BioScience, using appropriate primers to cover the whole insert from vector backbone to backbone. Verified entry clones were then recombined into destination vectors from the Drosophila Gateway Vector Collection (DGRC) (Table 2.6) using the Gateway LR Clonase II

enzyme mix (Invitrogen, Thermo). Reactions were incubated for 60 min at room temperature before proceeding to transformation and plasmid preparation, as above. Transformants were selected for carbenicillin resistance. Expression clones were checked by colony PCR to confirm insert presence, size and directionality. For constitutive over-expression in S2 cells, ORFs for Cln7, Rheb, APEX2, APEX2-Cln7, BioID and BioID-Cln7 were cloned into pAMW or pAFW, encoding an N-terminal 6xMyc tag or 3xFLAG tag, respectively. For inducible expression in S2 cells, ORFs for APEX2, APEX2-Cln7, BioID and BioID-Cln7 were cloned into pMT-DEST48, encoding a C-terminal V5 tag. To generate transgenic *Drosophila melanogaster* lines, ORFs for BioID and BioID-Cln7 were cloned into pTMW, encoding an N-terminal 6xMyc tag and carrying a genetic w^+ marker.

2.10 Cell culture

2.10.1 *Schneider S2R+ (S2) cells*

S2 cells were obtained from the Drosophila Genomics Resource Center (DGRC). Cells were grown in Schneider's *Drosophila* Medium (SchDM) containing L-glutamine (Gibco) supplemented with 10% (v/v) FBS and 1X PenStrep, with partial media changes every 2-3 days, and maintained at 27 °C with 5% w/w atmospheric CO_2 in a humidified incubator. Confluent flasks were passaged in the suspension phase by dissociating cell clumps and dislodging loosely adherent cells by moderate-intensity tapping and aspiration, and replacing 80-95% of the cell suspension with fresh media, depending on turbidity estimated by visual inspection.

Cells were cryopreserved by pelleting the cell suspension in a centrifuge at 1,000 x g for 5 min at room temperature, and resuspending the pellet to a concentration of 2 x 10^6

cells/ml in a 90:10 mixture of SchDM with 10% (v/v) FBS:DMSO, where the SchDM with FBS was a 50:50 mixture of fresh media and of conditioned media obtained from the supernatant after centrifugation. The suspension was split into 1 ml aliquots in cryovials and stored at -80°C.

2.10.2 *Transfection of S2 cells*

S2 cells were seeded in 6-well plates at approx. $3x10^6$ cells/well and settled for 24 h prior to transfection to allow cells to enter the adherent phase. A total of 2.5 µg DNA was transfected per well at a ratio of 1 µg DNA/3 µl TransIT-2020 transfection reagent (Mirus). To generate stable lines, the hygromycin resistance vector pCoHygro was co-transfected with construct DNA at a 1:1 mass ratio. Hygromycin-resistant cells were selected with 350 µg/ml hygromycin 72 h post-transfection. Every 48 h, cells were harvested and pelleted as above and were replated in the same wells with fresh selective media until resistant colonies were observed. Cells were allowed to reach confluence before expanding for cryopreservation.

2.10.3 *Mouse embryonic fibroblasts (MEFs)*

MEFs from wild-type (WT) mice and mice lacking CLN7 expression (strain *Cln7/Mfsd8*$^{tm1d/tm1d}$ (381), referred to here as CLN7$^{-/-}$) were obtained as a gift from Dr Stephan Storch (University Medical Centre Hamburg-Eppendorf). MEFs were immortalised by transducing the SV40 large T oncogene prior to the receipt of cells. MEFs were maintained at 37 °C with 5% w/w atmospheric CO_2 in a humidified incubator. Cells were grown in Dulbecco's Modified Eagle Medium (DMEM, Gibco) supplemented with 10% (v/v) FBS, 1X $_L$-glutamine and

1X PenStrep, with partial media changes every 2-3 days. When cells reached > 80% confluence, cells were passaged by first removing the media and washing the cells in PBS before incubating the cells in trypsin for 2 min, quenching with media and adding a fraction (between 10-50%, depending on experiments) to a new flask with fresh media.

Cells were cryopreserved by pelleting trypsinised cells in a centrifuge at 500 x g for 5 min at room temperature, and resuspending the pellet to a concentration of 10^6 cells/ml in a 90:10 mixture of DMEM with 10% (v/v) FBS:DMSO, where the DMEM with FBS was a 50:50 mixture of fresh media and of conditioned media obtained from cells prior to splitting. The suspension was split into 1 ml aliquots in cryovials and stored at -80 °C.

2.11 *In* vitro growth assays

MEFs were grown to approximately 70% confluence in T75 flasks before splitting and seeding into 6-well plates at 3 x 10^5 cells/well in 1 ml culture media described above. Cells were allowed to settle and grow for between 24-48 h until cells reached approximately 40% confluence. The media was removed and cells were washed of residual media in Earle's Balanced Salt Solution (EBSS) once and then starved by incubating in 1 ml EBSS for 24 h. For a full recovery, MEFs were then re-fed 1 ml of EBSS supplemented with 10% FBS + 4 µg insulin, 1X amino acid mixture and 5.5 mM $_D$-glucose, with the final solution adjusted to pH 8.0 to match unmodified EBSS. Partial recovery media was prepared by omitting one of the additions. Cells were incubated in recovery media for 1 h before harvesting, which entailed placing cells on ice, discarding the media and lysing cells directly by adding 100 µl 1X RIPA buffer with protease and phosphatase inhibitors to the wells and scraping the cells into the

buffer. Lysates were centrifuged at 15,000 x g for 10 min at 4 °C to pellet cell debris and the supernatants were transferred to fresh tubes. Protein concentration was quantified in 96-well plates by adding 150 µl Pierce 660 nm Protein Assay Reagent to 10 µl protein sample, performed in triplicate, and measuring the A_{660} in a plate reader. Protein concentration was equalised with ddH_2O before adding 1X Laemmli buffer and heating at 95 °C for 5 min ahead of Western blotting. Samples were either loaded immediately or stored at -20 °C.

2.12 Western blotting

Samples prepared in 1X Laemmli buffer were heated for 3-5 min at either 70 °C for membrane proteins or 95 °C for soluble proteins immediately before separation by SDS-PAGE. Where necessary, loading volumes were equalised for total protein concentration. Proteins were allowed to stack for 15 min at 75 V before being separated for 60-90 min at 150 V. Proteins were then either visualised in-gel by staining with InstantBlue (Expedeon) according to the manufacturer's instructions or continued onto Western blot. Blotting paper (3 mm, Whatman) and PVDF membranes (0.45 µm, Invitrogen) were cut to match gel size and were equilibrated in 1X transfer buffer; PVDF membranes were activated in 100% methanol for 30 s prior to equilibration. Gels were also equilibrated in 1X transfer buffer for 10 min. Proteins were transferred by wet transfer for 30-60 min at 1.5 mA.h/cm^2, using cold transfer buffer and an ice pack to minimize overheating. Membranes were blocked for 30 min at room temperature in fresh membrane blocking solutions (Table 2.3) before incubation with primary antibody overnight at 4 °C. Membranes were then washed five times for 5 min each in TBST, incubated in secondary antibody for 1 h at room temperature and washed again, five times

for 5 min each in TBST. Direct conjugates were treated like secondary antibodies. For visualisation by film, membranes were incubated in ECL (Thermo) for 1 min prior to exposure with X-ray sensitive film (Amersham). Alternatively, membranes were left in ECL for electronic chemiluminescence detection using a Fusion FX imager (Vilber).

2.13 Immunofluorescence

2.13.1 *Immunocytochemistry*

Sterile 15 mm circle coverslips were coated with concanavalin A for 1 h and washed with ddH_2O. Coated slips were seeded directly with 10^6 S2 cells and incubated for 2-4 h to allow cells to settle and adhere. Alternatively, slips were placed in plates being seeded at 3 x 10^6 cells/ml and cells were grown in the adherent phase to 70-80% confluence. Slips were gently washed with PBS to remove loosely adherent cells. All incubations were done with gentle rocking. Cells were fixed with ice cold 4% v/v formaldehyde in PBS for 10 min, then for 7 min in 100% methanol at -20 °C. Fixatives were washed off with PBS and cells were permeabilised and blocked in ICC block (Table 2.3) for 30 min at room temperature. Cells were incubated in primary antibody diluted in ICC block overnight at 4 °C. Slips were washed five times in TBST for 5 min each, and incubated in secondary antibody diluted in ICC block for 1 h at room temperature. Cells were washed again five times in TBST for 5 min each. Nuclei were stained with Hoechst 34580 (Thermo) for 10 min at a 1:10,000 dilution in TBST. Coverslips were dabbed dry with Kimwipes and mounted onto Superfrost Plus microscope slides (Thermo) in small drops of ProLong Gold Antifade Mountant (Thermo). Slips were set

overnight at 4 °C in the dark. Cells were imaged using a Zeiss LSM780 Confocal Microscope equipped with a Zen black edition interface. Images were edited in Zen blue edition.

2.13.2 *Immunohistochemistry*

Drosophila larval neuromuscular junction (NMJ) dissection and immunohistochemistry was performed by Richard Tuxworth as described previously (411, 412). Wandering third-instar larvae were dissected in cold HL3.1 medium under a dissecting microscope (413). Larvae were stunned by cold shock in HL3.1 for 3 min and pinned in place on sylgard dishes. Larvae were filleted along the dorsal midline and the organs were removed. Filleted larvae were fixed in 4% v/v formaldehyde in HL3.1 for 20 min at room temperature and then washed twice in HL3.1 for 5 min each. Fixed tissues were then transferred to 1.5 ml tubes and further incubations were performed at room temperature with gentle mixing on a nutator mixer unless otherwise specified. Tissues were permeabilised in PBS containing 0.3% v/v Triton X-100 (PBSTx) for 30 min, and then blocked in IHC block (Table 2.3) for 30 min. Samples were then stained in primary antibody diluted in IHC block overnight at 4 °C. Preps were washed three times in IHC block for 15 min each, and then incubated with secondary antibody diluted in IHC block for 2 h. Tissues were washed again three times in IHC block for 15 min each. Samples were mounted onto Superfrost Plus microscope slides (Thermo) in small drops of ProLong Gold Antifade Mountant (Thermo). Slides were set overnight at 4 °C in the dark. NMJ preps were imaged using a Zeiss LSM880 Confocal Microscope equipped with a Zen black edition interface. Images were edited in Zen blue edition.

2.14 Immunoprecipitation

2.14.1 *Immunoprecipitation from cells*

Transiently transfected cells were harvested 24 h post-transfection, washed once in PBS, and lysed in 0.5 ml S2 lysis buffer on ice. Lysates were clarified by centrifugation at 16,000 x g for 10 min at 4 °C. Lysate fractions were taken and the remainder was incubated with 20 µl Myc-Trap_MA beads (ChromoTek) or α-FLAG M2 Affinity gel (Sigma) overnight at 4 °C with end-over-end rotation. Precipitates were washed five times in S2 lysis buffer, eluted in 50 µl 0.2 M glycine-HCl pH 2.5, neutralised with 5 µl 1 M Tris-HCl pH 10 and prepared in Laemmli sample buffer. Samples were heated at 70 °C for 5 min prior to loading onto gels for analysis by Western blot.

2.14.2 *Immunoprecipitation from Drosophila tissue*

For native extraction of FLAG-VenusYFP-Cln7 from flies, all steps were performed on or immediately transferred to ice, or kept at 4 °C. Initially, 200 mg of a mixture of adult male and female flies were lysed in a bead homogeniser (FastPrep-24 5G) for 20 s at 6.5 m/s in 750 µl lysis buffer containing no detergent. Homogenates were centrifuged at 2,000 x g for 10 min to remove debris and 750 µl lysis buffer containing 2X detergent was added to the supernatants for 10 min. Samples were clarified by centrifugation at 15,000 x g for 10 min. A 50 µl sample of the supernatant was taken as the input and the remainder was incubated on 20 µl α-FLAG M2 affinity gel (Sigma) with rotation overnight. The unbound fraction was removed and the beads were washed in 1 ml lysis buffer five times for 5 min each. Bound proteins were eluted into five fractions each with 50 µl lysis buffer containing 100 µg/ml

3xFLAG peptide for 10 min, and 5 µl samples were taken from each. The eluates were pooled and incubated on 20 µl GFP-Trap MA beads (Chromotek) with rotation overnight. The unbound fraction was removed and the beads were washed as before. Proteins were eluted into two fractions with 50 µl 0.2 M glycine-HCl, pH 2.5 for 1 min and fractions were quenched with 5 µl 1M Tris-HCl, pH 10.0. All samples for analysis by Western blot were prepared in 1X Laemmli buffer and were either analysed immediately or stored at -20 °C. Samples were not boiled prior to SDS-PAGE to avoid the aggregation of membrane proteins in the wells of polyacrylamide gels.

When troubleshooting, 5-10 adult flies or third-instar larvae were mechanically lysed by hand using a micropestle with 500 µl lysis buffer and incubated for 20 min. Homogenates were centrifuged at 2,000 x g for 10 min to remove debris, and then once more at 15,000 x g for 10 min to clarify the samples. All further steps were performed as above, varying only by the changes specified in the text.

2.15 Proximity labelling

2.15.1 *In vitro APEX2 labelling*

The labelling protocol was followed according to Hung *et al.* (414). S2 cells expressing APEX2 and APEX2-Cln7 were grown in 6-well or 15 cm plates for small or large scale labelling, respectively. Cells were grown to 90% confluence in the adherent phase before initiating labelling. All labelling reagents were freshly prepared. Cells were incubated in media containing 500 µM biotin-phenol (BP) for at least 1 h. Labelling was initiated by incubation with 1 mM H_2O_2 for 1 min and then quenched by replacing the labelling media with three

washes of quencher solution. Cells were then processed for analysis by immunofluorescence or Western blot. All further steps were performed on ice or at 4 °C, or at room temperature with buffers containing SDS. Biotinylated proteins were extracted by lysis in 100 µl or 10 ml RIPA buffer (depending on plate size) supplemented with quenchers for 10 min. Lysates were clarified at 16,000 x g for 10 min. A lysate fraction was taken and the remainder was incubated on 10 µl or 50 µl NanoLink Streptavidin Magnetic Beads (TriLink Biotechnologies) pre-washed in TBST, overnight with end-over-end rotation. Flow-throughs were kept and beads were washed in 1 ml volumes with RIPA buffer twice, once each with APEX2 washes 1, 2 and 3 (Table 2.3), and twice again with RIPA buffer. Proteins were eluted in 50 µl Laemmli sample buffer supplemented with 2 mM biotin at 98 °C for 3 min.

2.15.2 *In vitro BioID labelling*

The labelling protocol was followed according to Roux *et al.* (415). S2 cells expressing BioID and BioID-Cln7 were grown in 6-well or 15 cm plates for small or large scale labelling, respectively. At first, cells were grown to 90% confluence with mixed adherent and suspension populations and incubated for 24 h with 500 µM biotin dissolved in 0.1 M NaOH. Later iterations omitted the incubation with biotin. Cells were washed in PBS three times to remove free biotin before being processed for analysis by immunofluorescence or Western blot. All further steps were performed on ice or at 4 °C, or at room temperature with buffers containing SDS. Biotinylated proteins were extracted by lysis in 100 µl or 10 ml BioID lysis buffer (depending on plate size) for 10 min. Lysates were sonicated for 10 s, followed by the addition of Triton X-100 to 2% (v/v) final concentration and an equal volume of 4 °C 50 mM Tris-HCl pH

7.4, with further sonication after each addition. Lysates were then clarified at 16,000 x g for 10 min. A lysate fraction was taken and the remainder was incubated on 10 µl or 100 µl NanoLink Streptavidin Magnetic Beads (TriLink Biotechnologies) pre-washed in TBST, overnight with end-over-end rotation. Flow-throughs were kept and beads were washed in 1 ml volumes twice with BioID wash 1, once with BioID washes 2 and 3, and twice with BioID wash 4 (Table 2.3). Proteins were eluted in 50 µl Laemmli sample buffer supplemented with 2 mM biotin at 98 °C for 3 min.

2.15.3 *In vivo BioID labelling*

Female *UAS-Myc-BioID-Cln7 (II)* flies were crossed to *Mef2-Gal4* males to drive Myc-BioID-Cln7 expression in muscles. Progeny were reared on SY food supplemented with 1 mM biotin from a 50 mM stock dissolved in 0.1 M NaOH. Absence of *CyO, GFP* inheritance was used to score for Myc-BioID-Cln7 expression. GFP^+ animals were used as no BioID controls. Proximity labelling was analysed either by immunohistochemistry or by Western blot. For Western blots, five wandering third-instar larvae and one-day-old adults were homogenised in 500 µl RIPA buffer and clarified by centrifugation at 2,000 x g for 10 min at 4 °C. Supernatants were spun again at 16,000 x g for 10 min at 4 °C. Laemmli sample buffer was added and samples were heated to 70 °C for 5 min. Samples were either immediately analysed by Western blot or stored at -20 °C.

2.16 Identification of proximity-labelled proteins

2.16.1 *Preparing gel slices for protein identification*

All equipment and surfaces were washed in 70% ethanol while wearing gloves to minimise contamination with keratin. Purified proteins labelled by BioID or BioID-Cln7 were separated by SDS-PAGE and visualised with InstantBlue stain overnight for maximum sensitivity. Stained gels were destained in ddH_2O for 10 min three times. Gels were illuminated on a light box with white light and lanes containing BioID and BioID-Cln7 were isolated with a razor and aligned. Both lanes were cut together into protein size-matched, 1 cm x 0.5 cm (h x w) slices and placed in 1.5 ml eppendorf tubes and sealed with parafilm. Slices were stored at -20 °C prior to protein extraction and analysis, performed by the Advanced Mass Spectrometry Facility, University of Birmingham according to their standard protocol as follows.

2.16.2 *Trypsin digestion*

Forty microliters of 100 mM NH_4HCO_3, pH 8.0, was added to gel slices (containing ~1-100 µg protein) followed by 50 µl of 10 mM dithiothreitol (DTT), and were incubated at 56 ^oC for 30 min. Samples were then cooled to room temperature. Cysteine residues were alkylated by addition of 50µl 50 mM iodoacetamide with a 30 min incubation at room temperature in the dark. Proteins were digested with 25 µl 6 ng/µl Trypsin Gold (Promega) and incubated at 37 ^oC overnight. Peptides were reconstituted in 0.1% formic acid (solvent A).

2.16.3 *High performance liquid chromatography-tandem mass spectrometry (HPLC-MS/MS)*

Peptide concentration and separation was performed using the UltiMate 3000 HPLC system (Dionex, Thermo). Samples were trapped on Acclaim PepMap 100 C18 u-Precolumn cartridges (300 µm x 5 mm, 5 µm, 100 Å, (Dionex, Thermo)) and separated in Acclaim PepMap 100 C18 columns (75 µm x 150 mm, 3 µm, 100 Å, (Dionex, Thermo)). A gradient of 3.2% to 44% solvent B (0.1% formic acid in acetonitrile) was applied for 30 min. Columns were then washed with 90% solvent B before re-equilibrating with 3.2% solvent B. Peptides were eluted (~350 nl min^{-1}) via a TriVersa NanoMate nano-electrospray ionisation (nESI) ion source (Advion) into a Q Exactive HF Quadrupole-Orbitrap Mass Spectrometer (Thermo). The spray voltage was set to 1.7 kV with a heated capillary at 275 °C.

The mass spectrometer performed a full Fourier transform (FT) MS scan (*m/z* 360−1600) and subsequent higher-energy collisional dissociation (HCD) MS/MS scans of the 20 most abundant ions with a dynamic exclusion time set to 20 s. Full scan mass spectra were recorded at a resolution of 120,000 at *m/z* = 200 and ACG target of 3 x 10^6. Precursor ions were fragmented in HCD MS/MS with resolution set to 15,000 and a normalized collision energy of 28%. The ACG target for HCD MS/MS was 1 x 10^5. The width of the precursor isolation window was 1.2 *m/z* and only multiply-charged precursor ions were selected for MS/MS. Spectra were acquired for 56 mins.

The MS and MS/MS scans were searched against the UniProt database using the Sequest HT algorithm in Protein Discoverer 2.2 (Thermo). Variable modifications were deamidation (N and Q), oxidation (M), phosphorylation (S, T and Y) and biotinylation (K and R). The precursor mass tolerance was 10 ppm and the MS/MS mass tolerance was 0.02 Da.

Two missed cleavage was allowed and hits with at least two high confidence peptides were accepted as true. The threshold for false discovery rate (FDR) was set at 1%. The results were exported to Microsoft Excel for filtering and analysis.

2.16.4 *Data filtering and lead identification*

A flow diagram illustrating the data filtering process is shown in Figure 2.2. Raw data files of all gel slices isolated from a common sample were combined into a master file. Contaminants were removed by filtering for *Drosophila melanogaster*. The data were then condensed, listing UniProt accession, protein description and the total peptide spectrum matches (PSMs), protein-unique peptides, biotin modifications and number of experiments in which hits had been identified. Peptides shared between orthologous proteins from different *Drosophila* species were re-classified as unique, whereas peptides shared between different proteins from *Drosophila melanogaster* only were not distinguished. Full-length protein mass and cellular localisation were obtained from UniProt. PSMs were normalised to the mass of the full-length protein (PSMs/10kDa) to account for differences in protein size and allow compartment labelling densities to be compared. For proteins with multiple cellular localisations, PSMs and PSMs/10kDa were split equally between compartments.

Hits were separated into groups of unique and shared proteins between BioID and BioID-Cln7 samples. For shared proteins, an enrichment factor (EF) was calculated as the ratio of PSMs between the samples. Proteins were then categorised by the fulfilment of several criteria: unique to BioID; unique to BioID-Cln7; shared with $EF \leq 0.5$, $0.5 < EF < 2$ or $EF \geq 2$; ≥ 5 PSMs; biotin label detected; identified in 2 experiments. Proteins with an enrichment factor

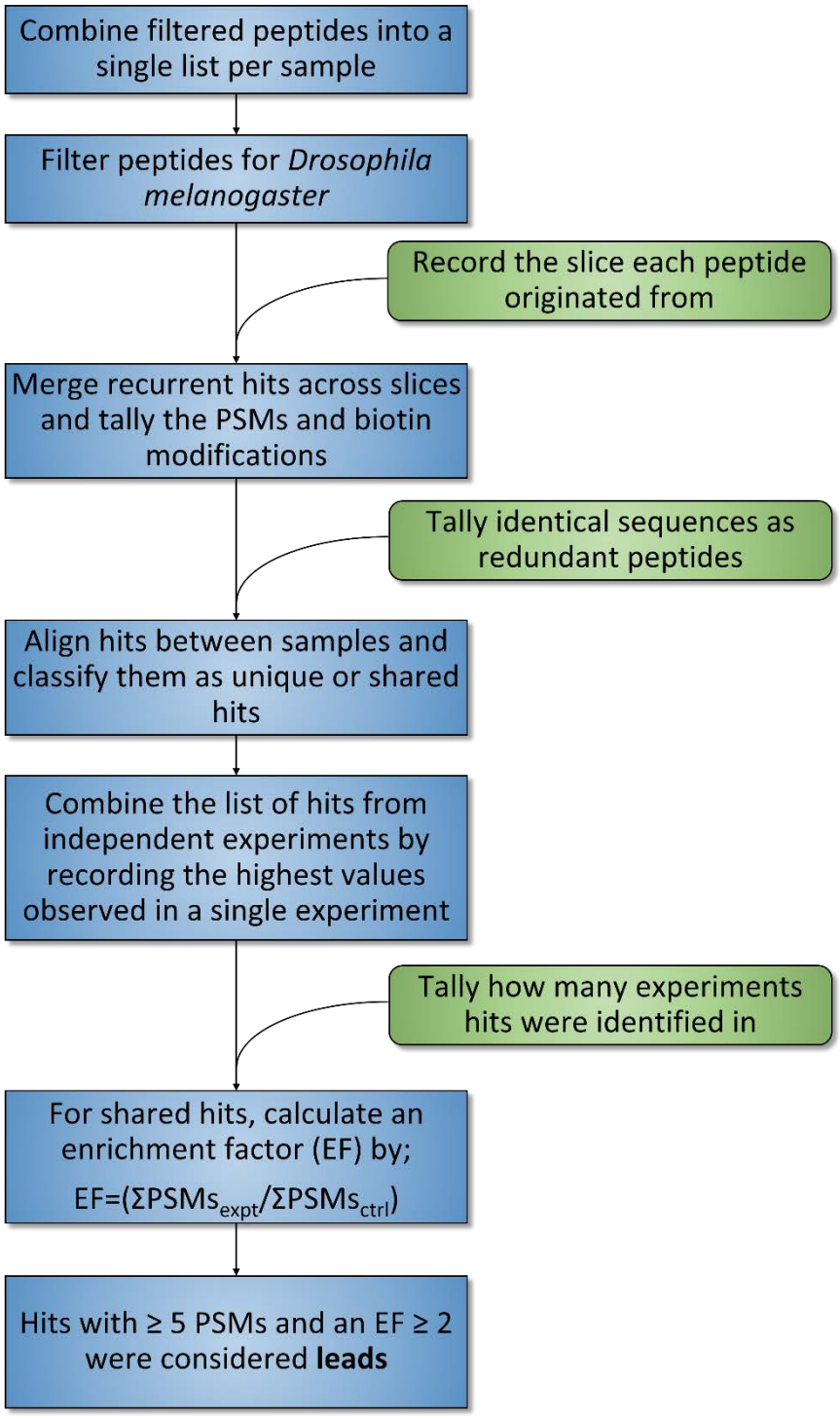

Figure 2.2. Flow diagram for filtering of hits labelled by BioID.

≥ 2 with ≥ 5 PSMs were identified as leads.

Tissue expression and function of leads within the nervous system of *Drosophila melanogaster* were identified by searching publications listed by FlyBase (flybase.org). Where protein expression within the nervous system was not explicitly stated, tissue expression was investigated using SCope (scope.aertslab.org), an interactive online tool that maps the expression patterns of 14,600 transcripts across 57,000 cells based on single-cell transcriptome analysis of the adult fly brain (416).

Table 2.1. Media for culturing *Drosophila melanogaster.*

Ingredient	Recipe			
	Standard[a]	Semi-defined[a]	SY[b]	Grape juice plates
Agar (g/l)	8	8	10	22
Glucose (g/l)	50	60		
Sucrose (g/l)		30	50	
Soy flour (g/l)	10			
Yeast (g/l)	50	80	100	
Yeast extract (g/l)		20		
Peptone (g/l)		20		
$MgSO_4.6H_2O$ (g/l)		0.5		
$CaCl_2.2H_2O$ (g/l)		0.5		
Methyl-4-hydroxybenzoate (g/l)[c,d]	0.1	0.1	0.1	
Propionic acid (% v/v)[c]	0.3	0.3	0.3	
Ethanol (% v/v)[e]	1	1	1	
Grape juice (% v/v)[c]				13
ddH2O (ml per 1 litre)	750	800	1,000	870

[a]Adapted from recipes by Bloomington Stock Centre.
[b]Described by (417). Quantities of sucrose and yeast were adjusted in nutrient supply experiments.
[c]Added after the food has been boiled and has cooled to ≤ 60 °C.
[d]Methyl-4-hydroxybenzoate is prepared as a 10% (w/v) stock in 100% ethanol and stored at 4 °C.
[e]The resulting ethanol concentration after the addition of 10% (w/v) methyl-4-hydroxybenzoate.

Table 2.2. Modified media for cell culture

Media	Recipe
Supplemented SchDM (SSchDM)	90% (v/v) SchDM, 10% (v/v) FBS, 1X PenStrep
S2 cryopreservation media	45% (v/v) fresh SSchDM, 45% (v/v) conditioned SSchDM, 10% (v/v) DMSO
Supplemented DMEM (SDMEM)	90% (v/v) DMEM, 10% (v/v) FBS, 1X PenStrep, 1X $_{L}$-glutamine
MEF cryopreservation media	45% (v/v) fresh SDMEM, 45% (v/v) conditioned SDMEM, 10% (v/v) DMSO
MEF full recovery media	EBSS, 10% (v/v) FBS, 4 µg/ml insulin, 1X amino acid mix, 5.5 mM $_{D}$-glucose, pH 8.0
MEF partial recovery media	Full recovery media with omission of amino acids, $_{D}$-glucose or FBS + insulin
E. coli cryopreservation media	85% (v/v) LB, 15% (v/v) glycerol

Table 2.3. Buffer solutions

Buffer	Recipe
Phosphate-buffered saline (PBS)[a]	ddH_2O, 137 mM (8.0 g/l) NaCl, 2.7 mM (0.2 g/l) KCl, 10 mM (1.44 g/l) Na_2HPO_4, 1.8 mM (0.24 g/l) KH_2PO_4, pH 7.4
PBS-Tween 20 (PBST)[a]	PBS, 0.1% (v/v) Tween 20
Tris-buffered saline (TBS)[a]	ddH_2O, 50 mM (6.06 g/l) Tris, 150 mM (8.76 g/l) NaCl, pH 7.6
TBS-Tween 20 (TBST)[a]	TBS, 0.1% (v/v) Tween 20
S2 lysis buffer[b]	TBS, 5 mM (0.48 g/l) $MgCl_2$, 1 mM EDTA.Na_2, 2% (w/v) DDM
BioID lysis buffer[b]	ddH_2O, 50 mM (6.06 g/l) Tris, 500 mM (29.25 g/l) NaCl, 0.4% (w/v) SDS, 5 mM EDTA.Na_2, 1 mM (0.15 g/l) DTT[b], pH 7.4
Drosophila native IP buffer[b]	TBS, 5 mM (0.48 g/l) $MgCl_2$, 1 mM EDTA.Na_2, 2% (w/v) SMA
RIPA[b]	TBS, 1% (v/v) NP-40, 0.5% (w/v) sodium deoxycholate, 0.1% (w/v) SDS
BioID wash 1	ddH_2O, 2% (w/v) SDS
BioID wash 2	ddH_2O, 50 mM (11.9 g/l) HEPES, 500 mM (29.3 g/l) NaCl, 1% (v/v) Triton X-100, 0.1% (w/v) sodium deoxycholate, 1 mM EDTA.Na_2, pH 7.5
BioID wash 3	ddH_2O, 10 mM (1.21 g/l) Tris, 250 (10.6 g/l) mM LiCl, 0.5% (v/v) NP-40, 0.5% (w/v) sodium deoxycholate, 1 mM EDTA.Na_2, pH 8.1
BioID wash 4	ddH_2O, 50 mM (6.06 g/l) Tris, 50 mM (2.93 g/l) NaCl, pH 7.4
APEX2 wash 1	ddH_2O, 1 M (74.6 g/l) KCl
APEX2 wash 2	ddH2O, 0.1 M (10.6 g/l) Na_2CO_3
APEX2 wash 3	ddH2O, 10 mM (1.21 g/l) Tris, 2 M (120.1 g/l) urea, pH 8.0
Laemmli sample buffer	ddH2O, 125 mM (15.1 g/l) Tris, 2% (w/v) SDS, 10% (v/v) glycerol, 100 mM (15.4 g/l) DTT[b], 0.004% (w/v) bromophenol blue, pH 6.8
Membrane block	TBST, 5% (w/v) skimmed non-fat milk or 5% (w/v) BSA
ICC block	TBST, 1% (w/v) BSA, 0.02% (w/v) sodium azide
IHC block	PBS, 0.3% (v/v) Triton X-100, 1% (w/v) BSA, 0.02% sodium azide
Quencher solution[c]	PBS, 10 mM (200 g/l) sodium ascorbate, 5 mM (125 g/l) Trolox, 0.065% (w/v) sodium azide
Squishing buffer	ddH_2O, 10 mM (1.21 g/l) Tris, 25 mM (1.46 g/l) NaCl, 0.05% (v/v) Triton X-100, 1 mM EDTA.Na_2, 4 mg/ml proteinase K[b], pH 8.0
HL3.1 dissection media[d]	ddH_2O, 5 mM (1.19 g/l) HEPES, 70 mM (4.1 g/l) NaCl, 5 mM (0.37 g/l) KCl, 1.5 mM (0.17 g/l) $CaCl_2$, 4 mM (0.38 g/l) $MgCl_2$, 10 mM (0.84 g/l) $NaHCO_3$, 5 mM (1.71 g/l) trehalose, 115 mM (39.4 g/l) sucrose, pH 7.3

[a]Can be made as 10X stocks.
[b]Protease/phosphatase inhibitors and specified additives were freshly added before use.
[c]Antioxidants were freshly prepared for each experiment.
[d]Obtained from (413).

Table 2.4. Electrophoresis buffer solutions

Electrophoresis buffers	Recipe
SDS-PAGE running buffer[a]	ddH_2O, 25 mM (3.03 g/l) Tris, 192 mM (14.4 g/l) glycine, 0.1 (w/v) SDS, pH 8.3
Tris-glycine transfer buffer[a]	ddH_2O, 25 mM (3.03 g/l) Tris, 192 mM (14.4 g/l) glycine, pH 8.3
Tris-borate-EDTA (TBE) buffer[a]	ddH_2O, 100 mM (12.11 g/l) Tris, 100 mM (6.18 g/l) boric acid, 20 mM (7.4 g/l) $EDTA\text{-}Na_2$

[a]Can be made as 10X stocks.

Table 2.5. Primers for transgene generation

Primer	Function	Template	Sequence (5'→3')[a,b,c]
BioID only FP	Cloning	BioID/BioID-Cln7	caccATGGACAAGGACAACACCG
BioID only RP	Cloning	BioID/BioID-Cln7	GCGGTTTAAACTTAAGCTTGG
N-tag APEX2 FP	Cloning	APEX2/APEX2-Cln7	caccATGGGAAAGTCTTACCCAACTGTG
APEX2 only RP	Cloning	APEX2/APEX2-Cln7	GTCCAGGGTCAGGCGCTCC
N-tag APEX2 RP	Cloning	APEX2-Cln7	gcctccgcttccgccGTCCAGGGTCAGGCGCTCC
N-tag CG8596 FP	Cloning	APEX2-Cln7	ggcggaagcggaggcGAGTTTGCCCGCCGAGTTTC
N-tag CG8596 RP	Cloning	APEX2-Cln7	CGCATGTGAAATCGAGTGC
SDM BioIDatg FP	SDM ins.	BioID/BioID-Cln7	atgGACAAGGACAACACCGTGCCCCTG
SDM BioIDatg RP	SDM ins.	pENTR	GGTGAAGGGGGCGGCCGC
SDM BioID stop RP	SDM del.	BioID-Cln7	GCAGCCAGCACTCGATTTCACATGCG
SDM BioID stop FP	SDM del.	Destination vectors	AAGGGTGGGCGCGCCGAC
APEX2-Cln7 SDM F	SDM sub.	APEX2/APEX2-Cln7	AGCTATGGGGcTTACTGACCA
APEX2-Cln7 SDM R	SDM sub.	APEX2/APEX2-Cln7	TTGCCAAACACATCTCTCAAATG
M13F	Sequencing	pENTR/pMT	GTAAAACGACGGCCAG
M13R	Sequencing	pENTR/pMT	CAGGAAACAGCTATGAC
GW5F	Sequencing	Destination vectors	ATCGAGGCCTGTCTAGAGAAGC
SVR	Sequencing	Destination vectors	GGCATTCCACCACTGCTCCC
Metallothionein FP	Sequencing	pMT	CATCTCAGTGCAACTAAA

[a]Uppercase characters describe annealing bases.

[b]Lowercase characters define overhangs.

[c]Underlined nucleotides denote motifs required for cloning.

Table 2.6. Destination vectors for transgene expression in *Drosophila melanogaster*

Vector	System	Promoter	Expression	Epitope
pAMW	*In vitro*	Actin5C	Constitutive over-expression	N-terminal 6xMyc
pAFW	*In vitro*	Actin5C	Constitutive over-expression	N-terminal 3xFLAG
pMT-DEST48	*In vitro*	Metallothionein	Cu^{2+} induction	C-terminal V5
pTMW	*In vivo*	UASt	UAS-Gal4 system	N-terminal 6xMyc

Table 2.7. Primary antibodies and direct conjugates

Description	Host	Experiment	Concentration	Block	Company
pAb α-Myc	Gt	ICC, IHC, WB	ICC: 1:500 IHC: 1:500 WB: 1:2,000	ICC: ICC block IHC: 1:500 WB: 5% milk	Abcam (ab9132)
mAb α-Myc	Rb	IHC	1:500	IHC: IHC block	Abcam (ab9106)
mAb α-FLAG M2	M	ICC, WB	ICC: 1:500 WB: 1:2,000	ICC: ICC block WB: 5% milk	Sigma (F3165)
pAb α-V5	Gt	ICC, WB	ICC: 1:500 WB: 1:1,000	ICC: IF block WB: 5% milk	Abcam (ab9137)
pAb α-GFP	Rb	WB	1:1,000	5% milk	Abcam (ab6556)
mAb α-β-actin	M	WB	1:5,000	5% milk	Abcam (ab8224)
mAb α-pS6K (Thr389)	Rb	WB	1:1,000	5% BSA	CST (#9234S)
mAb α-ERK1/2 (Thr202/Tyr204)	Rb	WB	1:1,000	5% BSA	CST (#9101)
pAb α-dlg	M	IHC	1:5	IHC block	DSHB (4F3)
Streptavidin-HRP	N/A	WB	1:10,000	5% milk	CST (#3999S)
405-Streptavidin	N/A	IHC	1:500	IHC block	Thermo (S32351)
488-Streptavidin	N/A	ICC	1:1,000	ICC block	Thermo (S11223)
594 α-HRP	Gt	IHC	1:400	IHC block	Jackson (123-585-021)

Gt = Goat, M = Mouse, Rb = Rabbit, ICC = immunocytochemistry, IHC = immunohistochemistry, WB = Western blot, CST = Cell signalling technologies, DSHB = Developmental studies hybridoma bank

Table 2.8. Secondary antibodies

Description	Host	Experiment	Concentration	Block	Company
HRP α-Mouse	Hr	WB	1:10,000	5% milk	CST (#7076S)
HRP α-Goat	Rb	WB	1:10,000	5% milk	Abcam (ab6741)
HRP α-Rabbit	Gt	WB	1:10,000	5% milk	CST (#7074S)
405 α-Mouse	Gt	IHC	1:500	IHC block	Abcam (ab175660)
488 α-Goat	Dk	ICC	1:2,000	ICC block	Abcam (ab150129)
488 α-Rabbit	Gt	IHC	1:500	IHC block	Abcam (ab150077)
594 α-Mouse	Dk	ICC	1:500	ICC block	Abcam (ab150108)

Dk = Donkey, Gt = Goat, Hr = Horse, Rb = Rabbit, ICC = immunocytochemistry, IHC = immunohistochemistry, WB = Western blot, CST = Cell signalling technologies

Table 2.9. *Drosophila melanogaster* genotypes

BDSC ID	Line	Full genotype
5905	w^{1118}	w^{1118}; +; +
	$Cln7^{84D}$	w^{1118}; +; $Cln7^{84D}$
55664	$Cln7^{RNAi}$	y^{1} sc* v^{1}; $Cln7^{TRiP.HMC03819}$; +
	UAS-Cln7, $Cln7^{84D}$	w^{1118}; +; UAS-Cln7, $Cln7^{84D}$/TM6B, Tb^{1} $Antp^{Hu}$
	FLAG-Venus-Cln7	v^{1}; +; FLAG-Venus-Cln7 (402)
	$rictor^{\Delta 42}$	w^{-}, $rictor^{\Delta 42}$/FM7, Dfd::YFP; +; +
	$rictor^{\Delta 42}$, $Cln7^{84D}$	w^{-}, $rictor^{\Delta 42}$/FM7, Dfd::YFP; +; $Cln7^{84D}$
3954	Actin-Gal4	y^{1} w*; +; Act5C-Gal4/TM6B, Tb^{1} $Antp^{Hu}$
458	Elav-Gal4	Elav-Gal4; +; +
	Repo-Gal4	w^{1118}; +; Repo-Gal4/TM6B, Tb^{1} $Antp^{Hu}$
27390	Mef2-Gal	y^{1} w*; +; Mef2-Gal4
7011	Cg-Gal4	w^{1118}; Cg-Gal4; +
	Actin-Gal4, $Cln7^{84D}$	w^{1118}; +; Act5C-Gal4, $Cln7^{84D}$/TM6B, Tb^{1} $Antp^{Hu}$
	Repo-Gal4, $Cln7^{84D}$	w^{1118}; +; Repo-Gal4, $Cln7^{84D}$/TM6B, Tb^{1} $Antp^{Hu}$ w^{+}
	Mef2-Gal4, $Cln7^{36H}$	w^{-}; +; Mef2-Gal4, $Cln7^{36H}$
	If/CyO, GFP	w^{1118}; $Kr^{If\text{-}1}$/CyO, GFP; +
	MKRS/TM6B	w^{1118}; +; MKRS, Sb^{1}/TM6B, Tb^{1} $Antp^{Hu}$
	If/CyO; MKRS/TM6B	w^{1118}; $Kr^{If\text{-}1}$/CyO; MKRS, Sb^{1}/TM6B, Tb^{1} $Antp^{Hu}$
	If/CyO, GFP; MKRS/TM6B	w^{1118}; $Kr^{If\text{-}1}$/CyO, GFP; MKRS, Sb^{1}/TM6B, Tb^{1} $Antp^{Hu}$
55821	vas-Cas9	y^{1} w^{1118} vas-Cas9.RFP-; +; +
	UAS-Myc-BioID-Cln7 (II)	w^{1118}; UAS-Myc-BioID-Cln7/(CyO, GFP); +
	UAS-Myc-BioID (II)	w^{1118}; UAS-Myc-BioID/(CyO, GFP); +
	UAS-Myc-BioID-Cln7 (III)	w^{1118}; +; UAS-Myc-BioID-Cln7/(TM6B, Tb^{1} $Antp^{Hu}$)
	UAS-Myc-BioID (III)	w^{1118}; +; UAS-Myc-BioID/(TM6B, Tb^{1} $Antp^{Hu}$)

3 CHARACTERISING A ROLE FOR CLN7 IN *DROSOPHILA* GROWTH AND DEVELOPMENT

3.1 Introduction

The life cycle of *Drosophila* consists of four phases; embryo, larva, pupa and adult. The progression through each of these phases is controlled by pulses of the steroid hormone ecdysone (418). During development there are three size checkpoints which larvae must pass to successfully progress through to adulthood; in chronological order, these are the threshold size for metamorphosis, the minimal viable weight and the critical weight (419-421). The threshold size for metamorphosis occurs prior to the penultimate moult, and determines that the following moult will be metamorphic. The minimal viable and critical weights occur early in the final instar and in *Drosophila* occur practically simultaneously, but do represent distinct outcomes. The minimal viable weight is defined as the threshold required to survive to adulthood in the absence of further feeding, which is decided by the amount of fat body storage that is sufficient to supply the necessary energy. The critical weight describes the size at which starvation will no longer to delay entry to metamorphosis (421).

The presence of these checkpoints means there is an intriguing relationship between growth and maturation. Several studies have shown that *Drosophila* growth and maturation pathways function as opposing forces within the prothoracic gland (PG) which controls the timing of development via secretion of ecdysone in response to hormonal inputs (422-424). By having a critical mass checkpoint, larval development can be considered in two phases: pre-checkpoint, when larvae favour speedy growth; and post-checkpoint, when maturation

becomes the priority (425). This was demonstrated by modulating insulin/IGF (insulin-like growth factor) signalling (IIS) either ubiquitously or specifically within the PG at various stages in larval development (422-424, 426). Reducing IIS pre-checkpoint caused significant delays in maturation through to pupation, which became more severe the earlier IIS was switched off, yet adult size, while small, remained unaltered regardless of when IIS was inhibited. In contrast, reduced IIS post-checkpoint had no further impact on development time but instead affected fly size, whereby the reduction to fly size was less severe when IIS was inhibited at later time points. Thus, IIS likely bolsters growth to reach critical mass as quickly as possible, after which flies enter a time-invariant phase where larvae commit to metamorphosis, regardless of nutrient availability or internal growth signals. Therefore, post-checkpoint IIS has no further influence on development time, but instead promotes growth in the interim phase between achieving critical mass and pupation, leading to larger adult flies (Figure 3.1).

Interestingly, the expression of active insulin receptor (InR), PI3K, Ras or Raf, but not Ral-GDS, dMyc or cyclin D/Cdk4 within PG cells resulted in premature pupation and reduced adult size (422-424), implying that simply the growth of PG cells does not cause larvae to prematurely pass the critical mass checkpoint. Instead, the evidence suggests that maturation is more specifically regulated by PI3K and Ras/Raf signalling in the PG, which in turn suggests a role for insulin signalling via Tor and MAPK pathways. Since the PG controls maturation by timing the release of ecdysone, growth occurring after critical mass is achieved likely no longer depends on the PG and is instead more likely to be a measure of general tissue growth in response to growth factors.

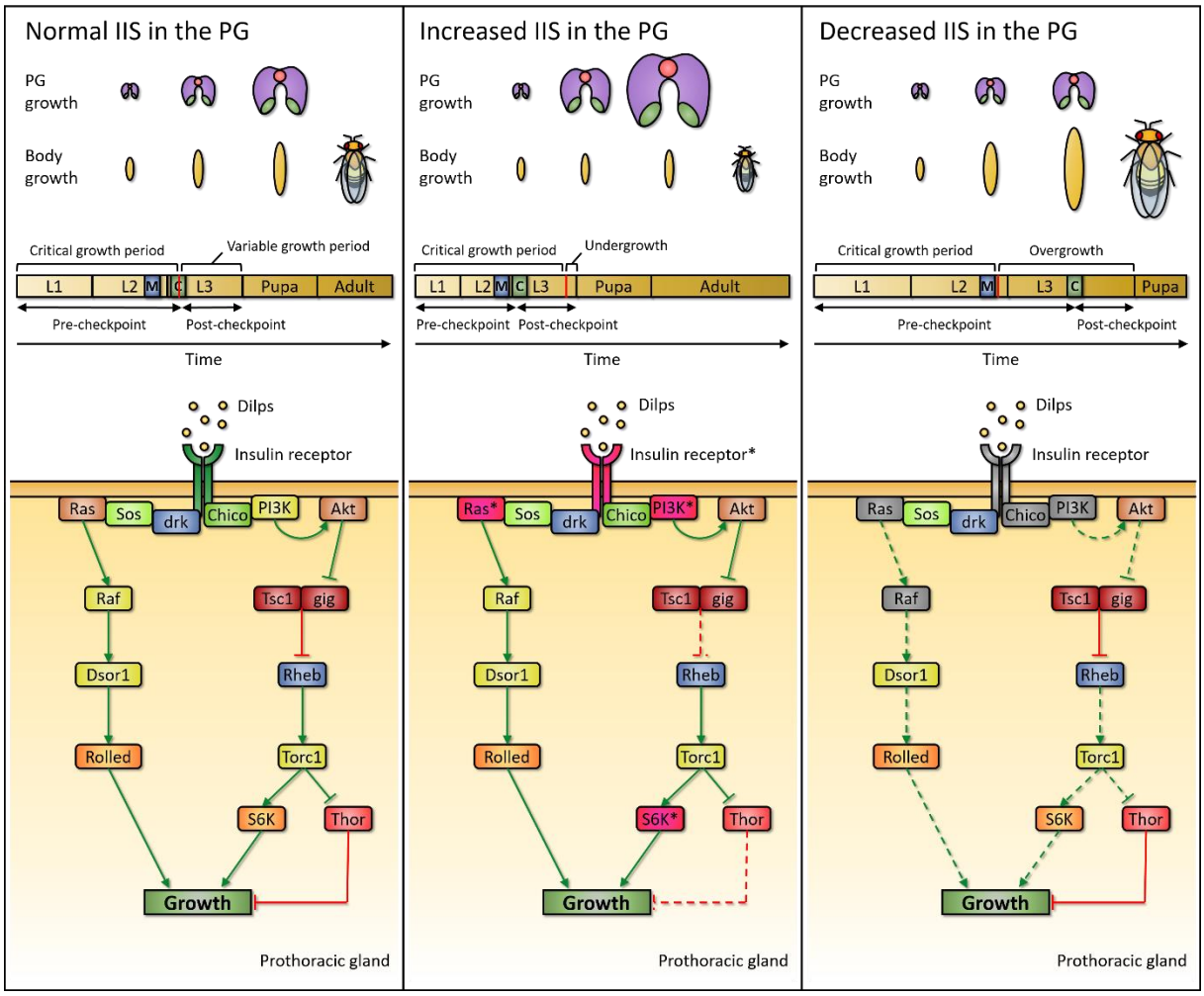

Figure 3.1. Control of *Drosophila* growth and maturation.

Growth within the PG determines the timing of ecdysone release and progression through larval stages and metamorphosis. Ecdysone release and its outcome coincides with various size thresholds that are intrinsic to the PG. The threshold for metamorphosis (blue box, M) occurs late in the second-instar and the critical weight threshold (green box, C) occurs early in the third-instar. Normally, the minimal viable weight (red line) to survive to adulthood and the critical weight are achieved simultaneously. Changes to PG growth rates alters the timing at which these thresholds are passed and lead to opposing whole-body phenotypes. Elevated PG growth hastens development and larvae commit to metamorphosis before the critical growth period is complete, yielding undergrown flies that narrowly pass the minimal viable threshold. Conversely, stunted PG growth prolongs development and extends the variable growth period, yielding overgrown flies. Several components of the IIS pathway have been reported to trigger these phenotypes when expressed in active (pink) or inactive (grey) forms (422-424).

In addition to the co-regulation of growth and maturation, biological organisms can dynamically sense nutrient abundance and respond accordingly by modulating tissue growth. Thus, nutrient sensors function as pivots that balance proper growth with timely maturation. The *Drosophila* fat body functions as a nutrient sensing tissue, regulating the growth of peripheral tissues by employing molecular nutrient sensors and relaying endocrine signals to the CNS. Downregulation of Tor signalling within the fat body severely restricts the growth of peripheral tissues and prolongs development. This phenotype is reproduced when the cationic amino acid transporter slimfast is downregulated in the fat body, and can be rescued by overexpressing the Tor target S6K (427). Furthermore, nutrient deprivation, or disrupted Tor signalling within the fat body by reducing slimfast or raptor expression or by increasing TSC1/2 expression, can remotely block dilp2 secretion from the insulin-producing cells (IPCs) within the *Drosophila* brain. This was well demonstrated in an experiment where brains from nutrient-deprived flies were co-cultured with the fat bodies of fed, starved or slimfast-deficient flies, and it was discovered that dilp2 secretion from IPCs was stimulated only in the presence of fat bodies from fed flies (428). In addition, the functional homologue of the human satiety hormone Leptin, Unpaired 2 (Upd2), is secreted by the fat body in response to fat and sugar intake and indirectly promotes dilp2 and dilp5 release from IPCs by activating the inhibitory JAK/STAT pathway within GABAergic neurons that regulate the IPCs (429). Altogether, the evidence suggests that the fat body regulates organismal growth by remotely sensing dietary amino acids through slimfast and Tor and dietary fats and sugars via Upd2, and modulating the secretion of dilp2 accordingly (428, 429).

Preliminary data identified an overgrowth phenotype in $Cln7^{84D}$ flies, in addition to greater resistance to starvation and oxidative stress than w^{1118} controls. Therefore, I sought

to investigate a role for *Cln7*^{84D} in the regulation of TORC1, since TORC1 functions at the lysosomal surface and is a key regulator of growth in response to both starvation and oxidative stress.

3.2 Results

3.2.1 *Sequence analysis of CLN7*

The early-onset manifestation of neurological phenotypes when CLN7 is deleted suggests that CLN7 performs a critical function within lysosomes and is required for neural health and development, however little is known about its function and regulation. As an initial enquiry, a bioinformatic approach was taken to investigate sequence relationships between CLN7 and similar proteins. CLN7 is estimated to fold into a 12-pass transmembrane protein, which is a characteristic of the Major Facilitator Superfamily (MFS) of transporters. These transporters are responsible for the facilitated diffusion of a range of solutes, including sugars, amino acids, nucleotides, vitamins, metabolites and drugs. The homology between CLN7 and MFS transporters suggests that CLN7 is itself a solute transporter, thus the evolutionary relationships between CLN7 and the different classes of MFS transporters, defined so by their substrate, were investigated.

The online Transporter Classification Database (TCDB) curates and classifies transporter proteins using nomenclature approved by the IUBMB, using an alphanumeric system analogous to the classification of enzymes by the Enzyme Commission (EC). The TCDB therefore provides a resource for the systematic and structured comparison of CLN7 and other transporters. The assigned ID for CLN7 is 2.A.1.2.56, which classes CLN7 as an electrochemical potential-driven porter (2.A) within the MFS (2.A.1) as a putative member of the broadly named Drug:H^+ Antiporter-1 (DHA1, 2.A.1.2) family. Firstly, to test the relationship between

CLN7 and DHA1 proteins, and other members belonging to the MFS (2.A.1)[1] family, multiple sequence alignment tools were used to compare the amino acid sequences of human CLN7 and all 88 other MFS (2.A.1) transporters in *Homo sapiens* listed by the TCDB. Illustrated in Figure 3.2A is the phylogenetic tree predicted by Simple Phylogeny from an alignment produced by Clustal Omega. Almost all proteins exclusively clustered by family with the exception of 3 proteins all belonging to the DHA1 family, including 2 related proteins 2.A.1.2.30 and 2.A.1.2.104, and CLN7. In fact, in terms of the frequency of changes per site (horizontal distance) between branch points, Clustal Omega predicted that CLN7 is equally distantly related to DHA1 proteins as it is to other MFS (2.A.1) proteins, with CLN7 sharing its most recent common ancestor with all other human MFS (2.A.1) transporters. This finding was consistent amongst predictions by alignment tools MAFFT, MUSCLE and T-Coffee, although in some instances CLN7 was predicted to be marginally more related to DHA1 proteins. As a note, there were fewer divergent events predicted between CLN7 and DHA1 members than of other families such as the sugar porters (SP) or the organic cation transporters (OCT). However, this is a less reliable measure of evolutionary distance because each protein likely undergoes many additional changes in the interim between the last common ancestor and the present structure.

[1] In the literature, MFS may refer to proteins belonging to the MFS (2.A.1) family or to the MFS superfamily, often without distinction. For disambiguation, the MFS (2.A.1) family will be referred to like so with the TCDB ID in parentheses. The MFS superfamily spans select 2.A families in addition to 4.D.2 and 9.B.111 and therefore cannot be defined by a single TCDB ID; instead, the term MFS superfamily will suffice.

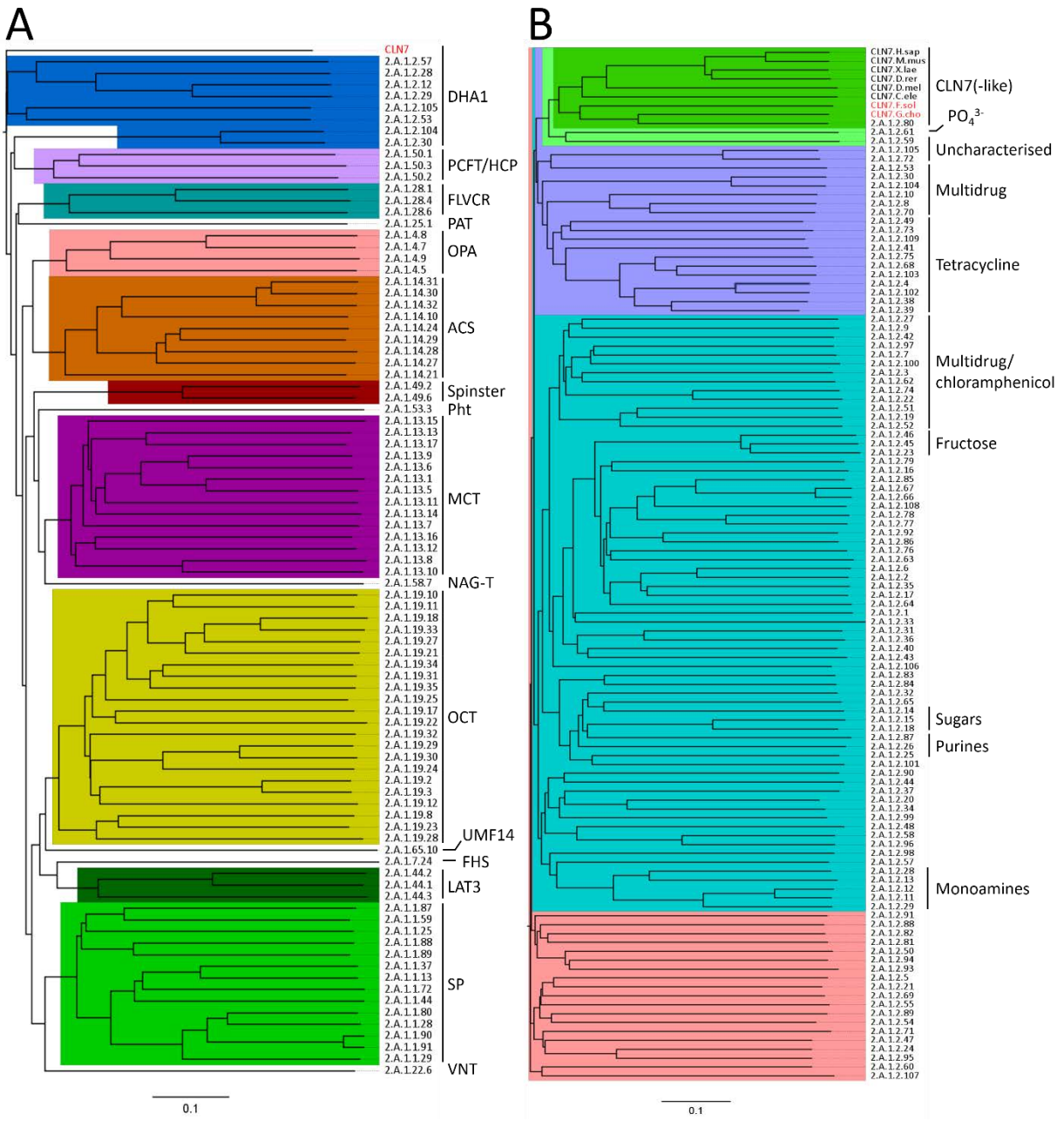

Figure 3.2. Multiple sequence analysis of CLN7 and MFS (2.A.1) transporters.

The phylogenetic trees shown were predicted from Clustal Omega alignments and drawn to scale (scale bar: 0.1 changes per site). Protein sequences are named according to their TCDB ID. Tree roots are on the left and present day sequences are represented by nodes on the right. A) Comparison of CLN7 to human MFS (2.A.1) transporters. Clades representing distinct families are highlighted and annotated by family name on the right. CLN7 is shown in red lettering. B) Comparison of CLN7 to pan-species DHA (2.A.1.2) transporters. Clades are highlighted to illustrate increasing phylogenetic distance from CLN7-like proteins, with established or putative substrates annotated on the right. In red lettering are two additional CLN7-like proteins that were identified by a blastp search of entry 2.A.1.2.80.

Given the classification of CLN7 as a DHA1 protein, CLN7 was next compared with other DHA1 proteins only (Figure 3.2B). Only 9 DHA1 proteins, including CLN7, were listed by the TCDB as identified in humans out of a total of 109 DHA1 proteins spanning all species from humans to bacteria, with functions ranging from the transport of antibiotics such as tetracycline and chloramphenicol to small molecules such as monoamines, nucleosides and phosphates. It seems unlikely that humans express just 9 of 109 DHA1 proteins, and that perhaps instead humans express homologues at least some of the remaining 100 that are either not yet identified or simply not listed. Therefore, the relationship between CLN7 and the remaining 100 non-human DHA1 proteins was investigated, which should serve as an adequate proxy to a comparison to putative human homologues by virtue of evolutionary conservation. To account for differences that could originate from and be exaggerated by comparisons between distantly related species, sequences for CLN7 homologues from humans to *Drosophila* and *C. elegans* were included in the alignment (no homologues were identified from prokaryotes). As expected, all CLN7 homologues clustered together, representing evolutionary conservation of CLN7 amongst eukaryotes (Figure 3.2B). Similar to in Figure 3.2A, all alignment tools agreed that CLN7 is distally related to most DHA1 proteins, with three particular exceptions 2.A.1.2.80, 2.A.1.2.61 and 2.A.1.2.59 (uncharacterised). The closest relative to CLN7 was predicted to be entry 2.A.1.2.80, a putative tetracycline:H^+ antiporter from the red alga species *Galdieria sulphuraria*. A blastp search of 2.A.1.2.80 found two additional CLN7-like proteins not identified in the initial search for CLN7 homologues from the red seaweed *Gracilariopsis chorda* and the oleaginous diatom *Fistulifera solaris*. A cluster of tetracycline:H^+ antiporters also showed marginally greater similarity to CLN7 compared to the majority of entries, which may suggest that CLN7 shares certain structural features with

tetracycline transporters. However, entry 2.A.1.2.80 is more closely related to CLN7 than to the cluster of tetracycline transporters, which may suggest that 2.A.1.2.80 and, by relation, CLN7 function is divergent to tetracycline transport. In fact, the second-most similar protein to CLN7 is 2.A.1.2.61, a putative vacuolar inorganic phosphate (Pi) transporter (VPT1) that regulates Pi storage and homeostasis in response to elevated Pi from *Arabidopsis thaliana* (430).

Prompted by the dissimilarity between CLN7 and MFS (2.A.1) transporters, the seemingly miscellaneous classification of drug transporters and the possible link between CLN7 and phosphate transport, the dataset for comparison with CLN7 was widened to capture a broader range of transporters. The TCDB contains 18,155 sequences in total, which is too large a dataset for MSA, thus the analysis was split into two parts. Firstly, sequences were filtered for *Homo sapiens* and the resulting 1,646 sequences spanning all families were compared to CLN7, and secondly CLN7 was compared to 1,136 proteins belonging to the wider MFS superfamily. MSAs were performed using Kalign as a more suitable tool for large alignments and the top clades were isolated and realigned to CLN7 using Clustal Omega. DHA1 proteins were included as control alignments against any new hits. Both analyses failed to detect any additional proteins related to CLN7 (not shown), and instead agreed with the alignment in Figure 3.2B showing the closest relationship between CLN7 and 2.A.1.2.80, followed by 2.A.1.2.59 and 2.A.1.2.61 (VPT1). Together, these results suggest that CLN7 is, at present, a largely unique MFS transporter, with structural similarities to tetracycline:H^+ antiporters and possibly functions as a transporter of phosphates or other small anions between cytosolic and luminal compartments.

3.2.2 *Characterisation of mass phenotypes by loss of Cln7*

To investigate the function of Cln7 empirically, the effects of mutating Cln7 were investigated in *Drosophila*. Loss of function *Cln7* alleles were created by the lab previously. Briefly, a genetic line containing the P-element NP0345, inserted immediately upstream of *Cln7*, was obtained to perform imprecise P-element excision. Here, flies containing the P-element are crossed with a line encoding a P-element transposase. Each excision event removes the P-element plus some surrounding genetic material, including portions of *Cln7*, and as each excision differs from cell to cell, each progeny inherits a unique allele. Two alleles were recovered; $Cln7^{84D}$ and $Cln7^{36H}$. Homozygous flies were viable and fertile, and both lines were backcrossed to an isogenic w^{1118} line over 6 generations to remove genetic variation between mutant flies and the w^{1118} control.

One observed difference between w^{1118} and *Cln7* mutant flies was that mutant flies were larger than controls. To quantify this under more controlled conditions, flies were reared on a high-nutrient food described previously (417). This food, named SY, was chosen because it was optimised for maximal fly growth and development speed, while also minimising deleterious outcomes such as decreased lifespan and fecundity. Fly growth was assessed by developing L_1 larvae on SY food and measuring adult fly mass 1-day post-eclosion. Under these conditions, both *Cln7* alleles caused overgrowth of male and female flies (Figure 3.3A and B). The $Cln7^{84D}$ allele was selected for use in subsequent experiments as it produced the largest overgrowth phenotype.

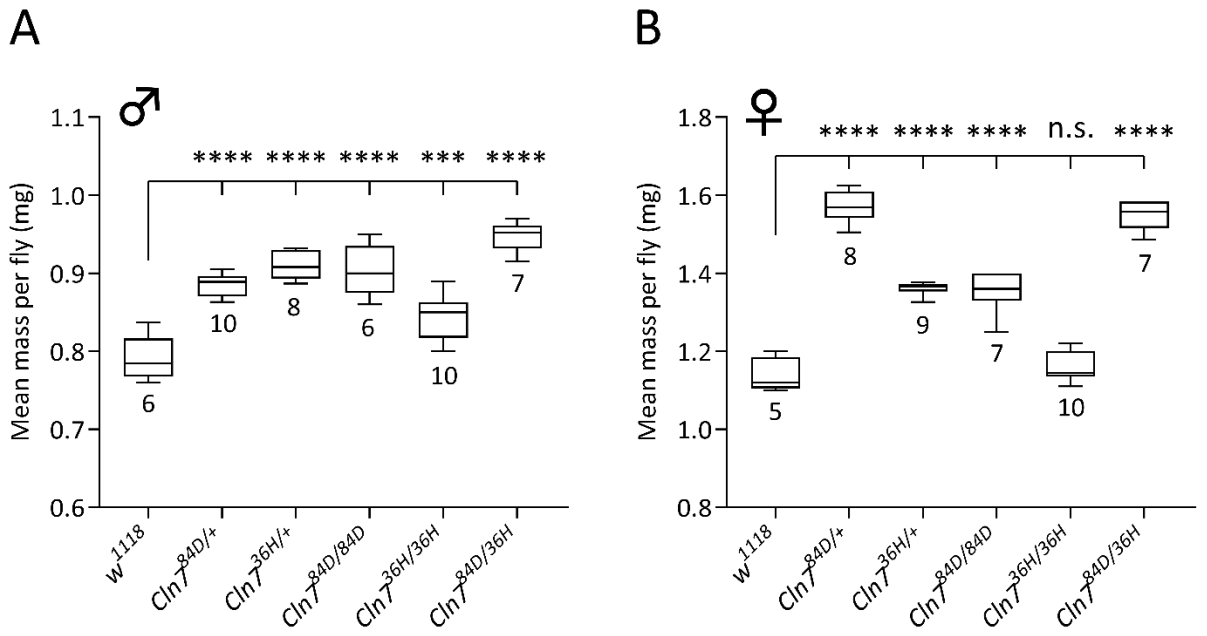

Figure 3.3. Loss of *Cln7* causes systemic overgrowth in *Drosophila* adults.

Masses of male (**A**) and female (**B**) flies carrying combinations of $Cln7^{84D}$ and $Cln7^{36H}$ alleles. Measurements were taken 1 day post-eclosion. Boxes show the mean of means from n groups of 10 flies weighed together, and bars represent min-max values. Numbers beneath the boxes state the value for n. Statistical analysis was performed using a one-way ANOVA with Sidak's multiple comparisons tests. N.s., $p>0.05$. *, $p \leq 0.05$. **, $p \leq 0.01$. ***, $p \leq 0.001$. ****, $p \leq 0.0001$.

3.2.3 *Genetic screen for Cln7 function using different tissue drivers*

To investigate which tissues underpin the *Cln7*^{84D} overgrowth phenotype, a screen of RNAi knockdowns and UAS/Gal4 over-expressions was performed. Firstly, *Cln7* RNAi was expressed ubiquitously (Actin-Gal4), followed by tissue-restricted knockdown in neurons (Elav-Gal4), glia (Repo-Gal4), muscles (Mef2-Gal4) and in the fat body (Cg-Gal4). These tissues were chosen to investigate if the overgrowth phenotype originated from cells within the nervous system (neurons or glia), from the post-synaptic cell, where Cln7 was shown to regulate synapse development (unpublished data), or from the fat body as a nutrient sensing tissue. Ubiquitous expression of *Cln7* RNAi failed to recapitulate the overgrowth seen in *Cln7* mutants (Figure 3.4A and B). Fly mass remained unchanged between controls and *Cln7* knockdown in muscles and in the fat body, however knockdown in glia increased fly mass in both males and females, suggesting that Cln7 may regulate fly growth from glial cells. To see if fly overgrowth is rescued when Cln7 is re-expressed in those cells, Cln7 was overexpressed in a mutant background with the same tissue drivers. Here, overexpression of Cln7 ubiquitously, in glia and in muscle partially rescued the overgrowth phenotype. Taken together, these observations suggest that the loss of Cln7 within glial cells is responsible for overgrowth in *Cln7*^{84D} flies, at least in part.

The relationship between Cln7 expression and fly overgrowth here is not straightforward. It is worth mentioning that both knockdown by RNAi and overexpression by UAS/Gal4 target Cln7 expression at the level of the mRNA by promoting mRNA degradation and transcription respectively, in contrast to deletion of genetic material in *Cln7*^{84D} flies. Therefore, it is uncertain the extent to which Cln7 protein expression is affected comparatively between the lines tested. Ideally this would be determined by Western blot, but no Cln7

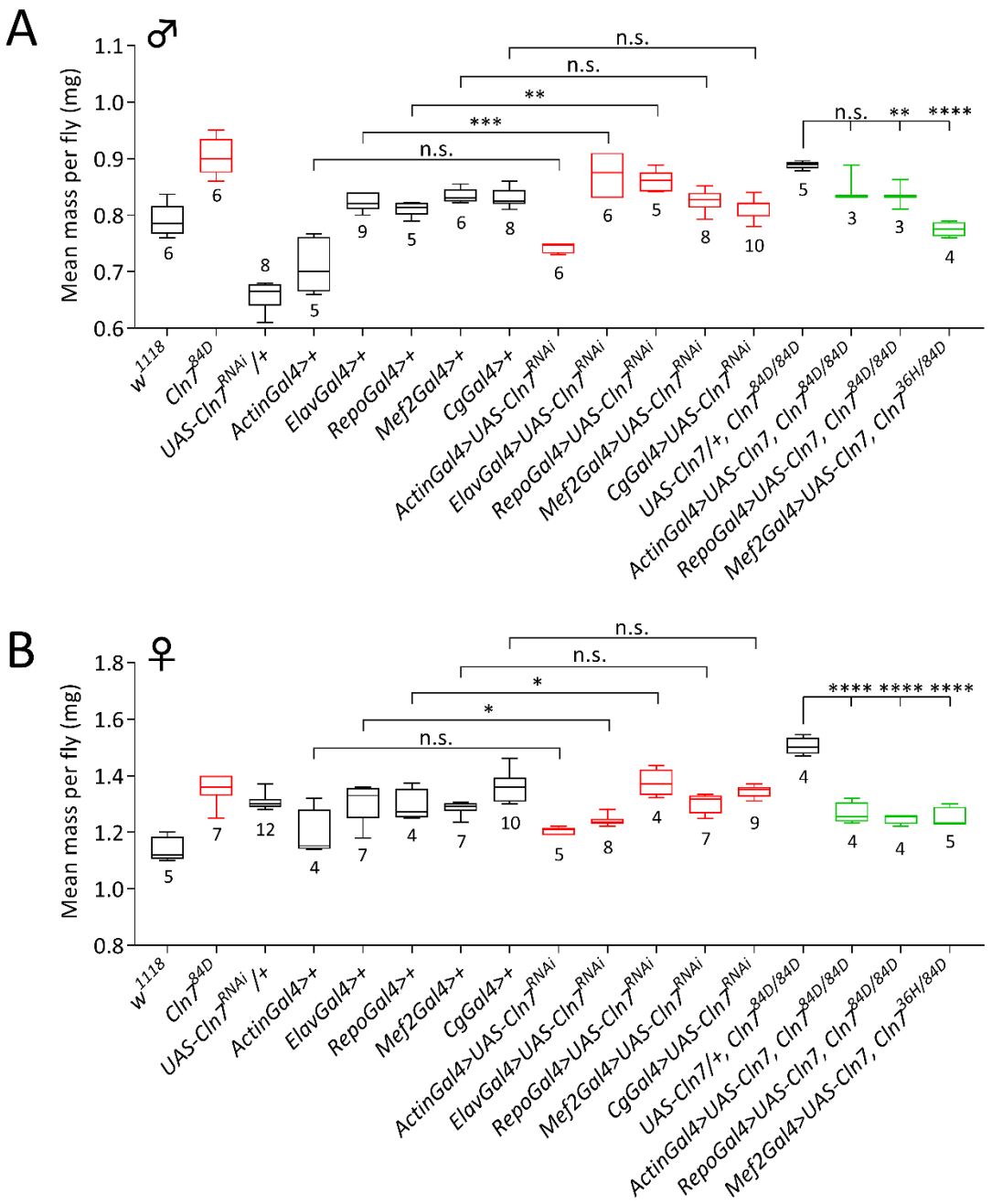

Figure 3.4. Knockdown and rescue of *Cln7* expression in glia modifies fly overgrowth.

Masses of male (**A**) and female (**B**) flies after tissue specific knockdown (red boxes) or re-expression (green boxes) of Cln7. Black boxes represent controls. Measurements were taken 1 day post-eclosion. Boxes show the mean of means from n groups of 10 flies weighed together, and bars represent min-max values. Numbers beneath the boxes state the value for n. Statistical analysis was performed using a one-way ANOVA with Sidak's multiple comparisons tests. N.s., p>0.05. *, p ≤0.05. **, p≤0.01. ***, p ≤0.001. ****, p ≤0.0001.

antibody is commercially available, and previous attempts to make an antibody were unsuccessful. Aside from how Cln7 protein levels are affected, a second factor that may reduce interpretability is genetic variation obscuring mass phenotypes. While the *Cln7*^{84D} allele was backcrossed to the *w*^{1118} control and therefore should be isogenic, this is not true for each of the RNAi, UAS or Gal4 lines. The backgrounds of these lines are as procured from Bloomington stock centre, and are each not only different to the *w*^{1118} line but also to each other. Crosses were performed in an ordered fashion to reduce variability by collecting females from Gal4 lines and males from *w*^{1118}, *Cln7*^{84D}, *Cln7*^{RNAi} or *UAS-Cln7* lines where possible, however this should only affect X chromosome inheritance in males. Genetic variation originating from the second, third and female X chromosomes can only be removed by backcrossing each line to the *w*^{1118} control, which is impractical. Tissue growth is a polygenic process, governed by multiple cross-talking pathways receiving inputs from many stimuli, making changes to growth potentially difficult to predict in mixed genetic populations. Therefore, the difference in fly mass is possibly too mild to detect amongst confounding factors within a varied gene pool.

3.2.4 *The effects of Tor inhibitors on Cln7*^{84D} *fly growth and development*

There are several possible explanations for the increase in *Cln7*^{84D} fly mass: 1) up-regulation of cell growth; 2) up-regulation of cell proliferation; 3) increased nutrient storage; 4) increased food consumption; 5) increased muscle mass, and; 6) decreased excretion and/or increased water retention. CLN7 disease is a lysosomal storage disease, a class of diseases characterised by accumulation of storage material in lysosomes, including lipids in many cases (312). Lipid storage in LSDs disrupts lysosomal function and often leads to a block in autophagy

through perturbed lysosome formation, maturation, fusion/fission and/or intralysosomal degradation. These disruptions frequently lead to misregulated Tor signalling, as lysosomes are the site of TORC1 activation. Given the link between lysosomal dysfunction and disrupted TORC1 signalling, it is feasible to hypothesise that ablating Cln7 activity promotes lipid storage and misregulation of Tor signalling by virtue of lysosomal dysfunction.

To test whether loss of Cln7 impacts on Tor signalling, flies were developed from L_1 larval stage to adulthood on SY food supplemented with the TORC1 inhibitor rapamycin or the TORC1/TORC2 inhibitor, Torin 1. In the absence of inhibitor, *Cln7*^{84D} flies were ~15% larger than *w*^{1118} flies (Figure 3.5A). Fly mass remained largely unaltered when developed on food containing up to 1 µM rapamycin, with increasing concentrations then resulting in significant size reduction and lethality at 10 µM rapamycin. In contrast, developing flies on food containing Torin 1 did not alter adult size at any concentration, but still resulted in lethality at 10 µM (Figure 3.5D). More importantly neither inhibitor rescued the overgrowth phenotype, with the exception of females fed on 2 µM rapamycin, suggesting that overgrowth of the *Cln7* mutant flies was not Tor-dependent.

During these experiments, it was noticed that flies fed with increasing concentrations of inhibitor seemed to take longer to develop to adulthood, and potentially this was exacerbated in *Cln7*^{84D} flies. To quantify this, the time taken to emerge as adult flies was measured in the same concentrations of inhibitor. Both genotypes experienced extended development times in response to rapamycin and this was concentration-dependent (Figure 3.5B). In addition, the development time of *Cln7*^{84D} flies was significantly delayed compared to *w*^{1118} control flies and the effect of increasing concentrations of rapamycin was more

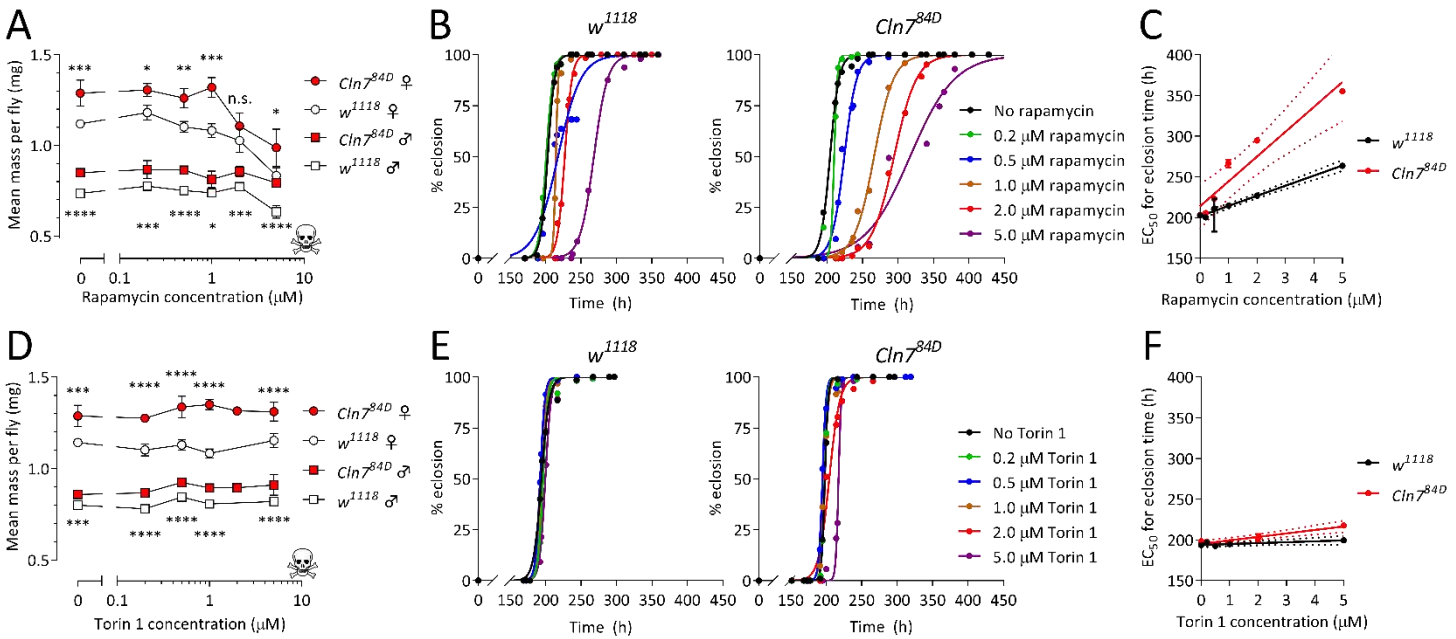

Figure 3.5. *Cln7*^{84D} flies are more sensitive to developmental delay induced by rapamycin.

A,D) Mean masses of adult *w*^{1118} (black) and *Cln7*^{84D} (red) flies developed on foods containing variable concentrations of rapamycin (**A**) or Torin 1 (**D**). One day old adults were separated by gender, counted and distributed equally among at least 3 groups, with a maximum of 10 flies per group. Each point represents the mean of group means, and error bars represent the SD. All larvae placed on food containing 10 μM of either inhibitor died before wandering L3. Stars above or below the curves relate to female or male genotype pairs, respectively. **B,E**) Eclosion timecourse for *w*^{1118} and *Cln7*^{84D} flies developed on foods containing rapamycin (**B**) or Torin 1 (**E**). EC_{50} values for eclosion time were plotted against inhibitor concentration (**C,F**). Error bars represent EC_{50} 95% confidence intervals and dashed lines represent regression line 95% confidence intervals. Statistical analysis for fly masses was performed using a one-way ANOVA with Sidak's multiple comparisons tests between genotype-pairs. Regression lines were fit using a linear model. N.s., $p>0.05$. *, $p\leq0.05$. **, $p\leq0.01$. ***, $p\leq0.001$. ****, $p\leq0.0001$.

dramatic in *Cln7*^{84D} flies than controls. This is shown more clearly by plotting the time taken for 50% of all flies successfully developed to adulthood as a function of inhibitor concentration (Figure 3.5C). Here, the slope for *Cln7*^{84D} flies is significantly steeper than that of *w*^{1118} flies. In contrast Torin 1 caused no significant delay to development in either genotype (Figure 3.5E-F). These data suggest that *Cln7*^{84D} flies have an underlying sensitivity to rapamycin, despite the limited rescue of the overgrowth phenotype. One possibility is that *Cln7*^{84D} flies have decreased TORC1 activity. Given that all foods were prepared with equal nutritional content, and assuming food consumption was equal between the genotypes, then a decrease in TORC1 activity would likely occur via a nutrient-independent mechanism. The sensitivity to rapamycin appears specific to inhibition of TORC1, as simultaneous inhibition of TORC1 and TORC2 by Torin 1 had minimal effect on fly mass or development time. However, the increased mass of *Cln7*^{84D} flies cannot be accounted for by elevated TORC1-dependent growth, and must be caused by another mechanism.

There are no drugs available that target TORC2 specifically. Rapamycin is more selective for TORC1, but there is evidence to suggest that chronic exposure to rapamycin does inhibit TORC2 to some extent by sequestration of Tor (431, 432). Therefore, TORC2 activity was blocked genetically using the *rictor*$^{\Delta 42}$ allele to test for an interaction with *Cln7*^{84D}. When grown on SY food, the *Cln7*^{84D} homozygote flies displayed the overgrowth phenotype but, in contrast, *rictor*$^{\Delta 42}$ homozygote flies were smaller than controls. Interestingly, when combined, the double mutant flies were the same size as *rictor*$^{\Delta 42}$ mutants (Figure 3.6). This indicates that *rictor* is epistatic of *Cln7*, and potentially places Cln7 upstream of Rictor in a common pathway.

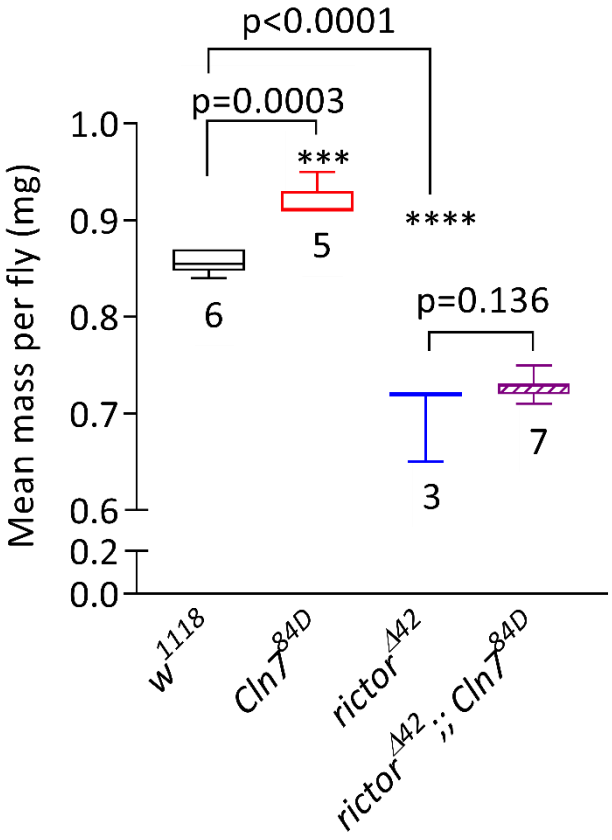

Figure 3.6. *Rictor* is epistatic of *Cln7* in regulating fly growth.

Comparing the masses of male single *Cln7*^{84D} and *rictor*$^{\Delta 42}$ mutant flies to a double *rictor*$^{\Delta 42}$*;; Cln7*^{84D} mutant. Measurements were taken 1 day post-eclosion. Boxes show the mean of means from n groups of 10 flies weighed together, and bars represent min-max values. Numbers beneath the boxes state the value for n. Statistical analysis was performed using a one-way ANOVA with Sidak's multiple comparisons tests. ***, p ≤0.001. ****, p ≤0.0001.

3.2.5 *Impact of nutrient supply on Cln7^{84D} fly growth and development*

It stands to reason that any growth pathway is reliant on nutrient intake, and therefore nutrients must regulate growth pathways. The relationship between nutrients and TORC1 signalling is well documented, but the function and regulation of TORC2 is less well known. The SY food used for previous experiments contains two nutrient sources: sucrose as a simple carbon source and yeast providing a complex mixture of amino acids, lipids and vitamins. To investigate a possible interaction between dietary intake and the growth of *Cln7^{84D}* flies, the mass of adult flies was measured as before with varying concentrations of each dietary component.

Both *w^{1118}* and *Cln7^{84D}* flies were severely undergrown in low yeast availability (0.1Y/0.2Y), and increasing yeast availability up to 1Y lead to step-wise increases in mass in both genotypes (Figure 3.7A). In contrast there was a weak negative relationship between fly mass and sucrose concentration, albeit a far milder response than with increases in yeast concentration. Flies developed on double-depleted food (0.1S 0.1Y) showed a more differential response, with *w^{1118}* flies remaining similar to those in 0.1Y food whereas *Cln7^{84D}* flies were even further undergrown, significantly more so than *w^{1118}* flies. At the other end of the spectrum, flies fed double-enriched food (5S 2Y) did not promote growth beyond that achieved at standard concentrations (SY). In a nutrient-rescue experiment, where one component was depleted and the other supplied in excess, low-sucrose high-yeast food (0.1S 2Y) yielded *Cln7^{84D}* flies that were even larger than those on standard food, with little change to *w^{1118}* flies, whereas high-sucrose low-yeast food (5S 0.1Y) was lethal before wandering L_3 stage. These results suggest that excess sucrose is deleterious to fly growth. More importantly, the data show that severe yeast restriction abolishes the overgrowth phenotype in *Cln7^{84D}*

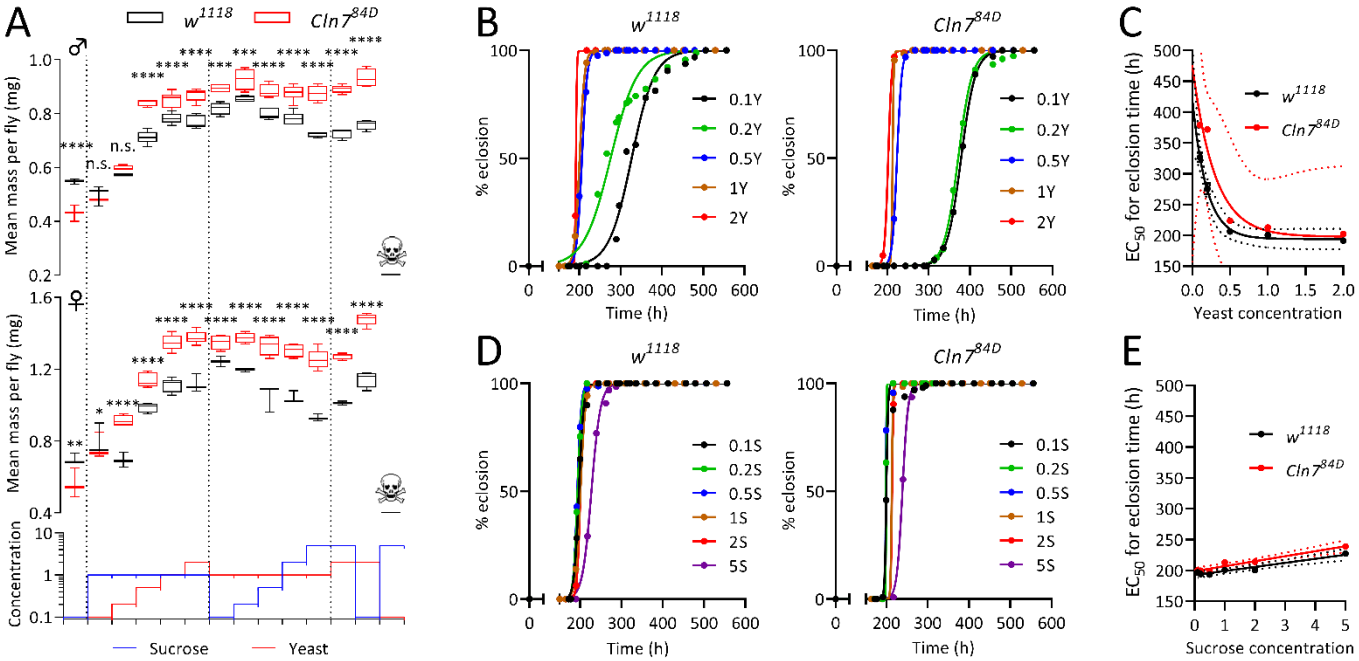

Figure 3.7. Overgrowth and developmental delay of *Cln7*^{84D} flies is dependent on dietary intake of yeast, but not sucrose.

A) Mean masses of adult *w*^{1118} (black) and *Cln7*^{84D} (red) flies developed on foods of varying in nutrient composition. One day old adults were separated by gender, counted and distributed equally among at least 3 groups, with a maximum of 10 flies per group. Box plots represent the mean of group means, flanked by upper and lower quartile masses and min/max bars. For reference, dotted lines bound stepwise increases in either sucrose or yeast while the other remains constant. All larvae placed on 5S 0.1Y food died before wandering L3. **B-E**) Eclosion timecourse for *w*^{1118} and *Cln7*^{84D} flies developed on foods with varying yeast (**B**) or sucrose (**D**) concentrations. EC_{50} values for eclosion time were plotted against nutrient concentration (**C,E**). Error bars represent EC_{50} 95% confidence intervals and dashed lines represent regression line 95% confidence intervals. Statistical analysis for fly masses was performed using a one-way ANOVA with Sidak's multiple comparisons tests between genotype-pairs. Regression lines were fit using one-phase decay (yeast) or linear (sucrose) models. N.s., $p>0.05$. *, $p\leq0.05$. **, $p\leq0.01$. ***, $p\leq0.001$. ****, $p\leq0.0001$.

flies, and that *Cln7*^{84D} flies become seemingly more reliant on sucrose than their *w*^{1118} counterparts when yeast is limited, as the phenotype is reversed in double-depleted food.

Development time was also measured for flies grown on each food (Figure 3.7B-E). For both genotypes, foods containing 0.5Y and above had little effect on the time taken to eclosion. More severe yeast depletion with 0.1Y and 0.2Y foods caused more profound delays in development, with *Cln7*^{84D} flies taking slightly longer than *w*^{1118} flies. In contrast, sucrose concentration had minimal effect on development time. Taking together the more severe size reduction and developmental delay on low-yeast foods in *Cln7*^{84D} flies, this suggests *Cln7*^{84D} flies are sensitive to yeast restriction during development. Interestingly, this suggests that the increased fly mass is not primarily caused by overconsumption or excess nutrient supply, but rather by changes to the dynamics of nutrient utilisation within the fly. If overconsumption was the root cause of overgrowth in *Cln7*^{84D} flies, the expected result would be that *Cln7*^{84D} flies are larger than *w*^{1118} flies in all foods. Equally if overgrowth was caused by excess nutrient provision, then it would be expected that *Cln7*^{84D} growth would match *w*^{1118} during mild yeast restriction before deleterious effects were observed (on 0.5Y food). As neither of these possibilities describe the data, *Cln7*^{84D} fly overgrowth is more likely the result of changes to nutrient utilisation, possibly increased nutrient storage within tissues.

3.2.6 *Growth signalling in CLN7*$^{-/-}$ *fibroblasts*

To investigate further possible interactions between Cln7 and nutrients, the activation of growth signalling in response to nutrients was tested in mouse embryonic fibroblasts lacking CLN7 expression. MEFs were starved in EBSS for 24 h and re-fed a combination of

glucose, amino acids and growth factors to stimulate growth. The phosphorylation of S6K and MAPK were measured as two main effectors of growth signalling, operating via PI3K and Ras pathways respectively. In WT MEFS, low levels of pS6K and pERK1/2 were detected in untreated samples but were robustly activated when re-stimulated after starvation with EBSS supplemented with glucose, amino acids and growth factors (Figure 3.8). The omission of growth factors reduced the phosphorylation of both S6K and ERK1/2, thus nutrients alone were not sufficient to activate mTORC1 or MAPK pathways. In the presence of growth factors, the omission of glucose or amino acids affected S6K and ERK1/2 phosphorylation differently. Amino acids, but not glucose, were necessary for S6K phosphorylation, whereas phosphorylation of ERK1/2 required glucose but not amino acids. This nicely allows the effects of glucose and amino acids to be separated in order to test the interactions between CLN7 and either nutrient.

In CLN7$^{-/-}$ MEFS, the overall activation of S6K and ERK1/2 was significantly reduced. The dependence of S6K phosphorylation on amino acids remained intact as pS6K levels were further reduced in their absence, however a further reduction of pERK1/2 in the absence of glucose was not observed. This suggests that CLN7 is involved in the phosphorylation of ERK1/2 in response to glucose, with the simplest hypothesis being that CLN7 functions as a glucose transporter. However, CLN7 shows little homology with glucose transporters by phylogenetic analysis. Given that the deletion of CLN7 affects both S6K and ERK1/2 activation, an alternate hypothesis is that CLN7 interacts with proteins further upstream that are common to both pathways. What is clear, however, is that CLN7 expression is at least necessary for intact growth signalling, as its deletion severely impedes responses through S6K and MAPK pathways.

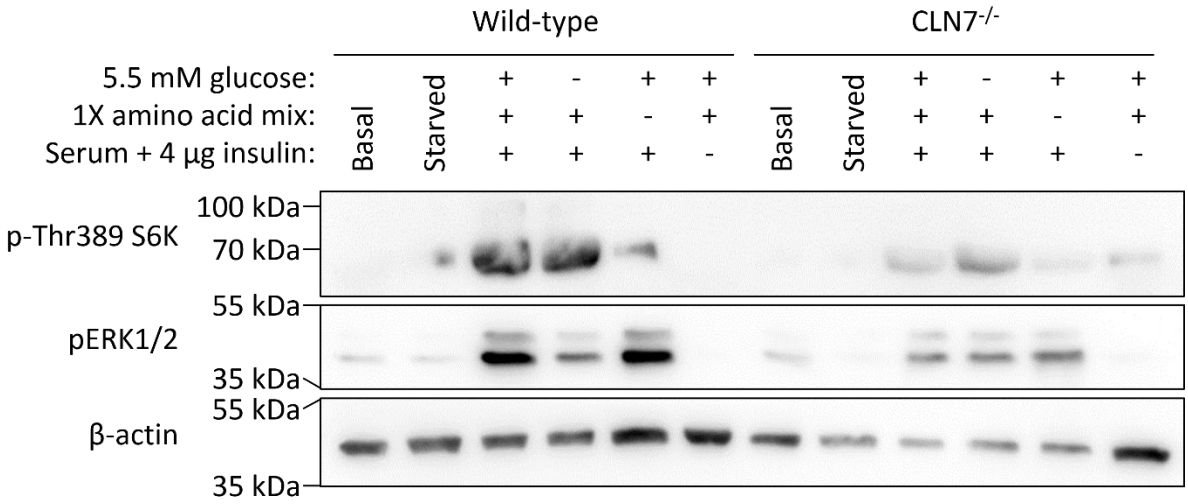

Figure 3.8. Loss of CLN7 impairs the activation of mTORC1 and MAPK signalling in MEFs.

Cell responsiveness to growth stimuli was primed by 24 h starvation in EBSS. Cells were then re-fed EBSS supplemented with a combination of glucose, amino acids and growth factors for 1 h before harvesting. Experiments were performed by Amy Roberts as part of a BMedSci project.

3.2.7 *Increased glyceride storage in Cln7^{84D} flies*

Under severe nutrient restriction, *Cln7^{84D}* flies grow to a similar mass or are even undergrown relative to *w^{1118}* flies. If *Cln7^{84D}* flies are overgrown due to excessive nutrient storage, it stands to reason that under severe nutrient depletion, nutrient storage would be sacrificed in favour of tissue growth. In this instance, the expected result would be that *w^{1118}* and *Cln7^{84D}* are equal in size under restricted diets, which agrees with the data. In order to determine which nutrient might be stored, carbohydrates, protein and fat were considered. Given that flies fed on sucrose-restricted food showed very little change to both adult mass and development time, the storage of carbohydrates seemed unlikely. Also, protein is not a nutrient that is stored in considerable quantities; amino acids are either utilised during protein synthesis or are converted into sugar or fat as an energy source. Therefore if flies are storing nutrients in excess, fat remains the most likely candidate to be stored.

Fat storage was tested using a commercially available kit to measure glyceride content. In principle, glycerides containing 1-3 fatty acids are hydrolysed by lipoprotein lipase to release glycerol, coupled to a sequence of redox reactions to yield a quinoneimine dye that can be quantified by colourimetry. Therefore the kit offers a readout of the sum total of glycerides and free glycerol within flies. Total glyceride content was measured from whole fly lysates and normalised to protein concentration as an internal control. Gram for gram, glyceride levels increased by approximately 3-fold relative to protein concentration in *Cln7^{84D}* flies (Figure 3.9). However this can only partially account for the increased mass in *Cln7^{84D}* flies, since the increase in glycerides equates to increases of 0.035 mg and 0.052 mg in males and females respectively, which correspond to 51% and 22% of the mass difference,

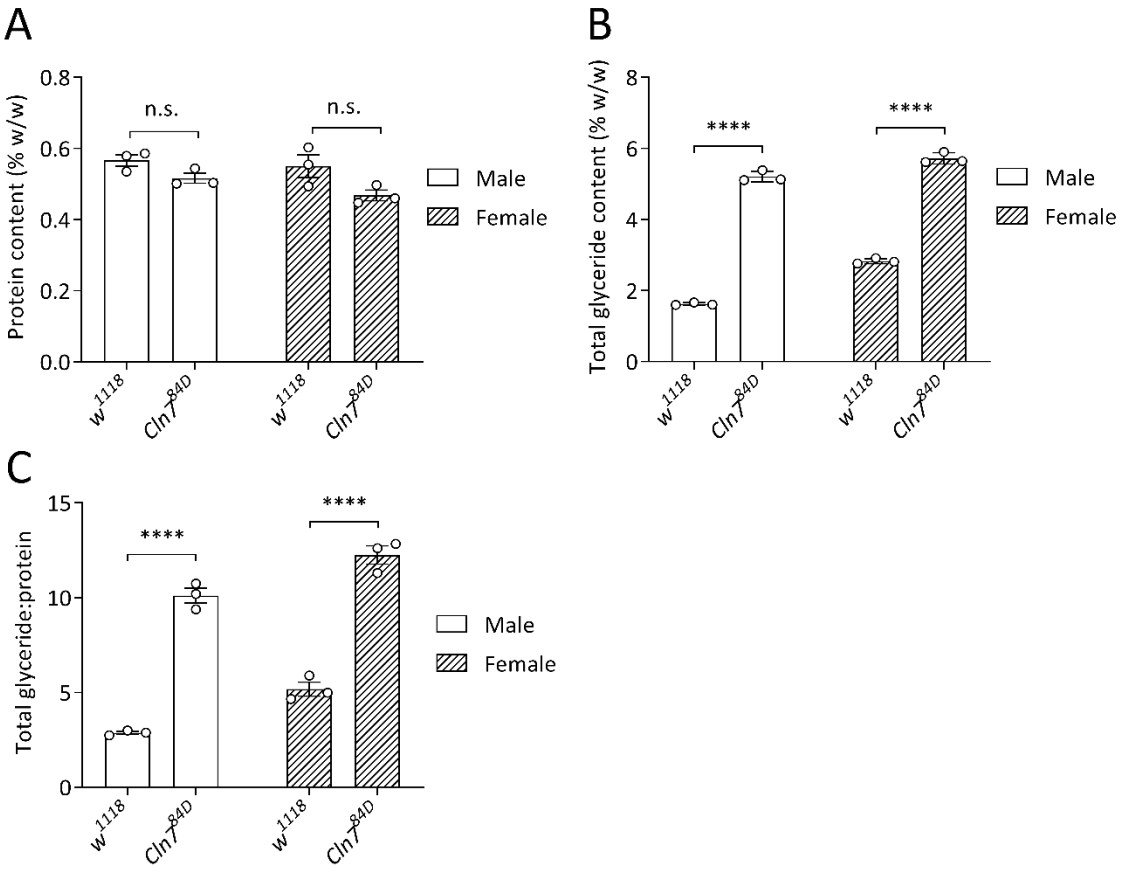

Figure 3.9. Overgrowth of *Cln7*^{84D} flies is partially due to excess glyceride storage.

Protein (**A**) and total glyceride (**B**) content were quantified in adult *w*^{1118} and *Cln7*^{84D} flies. The total glyceride:protein ratio (**C**) was calculated from these measurements. Measurements were taken 1 day post-eclosion. Each data point represents the mean of 3 repeats taken from a pooled sample of 5 flies. Bars represent the mean of the means, and error bars represent the SEM. Statistical analysis was performed using unpaired two-tailed t tests. N.s., $p>0.05$. ****, $p \leq 0.0001$.

respectively. It remains possible that the storage of other lipid species contributes to the increase in mass, as only glyceride content was measured in this assay.

3.2.8 *Lipidomic profiling of Cln7^{84D} flies*

To gain better insight into how lipid profiles are altered in *Cln7^{84D}* flies, changes in the concentration of individual lipid species were measured in an unbiased lipidomic screen. Lipid extracts from whole female *w^{1118}* and *Cln7^{84D}* flies were analysed by UPLC-MS. After QC filtering, changes in a total of 923 metabolite features were identified (Table 3.1), each with calculated fold changes and adjusted p values. Metabolites were grouped into eight broad categories, and then further divided into main classes. Once classified, the data was sorted to identify changes that were most likely to be of biological relevance. Features were ranked by ascending p value to signify metabolites that differ the most between genotypes, while remaining relatively invariant between replicates of the same genotype. In biological terms, this would represent molecules whose concentrations within the cell are normally tightly regulated (thus being invariant), but which display changes between *w^{1118}* and *Cln7^{84D}* flies.

In theory, if the metabolism of a particular category of lipids was specifically disrupted, then structurally-related lipids should cluster by rank. Conversely, a more general disruption would be expected to give a broad distribution of structurally-related lipids amongst the rankings. In addition, the relevance of changes in a particular metabolite cluster is dependent on its positioning within the ranking. To illustrate this, histograms were overlaid with moving average frequencies around a central median (Figure 3.10). Lipids belonging to the glycerophospholipids were found to change the most frequently, with 296 species accounting

Table 3.1. Frequency of differences in lipid content by category and class between female adult *w*^{1118} and *Cln7*^{84D} flies.

Lipid category	Main classes	Frequency
Glycerophospholipids		296
	Glycerophosphates	29
	Glycerophosphocholines	29
	Glycerophosphoserines	27
	Glycerophosphoethanolamines	19
	Glycerophosphoglycerols	18
	Glycerophosphoinositols	18
	Glycerophosphoglycerophosphoglycerols	5
	Glycerophosphoglycerophosphates	1
	Mixed classes	150
Fatty acyls		203
	Fatty acids and conjugates	59
	Fatty esters	33
	Fatty amides	29
	Fatty alcohols	22
	Eicosanoids	9
	Octadecanoids	4
	Docosanoids	3
	Mixed classes	43
	Other fatty acyls	1
Glycerolipids		105
	Triradylglycerols	71
	Diradylglycerols	29
	Monoradylglycerols	4
	Other glycerolipids	1
Sphingolipids		85
	Ceramides	46
	Acidic glycosphingolipids	17
	Sphingoid bases	9
	Phosphosphingolipids	7
	Neutral glycosphingolipids	3
	Mixed classes	3
Sterol lipids		52
	Bile acids and derivates	5
	Secosteroids	22
	Sterols	12
	Steroids	4
	Steroid conjugates	3
	Mixed classes	6
Prenol lipids		40
	Isoprenoids	28
	Polyprenols	7
	Quinones and hydroquinones	3
	Hopanoids	2
Polyketides		5
Mixed classes		135
Other classes		2
	Total	923

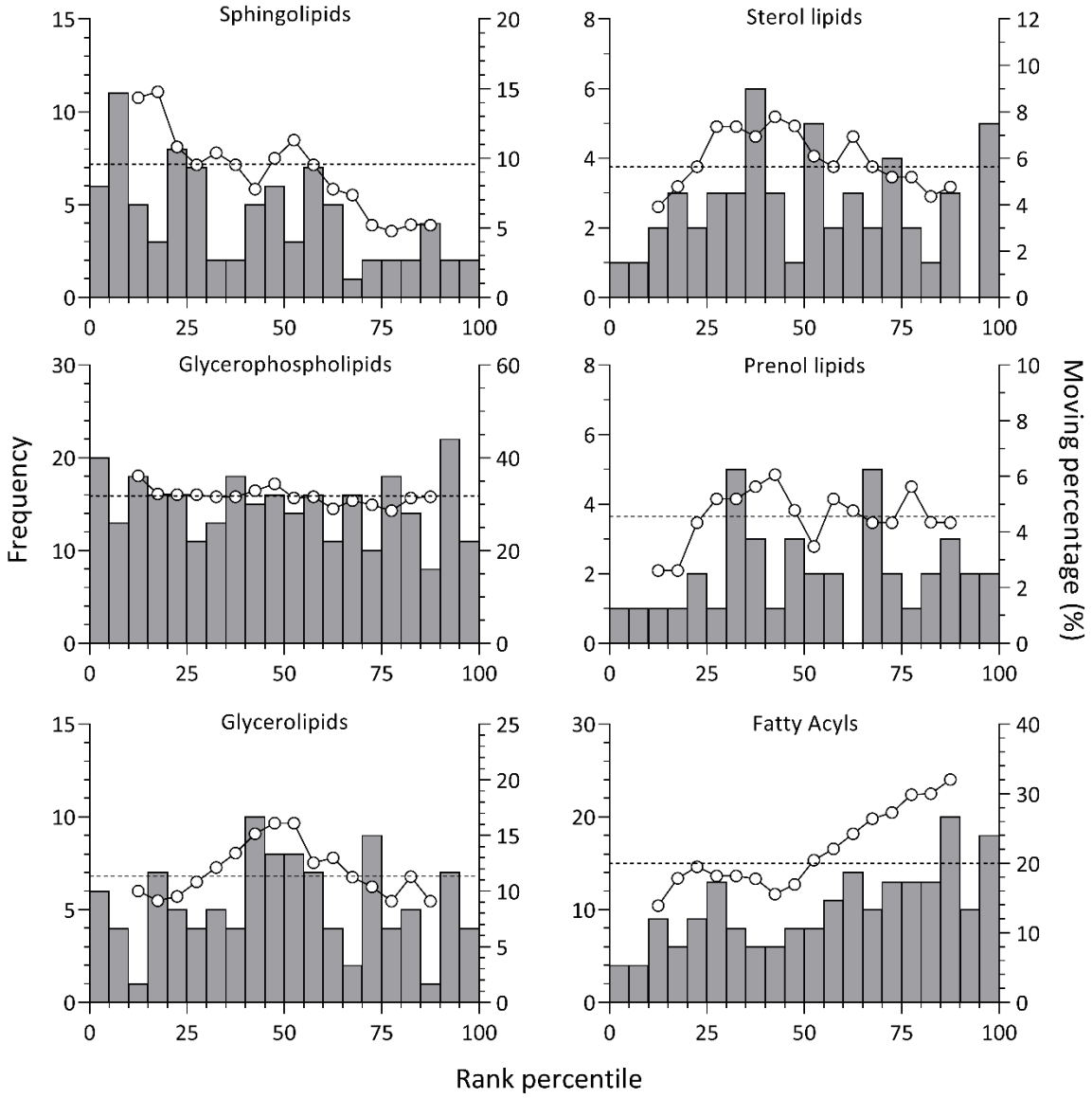

Figure 3.10. Changes to sphingolipid content in adult female *Cln7*^{84D} flies cluster at high ranks.

Features were ranked in ascending order by p value obtained from Mann-Whitney U-tests. Ranked metabolites were separated into twenty equally spaced bins (5 percentile groups) and the frequency distributions were plotted as histograms for each major lipid category (primary y axes). Moving percentages for each distribution were calculated by taking the sum frequency of metabolites in a query lipid category as a percentage of metabolites across all categories, across five adjacent bins (25 percentile groups) in 5 percentile intervals (secondary y axes). Each data point is plotted at the midpoint between corresponding bins. Median moving percentages (dashed line) are illustrated for reference.

for 32% of all detected metabolites. Over 50% of these were assigned as mixed classes. The remaining metabolites were reasonably evenly distributed between the top 6 classes. Overall, changes to glycerophospholipids did not appreciably cluster within the rankings, suggesting that although many changes were detected, these changes were more likely due to a general disruption in their metabolism.

Focussing instead on the positioning of metabolite clusters, one lipid category stood out in particular; the sphingolipids. In contrast to the glycerophospholipids, changes to sphingolipids were the 5th most frequent, out of a total of 8 possible categories (excluding other and mixed groups). However, sphingolipids showed a quartile distribution of 39:26:21:14, which is considerably more weighted towards high rank changes than the glycerophospholipid distribution of 28:25:22:25, bearing closer resemblance to an even 25:25:25:25 spread expected if lipids were distributed randomly amongst the ranks. Concerning the remaining categories, glycerolipids, sterol lipids and prenol lipids showed some clustering around central ranks, whereas fatty acyls were the least significant category with clustering at low ranks.

Next, the relative contributions of metabolite classes (with classes grouping structurally similar compounds) to the frequency distributions of each lipid category (with categories grouping compounds that share more general structural features) were investigated. The prenol lipids were excluded from this analysis as they represented <5% of the dataset, with 70% of metabolites belonging to a single class and did not cluster at high ranks. For clarity, mixed classes were excluded from datasets since they cannot be distinguished between single metabolites with several possible identities or multiple

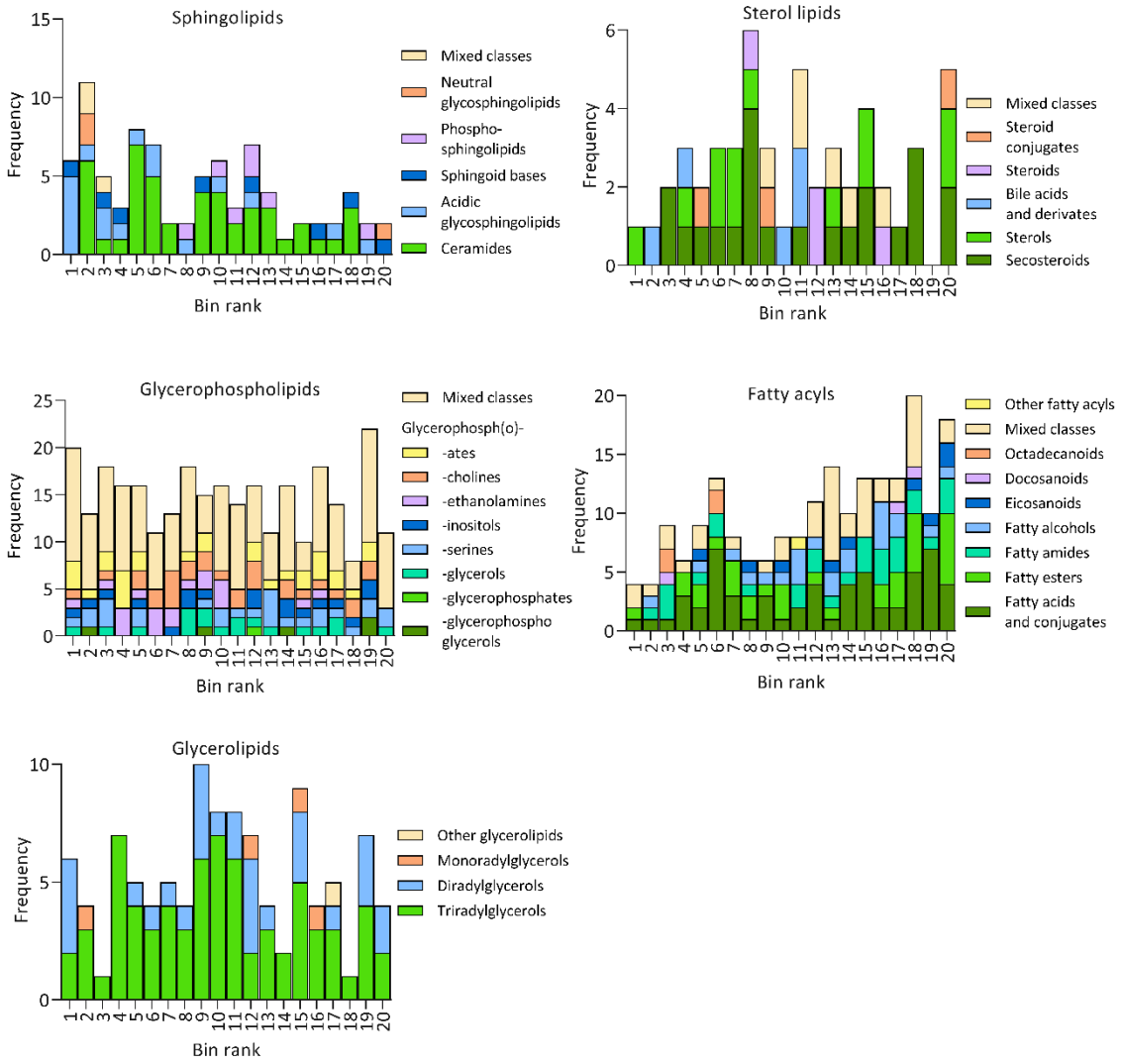

Figure 3.11. Changes to ceramides and acidic glycosphingolipids account for a large proportion of metabolite clustering at high ranks.

The frequency of metabolites belonging to different classes within each major category are plotted as stacked bars within each 5 percentile bin.

metabolites with the same *m/z* and retention time. Starting with the sphingolipids, changes to ceramides and particularly acidic glycosphingolipids were found to account for the majority of high rank changes, with 33% and 56% of all changes to ceramides and acidic glycosphingolipids, respectively, residing in the top quartile rank (Figure 3.11). Furthermore, changes to sphingolipids within the top 5th percentile were almost exclusively to acidic glycosphingolipids. Therefore, it is apparent that the metabolism of ceramides and acidic glycosphingolipids is disrupted significantly in *Cln7*^{84D} flies.

Although high rank clustering was not observed in the other lipid categories, their distributions of lipid classes were still analysed to identify any hidden trends within individual classes. Most classes belonging to the glycerophospholipids were evenly spread amongst the ranks, matching the overall trend when all glycerophospholipids are combined. One possible exception is the glycerophosphoethanolamines, with 33% of changes in the top quartile and 94% in the top half. However, 51% of metabolites within the glycerophospholipid category were placed in mixed classes which show a uniform distribution. Therefore, while changes to glycerophosphoethanolamines appear somewhat significant, this conclusion must carry the caveat that a high proportion of metabolites have an unknown identity. As for the remaining categories, no trends in lipid classes were seen. Therefore changes to glycerolipids, sterol lipids and fatty acyls as lipid categories are unlikely to be of biological significance.

To complement the ranking of lipid changes, the direction and magnitude of changes to lipids were also analysed. Changes to lipids were visualised category by category by plotting metabolite fold change against p value (Figure 3.12). Illustrated in this way, it is noticeable that the vast majority of metabolite changes across all categories had log2 fold changes of

between -5 and 5 , with p values of $<10^{-7}$. Of greater interest was the group of six metabolites belonging to the sphingolipids with very high significance, which was not observed in the other categories. Five out of six of these metabolites were acidic glycosphingolipids and were all downregulated, with reductions ranging from 2.2 to >2,000 fold. These changes were to four GM3 gangliosides and one GA1 ganglioside, in addition to the sphingoid base C19 sphingosine-1-phosphate which is a known signalling molecule. Looking through the identities of the acidic glycosphingolipids, seven GM3 gangliosides were identified in total and all of them were downregulated. In contrast, two GM1 gangliosides were found and were upregulated 13.7 and 87.3-fold. Trends to changes in other acidic glycosphingolipids were less clear, possibly due to several features containing multiple metabolites that were indistinguishable by UPLC-MS. Nevertheless, the consistent and opposing changes to GM3 and GM1 gangliosides suggests there may be a block in a pathway connecting GM3 and GM1 gangliosides, whereby GM3s are depleted and GM1s are accumulated.

Concerning other sphingolipid classes, 46 out of 85 (54%) sphingolipids belonged to the ceramides class. Thirty-three (72%) of these were upregulated, although many of these were only upregulated to a small degree. Of the sphingoid bases, four sphingosine-1-phosphates were identified and all were downregulated. The metabolite C19 sphingosine-1-phosphate was the second-most significant metabolite in the whole database, thus the general downregulation of sphingosine-1-phosphates may have some biological significance. Turning to the phosphosphingolipids, 6 out of 7 were identified as ceramide phosphoethanolamines, all showing minor upregulation with increases of between 1.5 and 2.6 fold. The remaining class, the neutral glycosphingolipids, were too few in number to draw any conclusions. In summary, the acidic glycosphingolipids exhibited the most striking

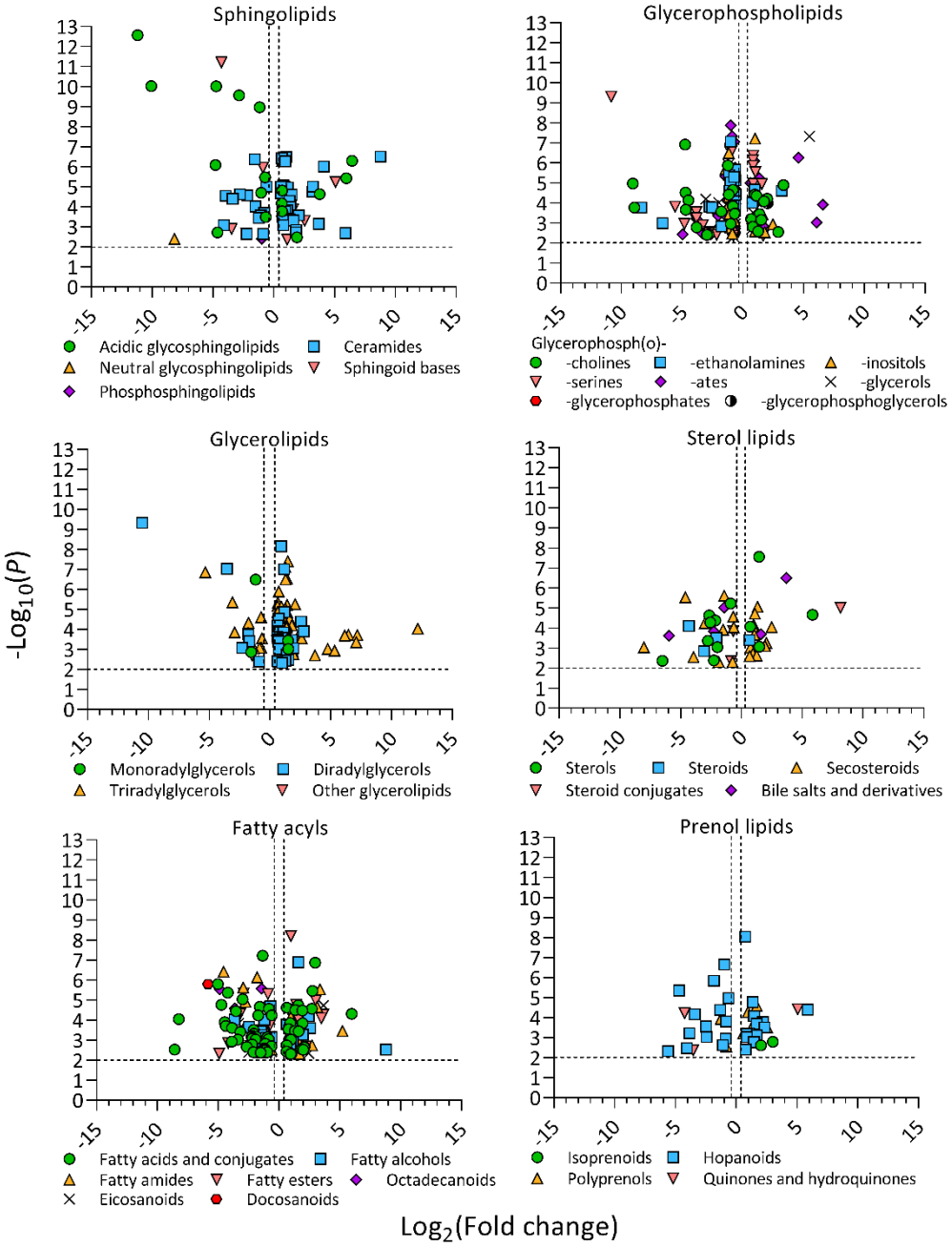

Figure 3.12. A population of acidic glycosphingolipids are significantly depleted in *Cln7*^{84D} flies.

Fold changes in metabolite concentration were calculated as a ratio of *Cln7*^{84D} to *w*^{1118}. The fold changes in $\log_2$ scale and p value in $\log_{10}$ scale were plotted as volcano plots. Negative $\log_2$(fold change) values (left) represent metabolite downregulation and positive values represent metabolite upregulation in *Cln7*^{84D} flies. The horizontal and vertical dashed lines represent cut-off values of $p < 0.01$ and fold change between 0.67-1.5, respectively. Beneath each volcano plot is a legend for the different lipid classes within each category.

changes, with clear trends suggesting GM3 ganglioside depletion and GM1 ganglioside accumulation. More subtle, yet consistent, trends observed included increases to ceramides and ceramide phosphoethanolamines and a decrease to sphingosine-1-phosphates. One possibility is that these minor trends are secondary to primary changes in GM1 and GM3 gangliosides, potentially as compensatory or knock-on effects to biosynthetic, turnover or signalling pathways.

Trends in classes from other lipid categories were also investigated. Sixty-four percent of all identified glycerophospholipids were downregulated. This was not attributable to any one particular class, rather all classes were downregulated in the majority, suggesting there may be a reduction in the synthesis of glycerophospholipids in general. In contrast, the majority of identified glycerolipids were upregulated, including 79% of diradylglycerols and 85% of triradylglycerols. These results agree with the 3-fold upregulation of total glycerides observed in the colourimetic glyceride assay. Regarding the sterol lipids, fatty acyls and prenol lipids, no clear trends were observed across the classes.

In conclusion, using metabolite rank and fold change distributions in combination identified changes to sphingolipids to be the most significant of all changes, despite being the 5th-most frequent of 8 possible categories within the list of metabolites. The most striking of trend was GM3 ganglioside downregulation, suggesting they may be depleted in *Cln7*^{84D} flies. This was accompanied by an accumulation of GM1 gangliosides, suggesting that the loss of Cln7 results in the defective degradation of GM1 gangliosides to GM3 gangliosides. Other, less pronounced trends included increases in ceramides and ceramide phosphoethanolamines and a decrease in sphingosine-1-phosphates, which are possibly secondary changes as a result

GM3 ganglioside depletion. In addition to sphingolipids, *Cln7*^{84D} flies showed a general reduction in glycerophospholipids, most notably in glycerophosphoethanolamines which clustered toward higher ranks and had the highest proportion of downregulated metabolites, plus a general increase in glycerolipids. Finally changes to sterol lipids, prenol lipids and fatty acyls were found to be neither significant nor were there any class-by-class trends, and so were concluded to be likely of little to no consequence.

3.3 Discussion

3.3.1 *Response of Cln7^{84D} flies to Tor inhibitors*

It was found that *Cln7*^{84D} flies were sensitive to TORC1 inhibition by rapamycin during larval development, exhibiting larger delays to development than in *w*^{1118} controls. This phenotype is consistent with an extended pre-critical mass phase in response to rapamycin, suggesting that not only do *Cln7*^{84D} flies have reduced TORC1 activity, but also that TORC1 activity is also reduced in the PG. This could occur in two distinct ways; intrinsically by dampening the response to growth signals within the PG, or extrinsically by limiting the bioavailability of growth factors, which may include reducing growth factor expression, limiting exocytosis of factors from secretory vesicles, increasing growth factor degradation or upregulating inhibitory binding partners like secreted decoy of insulin receptor (SDR) or acid labile subunit. In parallel, these possibilities require different distributions of Cln7 expression, where the intrinsic pathway minimally requires Cln7 expression within the PG, whereas the extrinsic pathway requires Cln7 to be expressed in tissues expressing the putative growth factors or regulatory proteins. At present the intrinsic pathway seems the most likely, given

that limiting growth factor bioavailability via an extrinsic pathway would be expected to yield small flies, such as when dilp2 expression is genetically ablated (433).

High concentrations of rapamycin reduced adult size in w^{1118} and $Cln7^{84D}$ flies, yet $Cln7^{84D}$ flies remained proportionally larger than w^{1118} flies in almost all cases. Adult size is determined by growth rate in the interim phase between reaching critical mass and pupation. The simplest explanation for the increased mass would be that $Cln7^{84D}$ flies have a faster growth rate than w^{1118} flies in this phase, but this directly contradicts the development phenotype where $Cln7^{84D}$ fly growth is slightly slower. An alternate possibility is that the post-critical mass phase is prolonged in $Cln7^{84D}$ larvae, allowing them more time to grow before pupating. There is evidence that the length of the post-checkpoint phase can vary in response to nutrient availability, whereby larvae pupate sooner when starved (422). However here nutrient availability is constant between genotypes, thus for the increased mass to be due to increased feeding time, this would argue an unlikely scenario where the loss of Cln7 skews the perception of nutrient supply in favour of being in greater abundance. Instead, a more likely explanation consistent with the findings shown above is that loss of Cln7 increases nutrient storage.

Curiously, treatment with Torin 1 did not replicate the effects of rapamycin on development time or adult size. Torin 1 is an inhibitor of both TORC1 and 2, which is a pharmacological equivalent to hypomorphic or amophic Tor alleles, which are often lethal before adulthood. In contrast, rapamycin targets TORC1 and spares TORC2 activity. Therefore, it is likely that the response to Torin 1 is more severe than rapamycin at efficacious doses,

which may explain why the margin between no response and lethality was just a 2-fold increase with Torin 1, whereas a 50-fold increase was required with rapamycin.

3.3.2 *Response of Cln7^{84D} flies to varied nutrition*

Given the size difference between *Cln7^{84D}* flies and controls, one possibility was that Cln7 regulates growth by functioning as a nutrient transporter, and that the size difference may be modified by diet. Sucrose restricted fly growth in a concentration-dependent manner but had little effect on development time. The lack of a developmental delay suggests that growth rate is unaffected by elevated sucrose concentrations, but that sucrose may shorten the growth period after critical mass is achieved. Importantly, *Cln7^{84D}* flies responded similarly to *w^{1118}* controls, suggesting that sucrose metabolism is largely intact. In contrast, reducing dietary yeast caused significant delays to development and produced severely undergrown adults. Interestingly, *Cln7^{84D}* flies appeared more sensitive to yeast depletion than *w^{1118}* controls and their overgrowth was abolished on yeast-restricted food; development was also delayed. Here, it is likely that reduced yeast significantly reduces growth rates and extends the pre-critical mass phase, and that this effect occurs to a greater extent in *Cln7^{84D}* flies. *Cln7^{84D}* and control adult flies are similar sizes on yeast-restricted food. One explanation is that the growth rates were slowed to such an extent that there was insufficient time after critical mass was achieved for *Cln7^{84D}* flies to become overgrown. Therefore, it could not be distinguished whether nutrients supplied by yeast underpin the mass phenotype, or whether the lack of overgrowth was due to a narrow post-critical mass window. Dietary yeast consists of a mixture of proteins, fats and vitamins, and while the effects on maturation and growth

under yeast restriction likely originate from protein limitation, it would be interesting to conduct similar experiments where dietary protein and fat intake are separated.

When nutrient dependence for growth signalling was tested in CLN7$^{-/-}$ MEFs, the responsiveness of both mTORC1 and MAPK growth pathways was reduced. These pathways were shown to be separable as amino acid- and glucose-dependent pathways, respectively, and while amino acid dependence remained intact, depletion of glucose failed to further reduce ERK phosphorylation in CLN7$^{-/-}$ MEFs. This suggests that CLN7 is involved in the regulation of MAPK signalling by glucose. While the most obvious possibility would be that CLN7 is a glucose transporter, several glucose transporters have been identified either through direct evidence or by amino acid sequence alignments. In addition, phylogenetic analysis of CLN7 in Figure 3.1 failed to detect similarities between CLN7 and sugar transporters, suggesting instead that CLN7 is loosely similar to tetracycline transporters, with perhaps greater similarity to a vacuolar phosphate transporter identified from *Arabidopsis thaliana*. Given that the deletion of CLN7 affects both S6K and ERK1/2 activation, an alternate hypothesis is that CLN7 interacts with proteins further upstream that are common to both pathways. An interesting possibility is that CLN7 functions as a glucose sensor, relaying signals to growth pathways, potentially at the receptor level, in response to glucose binding or transport to initiate signalling, akin to a quality assurance step before committing valuable resources to growth. However, it is difficult to cross-confirm this hypothesis with the *in vivo* data when testing the effects of nutrient supply on adult fly mass. Reduced growth signalling would be predicted to yield smaller flies, yet *Drosophila* Cln7 expression is not ubiquitous amongst tissues, and if Cln7 is expressed in the PG as discussed above, then reduced MAPK signalling that is restricted to the PG would be expected yield larger flies with extended

development times, consistent with the effects of reduced TORC1 signalling. Indeed, reducing sucrose concentration mildly increased *Cln7*^{84D} adult fly mass, with slightly shorter development periods, but these responses were observed similarly in *w*^{1118} flies. Thus it remains unknown whether a) MAPK signalling is reduced in *Cln7*^{84D} flies, or b) the dependence on CLN7 for glucose-dependent MAPK activation observed in MEFs is also true in *Drosophila*.

3.3.3 *Sphingolipid metabolism and neurodegeneration*

The sphingolipidoses are a subset of LSDs with defects in sphingolipid degradation that frequently present with impaired neurodevelopment and neurodegeneration. The pathways for sphingolipid biosynthesis and degradation in mammals and *Drosophila* are illustrated for reference in Figure 3.12. Defects in enzymes at many steps in sphingolipid degradation are associated with distinct diseases, demonstrating that maintaining sphingolipid turnover is essential within the nervous system. No disease has been attributed to mutations in biosynthetic enzymes, which given the severe neurological defects caused by deficiencies in degradative enzymes, where the balance of sphingolipid composition becomes compromised, mutations to biosynthetic enzymes that would completely preclude the synthesis of many structures may simply be lethal in humans. Each sphingolipidosis can be characterised by the sphingolipid structures that accumulate within lysosomes. Here, an unbiased lipidomic screen of adult *Cln7*^{84D} flies detected changes in the sphingolipid profile, specifically showing GM3 depletion and GM1 accumulation, with minor increases in ceramides and ceramide phosphoethanolamines. Given the necessity to tightly control the sphingolipid composition

with the nervous system, these changes in sphingolipids, at least in principle, would be expected to impinge on neuronal function.

The glycobiology of *Drosophila* has been used as a simplified, more linear model for studying the role of sphingolipids within the nervous system. Indeed, neuronal phenotypes have been observed in several lines defective for sphingolipid metabolism. Defective *de novo* sphingolipid biosynthesis caused by mutations in *spt-I* and *lace* lead to axonal mis-targeting in the mushroom bodies (434), and reduced bouton number but increased bouton size at the NMJ (435). Reducing CerPE synthesis by mutating Spt-I, schlank, Des1 or Pect in wrapping glia result in axonal defasciculation (436) and increases satellite bouton formation at the NMJ (435). In addition knockdown of *sply*, which is mutated in Charcot-Marie-Tooth disease in humans, and causes reductions in axon branching and bouton number at the NMJ (437). Furthermore, specifically targeting glycosphingolipid synthesis by mutating *egghead* or *brainiac* to reduce and increase the concentration of MacCer, respectively, identified that presynaptic MacCer promotes increased bouton number and reduced bouton size (435). Additionally deletion of *β4GalNAcTA* reduced the size, branching and bouton number of innervating neurons at the NMJ (438).

3.3.4 *A potential role for Cln7 in sphingolipid metabolism*

Whole lipidomic profiling of adult *Cln7*^{84D} flies identified that sphingolipid content was the most significantly and consistently altered, and predicted that these differences corresponded to changes in GM1 and GM3 gangliosides. However, *Drosophila* cannot synthesise ganglio-class sphingolipids, and instead synthesise arthro-series

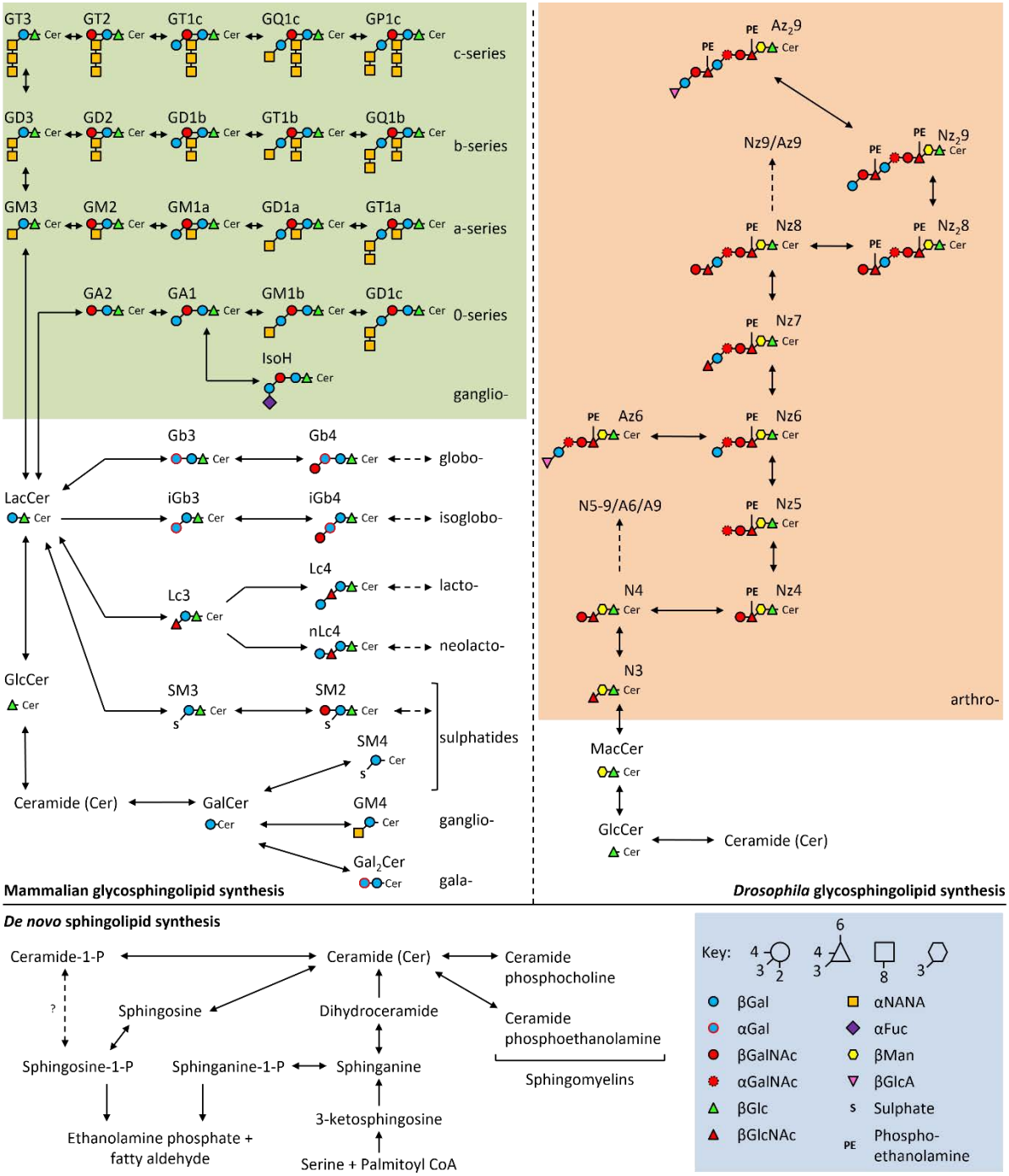

Figure 3.12. Pathways for glycosphingolipid metabolism in mammals and *Drosophila*.

Mammals and *Drosophila* share a common pathway for *de novo* sphingolipid synthesis, but synthesise extended glycosphingolipids via divergent pathways. Mammals can synthesise several classes of glycosphingolipid (as annotated down the right hand side) whereas *Drosophila* only make arthro-series glycosphingolipids. A key to the sequence and positioning of molecular species is provided in the bottom right.

Table 3.2. Increases in the molecular mass of glycosphingolipids, relative to ceramide

Molecule	Mass difference (Da)
Ceramide	+0
GA2	+473
GA1	+617
GM4	+417
GM3	+561
GM2	+746
GM1	+890
GD3	+834
GD2	+1019
GD1	+1163
GT3	+1107
GT2	+1292
GT1	+1436
GQ1	+1709
GP1	+1982
N3	+473
N4	+658
Nz4	+781
Nz5	+966
Nz6	+1110
Nz7	+1295
Nz8	+1480
$Nz_2$8	+1603
$Nz_2$9	+1747
Az6	+1286
Az9	+1800
$Az_2$9	+1923

glycosphingolipids. Similar to gangliosides, arthrosides are serially glycosylated, but are not sialylated and are instead modified by phosphoethanolamine (PE) and glucuronic acid (GlcA). These differences change the mass of respective glycosphingolipids, with mass differences of approximately 273 Da upon addition of sialic acid compared to 176 Da for GlcA (+55%), 123 Da for PE (+122%), 144 Da for hexose (+90%) and 185 Da (+48%) for HexNAc moieties. These differences show that sialic acid residues from human glycosphingolipids cannot be substituted like-for-like for a modification in *Drosophila*, and that acidic gangliosides (sialic acid-containing sphingolipids) are likely misidentified. However, based on what is known about the sequence of steps in *Drosophila* glycosphingolipid synthesis, predictions toward the true identify of detected metabolites can be made. GM3 gangliosides contain one sialic acid and two hexose residues (561 Da) with a mass that lies between the glycosyl chains of N3 (473 Da) and N4 (658 Da) arthrosides (Figure 3.13). Upon closer examination of the allocated metabolite identities, the acidic gangliosides were frequently predicted to possess long acyl chains of up to 26C in length in some cases. While acyl chain length and saturation likely influence retention time during UPLC, which is quantified and used to identify metabolites, a difference of up to 10C units can account for differences of as much as 141 Da. Therefore, given the fundamental differences between ganglioside and arthroside synthesis, one possibility is that additional carbons are added during ID allocation to bridge the difference in mass between the identified arthroside and the expected mass of the nearest ganglioside. In this eventuality, a long-chain GM3 ganglioside most likely represents an N4 arthroside. Extending this logic to cover other identified acidic gangliosides, reasonable substitutions are GA1 = N4, GM2 = Nz4, GM1 = Nz5, GD3 = Nz5 and GD2 = Nz6 (Table 3.2). This translates the original observation of GM3 depletion and GM1 accumulation, to N4 depletion and Nz5

accumulation. Based on these estimations, this would predict a block in the degradation of Nz5 to N4 arthrosides, covering two possible steps which remove a terminal αGalNAc residue and a phosphoethanolamine modification.

Sphingolipid degradation is surprisingly under-characterised in *Drosophila*. The human sphingolipidoses are exclusively defects in sphingolipid degradation, with defects in synthesis possibly being too severe to be viable, however the majority of research in *Drosophila* focusses on the role of biosynthetic enzymes on the developing nervous system, amongst other target organs. This may be in part due to the differences in how sphingolipid structures are assembled between humans and *Drosophila*, however the enzymes required for removing terminal residues like βGal, βGalNAc and βGlcNAc are likely conserved as these residues are present in structures from both species. Therefore, one would expect *Drosophila* to manifest storage disorders triggered by enzyme deficiency similar to humans when degradation is blocked. Whether or not these disorders would present similar phenotypes however is a different matter, since a deficiency in a homologous enzyme would cause dissimilar alterations in sphingolipid composition, thus particular diseases, like GM1-gangliosidosis or Tay-Sachs, may not be phenotypically modelled well in *Drosophila*.

Here, loss of Cln7 caused substantial changes to the sphingolipid profile, estimated to most significantly involve N4 depletion and Nz5 accumulation. In principle, this would be expected to interfere with neurodevelopment and function, as with any known defect in sphingolipid metabolism. Since Cln7 is conserved from humans to *Drosophila*, Cln7 function and its role in sphingolipid metabolism are likely also conserved, suggesting Cln7 regulates a common feature in human and *Drosophila* sphingolipid biology. The changes to N4 and Nz5

sphingolipids detected here narrow the candidate features to αGalNAc and phosphoethanolamine metabolism. In humans, αGalNAc linkages are present in blood group A sphingolipids, which belong to the lactosides. Deficiencies in α-Gal B, which hydrolyses terminal αGalNAc residues, cause Schindler's disease, also an early onset LSD. Thus, primary defects in αGalNAc degradation seems unlikely to be the mechanism for Cln7 disease. Alternatively, CerPE, a sphingomyelin, and phosphoethanolamine-arthroside derivatives comprise the majority of sphingolipid content in *Drosophila*. The only known instance of phosphoethanolamine modification of sphingolipids in humans is in CerPE synthesis, yet the major sphingomyelin in mammals is CerPC. In addition, defects in *SMPD1*, responsible for sphingomyelin degradation, have already been characterised in Niemann-Pick A/B disease. Therefore, the hydrolysis of phosphoethanolamine from sphingolipids as a mechanism for Cln7 disease also seems unattractive. There are, however, known examples of lysosomal storage disorders where the defect is not actually in the degradation itself, but in the efflux of products from lysosomes, for example, defective cholesterol efflux in Niemann-Pick type C. Cln7 is predicted to be a MFS transporter, so perhaps Cln7 disease is caused by the defective efflux of degradation products. Interestingly, phylogenetic analysis suggested that Cln7 was dissimilar to the sugar porters (ID 2.A.1.1) (Figure 3.1A), with a weak similarity to tetracycline transporters but also a possible connection to the vacuolar phosphate transporter from *Arabidopsis thaliana* (Figure 3.1B). Taken together, the hypothesis is that Cln7 is required for the efflux of phosphoethanolamine, or its products phosphate and ethanolamine, from lysosomes, and that accumulation of these molecules within lysosomes when their efflux is blocked leads to defective sphingolipid metabolism.

3.3.5 *Validation of lipid changes identified by UPLC-MS*

While performing an unbiased lipidomic screen was valuable in the narrowing of candidate lipids, from a possible 84 lipid classes spanning 8 major categories down to a single class, the limits of what this represents need to be considered. The data represents a snapshot of metabolism within whole adult female flies as a relative comparison between genotypes. What cannot be appreciated from MS is actual abundance of metabolites. Metabolites that did not change in abundance above a threshold amount were removed by QC filtering, and values were quantified as a relative fold change in peak area between genotypes. Therefore, by how much total sphingolipid or ganglioside content changed is unknown. In addition, lipid profiles differ from organ to organ and likely differ throughout development. One-day-old adults were chosen to correlate with measurements of fly mass and glyceride content taken at the same timepoint. The tissue or tissues in which Cln7 potentially functions to regulate tissue growth and lipid metabolism in *Drosophila* is unknown. In mammals, Cln7 is expressed in neurons and mutations result in early-onset neurodegeneration, thus the presumption is that Cln7 functions within neurons and is fundamental to neuronal health. In *Drosophila*, Cln7 expression is observed in the photoreceptors, in addition to expression in sub-perineurial glia, oenocytes and at the sub-synaptic reticulum of the post-synaptic density in the body wall muscles. Unpublished data has found that $Cln7^{84D}$ flies have undergrown synapses at the NMJ, but that this phenotype appears to be due to loss of Cln7 function in the muscle, not in neurons or glia. Given the high sensitivity of MS, whole flies were chosen to avoid the risk of eliminating the putative tissue of interest during lipid extraction.

To validate the UPLC-MS data, it would be informative to quantify the global sphingolipid and specific arthroside content throughout development, which can be done by

thin layer chromatography. This approach has sufficient resolution to distinguish between sphingolipids with different glycosyl chain lengths. It would also be interesting to visualise arthroside localisation, particularly at the NMJ and within photoreceptors as these are the most relevant tissues to Cln7 disease. This would identify any depletion, accumulation or mislocalisation of lipids, providing spatial resolution as an extra dimension to how lipid metabolism is disrupted. With this information, a genetic approach can be employed to screen for potential interactions between Cln7 and regulators of sphingolipid metabolism. Of particular interest would be the identification of enzymes the catalyse sphingolipid degradation and the characterisation of phenotypes when they are mutated. These experiments can be used to compare and contrast phenotypes with mutations to Cln7, to investigate the possibility of Cln7 disease as a disorder of sphingolipid degradation.

3.3.6 *Conclusions*

The experiments described in this chapter have characterised a potential role for Cln7 in *Drosophila* maturation and growth during development, in addition to the identification of excess lipid storage and defective sphingolipid metabolism when Cln7 is mutated. *Cln7*^{84D} flies were sensitised to developmental delays caused by rapamycin, suggestive of a reduced pool of active TORC1, and signalling via TORC1- and MAPK-dependent mechanisms was reduced in CLN7$^{-/-}$ MEFs. These are consistent with reduced growth signalling when Cln7 is mutated. In *Drosophila*, the PG balances tissue and organism growth with maturation timing, thus developmental delays potentially originate from mechanisms that alter growth rates within the PG. The sensitisation of *Cln7*^{84D} flies to developmental delays by rapamycin suggests that

TORC1 activity is reduced within the PG, and that Cln7 is expressed in and regulates growth and maturation from the PG. Analysis of lipid content within *Cln7*^{84D} flies also revealed increased triacylglyceride storage, accounting for part of the increase in mass, but more significantly defects in sphingolipid metabolism, leading to the depletion of N4 and accumulation of Nz5 arthrosides. Sphingolipids have important biophysical properties that govern the formation of membrane structures such as lipid rafts, and the clustering of membrane proteins in these rafts has in turn been shown to be required for signal transduction in certain signalling pathways. For example, interactions have been identified between sphingolipids and receptor tyrosine kinases, including the insulin receptor, and wingless.

Taking together the findings of this chapter, I propose the following model: Cln7 is required for the efflux of degradation products, potentially phosphoethanolamine or its derivatives from sphingolipid degradation, from lysosomes. Mutations to Cln7 may then trigger the accumulation of these molecules within lysosomes, disrupting lysosomal function. These disruptions may include the inhibition of lysosomal hydrolases and perturbations to the electrochemical gradient across lysosomal membranes, affecting lysosome acidification and maturation. The inhibition of lysosomal sphingolipid hydrolases may in turn account for defects in sphingolipid turnover, a frequent cause of LSDs that manifest with early onset neuropathology. Unpublished data from the lab has previously identified underdeveloped synapses at the NMJ in *Cln7*^{84D} flies, however Cln7 expression was not identified in motoneurons. Instead, Cln7 is expressed in the sub-synaptic reticulum within the muscle, thus the role of post-synaptic sphingolipid metabolism on synapse development needs to be investigated. Alterations to the sphingolipid composition of membranes likely inhibits

membrane protein function and signal transduction. This may account for the reduced growth signalling via MAPK and TORC1 observed when Cln7 is mutated. Concerning the overgrowth and delayed development phenotypes, the sensitisation of *Cln7*^{84D} flies to rapamycin suggests that these phenotypes originate from reduced TORC1 activity within the PG, suggesting that Cln7 is also expressed in the PG. Relating back to the human disease, these findings may suggest a role for disrupted sphingolipid turnover in the neuropathology of Cln7 disease.

4 CHARACTERISING PROTEIN-PROTEIN INTERACTIONS WITH CLN7

4.1 Introduction

Protein-protein interactions are biologically significant events that are fundamental to many cellular functions. They regulate protein function, localisation and stability, and can communicate signals between neighbouring cells and between distant tissues. Characterising these interactions therefore should be considered a key step in investigating protein function in the context of a living system. Approaches to investigate protein interactions commonly involve tagging a query protein with an affinity label for affinity purification. Proteins that interact with the query protein are co-purified and can be identified by MS. Alternatively, specific interactions can be probed directly by Western blotting for co-precipitated proteins. A challenge with affinity-based approaches is striking the balance between stringency to remove non-specific interactions, with preservation of native protein complexes. To avoid using too stringent conditions, tandem affinity purification (TAP) can be performed to capture protein complexes by successive purification a query protein with two epitope tags. This reduces the retention of non-specific interactions without the need to increase salt or detergent concentrations in wash buffers.

Most if not all proteins do not function in isolation and instead function with or alongside other proteins. Some proteins may require certain interactions to switch between active and inactive states, while others may influence protein distribution about cellular compartments. As an MFS transporter, Cln7 may interact with proteins that promote or inhibit

substrate permeability, act as a ligand or cofactor to Cln7, modify Cln7 through post-translation modifications, or regulate Cln7 localisation within or between membranes and membrane domains. In addition, some interactions may occur only in a subset of tissues in the regulation of tissue-specific pathways. Each of these possibilities are critical events that together provide a more holistic view of the role for Cln7 in cells and tissues.

The aim of this chapter was to investigate how Cln7 is regulated by capturing and identifying proteins that interact with Cln7 using affinity-based approaches.

4.2 Results

4.2.1 *Cln7 and Rheb coimmunoprecipitate in S2 cells*

Mutations to *Cln7* in flies triggers whole body overgrowth. Cells within the wing of $Cln7^{84D}$ flies are 10% larger than controls, suggesting that overgrowth is likely due to increased cell size rather than additional cell divisions (unpublished data). These phenotypes were hypothesised to originate unexpectedly from reduced TORC1 activity specifically within the PG, as opposed to a systemic over-activation in all tissues. Indeed, $Cln7^{84D}$ flies are sensitised to TORC1 inhibition by rapamycin suggesting that $Cln7^{84D}$ flies have a reduced pool of active TORC1. $Cln7^{84D}$ flies also display several phenotypes consistent with reduced TORC1 activity, such as increased lifespan and resistance to starvation and oxidative stress (unpublished data). Furthermore, $CLN7^{-/-}$ MEFs show diminished re-activation of the downstream target of TORC1, S6K, following nutrient deprivation, shown here and previously (383). Together these suggest that Cln7 may regulate TORC1 signalling. TORC1 is recruited to and activated at the lysosomal surface, thus, as a lysosomal protein, Cln7 is well placed to interact with TORC1 or its lysosomal binding partners.

To investigate whether Cln7 regulates TORC1 activation, an interaction between Cln7 and the TORC1 activator Rheb was tested. S2 cells were co-transfected with Myc-Cln7 and FLAG-Rheb. Reciprocal immunoprecipitations were performed and Western blots were probed for both proteins. In co-transfected cells a fraction of FLAG-Rheb co-immunoprecipitated with Myc-Cln7, and similarly a fraction of Myc-Cln7 co-immunoprecipitated with FLAG-Rheb (Figure 4.1A). Neither protein was pulled down in the absence of precipitating protein. In support of analysis by immunoprecipitation, protein co-

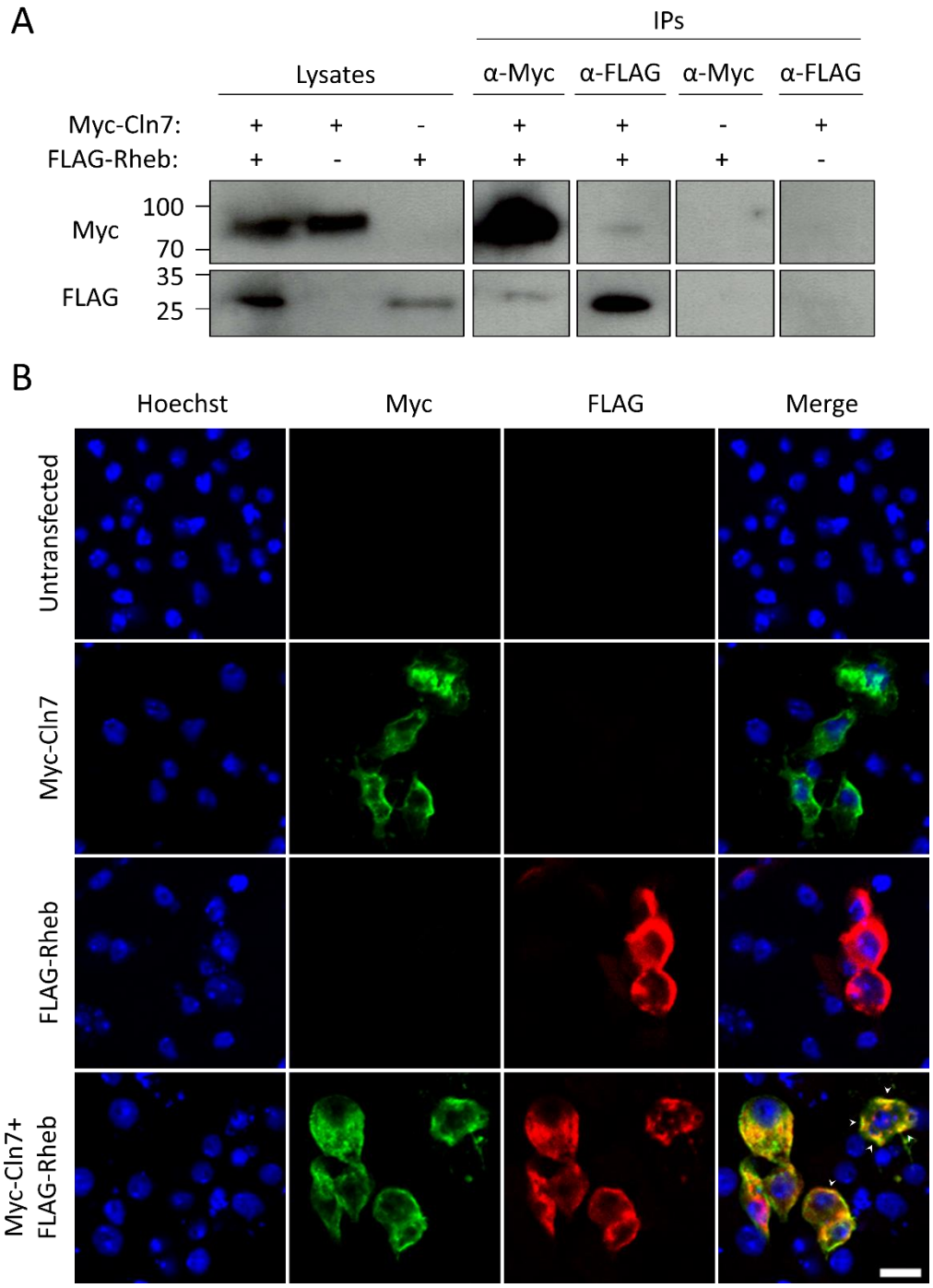

Figure 4.1. Cln7 interacts with the TORC1 activator Rheb.

Cells were co-transfected with Myc-Cln7 and FLAG-Rheb and processed 24 h post-transfection. **A**) Proteins were immunoprecipitated with α-Myc or α-FLAG beads. Lysate and eluate fractions were probed for both Myc and FLAG. A fraction of Rheb co-immunoprecipitated with Cln7 and vice versa. Singly transfected cells were included as controls. **B**) Protein localisation was analysed in single and double transfected cells by immunofluorescence. Arrowheads show areas of co-localisation. Scale bar = 10 µm.

localisation was also investigated by immunofluorescence. Myc-Cln7 and FLAG-Rheb both show some cytosolic staining but accumulate at the plasma membrane, independently of one another (Figure 4.1B). Curiously, intracellular punctae corresponding to lysosomes were largely unseen in cells transfected with Myc-Cln7 or FLAG-Rheb, which may due to membrane saturation and mislocalisation as a result of protein overexpression. Nonetheless, cells expressing both Myc-Cln7 and FLAG-Rheb contained foci at the plasma membrane where both proteins co-localise, indicated by arrowheads. Together, the evidence here suggests that Cln7 interacts with Rheb within the membrane and therefore may regulate TORC1 activation.

4.2.2 *Native IP of FLAG-Venus-Cln7 flies*

While Cln7 and Rheb co-precipitated, the interaction appears weak. It is possible that Cln7 and Rheb do not directly interact and instead may be components of a wider protein complex. In addition, their interaction may only be transient or be dependent on stimuli, which might explain why only a small fraction of protein co-precipitated. Several other proteins are involved in TORC1 recruitment and activation, including the Rag GTPases and the Ragulator complex, that may equally form complexes with Cln7. Thus an alternate approach was taken to avoid testing each component one by one.

A CRISPR knock-in line was recently engineered by our lab to express FLAG-Venus-Cln7 (FVCln7, Figure 4.2A) (402). This provided a convenient means to identify proteins that interact with Cln7 *in vivo* by native tandem affinity purification (TAP) for identification by mass spectrometry (MS). To track FVCln7 purification, samples were taken from the input and several eluate fractions for evaluation by Western blot. No FVCln7 was detected in the input

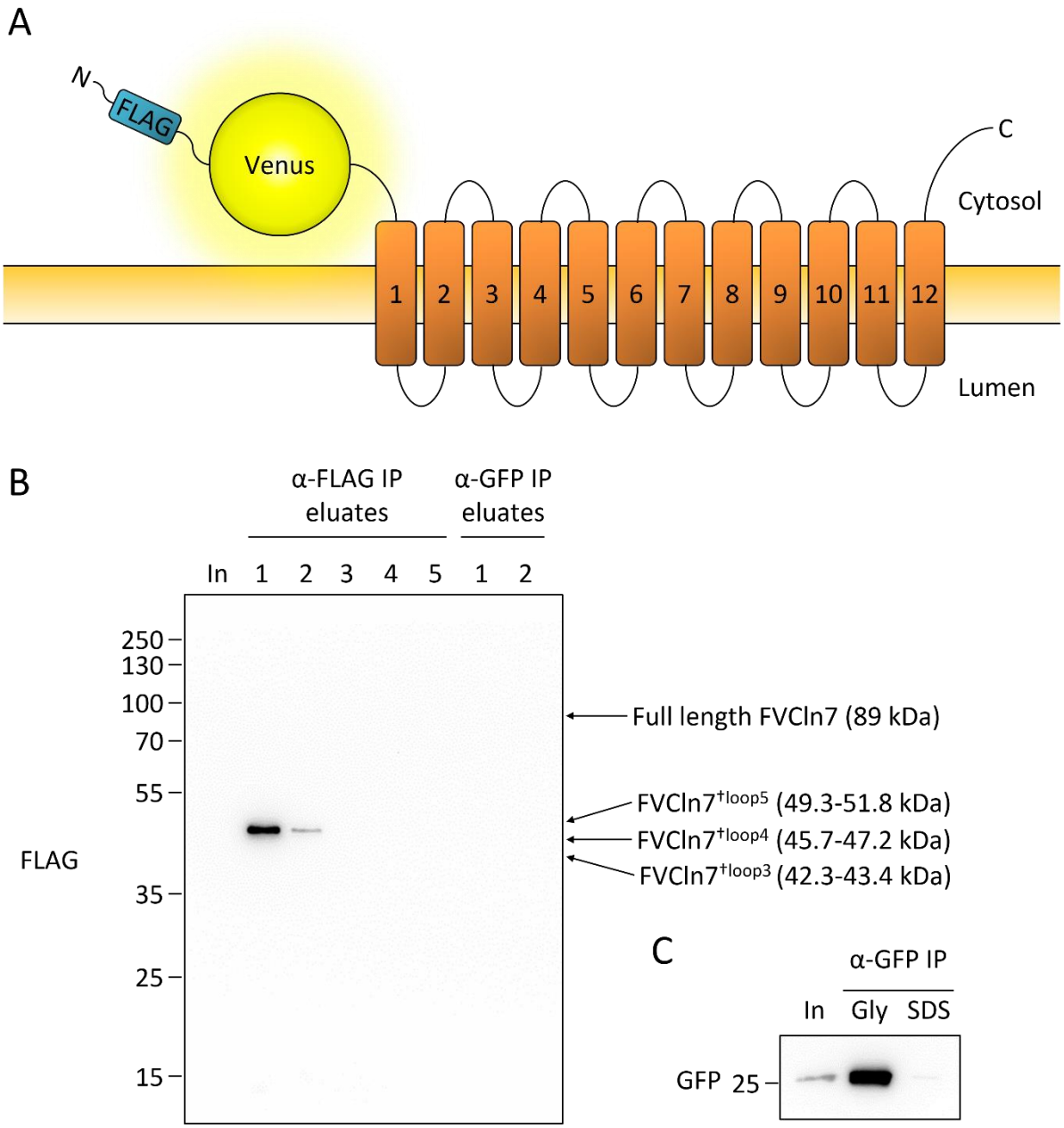

Figure 4.2. Native IP of FVCln7.

A) A schematic showing Cln7 fused to FLAG-Venus within the cytosolic N-terminal tail. **B**) Tandem affinity purification of FVCln7 on α-FLAG and α-GFP beads. Bound proteins were eluted in several fractions to ensure the release of all captured protein. The expected sizes of full-length and N-terminal fragments of FVCln7 are shown to the right († denotes cleavage at the given position). A positive control for IP on α-GFP beads is shown in (**C**). Size markers in kDa are shown on the left.

samples, suggesting that endogenous Cln7 expression is too low to be detected by Western blot without purification (Figure 4.2B). Bands were observed in the first two eluates from α-FLAG beads, but migrated as 45 kDa proteins and not as the expected 89 kDa full-length FVCln7. The presence of a single band rather than a ladder or smear of bands suggests that the 45 kDa band may be the product of a regulated proteolytic event and not of general protein degradation. It is possible Cln7 function or localisation is regulated by proteolytic cleavage, thus three possible N-terminal fragments, cleaved within progressive loop regions, that were expected to migrate a similar distance have been annotated. However, full length FVCln7 remained undetectable in the α-FLAG eluates, suggesting that the extraction or purification conditions may have been sub-optimal to purify full-length FVCln7. In addition, no FVCln7 was detected in the α-GFP eluates, yet GFP extracted from flies overexpressing free GFP (CyO, GFP) was successfully purified by α-GFP IP (Figure 4.2C), suggesting that binding and eluting conditions were suitable for GFP purification. Instead, these issues may have originated from conditions that were specifically incompatible with full-length FVCln7 purification, for example poor protein solubility.

4.2.3 *Troubleshooting –extraction conditions*

To overcome these problems, a set of diagnostic experiments were performed to optimise FVCln7 purification. Inadequate homogenisation was unlikely an issue, as flies were thoroughly homogenised in a bead homogeniser. On the other hand, the solubilisation of membrane proteins is a common problem in protein purification, often requiring optimisation of salt and detergent choice and concentration. In addition, membrane protein solubilisation

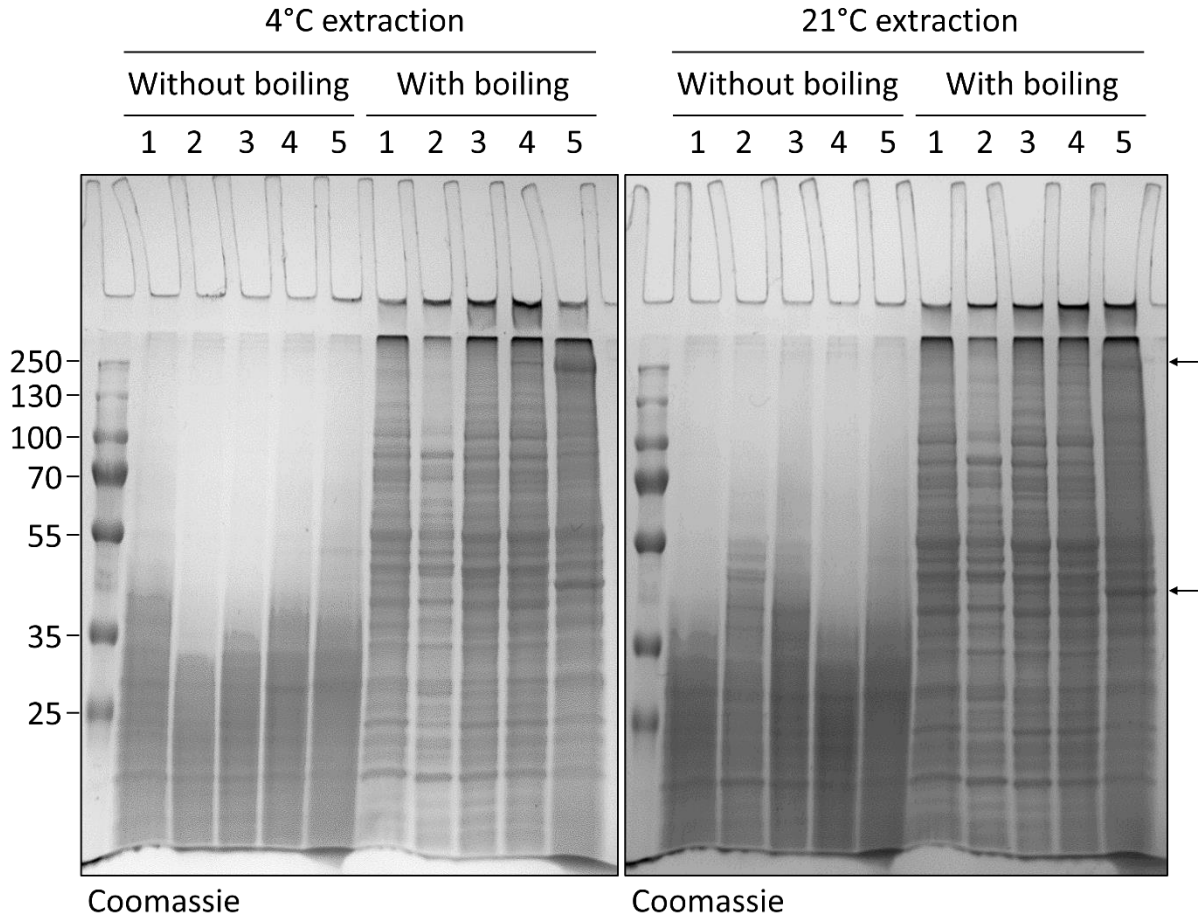

Figure 4.3 Extraction condition screening.

Flies were homogenised in buffers containing membrane solubilisers 1-5 at 4 °C or 21 °C and with or without sample boiling before loading on polyacrylamide gels. Protein extracts were analysed by Coomassie staining. Solubliser: 1 = 2% (w/v) DDM; 2 = 2% (w/v) OG; 3 = 1% (v/v) Triton X-100; 4 = RIPA; 5 = 1% (w/v) SMA. Arrows indicate bands favourably extracted with SMA. Size markers in kDa are shown on the left.

is dependent on their incorporation into detergent micelles, however the critical micellar concentration (CMC) can vary depending on pH, temperature and ionic strength. Manufacturers often only state the CMC at 20-25°C when dissolved in water, therefore the effect on CMC under the conditions used here were not known. To examine the efficiency of different detergents in extracting membrane proteins from adult flies, and to test whether low temperatures were limiting membrane protein solubilisation by reducing micelle formation, the performance of a set of detergents was screened at both 4°C and 21°C. Non-ionic detergents are non-denaturing and therefore more suitable for native immunoprecipitation, thus three non-ionic detergents were tested (DDM, *n*-Octyl-β-$_{D}$-glucopyranoside (OG) and Triton X-100). Also tested were the efficiencies of RIPA buffer, containing a mixture of ionic (SDS), non-ionic (NP-40) and bile salt (deoxycholate) detergents, and styrene-maleic acid (SMA) co-polymer, used for the detergent-free extraction of membrane proteins into discs of native lipid bilayer (439, 440). Extracts were analysed by Coomassie stain and Western blot in parallel. Strikingly, Coomassie staining above 45 kDa was largely absent from all lanes when samples were not heated, irrespective of the detergent and temperature during extraction (Figure 4.3). This was corrected by boiling the samples prior to loading, which was initially skipped to avoid the tendency of some membrane proteins to aggregate when boiled (441, 442), as can be seen here in the wells of boiled samples in contrast to the wells of unheated samples. Nevertheless, this correction upon sample heating may suggest that proteins are incompletely denatured when not heated, even in sample buffer containing SDS and DTT.

Comparing the extraction conditions between boiled samples, little difference was seen in the banding pattern between extractions at 4°C and 21°C, with perhaps slightly greater

yield at 21°C. However given the increased risk of protein degradation at higher temperatures, a 4°C extraction was more favourable than the slight increase in protein yield at 21°C. Of the non-ionic detergents, DDM and Triton X-100 performed similarly with matching banding patterns and protein yield, while extraction with OG was less efficient, particularly at higher molecular weights. Banding in DDM and Triton X-100 extracts was similar to RIPA buffer extracts, showing that these non-ionic detergents were sufficient and could match the efficiency of the stronger detergent mixture in RIPA buffer. Interestingly, additional and thicker bands were seen in SMA extracts, which suggests that SMA is indeed more favourable for the extraction of membrane proteins since the solubility of soluble proteins is unlikely to be affected by membrane solubilisers. Each condition was also analysed by Western blot to determine whether changing sample conditions allowed FVCln7 to be detected (data not shown). No signal was detected with α-FLAG, which may have been because too little FVCln7 was present in these un-purified samples, but given the absence of signal the effect these conditions had on FVCln7 extraction could not be concluded.

4.2.4 *Troubleshooting – sample preparation*

While sample heating resolved the issue with protein migration, it was still desirable to avoid heating the samples if possible to avoid aggregation. To test whether stronger denaturing conditions could circumvent the need for sample heating, 6 M urea was added to protein extracts using DDM or SMA from three adult fly lines, expressing FVCln7, soluble Ubi-GFP or YFP tethered to the pre-synaptic membrane protein brp, with low expression similar to Cln7. In parallel, the effect these conditions had on the detection of GFP by Western blot

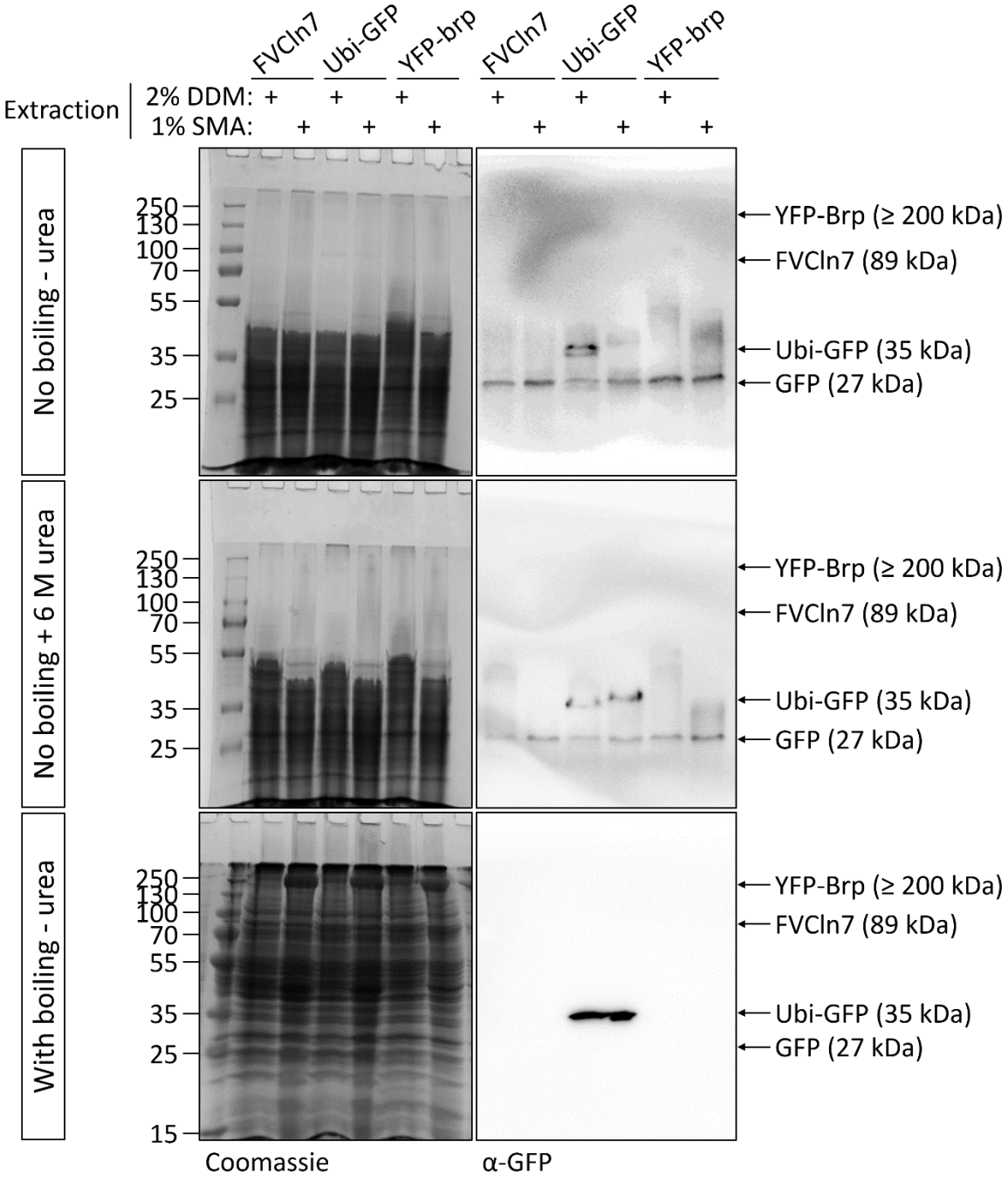

Figure 4.4. Treatment of samples with urea.

The effects of sample boiling or treatment with 6 M urea were compared on extracts from flies expressing FVCln7, soluble Ubi-GFP or membrane-bound YFP-brp. Total protein migration and GFP/YFP detection were analysed by Coomassie stain and Western blot, respectively. Expected sizes are shown on the right. The actual size of YFP-brp may vary depending on brp isoform. Size markers in kDa are shown on the left.

was tested. The addition of urea failed to restore protein migration in unheated samples, suggesting that this was not an issue with incomplete sample denaturation (Figure 4.4). Western blots from unheated samples detected bands corresponding to GFP in all lanes in addition to Ubi-GFP, but with a poor signal to noise ratio. In contrast, sample heating greatly improved signal clarity and removed background which intensified the Ubi-GFP bands. FVCln7 and YFP-brp however remained undetected, consistent with the idea that the expression of these proteins is too low to detect in un-purified samples.

Since sample heating could not be avoided, a range of temperatures and incubation times were tested to minimize any aggregation. Protein extracts were heated at five temperatures ranging from 35 °C to 95 °C in 15 °C steps for 2 min or 5 min and protein migration was analysed by Coomassie stain. A temperature-dependent recovery of protein migration was seen, with full recovery observed at ≥ 80 °C or ≥ 65 °C when heated for 2 min or 5 min, respectively (Figure 4.5). Heating at lower temperatures is more favourable, thus sample heating at 65 °C for 5 min was selected as optimal.

4.2.5 *Removing the source of aberrant protein migration*

To test whether this phenomenon is inherent of unheated samples or of sample type, the effect of sample heating of protein migration was tested on extracts from third-instar larvae and from insect (S2) and mammalian (HeLa) cell lines. Extracts from larvae showed a similar temperature-dependent recovery in protein migration as seen with extracts from adult flies, potentially requiring higher temperatures or longer incubations to fully recover migration (Figure 4.6). In addition, a distinct negative smear was present in unheated samples

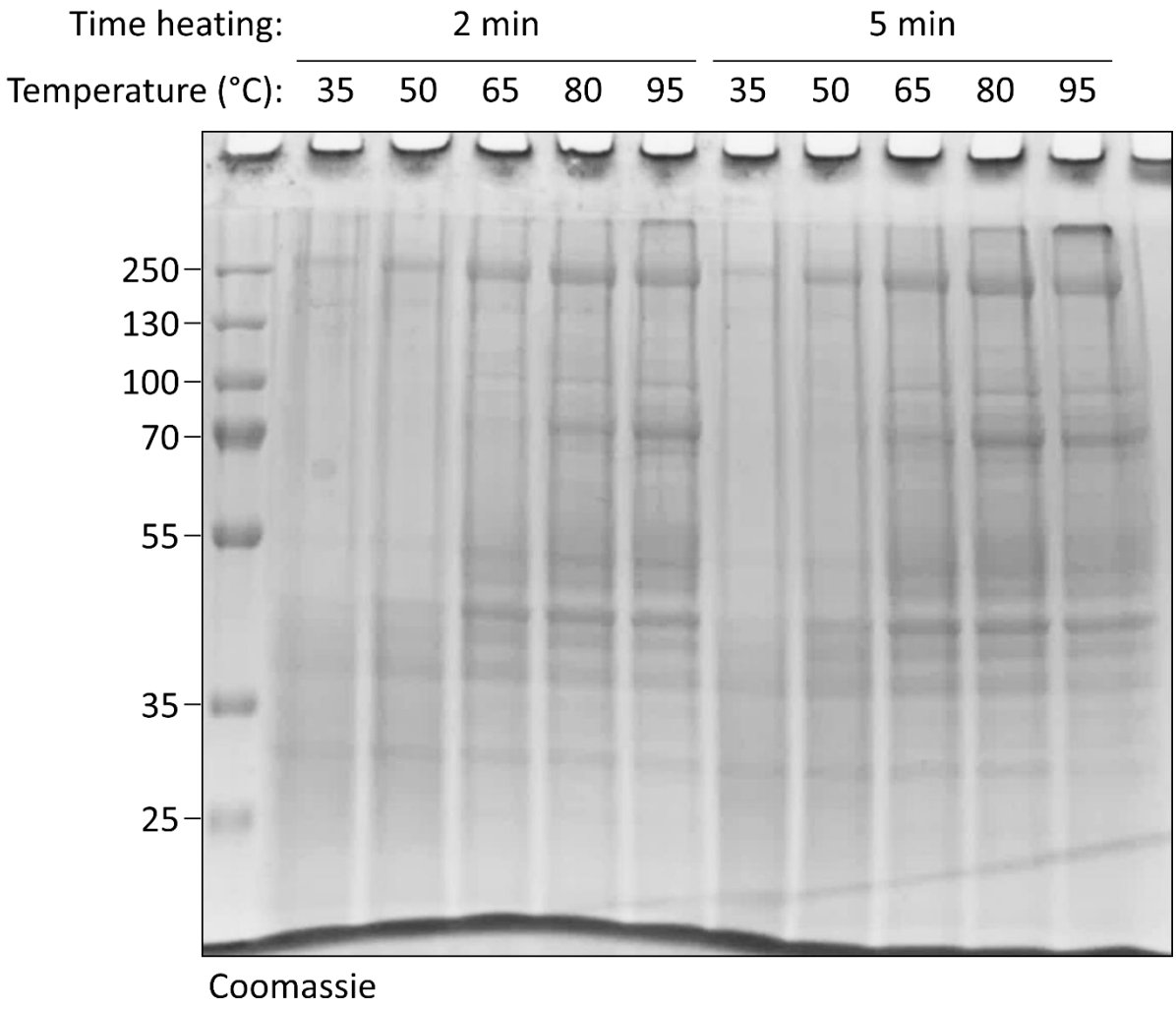

Figure 4.5. Dependence of protein migration on sample heating.

Extracts from flies were heated at the indicated range of temperatures for either 2 or 5 min. Size markers in kDa are shown on the left.

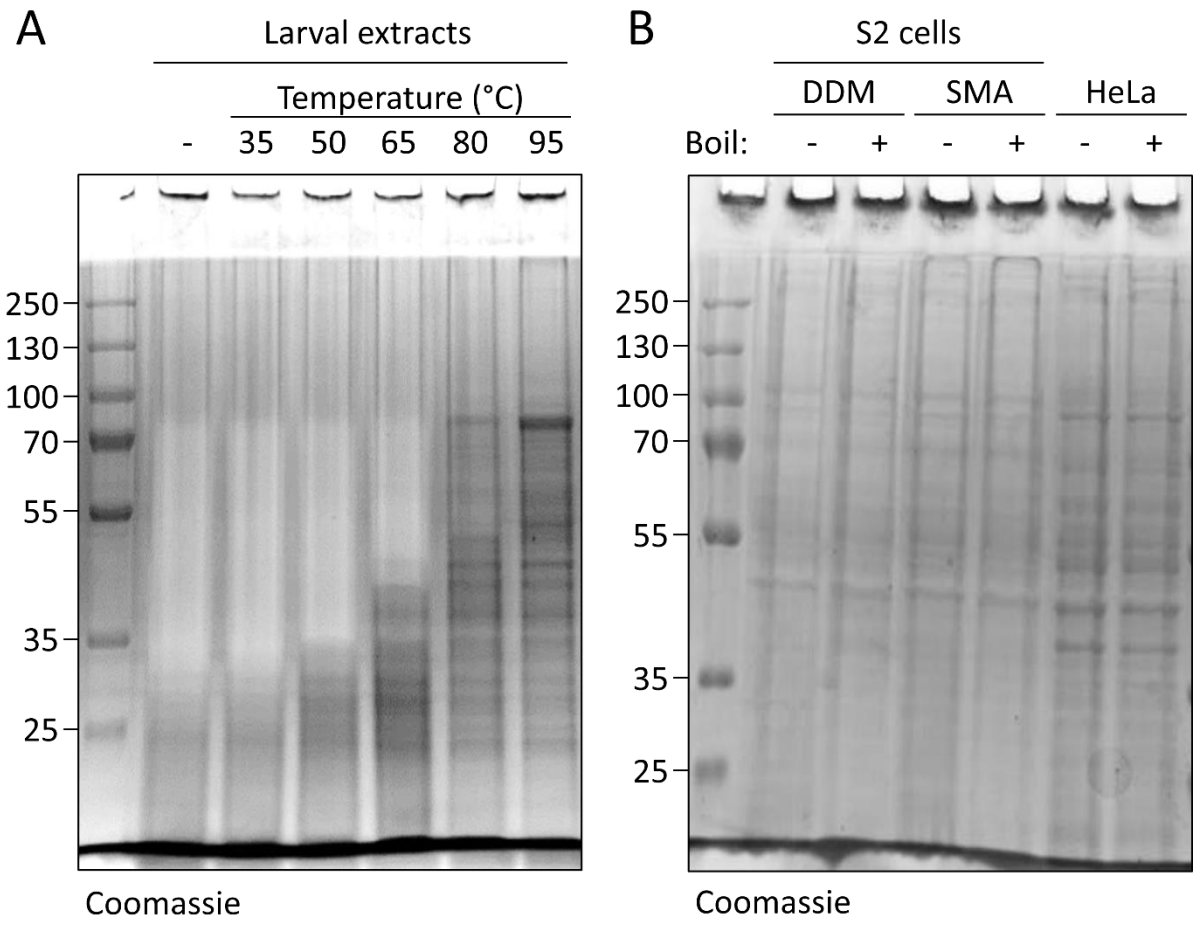

Figure 4.6. Comparison of protein migration between tissue and cell extracts.

Extracts from third-instar larvae were compared with extracts from insect (S2) and mammalian (HeLa) cells. Larval extracts were heated at the indicted temperatures for 5 min were heated at the indicated range of temperatures for 2 min with an unheated control (-). Cell extracts were either unheated or heated at 95 °C for 2 min. Size markers in kDa are shown on the left.

which retracted with increasing temperatures. In contrast, no interference with protein migration was seen in unheated extracts from either S2 or HeLa cell lines. Together, these suggest that aberrant protein migration was not entirely due to lack of heating, as extracts from cell lines migrated normally. Instead, the issue appears to be unique to extracts from *Drosophila* tissue.

The improper protein separation did not appear to be an intrinsic property of proteins themselves as strong denaturation with urea failed to improve migration, yet heating appeared essential. One possibility is that other constituents only present in *Drosophila* tissues associate with denatured proteins and interfere with their electrophoretic mobility. To test this hypothesis, proteins were purified by TCA precipitation. Protein precipitates were resolubilised in DDM and the DDM-insoluble fraction was resolubilised in SDS. As expected, protein was present in both DDM-soluble and insoluble fractions but not in the TCA-soluble supernatant (Figure 4.7). More pertinent, normal protein migration was observed in both heated and unheated samples, in support of the argument that proper protein migration may be aided by but not usually depend on sample heating. The data also suggests that protein migration was unchanged by the increased sample viscosity in unheated samples. Therefore it seems likely that aberrant protein migration is caused by interference from putative components within *Drosophila* tissue extracts, which can be resolved either by heating or purification.

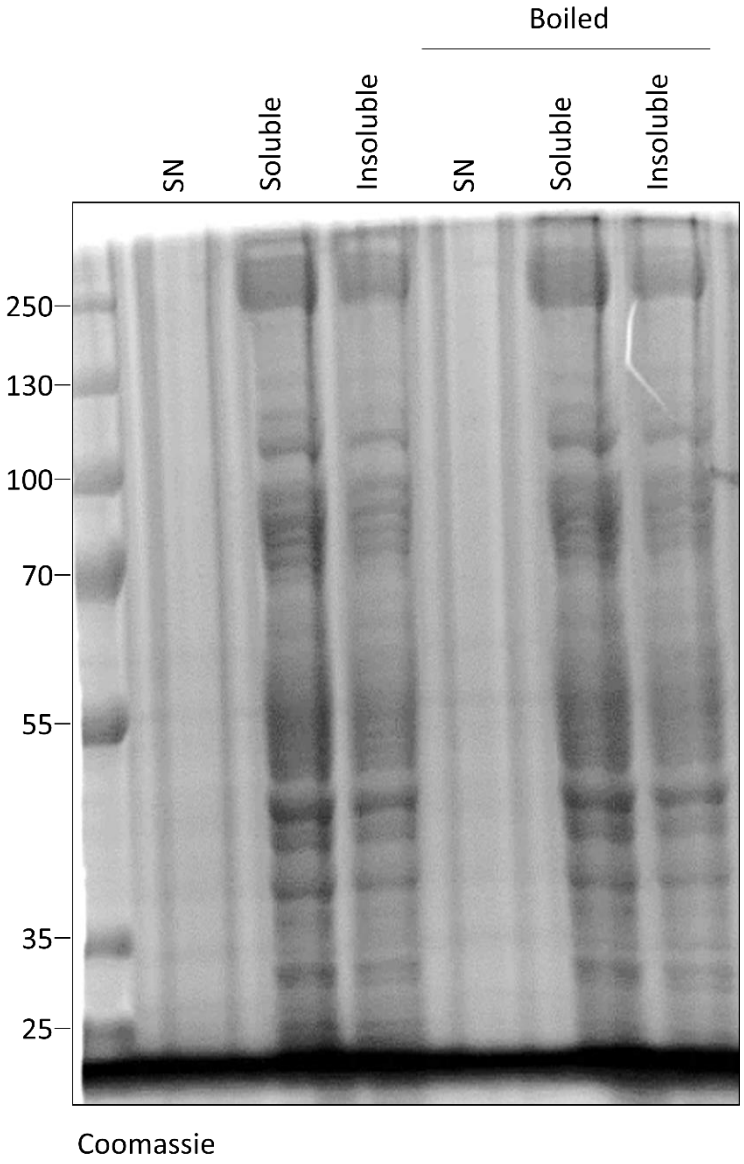

Figure 4.7. Protein purification restores protein migration without heating.

Proteins from flies expressing FVCln7 were purified by TCA precipitation and resolubilised in DDM (soluble) and SDS (insoluble) fractions. Supernatant (SN) fractions were taken from the protein-free TCA-soluble phase. Samples were either unheated or heated at 95 °C for 2 min. Size markers in kDa are shown on the left.

4.2.6 *Native IP of FVCln7 under optimised conditions*

The overall aim here was to optimise the conditions for the purification of native full-length FVCln7 from adult flies, to then characterise proteins interacting with Cln7 *in vivo*. For optimal protein extraction, membrane solubilisation with 1% SMA at 4°C was selected. Proteins were not purified by TCA precipitation here because proteins become denatured in the process, which would remove protein-protein interactions with Cln7. Since the concentration of FVCln7 may be too low to be detected from un-purified samples, extracts were immunoprecipitated on α-FLAG beads as before. For analysis by Western blot, samples were heated at 65°C for 5 min prior to SDS-PAGE. No addition of urea was required. However, despite optimising the conditions for membrane protein extraction and resolving issues with protein migration, full-length FVCln7 remained undetectable input and α-FLAG eluate fractions (Figure 4.8). A single ~24 kDa band was detected across all eluates, in contrast to the 45 kDa band present in the initial IP. Given the difficulties stated here with no guarantee of successful purification after further troubleshooting, no further attempts were made to purify full-length FVCln7.

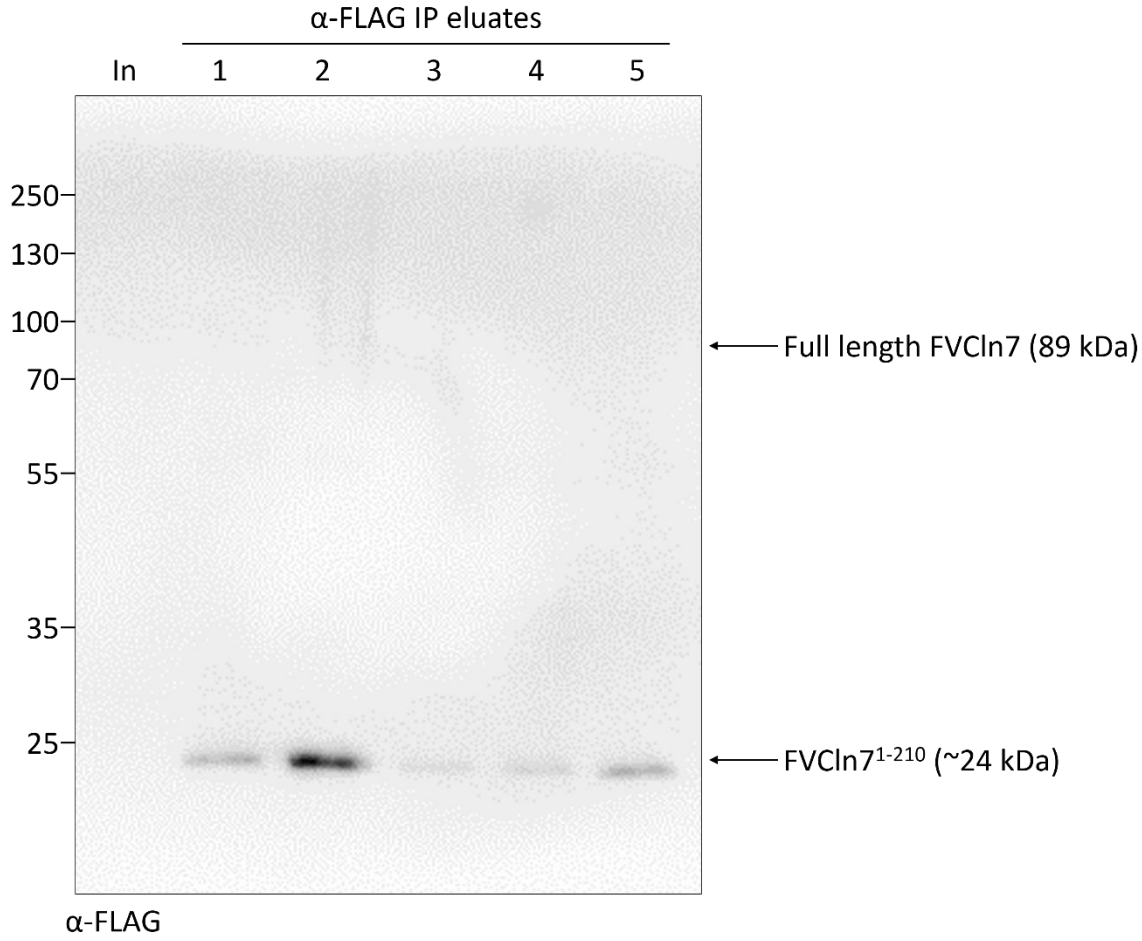

Figure 4.8. Condition optimisation failed to recover full-length FVCln7.

Proteins from flies expressing FVCln7 were extracted using optimised conditions and purified by IP on α-FLAG beads. The presence of FVCln7 was tested in unpurified (In) and five successive eluate fractions. Full-length FVCln7 was not detected, however a ~24 kDa band was present in all eluates. This band corresponds approximately to a FVCln7$^{1-210}$ fragment. Size markers in kDa are shown on the left.

4.3 Discussion

4.3.1 *Interaction between Cln7 and Rheb*

As an initial investigation, it was tested whether Cln7 and the TORC1 activator Rheb interacted *in vitro*. Preliminary evidence from phenotypes presented by *Cln7*^{84D} flies suggested that Cln7 may be involved in insulin signalling and may regulate TORC1 activity. Complementary co-immunoprecipitation and immunofluorescence approaches suggested that Cln7 interacts in a complex with Rheb. In conjunction with previous findings that TORC1 activity is reduced in *Cln7*$^{-/-}$ MEFs, this interaction may mean that Cln7 is required for TORC1 activation by Rheb, however it cannot be concluded from the data alone how this interaction actually modifies Cln7 or Rheb function. It also cannot be concluded whether the interaction is direct or indirect. TORC1 is recruited to the lysosomal membrane by a multi-protein complex containing Rag GTPases, the pentameric LAMTOR/Ragulator complex and the multimeric V-ATPase complex. Rheb interacts with this recruitment complex via Tor, thus the co-precipitation of Cln7 with Rheb may not be due to direct interaction with Rheb but rather with any member of the TORC1 recruitment machinery. This eventuality would account for the weak interaction between Cln7 and Rheb, but would also mean that Cln7 and Rheb might not regulate one another.

4.3.2 *Aberrant protein migration by SDS-PAGE from Drosophila tissue*

Unusual protein migration by SDS-PAGE was observed when separating proteins from *Drosophila* tissue extracts. Normal protein migration required moderate sample heating, however this was not required for insect or mammalian cellular extracts. The observation

appeared specific to *Drosophila* tissues, and was common to both third-instar and adult stages. To determine the cause of aberrant protein migration, the underlying factors that govern protein mobility by SDS-PAGE were considered. The electrophoretic mobility of proteins is determined by their mass, charge and molecular radius. During SDS-PAGE, proteins are linearised and uniformly coated in negative charge by SDS, resulting in a mixture of proteins with a constant mass to charge ratio and molecular radii proportional to their mass, thus proteins separate according to mass only. At least one of these assumptions ceased to be true in unheated fly extracts. There could not be any changes to mass since migration was recovered by heating, leaving possible interference with protein linearisation or charge. To accelerate protein migration would infer that proteins are either more compact or more negatively charged. Since proteins are coated in negative charge by SDS, the association of additional anions seems unlikely. Instead, proteins may have retained weak partial structures that reduce the molecular radius of proteins. The most effective solution to recover protein migration was to heat samples, but ideally this should be avoided to minimise protein aggregation. Protein purification by TCA precipitation also recovered protein migration, whereas samples treated with urea were unchanged. This was suggestive of a heat-sensitive non-proteinaceous contaminant within *Drosophila* tissues that, unless treated, interferes with SDS-PAGE.

4.3.3 *Evaluation of FVCln7 affinity purification*

Attempts to purify full-length FVCln7 were unsuccessful, with only 45 kDa or 25 kDa FLAG-positive fragments being detected in IP eluates. Multiple rounds of optimisation were

employed to improve conditions for protein extraction and sample treatment for FVCln7 solubilisation and detection. However FVCln7 could not be detected within unpurified homogenates. Extraction with 1% SMA was chosen due to more efficient extraction of certain proteins, assessed by larger bands by Coomassie stain. SMA was suggested to enhance the extraction of membrane proteins since SMA solubilises membranes into native membrane discs that preserve the local membrane environment. However it is possible that while SMA may be favourable for the extraction of some membrane proteins, SMA may not have favoured FVCln7 extraction. Since FVCln7 expression is most likely too low to be detected in un-purified samples, further optimisation would require FVCln7 to be concentrated by α-FLAG immunoprecipitation in order to evaluate conditions for FVCln7 extraction. Additional considerations not tested here include salt choice and concentration within lysis and wash buffers. However it is possible that release of FVCln7 in bead flow-through or wash fractions due to inappropriate binding and washing conditions would also be undetectable, given that FVCln7 was not detectable in un-purified samples. These factors created a difficult scenario whereby there was no positive control to assess optimisation screens.

4.3.4 *Limitations of affinity purification*

Affinity purification is commonly used to capture protein complexes for identification by MS. However there are several limitations to affinity purification that can preclude its use for the identification of certain protein interactions. Detergents are used to solubilise membranes but are disruptive to native lipid bilayers and can destabilise membrane proteins. Several alternatives have been developed for the extraction of native membrane proteins,

including solubilisation with amphipols (443) and incorporation into synthetic lipid bilayers (444) or membrane nanodiscs (445-447). Here, detergent-free extraction with SMA into nanodiscs was used to preserve the membrane lipid microenvironment, however this was insufficient to facilitate the purification of FVCln7. In addition, non-specific interactions are often retained during purification, requiring subtraction using blank controls to remove false positives. On the other hand, weak or transient interactions are easily lost during bead washing steps and contribute to false negatives. Given the difficulty with purifying FVCln7, it was concluded that alternate approaches that do not rely on affinity purification may be more appropriate to investigate protein interactions with Cln7.

5 PROXIMITY LABELLING OF THE CLN7 INTERACTOME

5.1 Introduction

The identification of protein-protein interactions often requires their preservation during extraction, which can be challenging, especially with membrane proteins. Detergents are often required to maintain protein solubility, but also cause disruptions to membrane microenvironments that can alter protein fold and interfere with hydrophobic interactions between proteins. To overcome these barriers, methods have been developed whereby proteins are covalently labelled *in situ* based on their proximity to a target protein. The labelling of proteins before protein extraction removes the need to preserve native protein complexes, facilitating the characterisation of protein-protein interactions with challenging proteins, in addition to transient or weak interactions that may be lost during purification steps. Given the difficulty with purifying FVCln7 by affinity purification, a proximity labelling approach was taken to characterise protein-protein interactions with Cln7.

Two proximity labelling techniques have been developed based on promiscuous protein biotinylation by the enzymes BioID and APEX2 (Figure 5.1) (414, 415, 448). Biotinylation is a rare, non-toxic protein modification and the femtomolar affinity of streptavidin for biotin makes biotinylation ideal for the stringent purification of labelled proteins. BioID is derived from the *E. coli* biotin ligase BirA that specifically biotinylates a narrow list of proteins in a two-step mechanism (449, 450). Firstly, biotin reacts with ATP to form a biotinyl-5'-AMP (bioAMP) intermediate which remains bound by BirA. The enzyme then transfers the activated biotin to a specific lysine residue within a biotin acceptor tag (BAT) on target proteins. Mutation of a conserved arginine (R118G, named BirA* or BioID) reduces

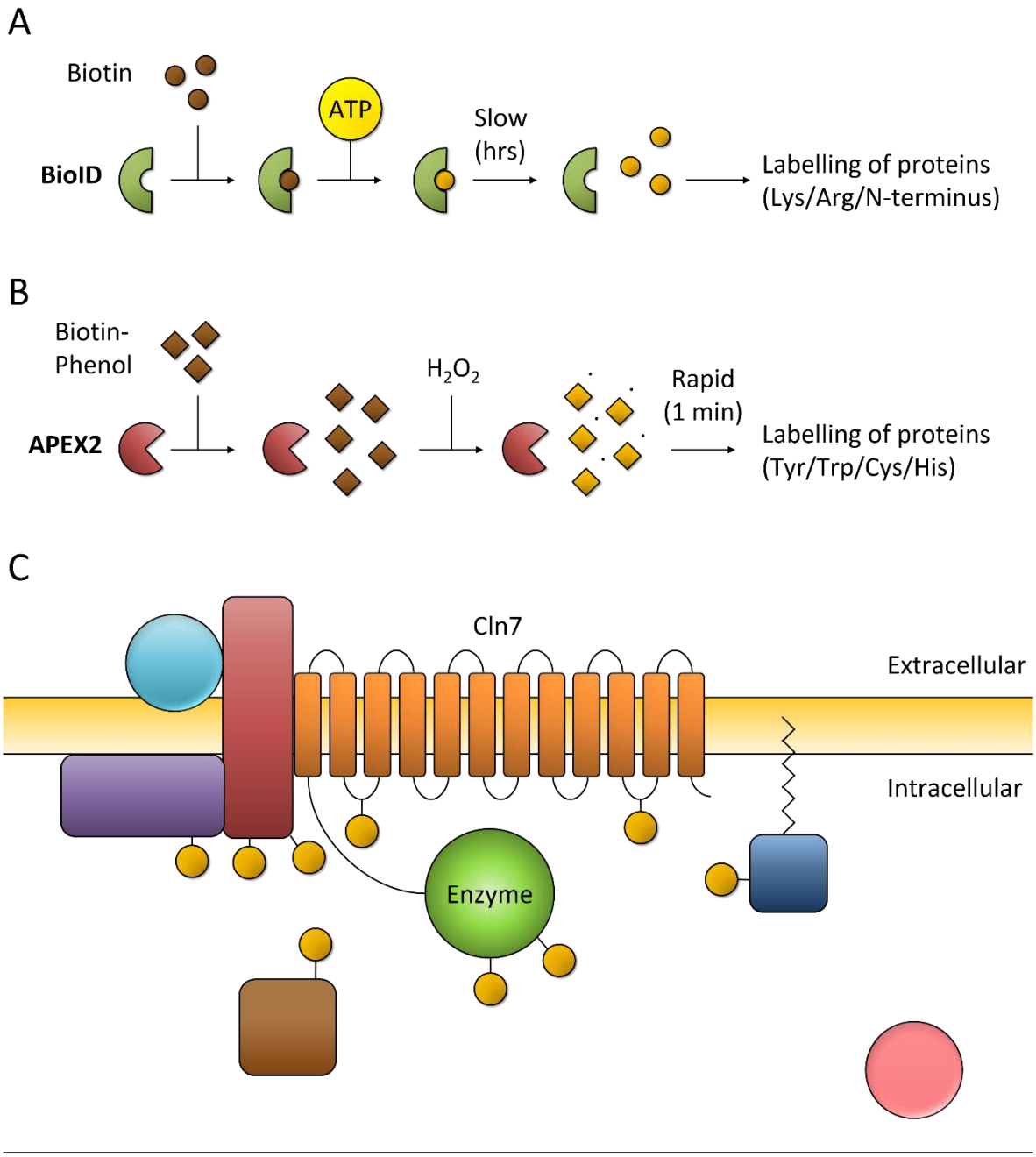

Figure 5.1. Illustration of proximity labelling with BioID and APEX2.

A) BioID uses biotin as a substrate, which is activated in the presence of ATP by conversion to bioAMP. BioAMP is slowly released by BioID and readily reacts with primary amines present on lysines, arginines and at the N-terminus. **B)** APEX2 oxidises biotin-phenol in the presence of H_2O_2 to generate reactive biotin-phenoxyl radicals. These radicals rapidly conjugate to electron-dense residues, such as tyrosine, tryptophan, histidine and cysteine. **C)** Labelling of proteins in proximity to Cln7 using an enzyme-Cln7 fusion.

the affinity for bioAMP approximately 450-fold, triggering its premature release from the active site (451). Free bioAMP readily reacts with primary amines and is labile, which self-limit the labelling of distant targets in favour of proximal proteins (Figure 5.1A) (452). Biointylation is reported to occur at lysine residues, but primary amines on arginines and at the N-terminus may also be labelled such that all proteins can be assumed to be susceptible to biotinylation. The biotinylation range of BioID is approximately 10 nm (approximately 30 amino acids), estimated in a study that measured biotinylation distances using a set of BioID-nuclear pore complex (NPC) protein fusions as molecular rulers (453). Maximal protein biotinylation by BioID is achieved between 18-24 h after supplementation with biotin. Therefore by fusing BioID to a protein of interest, labelled proteins represent a historical account of protein interactions over the labelling period, which can then be extracted and identified by MS.

The second enzyme, APEX2, is a second generation enzyme engineered by directed evolution from the soybean ascorbate peroxidase APX (414, 454-456). APEX2 catalyses the rapid oxidation of aromatic substrates in the presence of H_2O_2. This feature has given APEX2 bi-functionality for use in electron microscopy and proximity labelling, depending on the probe used. Biotin-phenol is used for proximity labelling and is converted by APEX2 into reactive biotin-phenoxyl radicals. These radicals conjugate to electron-dense moieties and has been shown to react with tyrosine residues, but may also react with tryptophan, cysteine and histidine (Figure 5.1B) (414). Protein biotinylation by APEX2 occurs on a much more rapid timescale, with sufficient labelling achieved after just 1 min. While labelling distance has not been directly measured for APEX2, the highly reactive and short-lived (1 ms) properties of biotin-phenoxyl radicals in combination with the short 1 min labelling window suggest that the APEX2 labelling distance is at least similar to the 10 nm of BioID, if not shorter. The

advantage of using APEX2 is the greater temporal control over proximity labelling, which can be used to capture snapshots of protein interactions and investigate their dynamics with changing stimuli. Proximity labelling with BioID and APEX2 are complimentary techniques, and by combining the simplified, non-toxic longitudinal labelling of BioID with the rapid, cross-sectional labelling of APEX2, a more complete description of protein interaction landscapes may be achieved.

The aims of this chapter were to generate tools and establish methodologies for proximity labelling by BioID and APEX2 both *in vitro* and *in vivo*, and to identify and evaluate candidate proteins that interact with Cln7.

5.2 Results

5.2.1 *Making cell lines for labelling by BioID and APEX2*

To establish tools for proximity labelling of Cln7, BioID and APEX2 were fused to Cln7 and cloned into expression vectors by Gateway cloning. Here, a 5' CACC sequence is added to cDNA sequences during amplification to facilitate cloning into an entry vector by topoisomerase. Inserted sequences are flanked by attL sites within the vector backbone to allow the recombination of one entry clone with a library of compatible destination vectors, providing a selection of N- or C-terminal epitope tags (6xMyc, 3xFLAG and 3xHA alone or in tandem) and fluorescent proteins (EGFP, ECFP, Venus and mRFP) with a choice of promoters for constitutive or inducible expression *in vitro* or *in vivo* (Table 2.6).

Four constructs were designed, namely BioID, BioID-Cln7, APEX2 and APEX2-Cln7. BioID-Cln7 was cloned into the entry vector by Richard Tuxworth prior to the work here. The first step was to flank and amplify cDNA sequences with a 5' CACC tag by PCR (Figure 5.2A). Analysis of PCR products by agarose gel electrophoresis detected bands of the correct size for BioID (1,063 bp) and APEX2 (783 bp) (Figure 5.2B). Positive transformants with inserts of the correct size and orientation were detected in BioID colony 1 and APEX2 colony 4 (Figure 5.2C,D). To generate APEX2-Cln7, APEX2 and Cln7 fragments were first amplified with complementary 15 bp overhangs (Figure 5.2E,F). The fragments were then mixed with external primers to generate and amplify APEX2-Cln7 cDNA by overlap extension PCR. A product migrating at approximately 3 kb corresponding to APEX2-Cln7 was detected and was purified for insertion into pENTR (Figure 5.2G). All entry clones were verified by sequencing before recombination into pAMW, pMT-DEST48 and pTMW vectors.

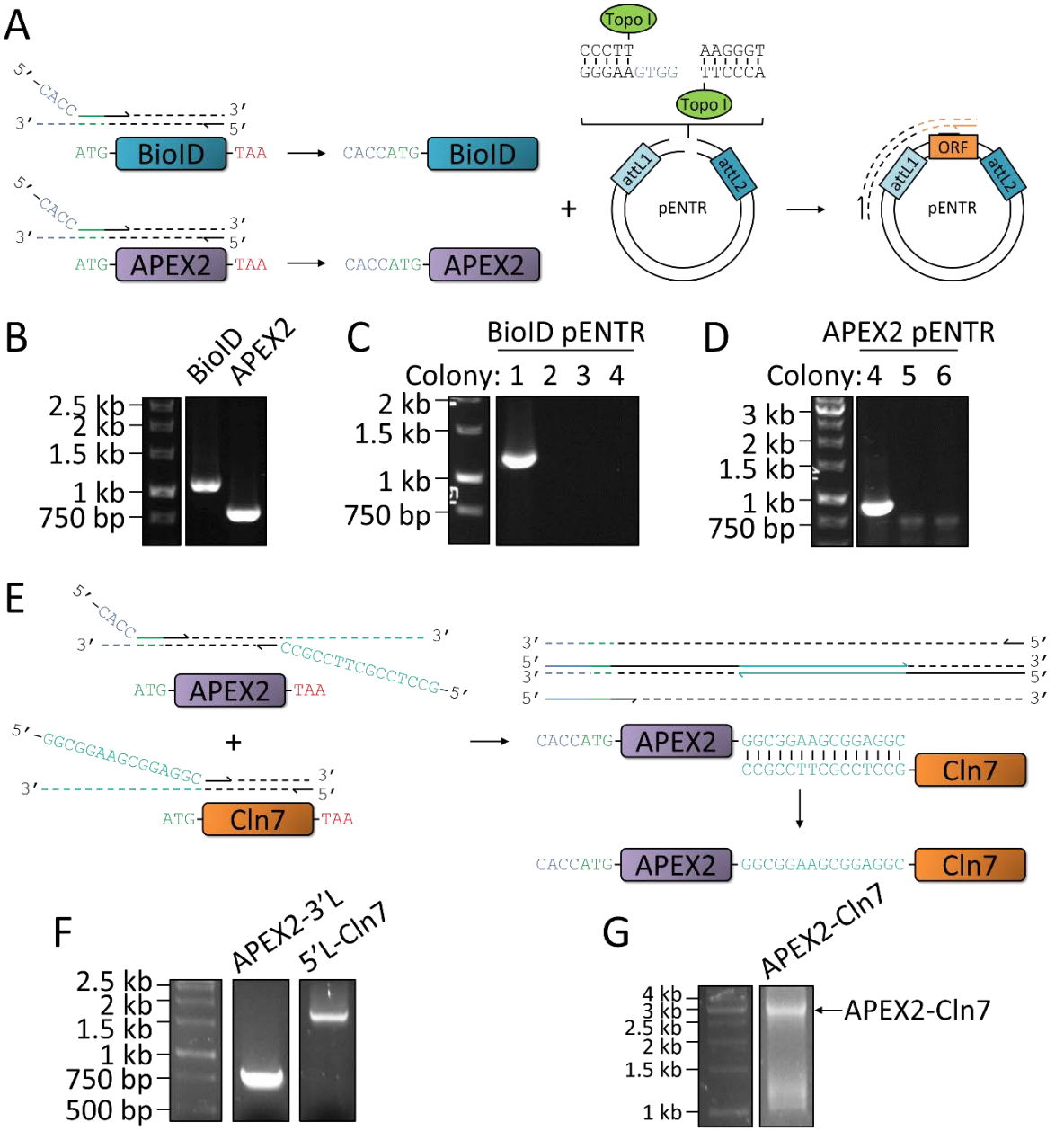

Figure 5.2. Cloning BioID, APEX2 and APEX2-Cln7.

A,E) Schematics illustrating how ORFs were cloned into pENTR for Gateway cloning. **B**) PCR products of the correct sizes were detected for BioID (1,063 bp) and APEX2 (783 bp). **C-D**) Colony PCR revealed clones containing inserts of correct size and directionality. **F**) Correctly sized APEX2 (805 bp) and Cln7 (1,650 bp) fragments with compatible overhangs 3'L and 5'L (L = linker) were amplified by PCR. **G**) Overlap extension PCR generated a band corresponding to APEX2-Cln7. All products in pENTR were verified by sequencing. Size markers are shown to the left of gel images.

Stable lines were made by transfecting S2 cells with pAMW (constitutive) or pMT (Cu^{2+}-inducible) expression clones under hygromycin selection. The expression of each construct was analysed by Western blot and immunofluorescence. Bands of the expected size were detected from cells constitutively expressing Myc-BioID-Cln7, Myc-BioID and Myc-APEX2-Cln7 (Figure 5.3A). Immunofluorescence confirmed the expression of these proteins, with Myc-BioID-Cln7 and Myc-APEX2-Cln7 predominantly localising to the plasma membrane and Myc-BioID residing in the cytosol (Figure 5.3B). Myc-APEX2 was not detected by Western blot but was detected at trace levels by immunofluorescence, perhaps because low-expression clones were selected.

The expression of APEX2-V5 and APEX2-Cln7-V5 by Cu^{2+} induction was also tested. Cells were incubated with a concentration gradient of Cu^{2+} and expression levels were compared. Step-wise increases in APEX2-V5 and APEX2-Cln7-V5 expression were seen with increasing Cu^{2+} concentrations (Figure 5.4A,C). No expression was detectable in the absence of Cu^{2+} by Western blot, however immunofluorescence revealed a considerable level of APEX2-Cln7-V5 expression was detectable (Figure 5.4B). Inducible transgenes were created in order to titrate protein expression down to low levels, similar to those observed *in vivo*, to circumvent potential issues with proximity labelling using over-expressed proteins. However, the expression of APEX2-Cln7-V5 even in the absence of Cu^{2+} meant that inducible transgene expression may not be an effective solution. It is worth noting that Cln7 and Cln7 fusions (BioID-Cln7 and APEX2-Cln7) localised to the plasma membrane when expressed with either N-terminal (Figure 5.3) or C-terminal (Figure 5.4) tags. This suggests that the epitope tags did not interfere with the trafficking of Cln7 to the plasma membrane, however an antibody to Cln7 is required to determine the native localisation of Cln7.

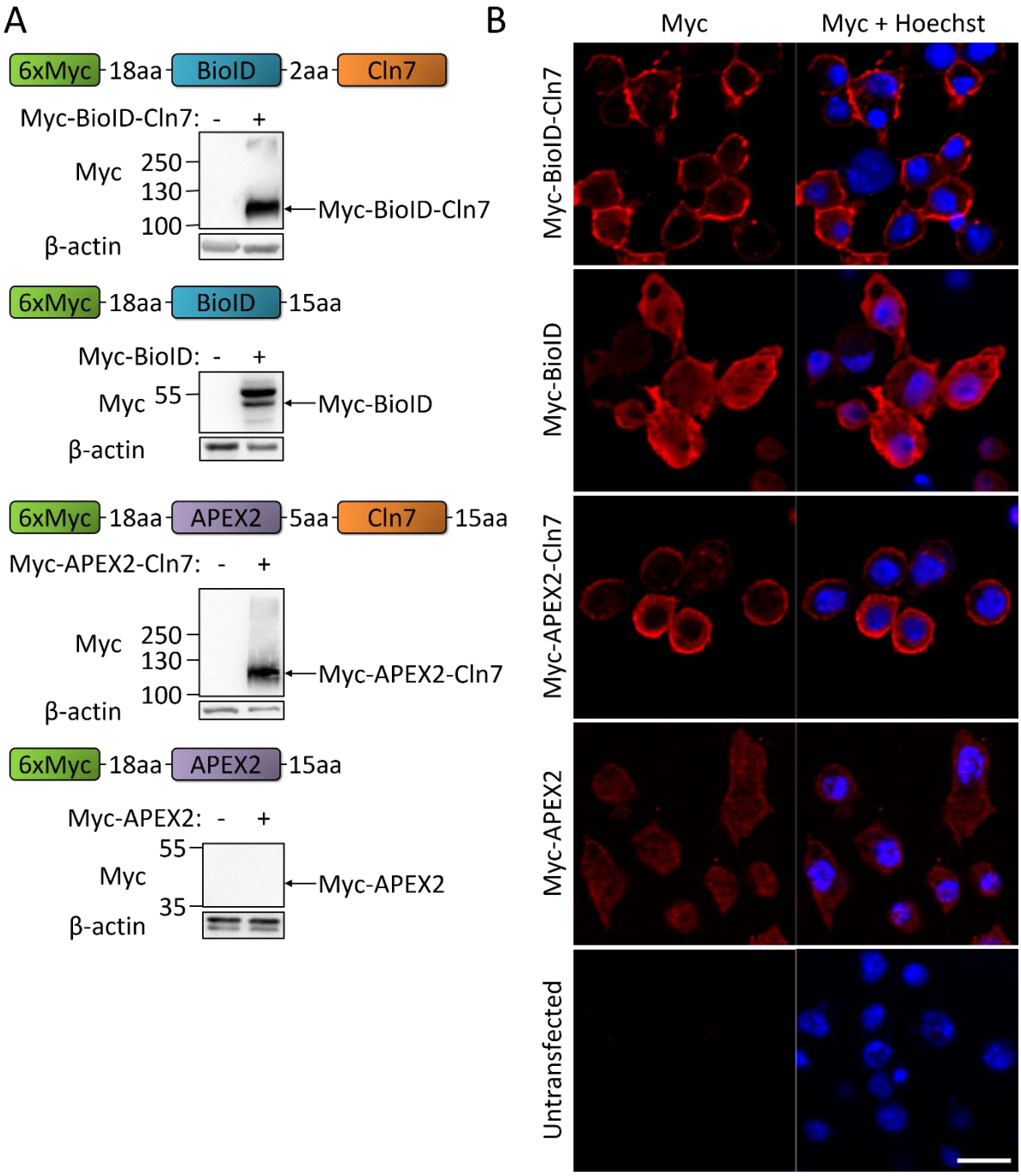

Figure 5.3. Myc-BioID, Myc-BioID-Cln7, Myc-APEX2 and Myc-APEX2-Cln7 were stably expressed in S2 cells.

The expression of Myc-BioID, Myc-BioID-Cln7, Myc-APEX2 and Myc-APEX2-Cln7 was tested by Western blot (**A**) and localisation by immunofluorescence (**B**). **A**) Cartoons illustrate the general structure of each construct. Expected sizes are indicated with arrows on the right. Size markers in kDa are shown to the left. **B**) Scale bar = 10 µm.

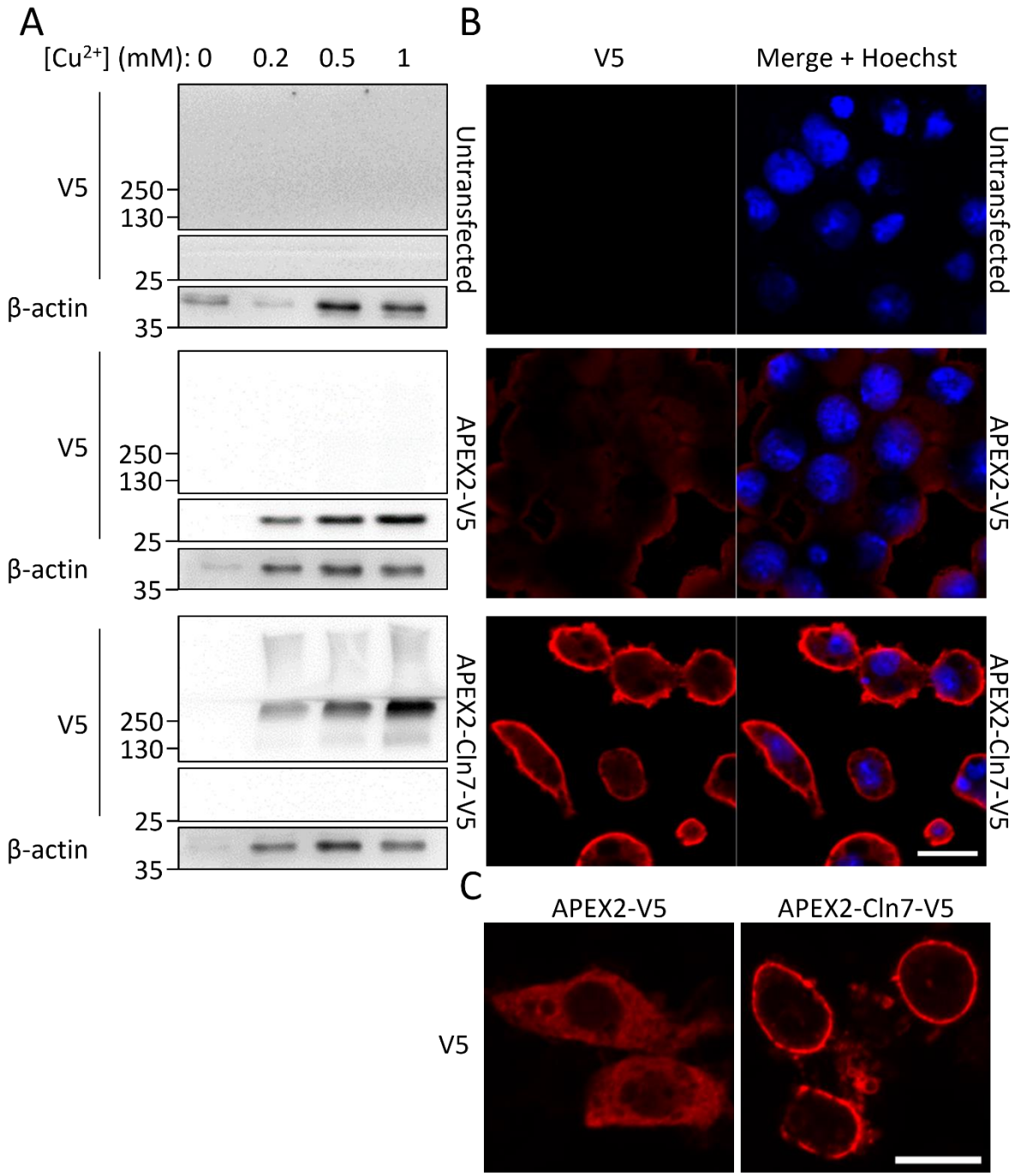

Figure 5.4. Inducible expression of APEX2-V5 and APEX2-Cln7-V5 with Cu^{2+}.

APEX2-V5 and APEX2-Cln7-V5 expression was induced for 24 h with a concentration gradient of Cu^{2+}. Expression levels were analysed by Western blot (**A**) and immunofluorescence (**B,C**). Uninduced cells (**B**) or cells induced with 1 mM Cu^{2+} (**C**) were immunostained for V5. Western blot size markers in kDa are shown to the left. Scale bar = 10 µm.

5.2.2 *Trialling proximity labelling by BioID and APEX2*

Next, proximity labelling experiments were trialled and analysed by Western blot and immunofluorescence. In the event that labelling only occurred at low levels, biotinylated proteins were also enriched by streptavidin pull-downs to aid their detection. Starting with BioID labelling, cells expressing Myc-BioID-Cln7 were incubated with or without biotin to test whether trace amounts of biotin in the culture media was sufficient to trigger labelling. Extracts from parental S2 cells were also included to distinguish between endogenously biotinylated proteins and proteins labelled by BioID. Staining of proteins enriched on streptavidin beads by Coomassie revealed an identical pattern of proteins present at low levels irrespective of BioID expression, suggesting that bead washing conditions should be more stringent to reduce non-specific binding (Figure 5.5). More importantly however, no unique bands were seen in samples containing BioID by Coomassie stain, and no biotinylated proteins were detected by Western blot. These results suggested that either no proteins were labelled by BioID, or that too few proteins were labelled to be detected by Western blot. In contrast, staining for biotinylated proteins by immunofluorescence detected enhanced signal from cells expressing Myc-BioID and particularly Myc-BioID-Cln7, compared to parental S2 controls (Figure 5.6). Furthermore, cells expressing Myc-BioID labelled proteins in a diffuse pattern throughout the cytosol, whereas proteins labelled by Myc-BioID-Cln7 predominantly localised to the plasma membrane or within cytosolic punctae. While efforts were made to remove excess free biotin from cells before staining, it remained possible that any signal was due to detecting free biotin and not biotinylated proteins. However the enhanced signal in cells expressing BioID together with the distinct labelling patterns between cells expressing Myc-BioID and Myc-BioID-Cln7 support the conclusion that proteins are indeed being labelled

in proximity to BioID. Therefore, a lack of labelling by BioID was not likely the reason for the failure to detect biotinylation by Western blot.

In parallel, labelling experiments with APEX2 were trialled. Similar to with BioID labelling, identical non-specific banding was detected in all streptavidin pull-downs independent of Myc-APEX2-Cln7 expression, and no biotinylated proteins were detected by Western blot (Figure 5.7). Yet, again consistent with BioID labelling, biotin labels were detected by immunofluorescence in cells expressing Myc-APEX2 or Myc-APEX2-Cln7 (Figure 5.8). In distinction from BioID labelling, biotin labels were only detected in cells expressing either construct treated with both biotin-phenol and H_2O_2. This presents an advantage over BioID labelling, as labelling only occurs when both substrates are provided, in contrast to the constant labelling in cells expressing BioID with trace biotin within the media. Interestingly, biotin labelling patterns were similar between cells expressing Myc-APEX2 or Myc-APEX2-Cln7, with both containing bright punctae within the cytosol and no diffuse or plasma membrane staining.

5.2.3 *Optimising conditions for the detection of biotinylated proteins*

Trials of both BioID and APEX2 labelling highlighted a common issue in the detection of biotinylated proteins by Western blot, which did not seem to originate specifically from BioID or APEX2 labelling procedures themselves as biotin labels were detected by immunofluorescence. It seemed unlikely that this was an issue of low level labelling given the high signal from immunofluorescence, in addition to the constitutive labelling occurring in cells expressing BioID without the need to supply additional biotin. In fact, additional attempts

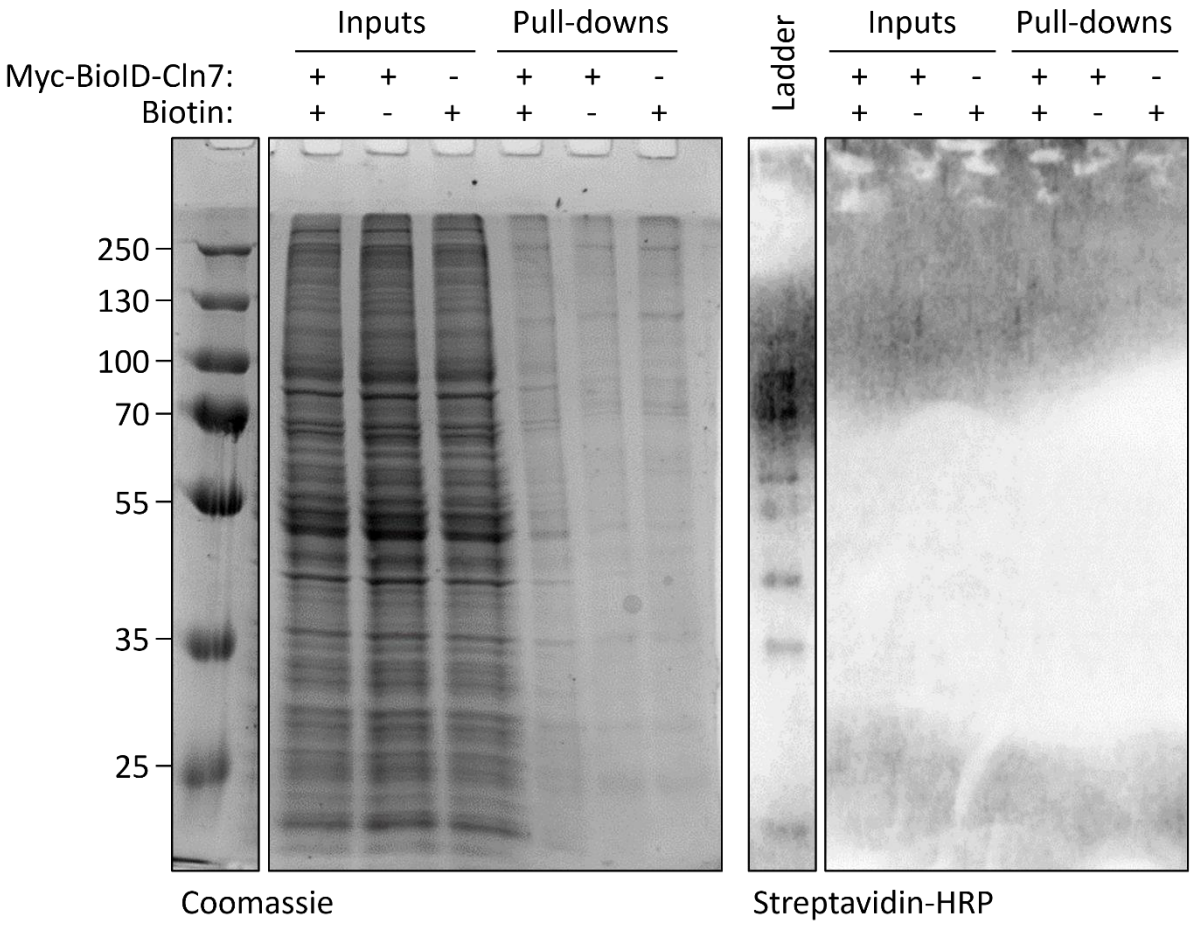

Figure 5.5. Detecting proteins labelled by BioID by Western blot.

Protein biotinylation within cells expressing Myc-BioID-Cln7 was compared with no enzyme (-BioID) and no label (-biotin) controls. Biotinylation in unpurified (input) and enriched (pull-down) samples was assessed by Coomassie (left) and Western blot (right). An additional biotinylated ladder was included as a positive control for biotin detection. Size markers in kDa are shown to the left.

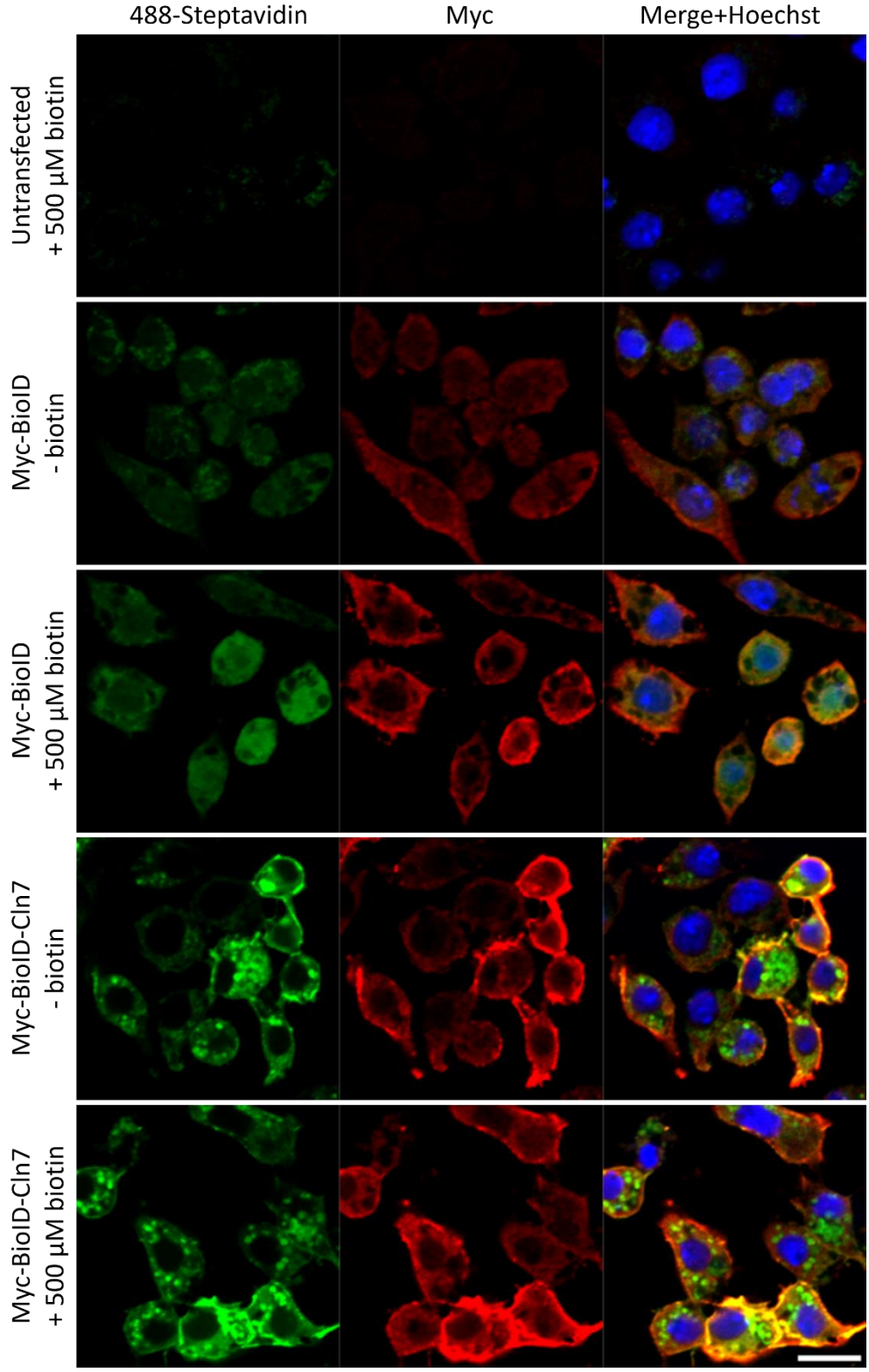

Figure 5.6. Detecting proteins labelled by BioID by IF.

Protein biotinylation patterns within cells expressing Myc-BioID and Myc-BioID-Cln7 were compared with no enzyme (-BioID) and no label (-biotin) controls. Scale bar = 10 µm.

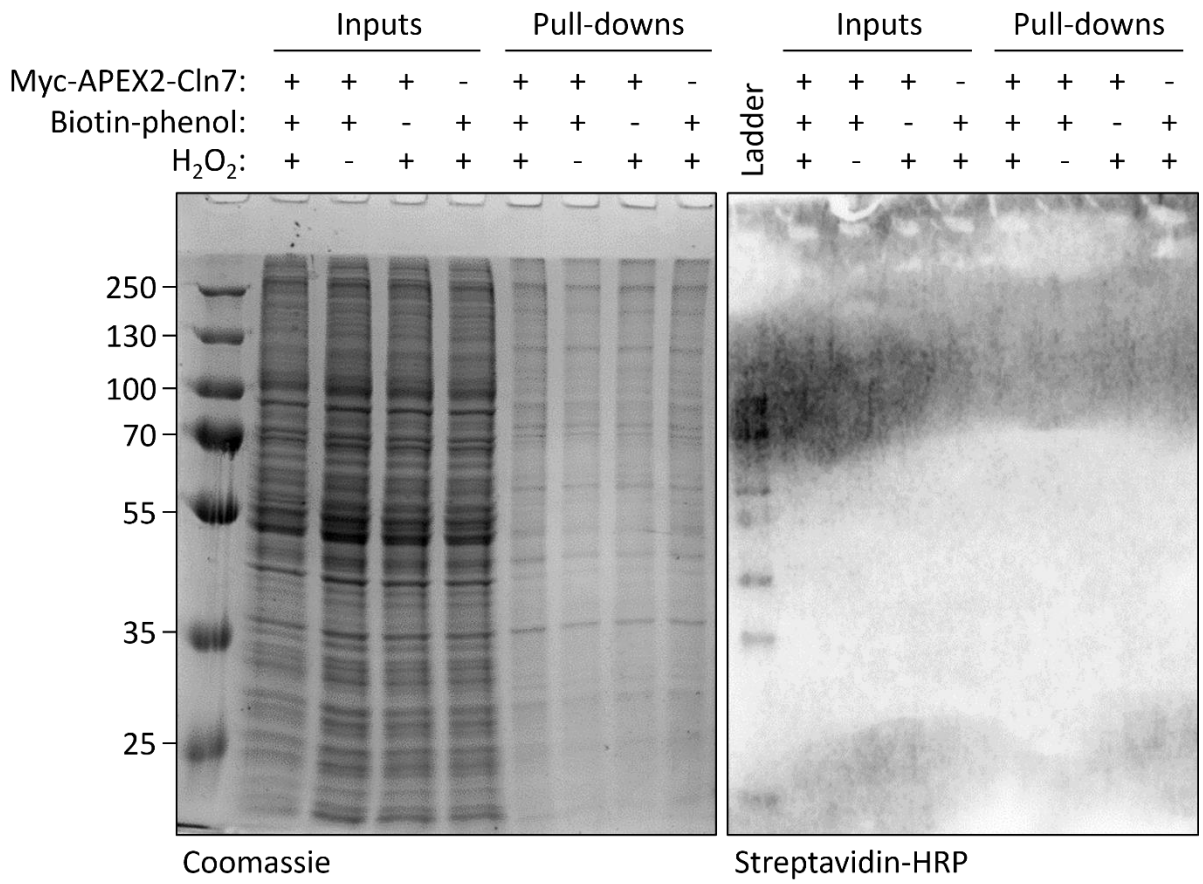

Figure 5.7. Detecting proteins labelled by APEX2 by Western blot.

Protein biotinylation within cells expressing Myc-APEX2-Cln7 was compared with no enzyme (-APEX2), no label (-BP) and no substrate (-H_2O_2) controls. Biotinylation in unpurified (input) and enriched (pull-down) samples was assessed by Coomassie (left) and Western blot (right). An additional biotinylated ladder was included as a positive control for biotin detection. Size markers in kDa are shown to the left.

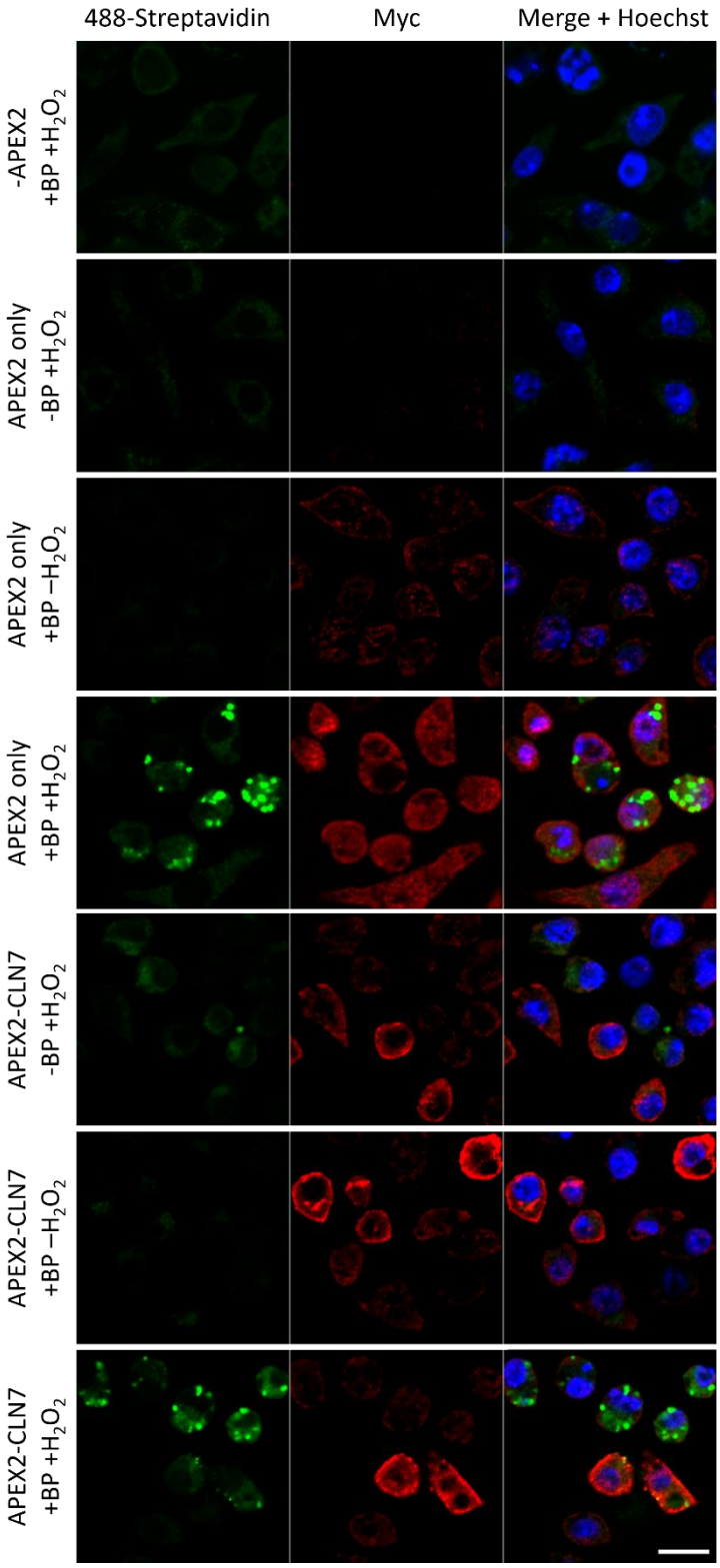

Figure 5.8. Detecting proteins labelled by APEX2 by IF.

Protein biotinylation patterns within cells expressing Myc-APEX2 and Myc-APEX2-Cln7 were compared with no enzyme (-APEX2), no label (-BP) and no substrate (-H_2O_2) controls. Scale bar = 10 µm.

to detect biotinylated proteins by Western blot consistently resulted in blots with extremely high background, thus attention was turned to optimising the Western blotting procedure itself.

Firstly, the efficiency of different blocking conditions were trialled on PVDF membranes prior to incubation with streptavidin-HRP. Six different blocking conditions were tested, including two proteinaceous blocking agents (5% milk and 5% BSA) dissolved in PBS or PBST plus two commercial protein-free blocks (Bloc-CH and SuperBlock) (Figure 5.9A). The difference in the signal to noise ratio was remarkable. Using a mid-range strength ECL, blocking with BSA (used in the labelling trials) or with either protein-free blocks resulted in very strong background almost completely covering the membrane in as little as 5 seconds, while blocking with milk facilitated the detection of a biotinylated protein ladder with significantly reduced background after 2 min exposure. When blocking with milk, the addition of Tween-20 made little difference to the background, but enhanced the signal from the biotinylated protein ladder. Despite the greatly improved signal to noise ratio, this alone was insufficient to account for the failure to detect biotinylated proteins, since still no signal was detected from samples expressing BioID.

Next, different probe conditions were tested. Membranes were incubated in streptavidin-HRP diluted 1:5,000 in 5% PBST-milk for 30 or 60 min at room temperature, or overnight at 4°C. Here, probing with streptavidin-HRP for 60 min at room temperature yielded the best signal to noise ratio (Figure 5.9B). In addition, faint bands could now be seen at 70 kDa and 25 kDa in samples containing BioID, but not when BioID is absent.

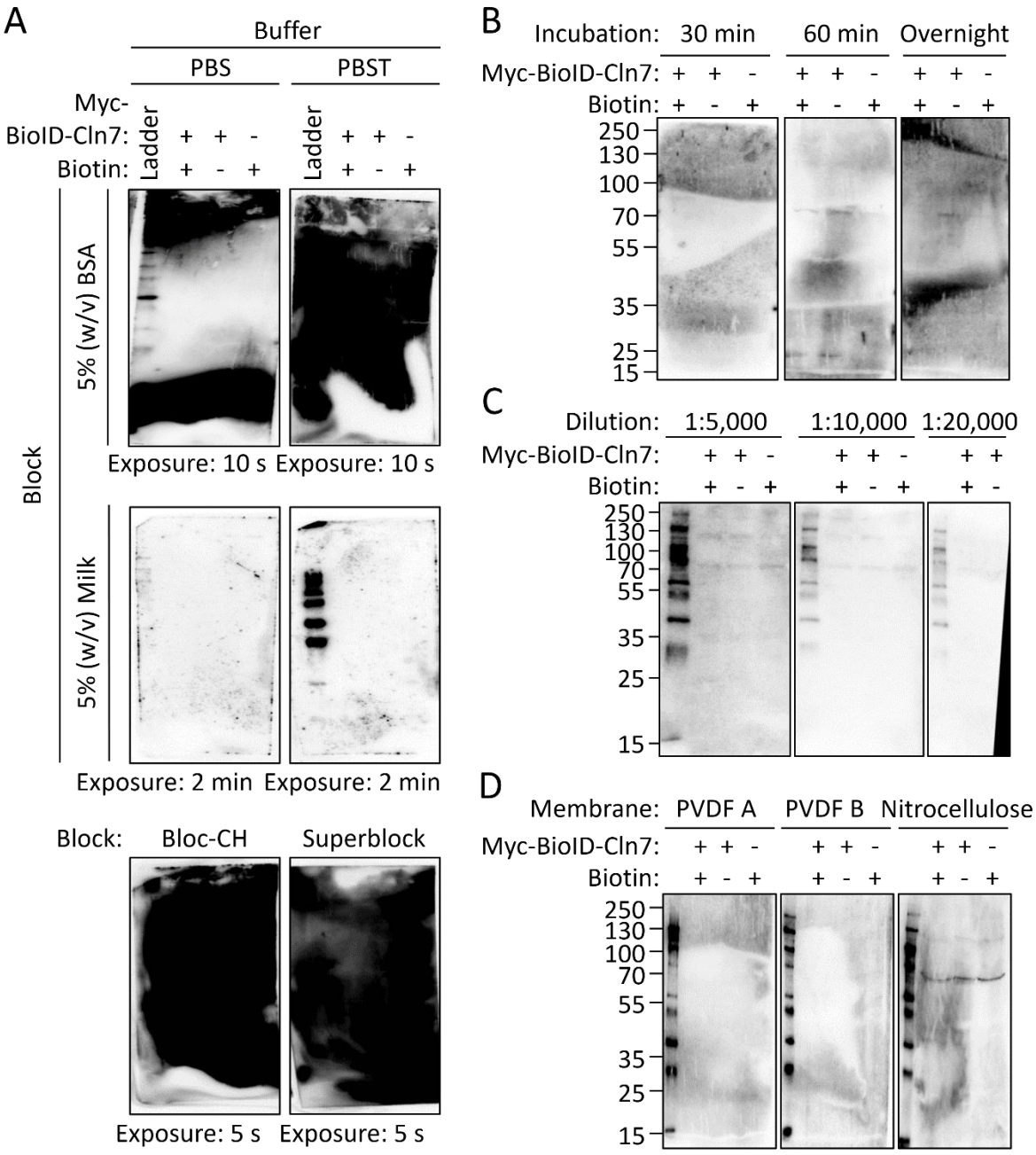

Figure 5.9. Optimising biotin detection by Western blot.

Different membrane blocking agents (**A**), probe incubations (**B**) and dilutions (**C**), and membrane types (**D**) were tested. **A**) Exposures are shown for comparison. **B**) Incubations were at room temperature for 30 or 60 min, or 4 °C overnight. **D**) Two brands of PVDF were tested (A = Amersham; B = Immobilon). Lysates from cells expressing Myc-BioID-Cln7 were loaded, with controls, to identify improvements in biotinylated protein detection within samples. A biotinylated ladder was included as a positive control. Size markers in kDa are shown to the left.

Moving on, when streptavidin-HRP was tested at concentrations ranging between 1:5,000 and 1:20,000, the signal to noise ratio did not appreciably improve (Figure 5.9C). Finally the effects of nitrocellulose and two different brands of PVDF membranes were tested. The amount of background did not change between membrane types, although bands were detected on nitrocellulose membranes only (Figure 5.9D). However bands had previously been detected on PVDF with similar intensity, thus focussing on the level of background only, membrane choice seemed to make little difference. Therefore, the Western blotting protocol to detect biotinylated proteins was revised to block PVDF membranes in 5% PBST-milk and probe with SA-HRP diluted 1:10,000 in block for 60 min at room temperature.

5.2.4 *Optimising conditions for the purification of biotinylated proteins*

The reduction in background signal using these conditions was now sufficient to detect biotinylated proteins from BioID labelling experiments, however bands were very weak. The next step therefore was to perform labelling experiments on a larger scale to increase the concentration of biotinylated proteins firstly to enhance the signal by Western blot and secondly to be detectable by Coomassie in order to be extracted for analysis by MS. Labelling experiments with Myc-BioID-Cln7 were expanded from a well of a 6-well plate to a 15 cm plate, which improved the detection of biotinylated proteins by Western blot (data not shown), however two problems remained; many non-specific proteins were consistently pulled down by streptavidin beads and no unique bands labelled by BioID were detected. The co-purification of non-specific proteins suggests that the streptavidin beads were not saturated since excess supply of biotinylated substrates should out-compete non-specific

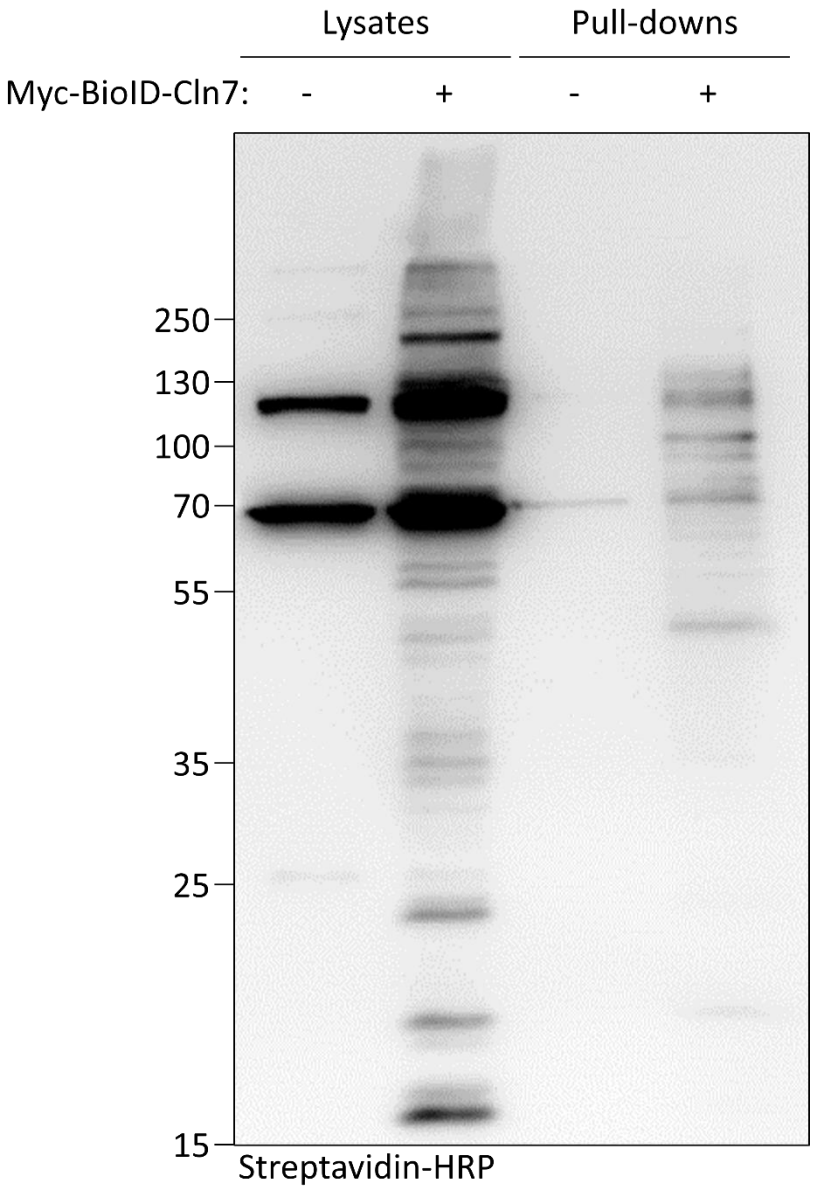

Figure 5.10. Large scale BioID labelling.

Biotinylated proteins in unpurified and enriched samples from cells expressing Myc-BioID-Cln7 were compared to parental controls. Cells were not incubated in biotin. Size markers in kDa are shown to the left.

interactions. For this reason, in addition to still not detecting unique bands by Coomassie, the labelling reaction was scaled further to fifteen 15 cm plates. Lysates from all fifteen plates were pooled in a total volume of 50 ml for enrichment on streptavidin beads. By significantly scaling the labelling reaction, promiscuous protein labelling was made astoundingly clear as many more bands were detected in samples from cells expressing Myc-BioID-Cln7 compared to controls (Figure 5.10). However a critical issue was identified; biotinylated proteins were detected in far greater abundance in 10 µl of a 50 ml unpurified lysate than in 10 µl of a 50 µl eluate. Clearly, saturating the streptavidin beads with biotin substrates did not correct the problem of poor detection of biotinylated proteins in eluates, thus two alternative explanations were considered; 1) the conditions used for binding, washing or eluting may be incompatible for enrichment on streptavidin beads, or 2) excess free biotin remains present in the lysates and out-competes the binding of biotinylated proteins.

To tackle this issue, cells were grown in a fresh batch of plates and were washed in 10 ml PBS for 5 min three times with gentle rocking to encourage the removal of any excess biotin before lysing and pooling the samples. Biotinylated proteins were then enriched from the pooled lysates as before. The lysates, flow-throughs and eluates were analysed to assess the significance of removing excess biotin. Much more signal was detected in the eluates than in the lysates, suggesting that the removal of excess biotin was a critical step to facilitate the purification of biotinylated proteins (Figure 5.11). However, similar levels of biotinylated protein was detected between lysate and flow-through samples, suggesting that despite significant enrichment of biotinylated proteins, a significant proportion remained unbound. In addition, a ladder of proteins stained by Coomassie was still present, albeit faintly, in eluates

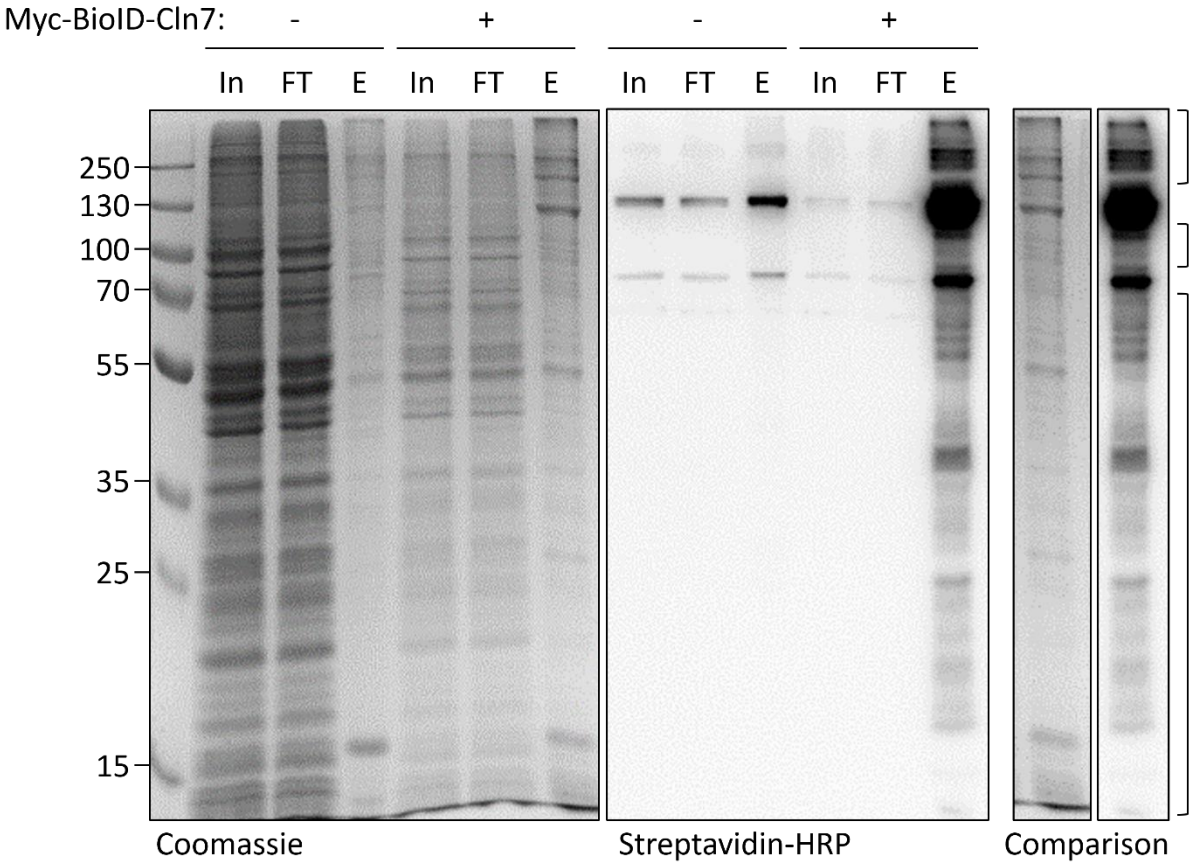

Figure 5.11. Improved capture of biotinylated proteins by removing excess biotin.

Cells were washed in PBS three times to remove free biotin before lysis. Lysates were then purified as before. Protein abundance and purity (Coomassie) and biotinylation (Western blot) were assessed in unpurified (In), flow-through (FT) and eluate (E) fractions from cells expressing Myc-BioID-Cln7, compared to parental controls. On the right is an alignment between total and biotinylated proteins from Myc-BioID-Cln7 elutates, for comparison. Brackets show proteins that were biotinylated by Myc-BioID-Cln7. Size markers in kDa are shown to the left.

from samples lacking Myc-BioID-Cln7 expression, suggesting that sub-optimal binding or washing conditions on streptavidin beads may still be a problem.

To resolve these issues, the quantity of streptavidin beads was increased from 50 µl to 200 µl, and the total protein content and the abundance of biotinylated proteins were assessed in fractions taken at every step between lysis and protein elution. A significant amount of protein is removed by the first wash with little further removal in the following four washes, showing that washing in 2% SDS is effective in removing the majority of non-specific proteins (Figure 5.12). Two different elution conditions were tested in tandem, firstly gently eluting proteins with 2 mM biotin followed by harsh elution by boiling in 1X Laemmli buffer supplemented with 2 mM biotin. Biotinylated proteins were absent in the first elution, suggesting that the competition of bound proteins with excess biotin was incapable of eluting proteins from beads. In contrast, boiling the beads in 1X Laemmli buffer was very effective at eluting biotinylated proteins. Very little biotinylated protein was detected in all fractions other than the final elution, suggesting that they are tightly bound by streptavidin beads until their elution. In addition, this suggests that significantly more biotinylated protein was captured by increasing the quantity of streptavidin beads such that clear bands corresponding to biotinylated proteins could now be seen by Coomassie stain. It was observed that Western blots frequently showed diminishing signal moving vertically from top to bottom, while protein abundance visualised by Coomassie stain did not follow the same pattern. This could be due to the persistence of non-specific proteins, however one other possibility is that a greater number of biotin labels are present on larger proteins than on smaller proteins. The activated biotin intermediate generated by BioID reacts with primary amines, thus larger

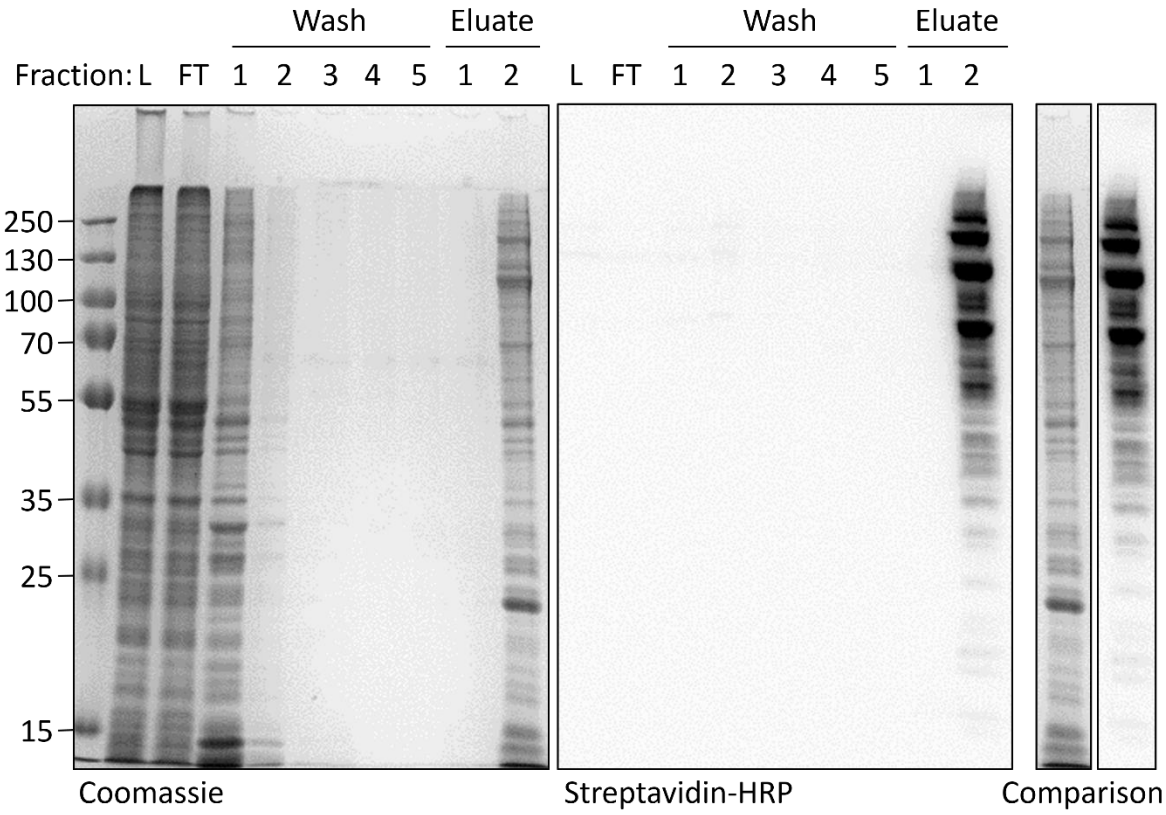

Figure 5.12. Evaluation of bead washing conditions.

The removal of non-specific proteins and release of biotinylated proteins from Myc-BioID-Cln7 cell extracts were monitored at each step during purification. Lysates (L) and flow-through (FT) fractions contain total and unbound proteins, respectively. Washes 1-5 correspond to sequential wash steps in the BioID bead washing protocol. Eluate 1 was obtained by elution in TBST with 2 mM biotin. Eluate 2 was obtained in Laemmli sample buffer with 2 mM biotin, at 98 °C for 3 min. On the right is an alignment between total and biotinylated proteins, for comparison. Size markers in kDa are shown to the left.

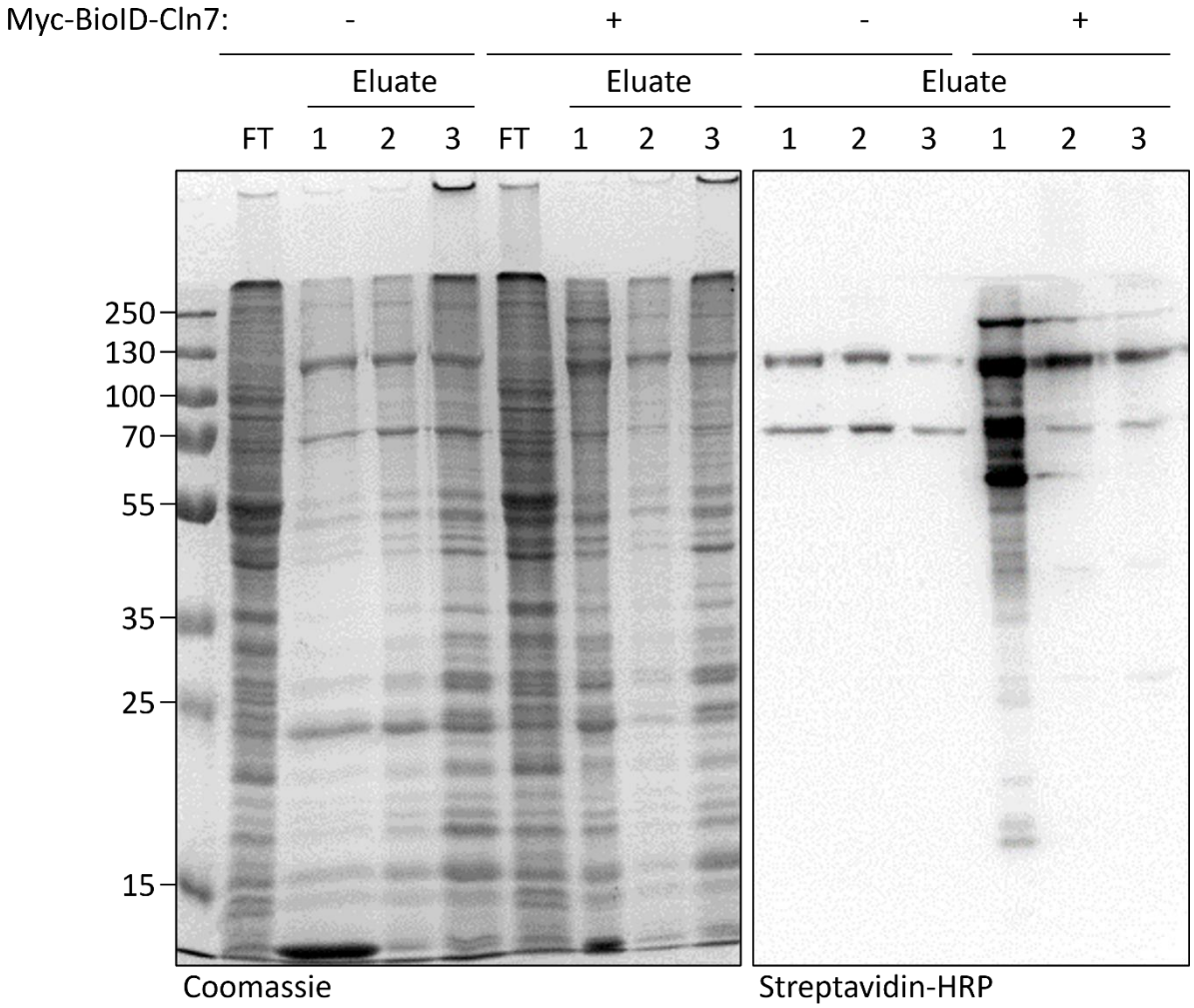

Figure 5.13. Additional washing did not improve stringency.

Extracts from parental and Myc-BioID-Cln7 cells were purified with three different wash regimes. Regime 1 was performed according to standard procedure. Regime 2 included an additional with 2 M NaCl, with further washes according to the APEX2 washing procedure in regime 3. Total and biotinylated proteins were compared between flow-throughs (FT) and eluates from the different regimes by Coomassie and Western blot. Size markers in kDa are shown to the left.

proteins likely have a greater number of modifiable sites. Therefore the relative signal strength between proteins of different sizes may not necessarily reflect their abundance.

To ensure that bead washes were as stringent as possible, the effectiveness of three washing regimes at removing non-specific proteins were tested. In addition to washing as before (regime 1), beads were subsequently washed with 2 M NaCl (regime 2) plus further washing according to the protocol for labelling with APEX2 (regime 3). Despite extensive washing at high ionic strength with various detergents, chaotropes and kosmotropes, significant binding of non-specific proteins remained in all eluates regardless of Myc-BioID-Cln7 expression (Figure 5.13). Therefore it was concluded that washing conditions were as stringent as possible.

5.2.5 *Large scale labelling with BioID and APEX2*

With the conditions for capturing and detecting biotinylated proteins now optimised, BioID and APEX2 labelling experiments were re-attempted on a large scale. Starting with BioID labelling, proteins were extracted from cells expressing Myc-BioID and Myc-BioID-Cln7. Both Myc-BioID and Myc-BioID-Cln7 were present in eluate fractions when probed with α-Myc, which correspond with bright bands at 55 kDa and 130 kDa, respectively, when blots were probed with streptavidin-HRP, showing that both enzymes auto-biotinylate (Figure 5.14A). Different banding patterns of labelled proteins were seen between eluates from Myc-BioID and Myc-BioID-Cln7 samples, suggesting that cytosolic BioID and membrane bound BioID-Cln7 label distinct protein populations. Labelled proteins from Myc-BioID and Myc-BioID-Cln7 eluates were extracted from gels in slices and analysed by HPLC-MS/MS (Figure 5.14B).

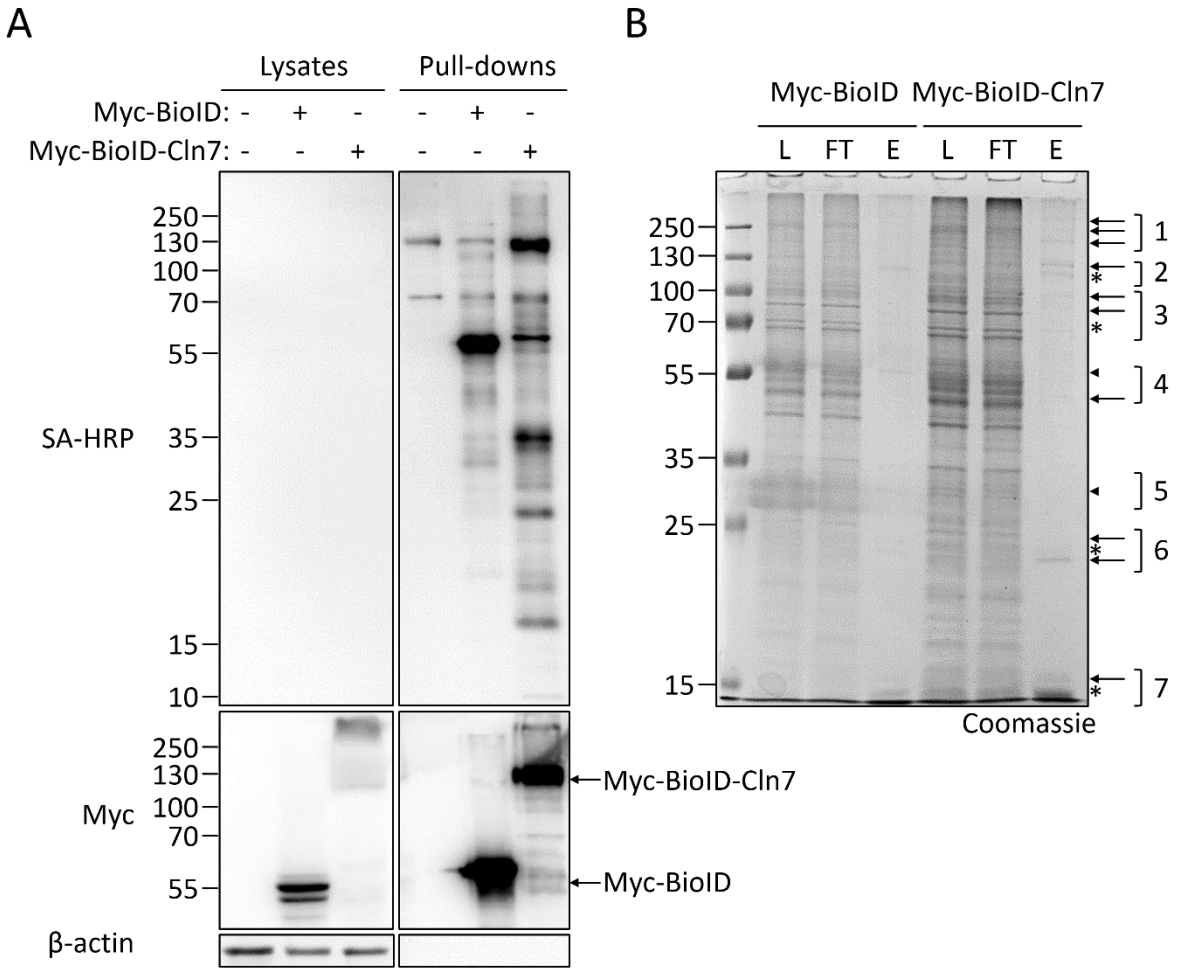

Figure 5.14. Extraction of proteins labelled by BioID.

Labelling was performed in cells expressing Myc-BioID and Myc-BioID-Cln7 with a no enzyme (-BioID) control. Biotinylated proteins were extracted and purified according to the optimised protocol. **A**) Protein biotinylation and presence of Myc-BioID or Myc-BioID-Cln7 was compared between lysates and pull-downs. Expected sizes for Myc-BioID and Myc-BioID-Cln7 are shown with arrows on the right. **B**) Total protein present in lysate (L), flow-through (FT) and eluate (E) fractions from labelling with Myc-BioID and Myc-BioID-Cln7. Eluates from both samples were aligned and gel slices 1-7 were taken from both lanes at positions marked by brackets. Arrows, arrowheads and asterisks show bands present in only Myc-BioID-Cln7, only Myc-BioID or both samples, respectively. Size markers in kDa are shown to the left.

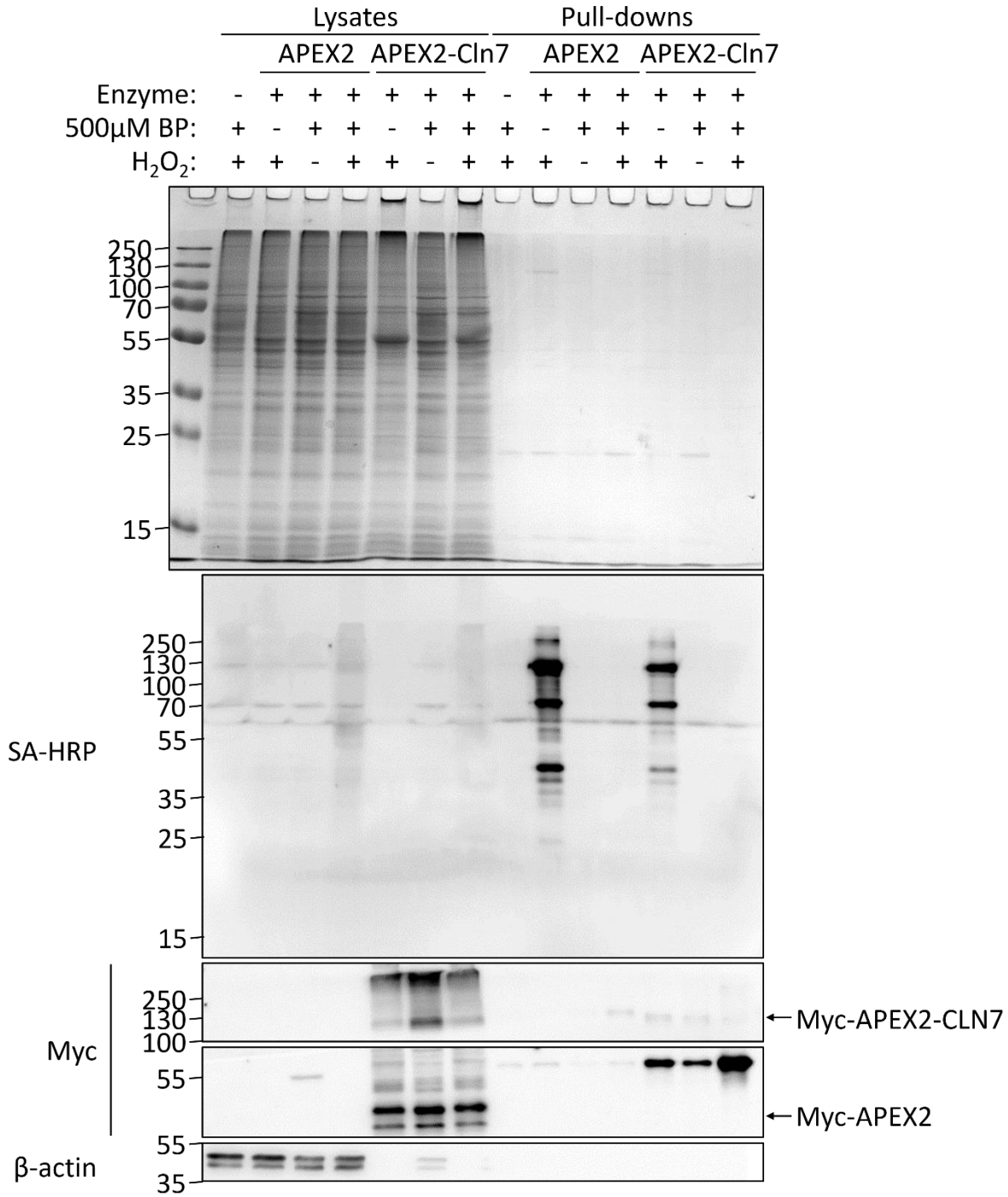

Figure 5.15. Large scale labelling with APEX2.

Labelling was performed in cells expressing Myc-APEX2 and Myc-APEX2-Cln7 alongside no enzyme (-APEX2), no label (-BP) and no substrate (-H_2O_2) controls. Biotinylated proteins were extracted and purified according to the optimised protocol. Total protein, protein biotinylation and presence of Myc-APEX2 or Myc-APEX2-Cln7 was compared between lysates and pull-downs. Expected sizes for Myc-APEX2 and Myc-APEX2-Cln7 are shown with arrows on the right. Size markers in kDa are shown to the left.

Next, APEX2 labelling was performed using cells expressing Myc-APEX2 and Myc-APEX2-Cln7. A fraction of Myc-APEX2-Cln7 was observed in eluate samples compared to the unpurified lysates (Figure 5.15). No Myc-APEX2 was observed in either fraction, but as previously discussed this may be due to low level expression. Indeed, faint smears of biotinylated proteins were observed in lysates from both Myc-APEX2 and Myc-APEX2-Cln7 samples treated with both BP and H_2O_2, but not from samples lacking one or the other. However, these proteins were not enriched by streptavidin pull-down. Bright bands were observed in pull-downs from Myc-APEX2 and Myc-APEX2-Cln7 samples lacking BP, however these show similar banding patterns and therefore likely represent pull-down of endogenously biotinylated proteins. Due to the limited success here, no further attempts to capture proteins by APEX2 labelling were made, focussing instead on BioID labelling.

5.2.6 *Hit categorisation, filtering and lead identification*

Hits identified by HPLC-MS/MS were filtered following the process shown in Figure 2.2 and placed into categories based on the fulfilment of four key criteria: 1) unique to BioID, unique to BioID-Cln7 or common to both; 2) identification of ≥ 5 peptide spectrum matches (PSMs); 3) detection of biotinylation at lysine or arginine residues; 4) identification of ≥ 1 PSM in two independent experiments. PSMs are a collective measure of the number of peptides and modifications, including those redundantly identified, belonging to a master protein and was used as an approximate measure of protein abundance. The distribution of hits among these criteria is shown in Figure 5.16. A total of 344 hits were identified, of which 143 (41.6%) were unique to BioID-Cln7, 105 (30.5%) were unique to BioID and 96 (27.9%) were identified

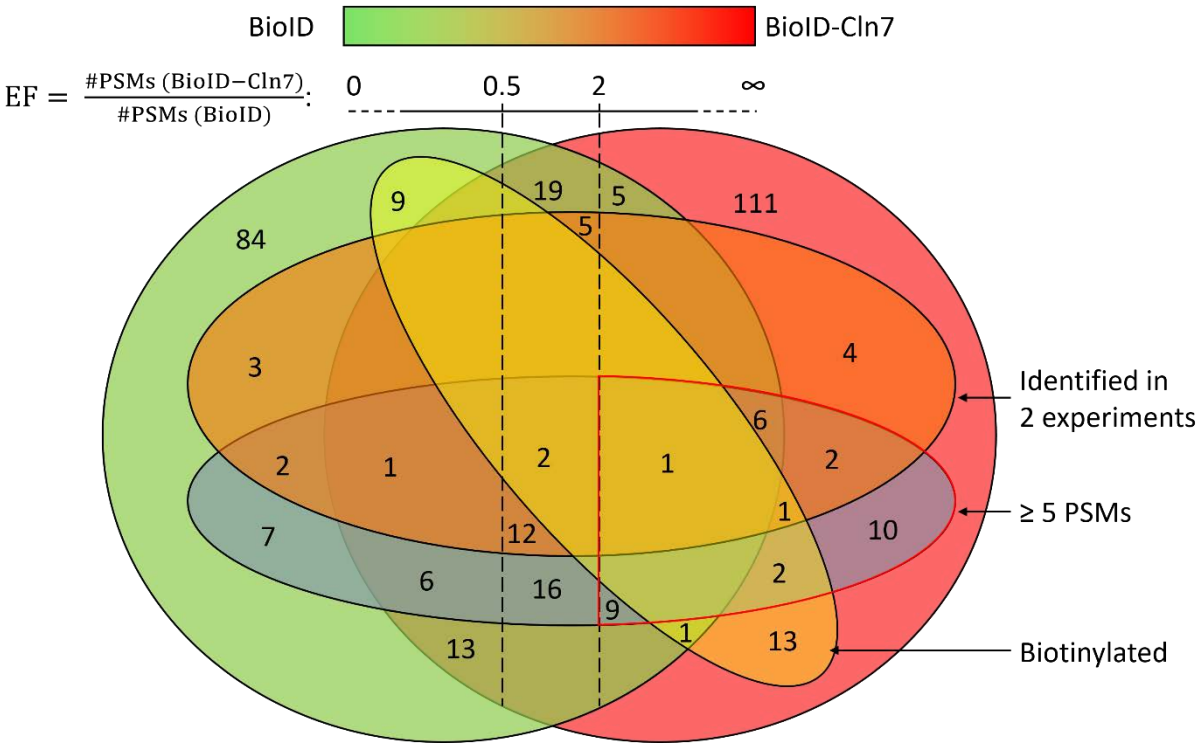

Figure 5.16. Distribution of hits from BioID labelling across four quality scores.

An Euler diagram was constructed to illustrate the distribution of hits labelled by BioID (left, green) and BioID-Cln7 (right, red). Numbers represent the number of hits belonging to each section. Hits were resolved by their satisfaction across four key criteria: 1) unique or shared; 2) ≥ 5 PSMs; 3) biotinylation; 4) identification in two independent experiments. Hits shared by BioID and BioID-Cln7 samples were split further by enrichment factor (EF), whereby EF ≤ 0.5 and EF ≥ 2 represent proteins predominantly labelled by BioID and BioID-Cln7, respectively. Hits with 0.5 < EF < 2 were interpreted to represent a mixture of non-specific proteins captured during enrichment, endogenously biotinylated proteins and proteins labelled equally within both samples. The gradient above the EF scale provides a visual demonstration of how EF scores hits by relative labelling frequency across BioID (green) and BioID-Cln7 (red) samples. Hits with ≥ 5 PSMs and EF ≥ 2 (red border) were interpreted as leads. Shapes are not drawn to scale.

at least once from both samples. Also, 77 (22.4%) hits were identified with ≥ 5 PSMs, 29 (8.4%) with biotinylation and 34 (10.1%) were detected in two independent experiments. Over two-thirds of hits identified (232, 67.4%) did not fulfil any of the internal criteria and so were ignored.

Proteins that were identified in both BioID and BioID-Cln7 samples likely include a mixture of proteins that represent multiple populations. Firstly, non-specific proteins that remained bound to streptavidin beads would be common to both samples. Secondly, endogenously biotinylated proteins should also be present in both samples. Thirdly, it is always possible that proteins can be labelled by both BioID and BioID-Cln7. However this does not take into consideration the relative abundance of proteins labelled by one sample versus the other. Thus hits that were common to both BioID and BioID-Cln7 were not immediately subtracted from analysis. Instead, an enrichment factor (EF) was constructed to calculate the ratio of PSMs between BioID-Cln7 and BioID samples. Shared hits were then sub-divided into categories of EF ≤ 0.5, EF ≥ 2 or 0.5 < EF < 2, representing hits that were twice as frequently labelled by BioID or by BioID-Cln7, or approximately equally between the two, respectively. This segregation therefore discriminates between non-specific and endogenously biotinylated proteins (0.5 < EF < 2) from proteins labelled by BioID or BioID-Cln7. Of the hits still in consideration, only a portion of shared hits (37, 10.8% of total hits, 38.5% of shared hits) was subtracted from analysis, keeping hits with EF ≥ 2 (17, 4.9% of total hits, 17.7% of shared hits).

To condense the list further, the importance of fulfilling the internal criteria was considered. High confidence hits would be those unique to BioID-Cln7 or with high EFs, with maximal protein coverage containing several biotinylated peptides, detected across multiple

independent experiments. However protein coverage for high quality hits was on average between 20-35% and up to 50% in exceptional cases, thus the majority of peptides belonging to master proteins remained undetected or unassigned to the spectra. Additionally, each protein may have multiple possible biotinylation sites and not every molecule will likely be biotinylated in the same way. Therefore biotinylated peptides may have feasibly been missed by the analysis. Moreover, any hit unique to BioID-Cln7 or with EF ≥ 2 should be biotinylated because if it were not, it would be a non-specific protein that should be equally present in BioID samples. Based on these arguments, biotinylation was considered desirable but not essential.

The remaining criteria of ≥ 5 PSMs and identification in two experiments measured hit reliability within and between experiments, respectively, in order to estimate the likelihood of hits being true or false positives. The more frequently a protein is identified, the greater the confidence. Ideally both criteria should be satisfied, but of the two it is more desirable to detect many PSMs in one experiment than it is to detect few PSMs in two. Therefore, only proteins with ≥ 5 PSMs remained in consideration, irrespective of biotinylation or number of experiments in which they were detected. These 31 hits (9.0%), satisfying EF ≥ 2 and ≥ 5 PSMs, were considered leads. Only two leads (Syb and bel) satisfied all criteria.

5.2.7 *Cellular distribution of labelled proteins*

The cellular distribution of labelled proteins should mirror the distribution of BioID for labelling to be specific. BioID is restricted to membranous regions predominantly at the plasma membrane in cells expressing Myc-BioID-Cln7, whereas cells expressing Myc-BioID

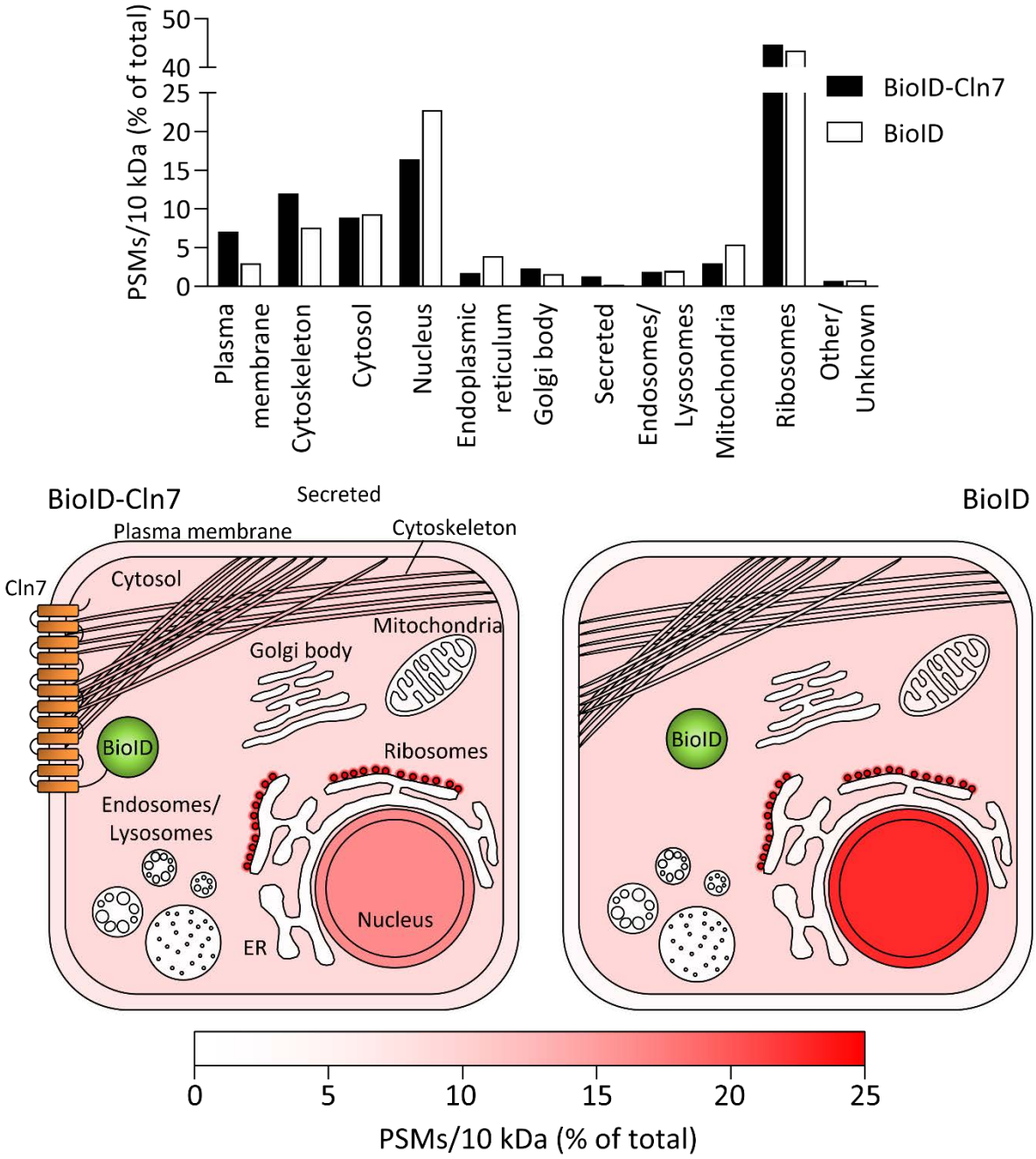

Figure 5.17. Cellular distribution of hits from BioID labelling.

PSMs were normalised to full-length protein size to measure labelling density, expressed as PSMs per 10 kDa fragment (approximately 90-100 amino acids). Labelling densities were totalled for each compartment and expressed as a percentage of the whole. Cartoon heatmaps illustrate labelling densities across compartments from BioID (right) and BioID-Cln7 (left) samples. A scale bar is provided to match colour intensity with labelling density. Hit localisations were obtained from UniProt. Hits localising to multiple compartments were split evenly.

show diffuse BioID distribution throughout the cytosol. Thus, greater labelling density should be present at the plasma membrane in cells expressing Myc-BioID-Cln7, whereas labelling by Myc-BioID should be more diffuse. To investigate this, all hits were assigned cellular compartments as listed by UniProt and all PSMs belonging to hits from each compartment were totalled. It became clear that PSMs did not accurately reflect labelling density. PSMs tally the number of peptide-spectrum matches per protein. However this gives a biased view of labelling density, as a 100 kDa protein may generate ten times more fragments than a 10 kDa protein, and should therefore be detected ten times more frequently. Therefore PSMs were normalised to full-length protein mass to more accurately reflect labelling density, measured as the number of PSMs per 10 kDa length (approximately 90-100 amino acids).

A comparison of labelling densities between BioID and BioID-Cln7 samples is shown in Figure 5.17. Unexpectedly, by far the most densely labelled compartment in both samples were the ribosomes (43.5% BioID, 44.7% BioID-Cln7), followed by the nucleus (22.8% BioID, 16.4% BioID-Cln7). Interestingly the plasma membrane and cytoskeleton were labelled 2.4-fold (3.0% BioID, 7.1% BioID-Cln7) and 1.6-fold (7.6% BioID, 12.0% BioID-Cln7) more by BioID-Cln7 than by BioID, respectively. In contrast, BioID labelled the endoplasmic reticulum and mitochondria 2.3-fold (3.9% BioID, 1.7% BioID-Cln7) and 1.8-fold (5.4% BioID, 3.0% BioID-Cln7) more than BioID-Cln7, respectively. Cytosolic labelling was almost equal between the two samples (9.3% BioID, 8.9% BioID-Cln7). Labelling with the remaining compartments was limited. A cartoon heatmap was constructed to compare labelling densities between compartments and between samples with spatial context (Figure 5.17). Here, colour intensities from cells expressing BioID can be visually subtracted from those expressing

Table 5.1. Description and criteria scores for identified leads

Sample	Protein[a]	PSMs/ 10 kDa	Coverage (%)	Biotins	Expts	EF
BioID-Cln7	Synaptobrevin (Syb)	3.0	23	1	2	
BioID-Cln7	Gustatory and pheromone receptor 33a (Gr33a)	1.1	3	2	1	
	Ran-binding protein M (RanBPM)	0.9	3	2	1	
BioID-Cln7	Fused (fu)/rolled (rl)/Src64B[b]	0.7	1	0	2	
	Integrin alpha-PS1 (mew)	0.4	4	0	2	
BioID-Cln7	60S RpL36	6.7	29	0	1	
	Insulin receptor substrate 1 (chico)	4.5	33	0	1	
	Lethal(2) giant larvae protein (l(2)gl)	4.0	27	0	1	
	60S RpL23	3.4	30	0	1	
	Protein coracle (cora)	2.6	31	0	1	
	Elongation factor 2 (EF2)	1.6	18	0	1	
	60S RpL7A	1.6	6	0	1	
	Pyruvate kinase (PyK)	1.2	16	0	1	
	RhoGAP92B (dRich)	0.6	6	0	1	
	Phosphoinositide phospholipase C (norpA)	0.6	7	0	1	
Shared	ATP-dependent RNA helicase (bel)	1.5	3	1	2	2.6
Shared	Formin-like protein (Frl)	10.2	42	0	2	136.0
	Protein hu-li tai shao (hts)	6.1	28	0	2	19.5
	40S RpS27A	10.6	56	0	2	19.0
	Histone H4 (His4)	8.8	40	0	2	2.5
	60S RpL37a	4.7	28	0	2	2.5
	40S RpS26	3.8	32	0	2	2.5
Shared	Septin-2 (Sep2)	4.1	35	0	1	20.0
	PI-binding clathrin assembly protein (lap/AP180)	3.0	28	0	1	15.0
	Spectrin alpha chain (α-Spec)	2.3	30	0	1	8.1
	Histone H2B (His2B)	5.1	37	0	1	7.0
	40S RpS6	2.1	23	0	1	3.0
	RhoGAPp190	1.0	12	0	1	2.4
	Heat shock protein 83 (Hsp83)	3.8	20	0	1	2.4
	Anillin (scra)	0.8	6	0	1	2.2
	Nucelostemin 1 (Ns1)	1.5	19	0	1	2.0

[a]Full protein names are provided with abbreviations for *Drosophila* given in parentheses.
[b]No peptides were distinguishable between fu, rl, Gr33a.

Abbreviations: EF = enrichment factor; Rp = ribosomal protein; GAP = GTPase activating protein; PI = phosphatidylinositol

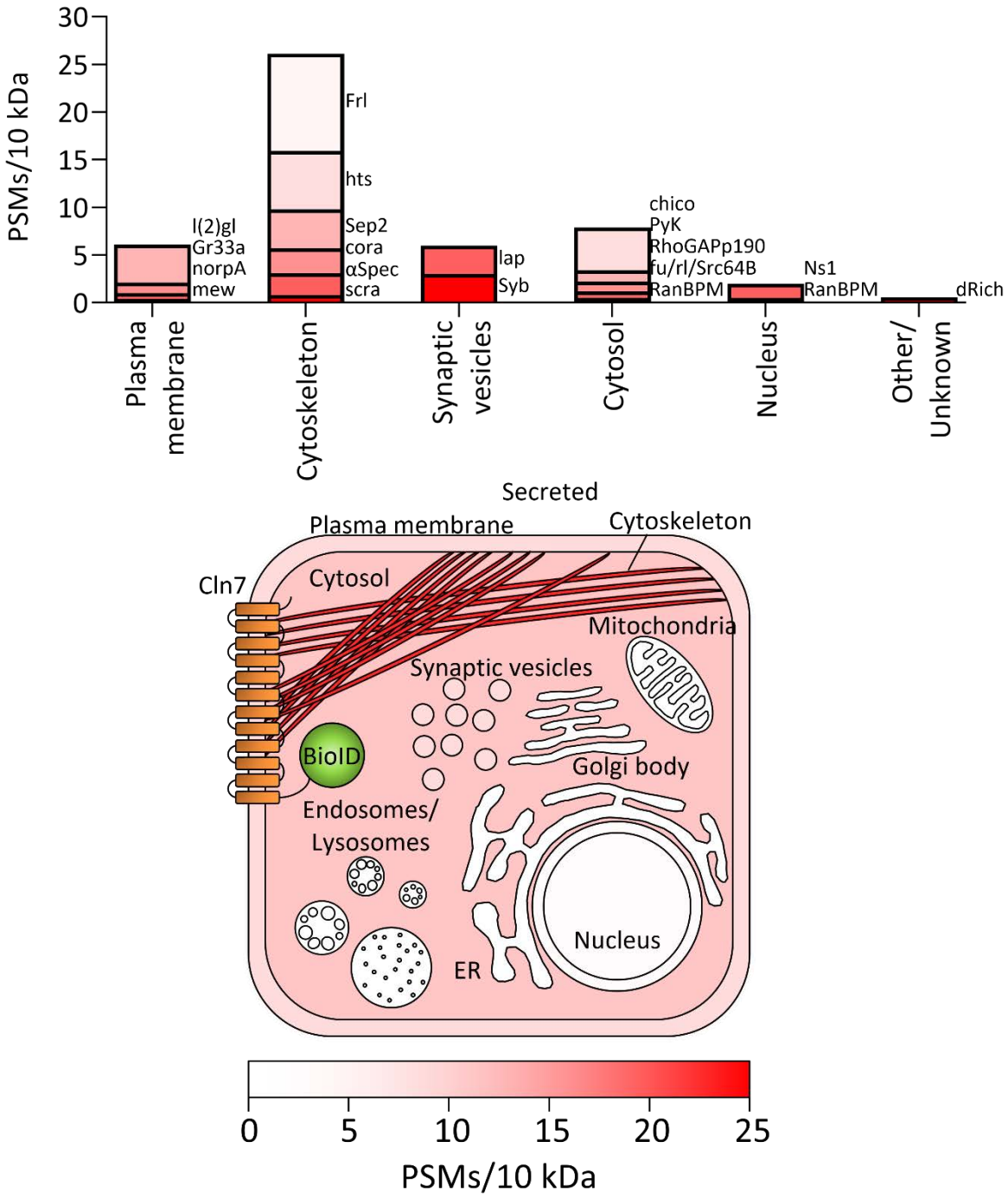

Figure 5.18. Cellular distribution of leads from BioID labelling.

Labelling densities per compartment were totalled amongst the identified leads and plotted as a stacked histogram. Protein names are given beside each stack in ascending order of abundance. A cartoon heatmap was constructed from labelling densities amongst the leads. A scale bar is provided to match colour intensity with labelling density.

BioID-Cln7. The juxtaposition of BioID-Cln7 to the plasma membrane and cytoskeleton likely explains the increased labelling at these compartments over BioID alone.

5.2.8 *Labelling density and localisation of leads*

The identities and criteria scores for all 31 leads are listed in Table 5.1. Several of these leads have niche roles in the cell and were excluded as unlikely candidates for Cln7 binding. These included ribosomal proteins (RpL7A/23/36/37A, RpS6/26/27A and EF2), histones (H2B and H4), heat shock proteins (Hsp83) and helicases (bel). This reduced the list to 19 leads. The distribution and labelling density of the remaining leads was analysed. Amongst the leads, the cytoskeleton was at least 3-fold more densely labelled than any other compartment (Figure 5.18). The cytosol, plasma membrane and synaptic vesicles had similar labelling densities, but interestingly 58% of the cytosolic labelling was specific to chico. Chico is the *Drosophila* insulin receptor substrate and functions by binding to the insulin receptor at the plasma membrane. Therefore, although a cytosolic protein, a significant proportion of chico labelling may have occurred at the plasma membrane. The labelling distribution here more clearly reflects the localisation of Myc-BioID-Cln7, labelling the intracellular juxtamembrane region including the cytoskeleton, plasma membrane and exocytic vesicles. Based on their high labelling densities, leads of interest were cytoskeletal proteins Frl, hts, Sep2, cora and αSpec, the plasma membrane protein l(2)gl, vesicular proteins lap and Syb, and the cytosolic protein chico.

5.2.9 *Common roles for leads within the Drosophila nervous system*

Proteins labelled by BioID have thus far been filtered based on criteria that assessed leads in the context of an *in vitro* labelling system. For these leads to be biologically relevant though, these leads must also be co-expressed with Cln7 within target organs *in vivo*. Therefore, the final step in lead characterisation was to investigate the expression pattern and function of leads within the *Drosophila* nervous system (Table 5.2). Where tissue expression was not explicitly defined, expression patterns were searched using SCope, an online tool that maps the expression patterns of 14,600 transcripts across 57,000 cells based on single-cell transcriptome analysis of the adult fly brain (416).

Most of the leads had reported roles in the development and function of tissues within the nervous system. Common roles included development and phototransduction within photoreceptors, olfactory learning and memory within the mushroom bodies, general axon guidance within neurons, and regulation of NMJ development and plasticity from pre- and post-synaptic compartments. Gr33a was excluded due to restricted tissue expression within a subset of gustatory receptor neurons. Sep2, scra and Ns1 had no known roles in the nervous system and were also excluded. Roles for leads in several signalling pathways were identified, including insulin, Ras, Rho, Notch, hedgehog and Hippo signalling. By cross-referencing lead functions with labelling densities in Figure 5.18, putative interactions between these pathways and Cln7 likely originate from 3 key proteins; Frl (Rho/Cdc42), l(2)gl (Notch and Hippo) and chico (insulin).

Roles for insulin, Cdc42 and Notch signalling in axon growth and guidance within the mushroom body neurons, photoreceptors and motor neurons have been reported (457-459).

Table 5.2. Reported expression and function of leads within the *Drosophila* nervous system.

Protein	Localisation	Expression within nervous system	Function in the nervous system	Refs.
Syb	Synaptic vesicles	Pan-glial. Functional paralogue nSyb highly expressed pan-neuronally	Vesicle docking and neurotransmitter release	(460)
Gr33a	Plasma membrane	Gustatory receptor neurons	Regulates bitter taste aversion and male courtship preference	(461, 462)
RanBPM	Cytosol / nucleus	Most neurons, highly expressed in Kenyon cells	Regulates larval feeding, light response and locomotion. May regulate NMJ branching and bouton number	(463, 464)
fu	Cytosol	Ubiquitous	Roles for hedgehog signalling in glial cell fate determination and commissural axon guidance	(465, 466)
rl	Cytosol / nucleus	Ubiquitous	Roles for Ras signalling in photoreceptor development, midline glia cell survival, sleep and plasticity and NMJ development	(467-471)
Src64B	Cytosol	Pan-neuronal	Regulates actin polymerisation. Roles in Rho-dependent axon retraction, mushroom body development and retrograde signalling to the NMJ	(472-474)
mew	Plasma membrane	Pan-neuronal	Roles in axon guidance and dendritic self-avoidance	(475, 476)
chico	Cytosol	Ubiquitous	Roles for insulin signalling in learning, long-term memory, photoreceptor axon guidance and synapse growth at the NMJ	(457, 477, 478)
l(2)gl	Basolateral membrane	Glial	Regulates Notch and Hippo signalling. Roles in cell polarity and sensory organ precursor development	(479, 480)
cora	Cytoskeleton	Ubiquitous, highly expressed in Kenyon cells and at the NMJ PSD	Anchors GluRIIA to the NMJ PSD	(481, 482)
PyK	Cytosol	Ubiquitous, enriched in mushroom body and ellipsoid body neurons	Catalyses pyruvate phosphorylation in glycolysis. Disrupted glucose metabolism is linked to reduced olfactory memory	(483)
dRich	Unknown	Ubiquitous at low levels, enriched at the NMJ PSD	Opposes dCIP4/Wsp signalling by inhibiting Cdc42. Promotes Gbb retrograde signalling and regulates DLG and GluRIIB distribution at the NMJ.	(484)
norpA	Plasma membrane	Ubiquitous, abundant in the retina	Hydrolyses PI into IP_3 and DAG. Essential role in phototransduction	(485, 486)
Frl	Cytoskeleton	Ubiquitous	Roles in actin nucleation and axon growth in mushroom bodies. Possible role in neural outgrowth. Activated by Cdc42.	(458, 487)
hts	Cytoskeleton	Ubiquitous, present in pre- and post-synaptic compartments at the NMJ	F-actin capping protein. Regulates NMJ growth and nerve to muscle adhesion from pre-synaptic and post-synaptic compartments.	(488-490)
Sep2	Cytoskeleton	Ubiquitous	Role in follicle cell encapsulation of female germline cysts. No known role in the nervous system.	(491)
lap	Synaptic vesicles	Pan-neuronal. Expressed in some glia	Required for synaptic vesicle recycling	(492, 493)
α-Spec	Cytoskeleton	Ubiquitous	Integral to the spectrin-actin cytoskeleton. Required pre-synaptically for synapse stability and post-synaptically for sub-synaptic reticulum folding and post-synaptic protein organisation at the NMJ.	(494, 495)
RhoGAPp190	Cytosol	Ubiquitous, abundant in neurons	Promotes axon extension by inhibiting RhoA-dependent retraction in mushroom bodies	(496)
scra	Cytoskeleton	Limited expression in few neurons and glia	Required for cytokinesis during embryonic development. No known role in the nervous system	(497)
Ns1	Nucleus	Ubiquitous	Possible role in nuclear export of ribosomal subunits. No known role in the nervous system	(498)

However, l(2)gl is a mainly glial protein and is only reported to regulate Notch in the development of sensory organ precursor cells (480). Frl, hts, α-Spec have important roles in synaptic plasticity by regulating actin dynamics. Axon growth and synaptic plasticity requires dynamic remodelling of the actin-spectrin cytoskeleton from both pre-synaptic and post-synaptic compartments. The co-enrichment of these proteins with high labelling densities suggest that these proteins may cooperatively regulate synaptic plasticity. Indeed, the sub-synaptic reticulum (SSR) within the neuromuscular junction (NMJ) post-synaptic density (PSD) is a specialised structure rich in plasma membrane folds and cytoskeletal proteins. As such, hts, α-Spec and cora are abundantly expressed at the PSD. Together, the common role for leads in regulating cytoskeleton organisation and axon guidance suggest that Cln7 may interact with a network of structural and signalling proteins that together regulate synaptic plasticity.

5.2.10 *Recruitment of Myc-BioID-Cln7 to the NMJ SSR*

In vitro proximity labelling with BioID identified candidate membrane and cytoskeletal proteins that may bind and regulate Cln7, with possible roles in regulating synaptic plasticity. Previous data has shown that Venus-Cln7, a CRISPR knock-in, is expressed in muscles at the NMJ and is enriched around synapses (402). Upon closer examination it was observed that Venus-Cln7 was recruited to the sub-synaptic space (Figure 5.19A-F). Transgenic UAS-Myc-BioID-Cln7 flies were generated to investigate the Cln7 interactome within this compartment *in situ*. Entry clones encoding Myc-BioID-Cln7 were recombined into the vector pTMW for injection into w^{1118} embryos. Transgenic insertions were mapped according to Figure 2.1.

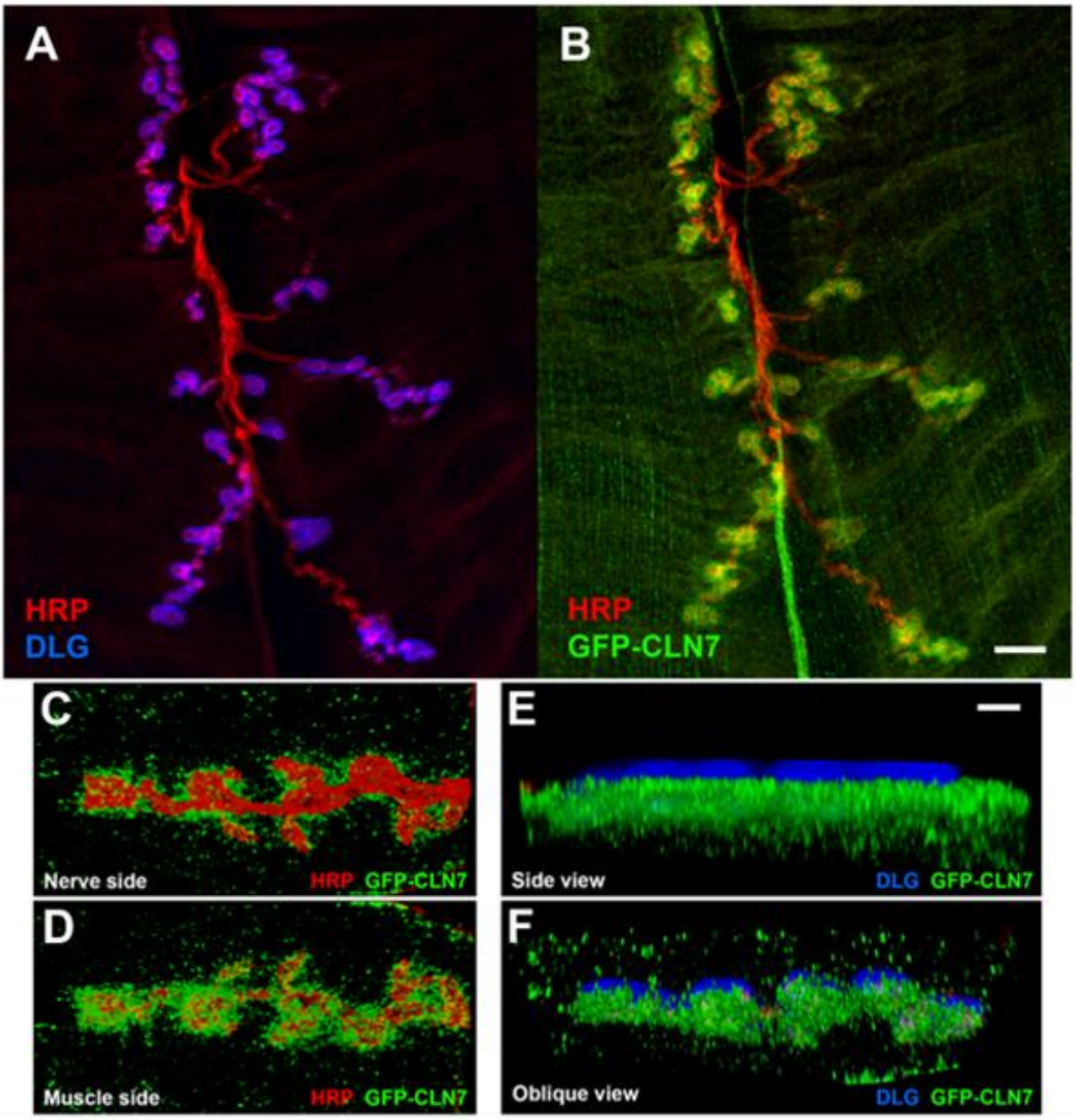

Figure 5.19. Cln7 is recruited to the sub-synaptic reticulum at the NMJ.

Type 1b NMJs at muscle 4 from L3 larvae expressing the CRISPR knock-in Venus-Cln7 were visualised. Pre-synaptic and post-synaptic compartments were immunostained for HRP and DLG, respectively. **A,B**) XY slices of the NMJ showing expression of Venus-Cln7 in muscles and recruitment to the PSD. **C-E**) 3D renders at higher magnification showing recruitment of Venus-Cln7 to the sub-synaptic space underlying the PSD, marked by DLG. Scale bars = 20 µm (**A,B**) and 10 µm (**C-E**). Experiments were performed by Richard Tuxworth.

Myc-BioID-Cln7 expression was driven in muscles using Mef2-Gal4 and preliminary labelling experiments were performed. Myc-BioID-Cln7 expression was detected in unpurified homogenates from adult flies, but not from L_3 larvae (Figure 5.20A). Biotinylated proteins were detected mainly in extracts from Myc-BioID-Cln7 and control adults fed on food containing biotin. However identical banding was observed between Myc-BioID-Cln7 and control extracts, suggesting that these were endogenously biotinylated proteins. It is possible that similar issues with protein extraction and detection were encountered here as were discussed in the chapter 4, and that proteins may require purification to facilitate their detection. Larval NMJs were also analysed by immunohistochemistry for Myc-BioID-Cln7 expression and protein biotinylation. When expressed in muscles, Myc-BioID-Cln7 was correctly recruited to the SSR, however only background biotinylation was detected (Figure 5.20B). Further optimisation may be needed to enhance the bioavailability of biotin and improve the detection of biotinylated proteins from fly tissues.

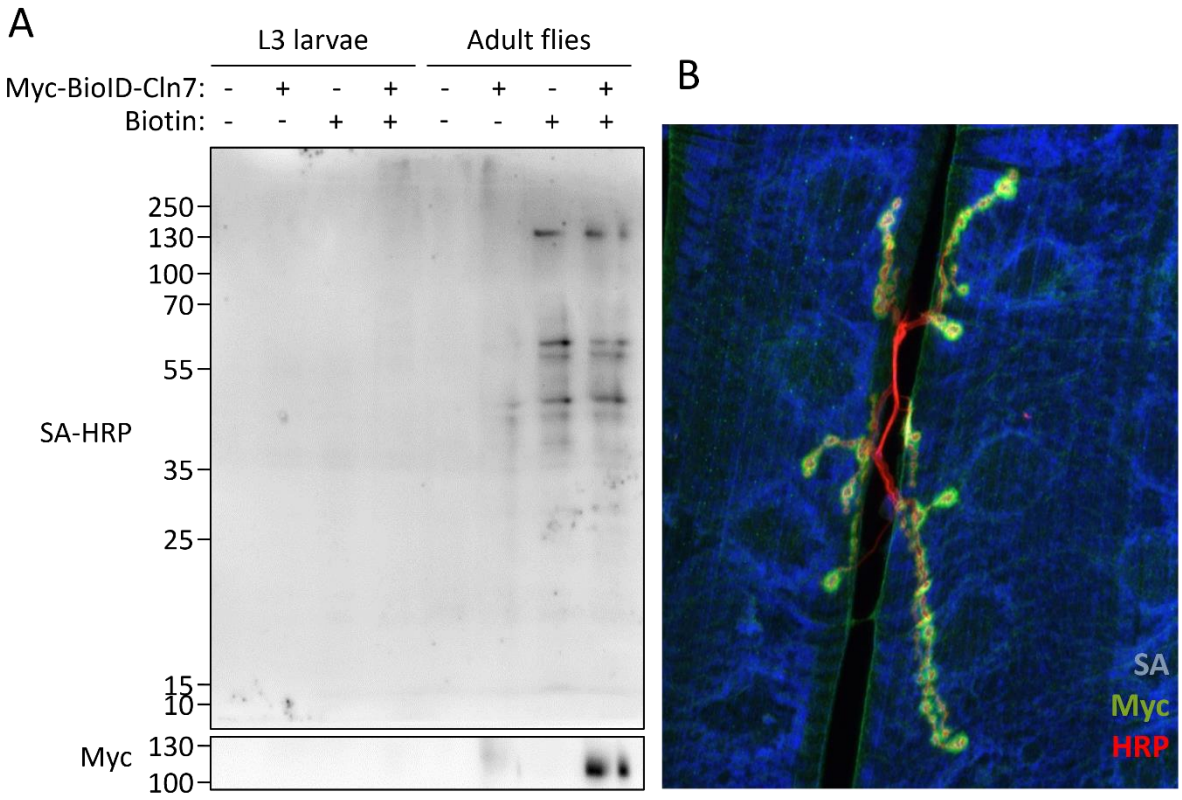

Figure 5.20. Myc-BioID-Cln7 localises to the SSR when expressed in muscles.

A) Preliminary labelling experiments were performed using L3 larvae and one day-old adult flies. Myc-BioID-Cln7 expression was driven throughout development using Mef2-Gal4. *CyO, GFP/+; UAS-Myc-BioID-Cln7/+* flies were used as the no BioID control. Flies were reared on food supplemented with 1 mM biotin. **A**) Myc-BioID-Cln7 was detectable in samples from adult flies but not from larvae. **B**) NMJs at muscles 6/7 from L3 larvae driving Myc-BioID-Cln7 in muscles were visualised. Myc-BioID-Cln7 was stained with α-Myc (green), biotinylated proteins were stained using 405-streptavidin (blue), and the innervating motorneuron was stained with HRP (red). Myc-BioID-Cln7 correctly localises to the sub-synaptic space. Only background biotinylation was detected. Scale bar = 20 µm. Immunohistochemistry was performed by Richard Tuxworth.

5.3 Discussion

5.3.1 *Evaluation of proteins labelled by BioID*

Proximity labelling of the Cln7 interactome with BioID identified 239 possible interactors (total number of proteins labelled by BioID-Cln7). Based on a set of unbiased *in silico* criteria, these hits were filtered down to 31 leads of which 21 were considered likely candidates. To translate these leads from an *in vitro* to a more relevant *in vivo* setting, the list was condensed further to 17 leads that were to known to be expressed and function within the *Drosophila* nervous system. Among the most frequently labelled proteins were the cytoskeletal proteins Frl, hts, cora and α-Spec, the plasma membrane protein l(2)gl, the cytosolic protein chico, and synaptic vesicle proteins lap and Syb.

Evaluation of the cytoskeletal proteins uncovered a potential role in regulating synaptic plasticity by controlling actin dynamics. These mechanisms were identified to operate in photoreceptors and at the NMJ, both of which present developmental phenotypes in $Cln7^{84D}$ flies. Roles in the development of mushroom body neurons were also reported amongst leads, therefore it would be interesting to investigate whether $Cln7^{84D}$ also show a mushroom body development phenotype.

Interestingly, chico was frequently labelled within BioID-Cln7 samples. This is consistent with the notion discussed in chapter 3 that Cln7 may interact with the insulin signalling pathway. Chico functions as the insulin receptor substrate at the plasma membrane and therefore an interaction between chico and Cln7 is a plausible link between Cln7 and insulin signalling. Roles for presynaptic PI3K-Tor signalling, downstream of chico, in NMJ synapse expansion and photoreceptor axon guidance have been reported (457), but the

contribution of insulin signalling from postsynaptic compartments is not fully understood. The recruitment of Cln7 to the SSR and the coupling of Cln7 to the site of insulin signal transduction together may suggest a role for post-synaptic insulin signalling in NMJ development. As such it would be interesting to investigate the distribution and activity of insulin receptors around the NMJ.

Most leads were predicted to be ubiquitously expressed across all cell types within the *Drosophila* nervous system. This is likely due to their identification within non-neural S2 cells, thus leads were unlikely to be expressed by specific cell types. By extension, this also means that the roles for leads within the nervous system may represent mechanisms common to many cell types that have been co-opted for specialist neural functions, like for example cytoskeletal organisation. Therefore *in vitro* labelling only captures mechanisms shared between different cell lineages and not those specific to neural cell types. Hence labelling of the Cln7 interactome *in vivo* would be useful not only to validate the leads identified *in vitro*, but also to detect specialist roles for Cln7 within the nervous system.

5.3.2 *Validity of lead identification*

It is important to consider factors that may have contributed to false positive identification in order to make balanced conclusions. The promiscuity of BioID labelling is a fundamental feature of the technique, but is also its own limitation. The labelling frequency of a target protein is governed by an inverse relationship between labelling probability and the average labelling distance over a length of time. Labelling probability is adjusted by parameters that influence reaction kinetics, including probe generation rate, concentration,

reactivity, half-life and substrate availability. In turn, the average distance to any target protein is determined by protein dynamics that describe both the labelling enzyme and the target protein, such as protein abundance, localisation, rate of movement within and between cellular compartments and microdomains, and stimuli that modulate any of these factors. The effect of these factors combined can be imagined as a diminishing probability distribution at greater labelling distances rather than a homogenous area-of-effect with a definite boundary. Since the probability of any one labelling event cannot be calculated, it is assumed that proteins more frequently labelled are more likely to be in closer proximity for greater periods of time. Thus, the filtering criteria of PSMs ≥ 5 was enforced as a critical condition during lead identification to promote the capture of proteins that were more likely to be true positives.

A potential limitation of the experimental paradigm here was the constant over-expression of Myc-BioID and Myc-BioID-Cln7 transgenes, compounded by the constitutive labelling by BioID with trace levels of biotin in the media. Together, these create an unlimited labelling window, providing greater opportunity for unlikely labelling events to occur. Cells, and their proteins, therefore likely exist in a state of biotinylation equilibrium. Moreover, BioID likely begins labelling as soon as it is translated and properly folded. Importantly for Myc-BioID-Cln7, this includes co-translational labelling while BioID is tethered to ribosomes awaiting the completion of Cln7 translation. This may explain why ribosomal proteins were so densely labelled by both proteins, and also provides frequent opportunities to label normally more distal proteins. Nuclear proteins were also richly labelled, yet they should be largely protected from both BioID and BioID-Cln7. However nuclear proteins become exposed to the cytosol when the nuclear envelope degrades during mitosis. An unlimited labelling window therefore limits the protection of nuclear proteins from biotinylation. Together these factors

can reduce labelling specificity and can occlude proximal labelling in unfiltered datasets. To address these issues, an enrichment factor was implemented as the second critical condition whereby proteins were required to be labelled at least twice more frequently by BioID-Cln7 than by BioID alone. This simple yet effective condition removed background biotinylation, including proteins occasionally labelled by chance through diffusion close to BioID-Cln7.

After filtering, a remarkable enrichment of biotinylated proteins at the cytoskeleton in BioID-Cln7 samples was achieved. Even cytosolic labelling was mostly attributed to chico, which associates with the insulin receptor at the plasma membrane. However an outstanding question is whether the more abundant labelling of cytoskeletal and membrane-associated proteins was due to interactions with Cln7, or through labelling bias alone because BioID-Cln7 localises to those compartments. To distinguish between these two possibilities, the expected outcomes for each scenario were compared to the observed outcome. Random labelling of proteins enriched within these compartments would argue a scenario where BioID-Cln7 is randomly distributed and that the probability of labelling any one protein is largely influenced its abundance. However this does not accurately describe the leads identified by BioID-Cln7. For example, one of the leads present at the cytoskeleton was α-Spec, an integral part of the actin-spectrin cytoskeleton. However its equally exposed and obligate binding partner β-spectrin was not once identified in the entire unfiltered dataset. Furthermore, actin was nearly equally labelled by both BioID-Cln7 and BioID alone with an enrichment factor of 1.05. These suggest that cytoskeletal proteins were not more frequently labelled by BioID-Cln7 solely due to their concentration at the plasma membrane, arguing instead that these proteins may interact with Cln7, either directly or in a complex. One way to test this further would be to tag BioID to an unrelated plasma membrane protein, ideally one of similar size, topology and

expression, for example another MFS transporter. The addition of this control would allow the subtraction of labelling bias toward proteins enriched at the plasma membrane.

5.3.3 *Verification of putative protein interactions*

Proximity labelling technologies were developed to overcome pitfalls with classic affinity-based techniques that require the retention of protein-protein interactions during extraction. However proximity labelling tags proteins within a short range that may not necessarily interact with the protein of interest. To verify physical interactions with candidate proteins, targeted affinity based techniques may be used such as directly probing by Western blot after co-immunoprecipitation as opposed to mass spectrometry. However this logic is circular since the very reason for using proximity labelling here was due to difficulties with affinity purification. One solution may be to chemically cross-link protein complexes before purification to capture transient or weak interactions without the need to preserve native conditions. This would not distinguish between direct or indirect interactions, but it would exclude proximal proteins that do not interact. Alternatively, the colocalisation of candidate proteins may be tested by immunofluorescence-based techniques, such as FRET, but this only provides evidence of protein proximity. With soluble proteins a yeast two hybrid (Y2H) approach can be used, where a transcription factor is split into DNA binding and transcription activation domains and fused separately to two candidate proteins. Binding between the proteins is detected by the expression of a reporter gene. However Cln7 is a membrane protein which precludes the use of this technology. An indirect genetic enhancer suppressor screen may be employed to test genetic interactions with candidate proteins. This gives no

direct evidence of protein interactions, but determines whether two proteins function within the same pathway and therefore provides biological context that makes a physical interaction more plausible. Lastly, additional proximity labelling experiments may be performed to cross-confirm putative interactions. Here, candidate proteins were identified by *in vitro* labelling to be examined by *in situ* labelling within *Drosophila* tissues. Proteins identified in both systems are more likely to interact.

5.3.4 *Improvements to proximity labelling*

The identification of protein-protein interactions by proximity labelling is a relatively new technique and is mainly performed using APEX2 or BioID. The advantages of APEX2 are the temporal control and speed of protein labelling, tagging sufficient protein for identification by mass spectrometry in as little as 1 min. Attempts at *in vitro* APEX2 labelling here were met with limited success, with protein biotinylation detected by immunofluorescence but failure to enrich biotinylated proteins on streptavidin beads. *In vivo* labelling with APEX2 is likely even more challenging due to poor probe solubility and penetration and H_2O_2 toxicity to tissues. On the other hand, BioID is a more straightforward and non-toxic approach, but temporal control is limited by slow kinetics.

Significant improvements to BioID labelling have been made since its inception in 2012 (415). In 2016, an improved enzyme named BioID2 was developed by the same group (499). BioID2 was engineered from a smaller biotin ligase from *A. aeolicus* lacking the DNA-binding domain in BioID from *E. coli*. The omission of this domain reduced the size by 38% from 321 to 233 amino acids (by comparison, GFP has 238 amino acids). N-terminal BioID2 fusions

demonstrated improved localisation to target sites and required 16-fold less biotin (50 µM to 3.2 µM) to achieve maximal labelling after 16 h. Interestingly, labelling by both BioID and BioID2 was detected with just trace biotin present in culture media (likely from the serum), consistent with observations made here. The improved K_M makes BioID2 more suitable for *in vivo* labelling where it is likely more difficult to deliver sufficient biotin to target tissues than with *in vitro* cultures. One potential pitfall however is that maximal biotinylation by BioID and BioID2 is achieved at 37 and 50 °C, respectively. While both enzymes perform similarly at 37 °C, biotinylation drops to around 20% for BioID and 40% for BioID2 at 25 °C. Typically, S2 cells are cultured at 27 °C and *Drosophila* are reared at 25 °C. The productivity of these enzymes are therefore substantially reduced within insects *in vitro* and *in vivo*.

In 2018, BioID was further improved by directed evolution (500). After screening 12 libraries of ~10^7-10^8 clones over 29 rounds of selection, the authors engineered the enzymes TurboID and miniTurbo. Relative to wild-type BirA, TurboID held 15 mutations and miniTurbo held 13 mutations with additional deletion of the N-terminal domain. These enzymes were capable of far superior labelling kinetics compared to BioID, achieving 15 (miniTurbo) to 23-fold (TurboID) greater yields after 18 h. In fact, TurboID was capable of generating similar levels of biotinylated protein within 10 min as BioID after 18 h. MiniTurbo on the other hand was approximately 2-fold less active than TurboID, but was less active in the absence of biotin supplementation and therefore offers greater temporal resolution. Crucially, the applicability of these enzymes for *in vivo* labelling was tested. Both flies and worms expressing TurboID contained substantially more biotinylated protein compared to BioID. When raised on food supplemented with biotin, animals expressing miniTurbo also generated significantly more

biotinylated protein than BioID. Enough biotinylated protein was generated by both enzymes to give strong signal by Western blot and *in situ* by immunohistochemistry.

It may be difficult to control proximity labelling with temporal precision by controlling biotin supplementation alone. Firstly, low level endogenous biotin generates background biotinylation that requires subtraction. Secondly, the labelling window would need to be extended to allow sufficient time for biotin absorption and distribution to target tissues. The advantage of fly genetics is that this can be overcome by timing transgene expression instead. Conditional expression of TurboID using the temperature sensitive Gal80 (tsGal80) and switching from 18 °C (inactive) to 29 °C (active) would more precisely time protein biotinylation. The increased temperature provides the additional advantage of enhanced TurboID activity. Alternatively, a GeneSwitch Gal4 system may be used to induce TurboID expression with dietary steroid intake. These inducible systems therefore combine more precise temporal control with the superior labelling activity of TurboID.

It would be interesting to compare the dependence on biotin concentration between BioID, BioID2 and TurboID. The activity of TurboID across a biotin concentration gradient was not reported. The promiscuity of BioID originates from a 450-fold reduced affinity for the reactive intermediate biotinoyl-5'-AMP, thus under biotin saturation the assumption is that its release is the rate-limiting factor. This would account for differences between BioID and TurboID, but not necessarily BioID2 which has a similar yield to BioID but does so with ~16-fold less biotin. The increased productivity of TurboID may in fact increase the biotin demand. These are important considerations because high biotin demand may hinder yield within *in vivo* systems where control over biotin concentration is limited; indeed, the reduced demand

for biotin was the very advantage of BioID2. TurboID was engineered using BioID from *E. coli*, whereas BioID2 was engineered from a smaller ligase from *A. aeolicus*. It would be interesting to see if equivalent mutations in TurboID can be made to BioID2 to combine the advantages of both systems.

5.3.5 *Conclusions*

The aims for this chapter were to generate tools and establish methodologies for *in vitro* and *in vivo* proximity labelling of the Cln7 interactome. *In vitro* BioID labelling reliably and robustly resulted in protein biotinylation that was detectable by Western blot and immunofluorescence. A total of 201 proteins labelling by BioID-Cln7 were identified by HPLC-MS/MS, which was reduced to 17 through a set of *in silico* exclusion criteria. Labelling density of the remaining 17 leads primarily localised to the cytoskeleton, in addition to the plasma membrane and exocytic vesicles. Literature searching identified common roles in cytoskeleton organisation which regulate synaptic plasticity at the NMJ and in photoreceptors and axon growth and guidance of mushroom body neurons. *Cln7*^{84D} flies display synaptic undergrowth at NMJ and in functional deficits within photoreceptors, thus a role for Cln7 in synaptic plasticity at these tissues is plausible. To cross-examine these findings *in vivo*, a genetic line encoding UAS-Myc-BioID-Cln7 has been generated. Preliminary data show that Myc-BioID-Cln7 correctly localises to the sub-synaptic space at the NMJ when expressed in muscles. Further optimisation such as protein enrichment by streptavidin pull-down may be required to facilitate the detection of biotinylated proteins.

6 DISCUSSION

6.1 Regulation of TORC1 by Cln7

The rapamycin-induced delay to *Drosophila* development was greater in *Cln7*^{84D} flies than in *w*^{1118} controls, suggesting that *Cln7*^{84D} flies were sensitised to rapamycin and therefore have a reduced pool of active TORC1 during development. Consistent with this, the activation of mTORC1 by growth factors was impaired in CLN7$^{-/-}$ MEFs. Shortly following these observations, a paper was published reporting that mTORC1 reactivation is indeed impaired in CLN7$^{-/-}$ MEFs, but by a different mechanism (383). Danyukova *et al*. observed mTORC1 reactivation after 8-12 h starvation without nutrient stimulation in WT MEFs, but was reduced in CLN7$^{-/-}$ MEFs. This represents mTORC1 reactivation by ALR, whereby the liberation of amino acids by autophagy stimulates nutrient sensing mechanisms, which recruit and reactivate mTORC1 in the absence of exogenous nutrient supply. In contrast, here cells were primed by starvation for 24 h and mTORC1 activation was assessed following a 1 h nutrient recovery. This does not measure mTORC1 reactivation by ALR, but instead measures the integrity of growth factor signalling and nutrient sensing mechanisms to promote mTORC1 activation. Interestingly, Danyukova *et al*. observed no defect in mTORC1 activation when amino acids were re-supplied, however they did not test the responsiveness to growth factors (383). In line with this, I also show that amino acid sensing is unaffected, but that impaired mTORC1 activation may be due to defects in RTK signal transduction. Indeed, impaired MAPK activation was also observed, suggesting that this defect may be common to both pathways.

It was recently reported that CLN7-deficient lysosomes show greater perinuclear distribution under basal conditions and have impaired anterograde transport (383, 384).

Interestingly, lysosome tubulation after starvation was reduced in CLN7$^{-/-}$ MEFs, suggesting there may be a defect in lysosome reformation by ALR (383). However, neither mTORC1 reactivation by ALR nor lysosome tubulation were observed in WT or CLN7$^{-/-}$ cerebellar neurons (384). The authors show that this is not due to impaired autophagy, which agrees with our observation that *Cln7*^{84D} flies do not accumulate undegraded p62 (unpublished data). There is evidence that autophagy is not induced by starvation within brain tissues (501), in which case perhaps mTORC1 reactivation and ALR are not neuronal responses to starvation because autophagy is not induced to liberate nutrients in bulk. Critically, this brings into question whether impaired autophagy-dependent reactivation of mTORC1 and/or ALR in only some CLN7$^{-/-}$ tissues are pathologically relevant.

As a distinction, post-starvation mTORC1 activation by growth factors is independent of autophagy. Since the responsiveness to exogenous amino acids was intact in CLN7$^{-/-}$ MEFs, mTORC1 recruitment to lysosomes is likely unaffected. Thus the reduced mTORC1 activity in CLN7$^{-/-}$ MEFs likely represents a defect in signalling from the plasma membrane to the lysosome. One possibility is that greater perinuclear clustering sequesters lysosomes from active signals at the plasma membrane. Previous studies have shown that forcing lysosomes to redistribute to peripheral or perinuclear regions is alone sufficient to enhance or dampen mTORC1 activity, respectively (86). Indeed, loss of CLN7 causes lysosomes to cluster within the perinuclear region (383). Alternatively, CLN7 may regulate mTORC1 by interacting with signalling molecules upstream.

6.2 Placing Cln7 in the TORC1 signalling pathway

In co-transfected S2 cells, Cln7 and Rheb co-immunoprecipitated in a complex (Figure 5.1A) and were shown to co-localise by immunofluorescence (Figure 5.1B), suggesting that Cln7 may regulate mTORC1 activation via Rheb. However, there are caveats to these observations. Firstly, both proteins were overexpressed and, as membrane/membrane-associated proteins, there is limited space for both proteins to distribute. Thus, the co-localisation of Cln7 with Rheb may have been due to space restrictions on membranes. Indeed, a significant proportion of Cln7 was trafficked to the plasma membrane, not to lysosomes (Figure 5.1B). Interestingly though, Rheb is inserted into membranes by acylation and as such does not require sorting through the secretory pathway, yet Rheb was observed to cluster with Cln7 into discreet domains, suggesting that Rheb may be recruited by Cln7.

Secondly, a very small proportion of Rheb co-precipitated with Cln7 and vice versa, which may be interpreted as a low fractional occupancy or a weak or transient interaction (Figure 5.1A). As with many technologies, a significant issue with detecting low signal is enhanced background, and a narrowed threshold to distinguish between the two. In this context, this would represent detecting non-specific pull-down of co-precipitating protein. As a negative control, the absence of precipitating protein precluded the pull-down of co-precipitating protein. Thus, to argue that the interaction is non-specific is to argue that the interaction is an artefact of overexpression. This is thermodynamically unlikely. In equilibria, the dissociation constant (K_d) is not affected by changing substrate concentrations. Importantly, this implies that the ratio of free:bound proteins does not change, unless there

is an additional event that changes protein properties, for example misfolding or aggregation. Therefore, the co-precipitation of Cln7 and Rheb is unlikely an artefact of overexpression.

Seeking validation of the Cln7-Rheb complex, native immunoprecipitation of FLAG-Venus-Cln7 (FVCln7), a CRISPR knock-in, from *Drosophila* tissues was performed. However this was met with significant technical issues and the purification of full-length FVCln7 was unsuccessful. Instead, a proximity labelling approach was taken using BioID-Cln7. The details of BioID labelling are discussed later, but Rheb was not detected in BioID-Cln7 samples. In addition, no other components of the lysosomal TORC1 recruitment machinery, such as the Rag GTPases, were identified. Thus, proximity labelling failed to detect an interaction between Cln7 and Rheb directly, or indirectly with known members of the lysosomal mTORC1 signalling complex.

Interestingly, chico, the insulin receptor substrate in *Drosophila*, was identified with high confidence in BioID-Cln7 samples. With a labelling density of 4.5 PSMs/10 kDa, chico was the third most densely labelled protein amongst 19 filtered leads (Table 6.1, Figure 6.18). However, it is important to consider the context of this interaction carefully. When overexpressed, BioID-Cln7, like Cln7 alone, localised predominantly to the plasma membrane (Figure 6.6). Therefore, the plasma membrane is likely the primary location for BioID labelling during steady state, but additional labelling will occur during trafficking. It was discussed in the previous chapter that BioID shows significant specificity for proximal proteins; for instance, α-spectrin was detected with an enrichment factor of 8.1, while actin had an enrichment factor of 1.05, and β-spectrin and tubulin proteins were completely absent. Thus, localisation of overexpressed BioID-Cln7 to the plasma membrane does not facilitate the

labelling of all proteins within or adjacent to the membrane, favouring the alternative conclusion that Cln7 putatively interacts with chico.

The next consideration is that Cln7 is natively a lysosomal protein, while chico binds the insulin receptor at the plasma membrane. Lysosomes are motile compartments, and lysosomes reposition to the cell periphery during conditions that favour growth, such as abundant nutrient supply. As proof of concept, lysosomes interact with cell membranes during lysosome exocytosis, where lysosomes dock and fuse with the plasma membrane. While an extreme example, it supports the notion that an interaction between a lysosomal protein (Cln7) and a plasma membrane-associated protein (chico) is possible. Alternatively, the activity of cell surface receptors is known to be regulated by endocytosis for degradation within lysosomes. There is evidence that endocytosis of receptors can briefly enhance signalling, potentially by sequestering growth factors and clustering receptors into vesicles that function as self-contained signalling compartments (8). In this system, Cln7 and chico may interact within endosomes during receptor trafficking.

An interaction between Cln7 and chico suggests that Cln7 could regulate insulin signalling at the receptor level. This is consistent with the finding that both MAPK and mTORC1 activity is reduced in CLN7$^{-/-}$ MEFs (Figure 3.6). An interesting speculation is that Cln7 functions as a nutrient transporter within nutrient-sensing machinery. The hydrophobic amino acid transporter SLC38A9 is known to function in this capacity, sensing intraluminal arginine to trigger RagA/B activation (165). However it would be difficult to test this directly without knowing the substrate for Cln7 transport. Instead, I have generated a *chico*^{1}*/CyO; Cln7*^{84D} line for follow-up testing of a genetic interaction in *Drosophila*.

6.3 Defective sphingolipid metabolism

In an unbiased lipidomic screen of adult *Cln7*^{84D} flies, a remarkable defect in sphingolipid metabolism was identified. As an LSD, evidence of perturbations to sphingolipid degradation in NCL7 is particularly interesting because the sphingolipidoses are a class of LSDs in their own right, all of which with primary defects in sphingolipid degradation. Several enzymes are required to hydrolyse diverse glycosphingolipid structures, one residue at a time, and mutations to any one of these enzymes causes a unique disease. The existence of these diseases argue that, in principle, defects in sphingolipid metabolism can cause LSD and neurodegeneration. In addition, the secondary accumulation of sphingolipids has been reported amongst several other LSDs, including Niemann-Pick type C, glycoproteinoses, mucolipidoses and mucopolysaccharidoses (502). Concerning the NCLs, a depletion of sphingomyelin, ceramides, and galactosylceramide in NCL8 patients (358, 359), and accumulation of GM3 and GM2 gangliosides in *CLN10*$^{-/-}$ mice (317) have been observed. The finding that N4 arthrosides are depleted and Nz5 arthrosides accumulate in *Cln7*^{84D} flies is the first evidence of a defect in sphingolipid degradation in NCL7.

Interestingly, a general depletion of several lysosomal hydrolases, including the lipases $LPLA_2$ and NAAA, in CLN7$^{-/-}$ MEFs was reported in a recent study (383). $LPLA_2$ is a broad specificity phospholipase that generates lysophospholipids by cleaving the *sn*-2 fatty acyl from phospholipids (503). NAAA is an *N*-acylethanolamine acid amidase which hydrolyases *N*-acylethanolamines into ethanolamine and a fatty acid (504). As such, deficiencies in neither of these enzymes is expected to directly limit the degradation of glycosphingolipids. It is unknown whether a similar depletion of orthologous or additional lysosomal proteins is true

in *Cln7*^{84D} flies, however the observation in CLN7$^{-/-}$ MEFs provides some evidence that glycosphingolipid accumulation is unlikely to be caused by enzyme deficiency.

While lipidomic analysis identified a specific defect in sphingolipid metabolism, it is important to consider that the analysis was performed whole 1-day-old adult female flies only. Further experiments are therefore required to determine whether the same depletion of N4 arthrosides and accumulation of Nz5 athrosides is present in males. It would be interesting to characterise what stage during *Drosophila* development this defect to sphingolipid metabolism first manifests and how rapidly it progresses with age. Furthermore, it would be useful to determine which tissues the defects to sphingolipid metabolism originate from. It is possible that because the lifespan of *Drosophila* is much shorter than mice and humans, *Drosophila* do not live long enough for autofluorescent material to accumulate or for the nervous system to deteriorate when Cln7 function is lost, like they do in mammals. On the other hand, loss of Cln7 in *Drosophila* larvae limits the negative phototactic response and causes the NMJ to underdevelop, leading to defects in crawling and coordination. Therefore our model of CLN7 disease in Drosophila recapitulate two key phenotypes of mammalian disease; deterioration of the visual system and of motor function. Thus, characterising the spatiotemporal dynamics of defects sphingolipid metabolism during *Drosophila* development may help correlate changes to sphingolipid metabolism with neurological phenotypes in *Drosophila*. As such, a disruption to sphingolipid metabolism may be an early molecular event that later underpins neurodegeneration in mammalian Cln7 disease.

Another important caveat to consider is the fundamental difference in mammalian and *Drosophila* glycosphingolipids. Mammals make several distinct classes of glycosphingolipid,

determined (mainly) by the exact sequence and positioning of sugar residues. These include ganglio, globo, isoglobo, lacto, neolacto and gala series, in addition to sulphatides that are distinguished by sulphation. In contrast, *Drosophila* make only one class, the arthrosides. In fact, the only common glycosphingolipid between mammals and *Drosophila* is glucosylceramide, one of the simplest of glycosphingolipids. In addition, no reference database of *Drosophila* lipids is available for feature identification during lipidomic analysis. Therefore, a human reference database was used, which led to the misidentification of gangliosides that *Drosophila* cannot synthesise. However, metabolites are identified using both the retention time by UPLC and the accurate mass:charge ratio by MS. The separation of lipid species by UPLC is critical to distinguish between structurally unrelated metabolites that share the same mass. This also means that the misidentified GM1 and GM3 are likely to be glycosphingolipids. Thus, a nearest neighbour method was employed to predict that GM1 gangliosides corresponded to Nz5 arthrosides, and GM3 to N4. Nonetheless, as a minimum, lipidomic analysis identified a specific depletion of a mid-chain glycosphingolipid and an accumulation of a longer chain glycosphingolipid, which suggests a block in sphingolipid degradation. Based on these observations, it would be interesting to investigate changes to sphingolipid metabolism in CLN7$^{-/-}$ mouse brains, particularly in the cerebellum.

6.4 Toward predicting a substrate for CLN7

To explore evolutionary relationships between CLN7 and other MFS transporters, the amino acid sequence for CLN7 was compared to all human MFS (2.A.1) transporters by multiple sequence alignment (Figure 3.1A). However, CLN7 segregated distal to all known human MFS (2.A.1) transporters. Interestingly, phylogenetic analysis of CLN7 using a different approach was published recently (505). The authors identified 28 atypical MFS-type solute carriers (SLCs), including CLN7, plus one non-MFS SLC, CLN3, and sought to cluster these proteins into families. Consistent with the analysis presented here, the authors failed to group CLN7 with any other atypical SLC, supporting the conclusion that CLN7 may be unique human MFS transporter.

Due to lack of similarity with known human MFS (2.A.1) transporters, a comparison of CLN7 with pan-species DHA1 (2.A.1.2) transporters was made (Figure 3.1B). Again, CLN7 showed mainly distal relationships to other DHA1 transporters, with slight similarity toward tetracycline transporters. Only two transporters with known function showed greater similarity (2.A.1.2.80 and VPT1), of which 2.A.1.2.80 was another tetracycline transporter that did not cluster with the others. VPT1 is a vacuolar phosphate transporter from *Arabidopsis thaliana*, and as such localises to acidic, lysosome-like organelles similar to Cln7 (430).

Lipidomic analysis identified an accumulation of GM1 and depletion of GM3 gangliosides, which was suggested to correspond to a putative block in glycosphingolipid degradation between Nz5 and N4 arthrosides (Figure 3.11). This was suggested to cover two steps; hydrolysis of a terminal αGalNAc residue and removal of phosphoethanolamine. Not much is known about *Drosophila* glycosphingolipid synthesis or degradation past N3

arthosides; the pathway in Figure 3.11 was assembled based on biochemical analysis of the major glycosphingolipids in *Drosophila*, resembling a predominant route (506). Thus, while each molecule in the pathway has been identified empirically, the exact sequence of steps and enzymes are not known. However, arthroside synthesis and degradation pathways in *Drosophila* likely mirror the mammalian pathway with the stepwise condensation and hydrolysis of terminal residues, differing only by the positioning and sequence of residues within the chain.

Comparing the lipidomic and phylogenetic analyses, a candidate substrate for transport by CLN7 is phosphoethanolamine. The block in Nz5 to N4 degradation covers both the hydrolysis of αGalNAc and removal of phosphoethanolamine. As a membrane protein with no suggestion of hydrolase activity, CLN7 is unlikely to directly participate in the removal of these structures. Instead, a more likely scenario is that CLN7 is required for the export of the products of degradation. Phylogenetic analysis failed to detect a relationship between CLN7 and other sugar porters (Figure 3.1A/B), making αGalNAc an unattractive candidate. On the other hand, phosphoethanolamine is known to be generated within lysosomes by sphingolipid degradation, such as by the hydrolysis of sphingosine-1-phosphate into phosphoethanolamine and hexadecenal. However not much is known about how phosphoethanolamine is transported between cellular compartments. Crucially, if CLN7 functions as a transporter for the efflux of phosphoethanolamine from lysosomes, then loss of CLN7 would be expected to result in the accumulation of phosphoethanolamine within lysosomes. This accumulation of free phosphoethanolamine may in turn interfere with the hydrolysis of phosphoethanolamine residues from sphingolipids, therefore impeding their degradation. Therefore, the hypothesis that Cln7 is a transporter for phosphoethanolamine

may link Cln7 function to defective sphingolipid metabolism in *Drosophila*, which, as discussed in the previous section, may be an early molecular event that underpins neurological phenotypes in CLN7 disease.

Prompted by this, all transporters listed by the TCDB were searched using the substrate search tool for known specificity to ethanolamine or phosphoethanolamine, however no human transporters were identified. Several bacterial transporters were identified, including an ethanolamine import permase, but none were MFS (2.A.1) transporters. A wider search for transporters of the ethanolamine-related molecules serine, choline and phosphocholine was made. Only broad specificity transporters of amino acids were identified to transport serine in humans, and no MFS (2.A.1) transporters were found. In addition, five choline transporters were identified in humans, however only one was an MFS (2.A.1) transporter in synaptic vesicles belonging to the organic cation transporter 2 (OCT2, 2.A.1.19) family. Thus, although it is likely lysosomes require an efflux mechanism for phosphoethanolamine, no lysosomal transporters of phosphoethanolamine, or related molecules, have been characterised.

6.5 A role for Cln7 in synaptic plasticity

Proximity labelling with BioID was used to investigate protein-protein interactions with Cln7. *In vitro* labelling led to the identification of 201 hits in unfiltered BioID-Cln7 samples, covering proteins that were heterogenous in their cellular distribution. These hits were filtered to 19 leads using internal quality scores, which uncovered high labelling densities at the cytoskeleton and at the plasma membrane/juxtamembrane space. BioID-Cln7 localises to the plasma membrane at steady state, thus labelling within these regions corresponds with BioID-Cln7 localisation. Chico, the *Drosophila* insulin receptor substrate, was the third-most densely labelled lead, placing Cln7 early within the insulin signalling pathway. Interestingly, Frl, hts and α-Spec are cytoskeletal proteins with known roles in cytoskeletal remodelling and synaptic plasticity. In addition, cora is enriched at the *Drosophila* NMJ PSD and anchors GluRIIA to active synapses. In *Drosophila*, Cln7 is expressed in body-wall muscles and localises to the sub-synaptic reticulum beneath the NMJ PSD (402). This places Cln7 at the site where Frl, hts, α-Spec, cora are reported to function *in vivo*. To investigate whether Cln7 interacts with these proteins *in vivo*, transgenic lines encoding UAS-BioID-Cln7 were generated for proximity labelling at the NMJ *in situ*. BioID-Cln7 correctly localises to the NMJ sub-synaptic reticulum when expression is driven using Mef2-Gal4, however further optimisation is required to facilitate protein biotinylation. Recent improvements in BioID technology have resulted in the development of TurboID and miniTurbo, which were shown to efficiently label proteins in *Drosophila*, within a shorter time frame and at physiological concentrations of biotin (500). Thus, to facilitate protein labelling *in vivo* and corroborate the *in vitro* data here, it may be necessary to generate transgenic TurboID-Cln7 and/or miniTurbo-Cln7 lines.

6.6 Conclusions

In mammals, CLN7 disease targets neurons within the cerebral and cerebellar cortices and photoreceptors. Lipofuscin accumulates within photoreceptors and the granule cell layer at early stages, suggesting that lysosomal dysfunction is an early event in the disease. The disease progresses with thinning of the retina and large scale loss of granule and Purkinje cells within the cerebellum, in addition to widespread activation of astroglia and microglia. Thus, characterising the molecular events that underpin early lysosomal dysfunction will be instrumental not only in understanding the cause of CLN7 disease, but also in elucidating a fundamental role for lysosomes in the development and function of the nervous system. Using *Drosophila* to model CLN7 disease, I made three key discoveries.

Firstly, loss of Cln7 results in a profound defect in sphingolipid metabolism that is likely due to a block in sphingolipid degradation. Primary defects in sphingolipid degradation are known causes of other LSDs, thus the discovery of a similar defect in CLN7 disease is an exciting discovery. By comparing lipidomic and phylogenetic analyses, I also propose phosphoethanolamine to be a candidate substrate for transport by CLN7. As an MFS transporter, the primary function of CLN7 is likely to be the efflux of products generated by lysosomal degradation for recycling in the cell and to prevent toxic accumulation within the lysosome. Therefore, the characterisation a substrate for CLN7 will be crucial in advancing our understanding of Cln7 function.

Secondly, loss of CLN7 disrupts mTORC1 signalling *in vitro* and *in vivo*. By close comparison between the data here and those recently published (383), I suggest that reduced mTORC1 activity originates from an upstream signalling defect and not from diminished amino

acid sensing by lysosomes. Specifically, chico, the *Drosophila* insulin receptor substrate, was identified as a putative interactor of Cln7. mTORC1 is a central regulator of several lysosomal functions, including switching between anabolic and catabolic states, repositioning of lysosomes and lysosome biogenesis. Disrupted mTORC1 signalling therefore likely uncouples lysosomal adaptation to a changing environment, and may therefore diminish lysosomal function within the developing nervous system.

Lastly, I developed tools for *in vitro* and *in vivo* labelling of the Cln7 interactome, and established *in silico* criteria for the filtering of hits identified by HPLC-MS/MS. *In vitro* proximity labelling experiments identified several proteins within the cytoskeleton that have known roles in synaptic plasticity *in vivo*. These proteins, namely Frl, hts, cora and α-Spec, are structural components within the PSD of the *Drosophila* NMJ that remodel the actin-spectrin cytoskeleton and cluster neurotransmitter receptors to match and consolidate synapses in growing pre and post-synaptic compartments. Remarkably, these proteins were identified *in vitro* in an embryonic cell line of ambiguous lineage, yet they localise and function *in vivo* at precisely the location that Cln7 is recruited to within the post-synaptic cell. These findings suggest a role for Cln7 in synaptic plasticity in the developing *Drosophila* nervous system, and may underpin the synapse undergrowth phenotype observed in wandering L_3 $Cln7^{84D}$ larvae. This raises two interesting questions; firstly, do lysosomes regulate synaptic plasticity, and secondly, is NCL7 a disease of dysfunctional synapses (a synaptopathy)? Indeed, CLN7 is recruited to pre-synaptic terminals in mouse photoreceptors, and are amongst, if not *the* first tissue to degenerate when CLN7 is deleted (373, 381). Therefore, it would be interesting to characterise the Cln7 interactome both at the *Drosophila* NMJ and within photoreceptors to potentially characterise a disease-relevent role for CLN7 in synaptic plasticity.

7 APPENDIX – LIST OF HITS FROM BIOID LABELLING

Table 7.1. Hits unique to BioID-Cln7 samples with ≥ 5 PSMs detected

UNIQUE HITS WITH 5+ PSMs
BIOID-CLN7

Accession	Description	PSMs	PSMs/ kDa*10	Coverage (%)	# biotin tags	# expts	Mass (kDa)	Localisation
P18489	Synaptobrevin	5	3.0	23	1	2	16.7	PM
P23647	Serine/threonine-protein kinase fused	6	0.7	1	0	2	90.3	Cytosol
Q24247	Integrin alpha-PS1	5	0.4	4	0	2	128.0	PM
Q4Z8K6	Ran-binding proteins 9/10 homolog	10	0.9	3	2	1	106.7	Membrane/ Cytoplasm/ Nucleus
Q9VKA5	Gustatory and pheromone receptor 33a	6	1.1	3	2	1	54.6	PM
P08111	Lethal(2) giant larvae protein	51	4.0	27	0	1	126.9	PM/secreted
Q9XTN2	Insulin receptor substrate 1	49	4.5	33	0	1	107.8	PM/cytosol/ nucleus
Q9V8R9	Protein 4.1 homolog	47	2.6	31	0	1	184.2	Septate junction
P13060	Elongation factor 2	15	1.6	18	0	1	94.5	Ribosome
P49630	60S ribosomal protein L36	9	6.7	29	0	1	13.5	Ribosome
P13217	1-phosphatidylinositol 4,5-bisphosphate phosphodiesterase	7	0.6	7	0	1	124.9	PM
O62619	Pyruvate kinase	7	1.2	16	0	1	57.4	Cytosol
Q9VDS5	Rho GTPase-activating protein 92B	5	0.6	6	0	1	83.1	Cytoplasm
P48159	60S ribosomal protein L23	5	3.4	30	0	1	14.9	Ribosome
P46223	60S ribosomal protein L7a	5	1.6	6	0	1	30.7	Ribosome

Table 7.2. Hits unique to BioID samples with ≥ 5 PSMs detected

UNIQUE HITS WITH 5+ PSMs
BIOID

Accession	Description	PSMs	PSMs/ kDa*10	Coverage (%)	# biotin tags	# expts	Mass (kDa)	Localisation
P08928	Lamin Dm0	12	1.7	19	0	2	71.3	Nucleus
Q9VL18	Probable elongation factor 1-delta	2	0.7	9	0	2	28.9	Ribosome
Q8INM3	Protein slender lobes	19	1.2	15	0	1	158.7	Nucleolus
Q9VVI2	Enhancer of mRNA-decapping protein 3	8	1.1	11	0	1	73.4	P-body
Q94920	Voltage-dependent anion-selective channel	7	2.3	31	0	1	30.6	Mitochondria
P39736	Puff-specific protein Bx42	7	1.1	15	0	1	61.2	Nucleus
Q86S05	Protein lingerer	6	0.4	6	0	1	139.5	Cytoplasm
P13469	DNA-binding protein modulo	5	0.8	11	0	1	60.3	Nucleus
Q9VH07	RuvB-like helicase 1	5	1.0	14	0	1	50.2	Nucleus

Table 7.3. Hits unique to BioID-Cln7 samples with < 5 PSMs detected

UNIQUE HITS WITH <5 PSMS
BIOID-CLN7

Accession	Description	PSMs	PSMs/ kDa*10	Coverage (%)	# biotin tags	# expts	Mass (kDa)	Localisation
Q9VMJ7	Lysine-specific demethylase lid	3	0.1	1	0	2	204.0	Nucleus
P11584	Integrin beta-PS	1	0.1	1	0	2	92.7	PM
P36975	Synaptosomal-associated protein 25	1	0.4	7	0	2	23.7	Synaptosome
P84236	Histone H3	1	0.6	9	0	2	15.4	Nucleus
Q7K3B9	Methyltransferase-like protein 16 homolog	1	0.3	2	2	1	35.1	Nucleus
Q9VK89	Probable tRNA (guanine(26)-N(2))-dimethyltransferase	3	0.5	3	1	1	65	Nucleus
Q7K4B4	Augmin complex subunit dgt5	2	0.3	2	1	1	78	Cytoskeleton
Q9VQD2	Probable cytochrome P450 309a1	2	0.3	3	1	1	57.4	ER membrane
Q9V9L1	Probable cytochrome P450 6w1	2	0.3	3	1	1	59.3	ER membrane
P25867	Ubiquitin-conjugating enzyme E2-17 kDa	1	0.6	4	1	1	16.7	Cytosol
A8DYE2	Transient receptor potential cation channel trpm	1	0.0	1	1	1	225.5	Membrane
Q9VSL3	Pyrimidodiazepine synthase	1	0.4	3	1	1	28.4	Cytoplasm
P32392	Actin-related protein 3	1	0.2	3	1	1	47	Cytoskeleton
B3LZN3	Eukaryotic translation initiation factor 3 subunit D-2	1	0.2	3	1	1	62.2	Ribosome
Q9VGW6	DNA replication licensing factor Mcm5	1	0.1	2	1	1	82.3	Cytosol/ Nucleus
Q9VGU5	Tetratricopeptide repeat protein 14 homolog	1	0.1	2	1	1	99.9	Cytoplasm
Q8T3Y0	Probable E3 ubiquitin-protein ligase sinah	1	0.3	2	1	1	39.4	Nucleus
P98081	Protein disabled	4	0.2	2	0	1	243.1	Cytoplasm
Q9VVG4	Exocyst complex component 1	4	0.4	5	0	1	102.7	PM
Q95R48	Organic cation transporter-like protein	4	0.6	5	0	1	63.2	Membrane
Q9XYM0	Adapter molecule Crk	4	1.3	12	0	1	31.2	Cytoplasm
Q9W237	40S ribosomal protein S16	4	2.4	28	0	1	16.8	Ribosome
Q8T3U2	40S ribosomal protein S23	4	2.5	28	0	1	16.0	Ribosome
P08985	Histone H2A.v	4	2.7	25	0	1	15.0	Nucleus
P48588	40S ribosomal protein S25	4	3.0	29	0	1	13.2	Ribosome
P48375	12 kDa FK506-binding protein	4	3.4	37	0	1	11.7	Cytoplasm
P25007	Peptidyl-prolyl cis-trans isomerase	4	1.6	11	0	1	24.7	Cytoplasm
P13607	Sodium/potassium-transporting ATPase subunit alpha	3	0.3	3	0	1	115.6	PM
P31007	Disks large 1 tumor suppressor protein	3	0.3	4	0	1	106.7	PM/ cytoskeleton
Q9VKJ9	Coiled-coil and C2 domain-containing protein 1-like	3	0.3	4	0	1	89.0	Cytoplasm
Q23983	Alpha-soluble NSF attachment protein	3	0.9	12	0	1	33.0	Vesicle membrane
Q9VSU7	Vesicle transport protein USE1	3	1.1	12	0	1	28.3	ER membrane
P41094	40S ribosomal protein S18	3	1.7	15	0	1	17.6	Ribosome
Q9VMU4	60S ribosomal protein L37a	3	2.9	29	0	1	10.3	Ribosome
Q9VH69	40S ribosomal protein S29	3	4.5	30	0	1	6.6	Ribosome
Q9VDW3	Dystrophin, isoform B	3	0.2	1	0	1	185.3	PM/ cytoskeleton

Accession	Description	PSMs	PSMs/ kDa*10	Coverage (%)	# biotin tags	# expts	Mass (kDa)	Localisation
P91685	Metabotropic glutamate receptor	3	0.3	1	0	1	108.5	PM
B3NY19	Molybdenum cofactor sulfurase	3	0.3	2	0	1	87.9	Unknown
Q709R6	LEM domain-containing protein Bocksbeutel	3	0.7	5	0	1	44.2	ER/Nucleus
Q9W0S9	Disco-interacting protein 2	2	0.1	1	0	1	194.2	Nucleus
Q9W1B0	Serine/threonine-protein kinase Genghis Khan	2	0.1	1	0	1	186.7	Cytoplasm
Q9I7D3	Caprin homolog	2	0.2	3	0	1	103.6	Lipid droplet
P29349	Tyrosine-protein phosphatase corkscrew	2	0.2	3	0	1	93.0	Cytoplasm
Q7KN62	Transitional endoplasmic reticulum ATPase TER94	2	0.2	3	0	1	88.9	Nucleus
B4Q9E6	Protein hook	2	0.3	4	0	1	76.7	Endosome/ cytoskeleton
Q24046	Sodium/potassium-transporting ATPase subunit beta-1	2	0.6	6	0	1	35.3	PM
P17917	Proliferating cell nuclear antigen	2	0.7	8	0	1	28.8	Nucleus
P02255	Histone H1	2	0.8	6	0	1	26.4	Nucleus
Q9GU68	Eukaryotic translation initiation factor 5A	2	1.1	14	0	1	17.6	Ribosome
Q03334	40S ribosomal protein S13	2	1.2	11	0	1	17.2	Ribosome
B3MLA8	40S ribosomal protein S21	2	2.2	23	0	1	9.2	Ribosome
Q9W334	40S ribosomal protein S28	2	2.7	32	0	1	7.5	Ribosome
Q9VM75	HEAT repeat-containing protein 1 homolog	2	0.1	0	0	1	237.2	Nucleolus
O18475	DNA polymerase theta	2	0.1	0	0	1	229.9	Nucleus
P91875	DNA-directed RNA polymerase I subunit RPA1	2	0.1	1	0	1	185.4	Nucleolus
Q6NN85	Protein phosphatase Slingshot	2	0.2	1	0	1	115.0	Cytoskeleton
P12297	Protein suppressor of white apricot	2	0.2	1	0	1	106.1	Nucleus
Q7KVW5	Small conductance calcium-activated potassium channel protein	2	0.2	3	0	1	101.9	Membrane
B3NAN8	DNA repair and recombination protein RAD54-like	2	0.2	2	0	1	89.5	Nucleus
Q6WV20	Polypeptide N-acetylgalactosaminyltransferase 1	2	0.3	4	0	1	69.0	Golgi
Q9GYV5	NF-kappa-B essential modulator	2	0.5	2	0	1	43.9	Cytoplasm/ nucleus
Q6XHI1	Thioredoxin-2	2	1.7	10	0	1	11.7	Nucleus
Q24154	60S ribosomal protein L29	2	2.2	14	0	1	8.9	Ribosome
Q9VPL3	39S ribosomal protein L10, mitochondrial	2	0.7	2	0	1	28.3	Mitochondria
Q9VLT5	Protein purity of essence	1	0.0	0	0	1	590.7	P granule
Q9VEU1	Cadherin-89D	1	0.0	0	0	1	250.6	PM
B3MFV7	Latrophilin Cirl	1	0.1	1	0	1	188.7	PM
Q9NBD7	CLIP-associating protein	1	0.1	1	0	1	165.6	Cytoskeleton
Q8MT36	Probable histone-lysine N-methyltransferase Mes-4	1	0.1	2	0	1	159	Nucleus
P25455	1-phosphatidylinositol 4,5-bisphosphate phosphodiesterase classes I and II	1	0.1	1	0	1	146.4	Cytoplasm
P20241	Neuroglian	1	0.1	1	0	1	143.6	PM/ tight junction
P13496	Dynactin subunit 1	1	0.1	1	0	1	141.2	Cytoskeleton
Q0KHQ5	Serine/threonine-protein kinase Tao	1	0.1	1	0	1	118.3	Cytoskeleton

Accession	Description	PSMs	PSMs/ kDa*10	Coverage (%)	# biotin tags	# expts	Mass (kDa)	Localisation
Q23978	Myosin-IA	1	0.1	1	0	1	117.1	Cytoplasm
P45437	Coatomer subunit beta	1	0.1	1	0	1	107.4	Golgi
P18091	Alpha-actinin, sarcomeric	1	0.1	1	0	1	107.0	Z line
P91926	AP-2 complex subunit alpha	1	0.1	1	0	1	105.6	PM
Q9V4Z9	Protein lines	1	0.1	1	0	1	96.3	Cytoplasm/ nucleus
P08155	Krueppel homolog 1	1	0.1	1	0	1	91.5	Nucleus
Q9W4S7	Myc protein	1	0.1	3	0	1	79.3	Cytoplasm/ nucleus
Q9W1F4	THO complex subunit 5	1	0.1	1	0	1	70.9	Cytoplasm/ nucleus
Q8SX68	Uncharacterized protein CG10915	1	0.2	2	0	1	65.4	Unknown
Q9VVB4	Coiled-coil domain-containin protein 22 homolog	1	0.2	1	0	1	63	Unknown
P54385	Glutamate dehydrogenase, mitochondrial	1	0.2	1	0	1	62.5	Mitochondria
Q9VLU4	Serine protease inhibitor 28Dc	1	0.2	2	0	1	59.4	Secreted
P33085	Innexin shaking-B	1	0.2	2	0	1	44.4	PM/ gap junction
Q9VPD5	Transcription termination factor 3, mitochondrial	1	0.2	2	0	1	41.3	Mitochondria
P48603	F-actin-capping protein subunit beta	1	0.3	3	0	1	31.4	Cytoskeleton
Q9VHD3	Probable maleylacetoacetate isomerase 1	1	0.4	5	0	1	27.9	Cytoplasm
Q9VQE5	Probable proteasome subunit beta type-2	1	0.4	3	0	1	23.7	Cytoplasm
Q9I7K0	Microtubule-associated protein Jupiter	1	0.4	4	0	1	22.3	Cytoskeleton
Q4V4I9	Neuropeptide CCHamide-1	1	0.5	5	0	1	20.5	Secreted
Q8MS27	39S ribosomal protein L35, mitochondrial	1	0.5	5	0	1	20.0	Mitochondria
O76206	Putative riboflavin kinase	1	0.6	7	0	1	17.0	Cytoplasm
A1ZB42	Mediator of RNA polymerase II transcription subunit 9	1	0.6	5	0	1	16.8	Nucleus
P62152	Calmodulin	1	0.6	6	0	1	16.8	Cell cortex
C0HKA0	40S ribosomal protein S14a	1	0.6	7	0	1	16.3	Ribosome
Q9VF08	Mitochondrial import inner membrane translocase subunit Tim16	1	0.6	8	0	1	15.7	Mitochondria
P17704	40S ribosomal protein S17	1	0.7	11	0	1	15.3	Ribosome
Q6XIM8	40S ribosomal protein S15a	1	0.7	11	0	1	14.8	Ribosome
Q9V597	60S ribosomal protein L31	1	0.7	7	0	1	14.5	Ribosome
P25843	Profilin	1	0.7	7	0	1	13.7	Cytoplasm
Q9XZH6	V-type proton ATPase subunit G	1	0.7	8	0	1	13.6	PM
P55828	40S ribosomal protein S20	1	0.7	10	0	1	13.5	Ribosome
P05389	60S acidic ribosomal protein P2	1	0.8	12	0	1	11.8	Ribosome
Q9W1U6	Probable 60S ribosomal protein L37-B	1	1.0	13	0	1	10.2	Ribosome
Q9W5N2	60S ribosomal protein L38	1	1.2	14	0	1	8.2	Ribosome
Q9VXN2	Protein stunted	1	1.5	25	0	1	6.8	Secreted/ mitochondria
P13368	Protein sevenless	1	0.0	0	0	1	287	PM
Q7JRE4	Inner nuclear membrane protein Man1	1	0.1	1	0	1	73.9	Cytoskeleton/ Nucleus
Q9VDG2	RalA-binding protein 1	1	0.1	1	0	1	71.9	Membrane
P49021	Protein timeless	1	0.1	1	0	1	156.4	Nucleus
Q95029	Cathepsin L	1	0.2	2	0	1	41.6	Lysosome

Accession	Description	PSMs	PSMs/ kDa*10	Coverage (%)	# biotin tags	# expts	Mass (kDa)	Localisation
Q9VT70	Nuclear distribution protein nudE homolog	1	0.3	2	0	1	36.2	Cytoskeleton
Q9W020	Nucleolar MIF4G domain-containing protein 1 homolog	1	0.1	1	0	1	99.1	Nucleolus
Q9VS34	60S ribosomal protein L18	1	0.5	5	0	1	21.7	Ribosome
B7TB45	Neurotrophin 1	1	0.1	1	0	1	100.3	Secreted
Q9VEC1	Mediator of RNA polymerase II transcription subunit 17	1	0.1	1	0	1	71.6	Nucleus
Q9VW71	Fat-like cadherin-related tumor suppressor homolog	1	0.0	0	0	1	523.8	PM
Q9VUJ0	39S ribosomal protein L39, mitochondrial	1	0.3	5	0	1	37.3	Mitochondria
B3MZN7	Molybdenum cofactor sulfurase	1	0.1	3	0	1	86.9	Cytoplasm
P09208	Insulin-like receptor	1	0.0	0	0	1	239.8	Membrane
Q9N4M4	Nuclear anchorage protein 1	1	0.0	0	0	1	956.5	Cytoskeleton/ Nucleus
Q8INR6	Histone-lysine N-methyltransferase, H3 lysine-79 specific	1	0.0	0	0	1	201.3	Nucleus
Q8MRC9	Putative polypeptide N-acetylgalactosaminyltransferase 9	1	0.1	1	0	1	73.2	Golgi membrane
Q9VXN9	Peptidoglycan-recognition protein LE	1	0.3	2	0	1	39.4	Secreted
M9NEY8	DNA N6-methyl adenine demethylase	1	0.0	0	0	1	306.7	Nucleus
P47947	Troponin C, isoform 1	1	0.6	5	0	1	17.2	Cytoskeleton

Table 7.4. Hits unique to BioID-Cln7 samples with < 5 PSMs detected

UNIQUE HITS WITH <5 PSMS
BIOID

Accession	Description	PSMs	PSMs/ kDa*10	Coverage (%)	# biotin tags	# expts	Mass (kDa)	Localisation
P15007	Enolase	1	0.2	1	0	2	54.3	Cytoplasm
Q9VWW0	Cyclic AMP response element-binding protein B	1	0.3	3	0	2	37.9	Nucleus
Q9V3G1	60S ribosomal protein L8	1	0.4	4	0	2	27.9	Ribosome
B3P100	Protein asunder	2	0.3	2	2	1	75.6	Nucleus/ Cytoplasm
Q9VMX6	SWI/SNF-related matrix-associated actin-dependent regulator of chromatin subfamily A-like protein 1	1	0.1	2	2	1	84.6	Nucleus
Q9VLM8	Alanine--tRNA ligase, cytoplasmic	3	0.3	2	1	1	107.7	Cytoplasm
Q9VNA8	Protein downstream neighbor of son homolog	2	0.3	1	1	1	63.4	Nucleus
Q9VIE6	Protein MCM10 homolog	2	0.2	2	1	1	86.5	Nucleus
Q94519	Acyl carrier protein, mitochondrial	1	0.6	13	1	1	17.2	Mitochondria
P35220	Catenin alpha	1	0.1	1	1	1	102.4	Cytoskeleton/ PM
Q9VB26	Putative gustatory receptor 98b	1	0.2	2	1	1	46.9	PM
Q9VIF5	Protein deadlock	1	0.1	1	1	1	110.8	Nucleus/ Cytoskeleton
P19889	60S acidic ribosomal protein P0	4	1.2	15	0	1	34.2	Ribosome
Q26365	ADP,ATP carrier protein	4	1.2	12	0	1	34.2	Mitochondria IM
P29413	Calreticulin	4	0.9	8	0	1	46.8	ER
P22464	Annexin B9	3	0.8	8	0	1	36.1	Cell cortex
Q9XZJ4	Proteasome subunit alpha type-6	3	1.1	11	0	1	27.2	Nucleus
Q7K0E3	MOB kinase activator-like 4	3	1.2	14	0	1	25.7	Cytosol
Q9V3P0	Peroxiredoxin 1	3	1.4	15	0	1	21.7	Cytoplasm
Q9VYD1	Probable histone-lysine N-methyltransferase CG1716	3	0.1	1	0	1	256.8	Nucleus
P19334	Transient receptor potential protein	3	0.2	2	0	1	142.6	PM
Q9V9N1	Ionotropic receptor 40a	3	0.4	3	0	1	84.1	PM
P22769	Proteasome subunit alpha type-7-1	3	1.1	10	0	1	28.0	Cytoplasm/ nucleus
Q7KQM6	PERQ amino acid-rich with GYF domain-containing protein CG11148	2	0.1	1	0	1	173.7	Unknown
Q9W062	Microfibrillar-associated protein 1	2	0.4	6	0	1	56.1	Nucleus
Q9VL78	FK506-binding protein 59	2	0.4	5	0	1	48.8	PM
P18053	Proteasome subunit alpha type-4	2	0.7	8	0	1	29.4	Cytoplasm/ nucleus
P31009	40S ribosomal protein S2	2	0.7	7	0	1	28.9	Ribosome
Q9VR59	Inositol hexakisphosphate and diphosphoinositol-pentakisphosphate kinase	2	0.1	1	0	1	188.7	Cytosol
P04146	Copia protein	2	0.1	1	0	1	162.8	Extracellular
O96433	Cyclin-T	2	0.2	1	0	1	118.3	Nucleus
Q9VG82	Probable cytochrome P450 9f2	2	0.3	1	0	1	60.3	ER

Accession	Description	PSMs	PSMs/ kDa*10	Coverage (%)	# biotin tags	# expts	Mass (kDa)	Localisation
Q9VNE2	Protein krasavietz	2	0.4	5	0	1	49.2	Cytoplasm/ axon/ filopodia
Q02748	Eukaryotic initiation factor 4A	2	0.4	4	0	1	45.9	Ribosome
B3N6U7	Protein crossbronx	2	0.7	5	0	1	28.1	Nucleus
Q9VTP4	60S ribosomal protein L10a-2	2	0.8	10	0	1	24.3	Ribosome
P02517	Heat shock protein 26	2	0.9	10	0	1	23.0	Cytoplasm
A1Z8P9	Nucleoprotein TPR	1	0.0	0	0	1	262.4	Nuclear pore complex
Q9W517	Protein wings apart-like	1	0.1	1	0	1	185.2	Nucleus
Q9V3C5	Guanine nucleotide exchange factor subunit Rich	1	0.1	1	0	1	159.2	Golgi
P10394	Retrovirus-related Pol polyprotein from transposon 412	1	0.1	1	0	1	143.0	Unknown
Q86NP2	Negative elongation factor A	1	0.1	1	0	1	134.9	Nucleus
A4VCL2	Extracellular serine/threonine protein CG31145	1	0.1	1	0	1	109.7	Golgi
B3MJ69	Serrate RNA effector molecule homolog	1	0.1	1	0	1	107.2	Nucleus
Q9W0V1	3-phosphoinositide-dependent protein kinase 1	1	0.1	1	0	1	94.1	Cytoplasm
P18824	Armadillo segment polarity protein	1	0.1	1	0	1	91.2	PM
Q9W1A2	N-alpha-acetyltransferase, 35 NatC auxiliary subunit homolog	1	0.1	1	0	1	89.2	Cytoplasm
Q7KN90	Cysteine--tRNA ligase, cytoplasmic	1	0.1	1	0	1	84.3	Cytoplasm
P54351	Vesicle-fusing ATPase 2	1	0.1	2	0	1	83.4	Cytoplasm
Q24143	Nuclear hormone receptor HR96	1	0.1	2	0	1	81.0	Nucleus
P22808	Homeobox protein vnd	1	0.1	1	0	1	76.4	Nucleus
P10090	Protein white	1	0.1	2	0	1	75.7	Membrane
Q24246	Cytoplasmic dynein 1 intermediate chain	1	0.1	1	0	1	73.9	Cytoskeleton
P21187	Polyadenylate-binding protein	1	0.1	2	0	1	69.9	Spliceosome
Q03427	Lamin-C	1	0.1	2	0	1	69.9	Nucleus
Q24492	Replication protein A 70 kDa DNA-binding subunit	1	0.2	2	0	1	66.6	Nucleus
Q7KN79	Protein LTV1 homolog	1	0.2	2	0	1	57.2	Cytoplasm
P49455	Tropomyosin-1, isoforms 33/34	1	0.2	2	0	1	54.6	Cytoskeleton
P41573	6-phosphogluconate dehydrogenase, decarboxylating	1	0.2	1	0	1	52.4	Cytosol
P29774	DNA-binding protein D-ETS-3	1	0.2	2	0	1	52.1	Nucleus
P51406	Bystin	1	0.2	2	0	1	50.0	Nucleolus
O16797	60S ribosomal protein L3	1	0.2	3	0	1	46.9	Ribosome
Q24537	High mobility group protein DSP1	1	0.2	3	0	1	44.9	Nucleus
Q45VV3	Transcriptional coactivator yorkie	1	0.2	3	0	1	43.6	Cytoplasm/ nucleus
P52654	Transcription initiation factor IIA subunit 1	1	0.3	4	0	1	39.3	Nucleus
Q9VCU5	Mitochondrial ribosome-associated GTPase 1	1	0.3	6	0	1	36.5	Mitochondria
P22465	Annexin B10	1	0.3	3	0	1	35.7	Membrane
P07486	Glyceraldehyde-3-phosphate dehydrogenase 1	1	0.3	4	0	1	35.4	Cytoplasm
Q9VNH1	Probable RNA methyltransferase CG1239	1	0.3	2	0	1	34.7	Unknown

Accession	Description	PSMs	PSMs/ kDa*10	Coverage (%)	# biotin tags	# expts	Mass (kDa)	Localisation
Q9VNH1	Probable RNA methyltransferase CG1239	1	0.3	2	0	1	34.7	Unknown
Q9VQ93	Golgi phosphoprotein 3 homolog sauron	1	0.3	3	0	1	33.5	Golgi
B3NHV5	Ubiquinone biosynthesis protein COQ4 homolog, mitochondrial	1	0.3	5	0	1	31.0	Mitochondria IM
Q94516	ATP synthase subunit b, mitochondrial	1	0.4	5	0	1	27.4	Mitochondria IM
B4HXL7	Anamorsin homolog	1	0.4	6	0	1	27.1	Mitochondria IMS
O18404	3-hydroxyacyl-CoA dehydrogenase type-2	1	0.4	6	0	1	26.9	Mitochondria
P56538	Eukaryotic translation initiation factor 6	1	0.4	6	0	1	26.5	Ribosome
P54611	V-type proton ATPase subunit E	1	0.4	4	0	1	26.1	PM
P35122	Ubiquitin carboxyl-terminal hydrolase	1	0.4	4	0	1	25.9	Cytoplasm
P02518	Heat shock protein 27	1	0.4	5	0	1	23.6	Cytoplasm/ nucleus
Q6XJ13	60S ribosomal protein L17	1	0.5	5	0	1	21.6	Ribosome
Q05856	Small nuclear ribonucleoprotein-associated protein B	1	0.5	4	0	1	21.0	Nucleus/ Cajal body
P08510	Potassium voltage-gated channel protein Shaker	1	0.1	2	0	1	74.2	PM
P13709	Homeotic protein female sterile	1	0.0	0	0	1	205.3	Membrane
P18106	Tyrosine-protein kinase Fer	1	0.1	1	0	1	150.3	Membrane
Q27368	Transcription factor E2f1	1	0.1	3	0	1	87.5	Nucleus
P22817	Insulin-degrading enzyme	1	0.1	1	0	1	113.7	PM/ Mitochondria/ Peroxisome
P14003	Protein hairy	1	0.3	3	0	1	37	Nucleus
Q8MR31	Slo-interacting protein 1	1	0.1	1	0	1	85.8	Membrane
Q9I7W5	Something about silencing protein 10	1	0.2	3	0	1	49.5	Nucleus
Q8WXH0	Nesprin-2	1	0.0	0	0	1	796.4	Cytoskeleton/ Nucleus/ PM
Q9V412	UPF0428 protein CG16865	1	0.4	4	0	1	27.7	Nucleus
P26270	26S proteasome non-ATPase regulatory subunit 7	1	0.3	4	0	1	38.1	Cytosol/ Nucleus
Q27580	Adenosylhomocysteinase	1	0.2	2	0	1	47.4	Cytosol
Q95083	Proteasome subunit alpha type-5	1	0.4	4	0	1	26.8	Nucleus/ Cytoplasm
B3MUX9	Pescadillo homolog	1	0.1	3	0	1	74.1	Nucleus
O17445	60S ribosomal protein L15	1	0.4	4	0	1	24.3	Ribosome
Q8MVS5	Polypeptide N-acetylgalactosaminyltransferase 35A	1	0.1	2	0	1	71.8	Golgi membrane

Table 7.5. Hits detected in BioID-Cln7 samples common to BioID samples

NON-UNIQUE HITS
BIOID-CLN7

Accession	Description	PSMs	PSMs/ kDa*10	Coverage (%)	# biotin tags	# expts	Mass (kDa)	Localisation
Q9VUC6	Formin-like protein CG32138	136	10.2	42	0	2	133.2	Cytoskeleton
P54359	Septin-2	20	4.1	35	0	1	48.5	Cytoskeleton
Q02645	Protein hu-li tai shao	78	6.1	28	0	2	127.9	PM/ cytoskeleton
P15357	Ubiquitin-40S ribosomal protein S27a	19	10.6	56	0	2	17.9	Ribosome
Q9VI75	Phosphatidylinositol-binding clathrin assembly protein LAP	15	3.0	28	0	1	49.9	Golgi
P13395	Spectrin alpha chain	65	2.3	30	0	1	278.3	Golgi/ cytoskeleton
P17271	Histone H2B	7	5.1	37	0	1	13.7	Nucleus
P29993	Inositol 1,4,5-trisphosphate receptor	3	0.1	1	2	1	319.1	ER membrane
P29327	40S ribosomal protein S6	6	2.1	23	0	1	28.4	Ribosome
Q9VHP0	ATP-dependent RNA helicase bel	13	1.5	3	1	2	85.1	Cytoplasm
P84040	Histone H4	10	8.8	40	0	2	11.4	Nucleus
Q9VXX8	Probable 60S ribosomal protein L37-A	5	4.7	28	0	2	10.6	Ribosome
P13008	40S ribosomal protein S26	5	3.8	32	0	2	13.3	Ribosome
Q9VX32	Rho GTPase-activating protein 190	17	1.0	12	0	1	178.8	Cytosol
P02828	Heat shock protein 83	31	3.8	20	0	1	81.9	Cytoplasm
Q9V4P1	Anillin	11	0.8	6	0	1	136.0	Nucleus
Q8MT06	Guanine nucleotide-binding protein-like 3 homolog	10	1.5	19	0	1	66.0	Nucleolus
Q9W5R8	60S ribosomal protein L5	4	1.2	8	0	1	34.0	Ribosome
P08120	Collagen alpha-1(IV) chain	2	0.1	2	0	1	174.3	Secreted
Q9VNA0	Probable mitochondrial import inner membrane translocase subunit Tim17 1	2	1.1	6	0	1	18.7	Mitochondria
C0HK92	Uncharacterized protein CG45076	2	0.3	2	0	1	68.6	Membrane
P07909	Heterogeneous nuclear ribonucleoprotein A1	2	0.5	4	0	1	39.0	Nucleus
Q9VVI9	Charged multivesicular body protein 5	7	2.8	30	0	1	25.2	Endosome
Q9I7T7	La-related protein CG11505	7	0.4	3	0	1	162.0	Unknown
P36241	60S ribosomal protein L19	40	16.7	41	0	2	24.0	Ribosome
Q24560	Tubulin beta-1 chain	10	2.0	21	0	1	50.1	Cytoskeleton
P00522	Tyrosine-protein kinase Abl	6	0.3	4	0	1	171.6	Cytoplasm
P45594	Cofilin/actin-depolymerizing factor homolog	6	3.5	28	0	1	17.2	Nucleus/ cytoskeleton
Q9VZ23	GTP-binding nuclear protein Ran	3	1.2	15	0	1	24.7	Nucleus/ cytoskeleton
Q94522	Succinate--CoA ligase [ADP/GDP-forming] subunit alpha, mitochondrial	3	0.9	4	0	1	34.4	Mitochondria
Q9VCR7	Cystinosin homolog	3	0.7	2	0	1	44.9	Lysosome
O61231	60S ribosomal protein L10	4	1.6	20	0	1	25.5	Ribosome
P35381	ATP synthase subunit alpha, mitochondrial	14	2.4	9	0	2	59.4	Mitochondria
O02649	60 kDa heat shock protein, mitochondrial	5	0.8	5	0	1	60.8	Mitochondrial matrix
B4IL76	40S ribosomal protein S3a	11	3.6	30	0	1	30.4	Ribosome

Accession	Description	PSMs	PSMs/ kDa*10	Coverage (%)	# biotin tags	# expts	Mass (kDa)	Localisation
O18640	Guanine nucleotide-binding protein subunit beta-like protein	7	2.0	20	0	1	35.6	Cytosol/ nucleus
P10987	Actin-5C	20	4.8	21	0	2	41.8	Cytoskeleton
P41092	60S ribosomal protein L27a	6	3.5	32	0	2	17.0	Ribosome
Q8T8R1	CCHC-type zinc finger protein CG3800	4	2.3	24	0	2	17.6	Nucleus
P08879	Nucleoside diphosphate kinase	2	1.2	16	0	2	17.2	Cytoskeleton
Q8MSS1	Protein lava lamp	73	2.3	32	0	1	315.9	Golgi
Q9VEN1	Filamin-A	10	0.4	6	0	1	239.2	PM/ cytoskeleton
P20240	Otefin	10	2.1	29	0	1	46.6	Nucleus/ cytoskeleton
Q06559	40S ribosomal protein S3	8	2.9	31	0	1	27.5	Ribosome
P39018	40S ribosomal protein S19a	6	3.5	31	0	1	17.3	Ribosome
Q9VJ26	EF-hand domain-containing protein D2 homolog	4	1.6	25	0	1	25.1	PM
Q9VE11	UPF0488 protein CG14286	2	0.9	10	0	1	22.0	Unknown
Q99323	Myosin heavy chain, non-muscle	2	0.1	1	0	1	236.6	Cilia
Q94518	Nascent polypeptide-associated complex subunit alpha	2	0.9	13	0	1	23.0	Ribosome
O97069	Argininosuccinate synthase	2	0.4	2	0	1	46.6	Cytoplasm
O01939	Protein misato	2	0.3	3	0	1	64.8	Mitochondria
P05205	Heterochromatin protein 1	2	0.9	12	0	1	23.2	Nucleus
O97159	Chromodomain-helicase-DNA-binding protein Mi-2 homolog	1	0.0	1	0	1	224.2	Nucleus
P50882	60S ribosomal protein L9	1	0.5	5	0	1	21.4	Ribosome
P82804	Partner of Y14 and mago	1	0.4	4	0	1	23.5	Cytoplasm/ nucleus
Q7YZA2	Uncharacterized protein CG7065	1	0.1	1	0	1	136.8	Unknown
Q9VMC9	Kynurenine formamidase	1	0.3	2	0	1	34.9	Cytoplasm
Q9VYS3	Regulator of nonsense transcripts 1 homolog	1	0.1	1	0	1	129.9	Cytoplasm
Q8SWR8	Ataxin-2 homolog	1	0.1	1	0	1	117.6	Cytoplasm
Q8MT08	Growth arrest-specific protein 8 homolog	1	0.2	1	0	1	57.2	Cytoskeleton
Q9VSH4	Cleavage and polyadenylation specificity factor subunit CG7185	57	8.0	19	0	1	71.1	Nucleus
P06603	Tubulin alpha-1 chain	11	2.2	23	0	1	49.9	Cytoskeleton
P08736	Elongation factor 1-alpha 1	28	5.6	21	0	2	50.3	Ribosome
Q8MLY8	40S ribosomal protein S8	10	4.2	50	0	2	23.8	Ribosome
P04359	60S ribosomal protein L32	13	8.1	41	0	2	16.0	Ribosome
P55841	60S ribosomal protein L14	3	1.6	12	0	2	19.2	Ribosome
P41126	60S ribosomal protein L13	6	2.4	28	0	2	25.0	Ribosome
P92177	14-3-3 protein epsilon	2	0.7	3	0	2	29.8	Ubiquitous
P29845	Heat shock 70 kDa protein cognate 5	2	0.3	1	0	1	74.1	Mitochondria
P51140	Segment polarity protein dishevelled	5	0.7	10	0	1	68.9	Nucleus/ cytoplasm/ membrane
P29310	14-3-3 protein zeta	3	1.1	8	0	1	28.2	Endosome
Q8I7C3	LIM and SH3 domain protein Lasp	4	0.5	7	0	2	74.2	Cytosol
Q7JWR9	Zinc finger CCCH domain-containing protein 15 homolog	4	0.9	9	0	1	45.3	Cytosol
P54399	Protein disulfide-isomerase	7	1.3	9	0	1	55.8	ER
P29844	Heat shock 70 kDa protein cognate 3	8	1.1	4	0	1	72.3	ER

Accession	Description	PSMs	PSMs/ kDa*10	Coverage (%)	# biotin tags	# expts	Mass (kDa)	Localisation
Q7K550	Eukaryotic translation initiation factor 3 subunit J	29	10.9	57	1	2	26.6	Ribosome
Q24276	Hsp90 co-chaperone Cdc37	2	0.4	7	0	1	45.2	Cytoplasm
Q9V4S8	COP9 signalosome complex subunit 7	2	0.6	6	0	1	31.1	Nucleus
Q9BJZ5	RNA-binding protein fusilli	2	0.2	1	0	1	102.7	Nucleus
Q9XYZ5	DNA damage-binding protein 1	1	0.1	1	0	1	126	Nucleus/ Cytoplasm
P15348	DNA topoisomerase 2	1	0.1	1	0	1	164.4	Nucleus
P48601	26S protease regulatory subunit 4	1	0.2	2	0	1	49.3	Nucleus
Q9VFE4	40S ribosomal protein S5b	1	0.4	4	0	1	25.7	Ribosome
Q9VD26	Zinc finger protein-like 1 homolog	1	0.3	3	0	1	33.5	Membrane
P07339	Cathepsin D	1	0.2	2	0	1	44.6	Lysosome/ Secreted
P11147	Heat shock 70 kDa protein cognate 4	14	2.0	12	0	1	71.1	Nucleus
P13468	DNA-binding protein K10	3	0.6	8	0	1	51.3	Nucleus
B4I3P3	Eukaryotic translation initiation factor 3 subunit A	1	0.1	1	0	1	133.9	Cytoplasm
Q9V438	Protein disulfide-isomerase A6 homolog	1	0.2	2	0	1	46.8	ER
B3P935	Eukaryotic translation initiation factor 3 subunit G-A	1	0.3	5	0	1	30.0	Ribosome
Q9VRV7	Splicing factor 3B subunit 6-like protein	1	0.7	7	0	1	14.2	Nucleus
Q05825	ATP synthase subunit beta, mitochondrial	1	0.2	1	0	1	54.1	Mitochondria IM
O96827	Probable elongation factor 1-beta	1	0.4	5	0	1	24.2	Ribosome
Q9U5L1	Signal recognition particle receptor subunit alpha homolog	2	0.3	3	0	1	67.8	ER
P23226	205 kDa microtubule-associated protein	1	0.1	1	0	1	126.7	Cytoskeleton
P46150	Moesin/ezrin/radixin homolog 1	1	0.1	2	0	1	68.1	PM/ cytoskeleton/ nucleus

Table 7.6. Hits detected in BioID samples common to BioID-Cln7 samples

NON-UNIQUE HITS

BIOID

Accession	Description	PSMs	PSMs/ kDa*10	Coverage (%)	# biotin tags	# expts	Mass (kDa)	Localisation
Q9VUC6	Formin-like protein CG32138	1	0.1	1	0	1	133.2	Cytoskeleton
P54359	Septin-2	1	0.2	1	0	1	48.5	Cytoskeleton
Q02645	Protein hu-li tai shao	4	0.3	3	0	2	127.9	PM/ cytoskeleton
P15357	Ubiquitin-40S ribosomal protein S27a	1	0.6	10	0	2	17.9	Ribosome
Q9VI75	Phosphatidylinositol-binding clathrin assembly protein LAP	1	0.2	2	0	1	49.9	Golgi
P13395	Spectrin alpha chain	8	0.3	3	0	1	278.3	Golgi/ cytoskeleton
P17271	Histone H2B	1	0.7	6	0	1	13.7	Nucleus
P29993	Inositol 1,4,5-trisphosphate receptor	1	0.0	0	0	1	319.1	ER membrane
P29327	40S ribosomal protein S6	2	0.7	8	0	1	28.4	Ribosome
Q9VHP0	ATP-dependent RNA helicase bel	5	0.6	3	1	1	85.1	Cytoplasm
P84040	Histone H4	4	3.5	19	0	1	11.4	Nucleus
Q9VXX8	Probable 60S ribosomal protein L37-A	2	1.9	13	0	1	10.6	Ribosome
P13008	40S ribosomal protein S26	2	1.5	8	0	1	13.3	Ribosome
Q9VX32	Rho GTPase-activating protein 190	7	0.4	4	0	1	178.8	Cytosol
P02828	Heat shock protein 83	13	1.6	12	0	1	81.9	Cytoplasm
Q9V4P1	Anillin	5	0.4	5	0	1	136.0	Nucleus
Q8MT06	Guanine nucleotide-binding protein-like 3 homolog	5	0.8	8	0	1	66.0	Nucleolus
Q9W5R8	60S ribosomal protein L5	2	0.6	4	0	1	34.0	Ribosome
P08120	Collagen alpha-1(IV) chain	1	0.1	1	0	1	174.3	Secreted
Q9VNA0	Probable mitochondrial import inner membrane translocase subunit Tim17 1	1	0.5	6	0	1	18.7	Mitochondria
C0HK92	Uncharacterized protein CG45076	1	0.1	2	0	1	68.6	Membrane
P07909	Heterogeneous nuclear ribonucleoprotein A1	1	0.3	2	0	1	39.0	Nucleus
Q9VVI9	Charged multivesicular body protein 5	4	1.6	22	0	1	25.2	Endosome
Q9I7T7	La-related protein CG11505	4	0.2	3	0	1	162.0	Unknown
P36241	60S ribosomal protein L19	24	10.0	42	0	2	24.0	Ribosome
Q24560	Tubulin beta-1 chain	6	1.2	17	0	1	50.1	Cytoskeleton
P00522	Tyrosine-protein kinase Abl	4	0.2	2	0	1	171.6	Cytoplasm
P45594	Cofilin/actin-depolymerizing factor homolog	4	2.3	11	0	1	17.2	Nucleus/ cytoskeleton
Q9VZ23	GTP-binding nuclear protein Ran	2	0.8	10	0	1	24.7	Nucleus/ cytoskeleton
Q94522	Succinate--CoA ligase [ADP/GDP-forming] subunit alpha, mitochondrial	2	0.6	4	0	1	34.4	Mitochondria
Q9VCR7	Cystinosin homolog	2	0.4	2	0	1	44.9	Lysosome
O61231	60S ribosomal protein L10	3	1.2	12	0	1	25.5	Ribosome
P35381	ATP synthase subunit alpha, mitochondrial	11	1.9	20	0	2	59.4	Mitochondria
O02649	60 kDa heat shock protein, mitochondrial	4	0.7	4	0	1	60.8	Mitochondrial matrix
B4IL76	40S ribosomal protein S3a	9	3.0	34	0	1	30.4	Ribosome

Accession	Description	PSMs	PSMs/ kDa*10	Coverage (%)	# biotin tags	# expts	Mass (kDa)	Localisation
O18640	Guanine nucleotide-binding protein subunit beta-like protein	6	1.7	19	0	1	35.6	Cytosol/ nucleus
P10987	Actin-5C	19	4.5	20	0	2	41.8	Cytoskeleton
P41092	60S ribosomal protein L27a	6	3.5	12	0	1	17.0	Ribosome
Q8T8R1	CCHC-type zinc finger protein CG3800	4	2.3	13	0	1	17.6	Nucleus
P08879	Nucleoside diphosphate kinase	2	1.2	22	0	1	17.2	Cytoskeleton
Q8MSS1	Protein lava lamp	73	2.3	30	0	2	315.9	Golgi
Q9VEN1	Filamin-A	10	0.4	5	0	1	239.2	PM/ cytoskeleton
P20240	Otefin	10	2.1	33	0	2	46.6	Nucleus/ cytoskeleton
Q06559	40S ribosomal protein S3	8	2.9	30	0	1	27.5	Ribosome
P39018	40S ribosomal protein S19a	6	3.5	32	0	1	17.3	Ribosome
Q9VJ26	EF-hand domain-containing protein D2 homolog	4	1.6	17	0	2	25.1	PM
Q9VE11	UPF0488 protein CG14286	2	0.9	10	0	1	22.0	Unknown
Q99323	Myosin heavy chain, non-muscle	2	0.1	1	0	1	236.6	Cilia
Q94518	Nascent polypeptide-associated complex subunit alpha	2	0.9	10	0	1	23.0	Ribosome
O97069	Argininosuccinate synthase	2	0.4	2	0	1	46.6	Cytoplasm
O01939	Protein misato	2	0.3	3	0	1	64.8	Mitochondria
P05205	Heterochromatin protein 1	2	0.9	5	0	1	23.2	Nucleus
O97159	Chromodomain-helicase-DNA-binding protein Mi-2 homolog	1	0.0	1	0	1	224.2	Nucleus
P50882	60S ribosomal protein L9	1	0.5	5	0	1	21.4	Ribosome
P82804	Partner of Y14 and mago	1	0.4	4	0	1	23.5	Cytoplasm/ nucleus
Q7YZA2	Uncharacterized protein CG7065	1	0.1	1	0	1	136.8	Unknown
Q9VMC9	Kynurenine formamidase	1	0.3	2	0	1	34.9	Cytoplasm
Q9VYS3	Regulator of nonsense transcripts 1 homolog	1	0.1	1	0	1	129.9	Cytoplasm
Q8SWR8	Ataxin-2 homolog	1	0.1	1	0	1	117.6	Cytoplasm
Q8MT08	Growth arrest-specific protein 8 homolog	1	0.2	1	0	2	57.2	Cytoskeleton
Q9VSH4	Cleavage and polyadenylation specificity factor subunit CG7185	58	8.2	15	0	1	71.1	Nucleus
P06603	Tubulin alpha-1 chain	12	2.4	18	0	1	49.9	Cytoskeleton
P08736	Elongation factor 1-alpha 1	33	6.6	23	1	2	50.3	Ribosome
Q8MLY8	40S ribosomal protein S8	12	5.0	40	0	2	23.8	Ribosome
P04359	60S ribosomal protein L32	17	10.6	34	0	1	16.0	Ribosome
P55841	60S ribosomal protein L14	4	2.1	19	0	1	19.2	Ribosome
P41126	60S ribosomal protein L13	9	3.6	40	0	2	25.0	Ribosome
P92177	14-3-3 protein epsilon	3	1.0	9	0	1	29.8	Ubiquitous
P29845	Heat shock 70 kDa protein cognate 5	3	0.4	5	0	1	74.1	Mitochondria
P51140	Segment polarity protein dishevelled	8	1.2	13	0	1	68.9	Nucleus/ cytoplasm/ membrane
P29310	14-3-3 protein zeta	5	1.8	13	0	1	28.2	Endosome
Q8I7C3	LIM and SH3 domain protein Lasp	7	0.9	13	0	2	74.2	Cytosol
Q7JWR9	Zinc finger CCCH domain-containing protein 15 homolog	7	1.5	16	0	2	45.3	Cytosol
P54399	Protein disulfide-isomerase	13	2.3	22	0	1	55.8	ER
P29844	Heat shock 70 kDa protein cognate 3	15	2.1	20	0	2	72.3	ER

Accession	Description	PSMs	PSMs/ kDa*10	Coverage (%)	# biotin tags	# expts	Mass (kDa)	Localisation
Q7K550	Eukaryotic translation initiation factor 3 subunit J	57	21.4	64	1	2	26.6	Ribosome
Q24276	Hsp90 co-chaperone Cdc37	4	0.9	11	0	1	45.2	Cytoplasm
Q9V4S8	COP9 signalosome complex subunit 7	4	1.3	14	0	1	31.1	Nucleus
Q9BJZ5	RNA-binding protein fusilli	4	0.4	1	0	1	102.7	Nucleus
Q9XYZ5	DNA damage-binding protein 1	2	0.2	1	0	1	126	Nucleus/ Cytoplasm
P15348	DNA topoisomerase 2	2	0.1	1	0	1	164.4	Nucleus
P48601	26S protease regulatory subunit 4	2	0.4	4	0	1	49.3	Nucleus
Q9VFE4	40S ribosomal protein S5b	2	0.8	8	0	1	25.7	Ribosome
Q9VD26	Zinc finger protein-like 1 homolog	2	0.6	7	0	2	33.5	Membrane
P07339	Cathepsin D	2	0.4	2	0	1	44.6	Lysosome/ Secreted
P11147	Heat shock 70 kDa protein cognate 4	30	4.2	30	0	1	71.1	Nucleus
P13468	DNA-binding protein K10	8	1.6	12	0	1	51.3	Nucleus
B4I3P3	Eukaryotic translation initiation factor 3 subunit A	3	0.2	2	0	1	133.9	Cytoplasm
Q9V438	Protein disulfide-isomerase A6 homolog	3	0.6	8	0	1	46.8	ER
B3P935	Eukaryotic translation initiation factor 3 subunit G-A	3	1.0	9	0	1	30.0	Ribosome
Q9VRV7	Splicing factor 3B subunit 6-like protein	4	2.8	7	0	1	14.2	Nucleus
Q05825	ATP synthase subunit beta, mitochondrial	5	0.9	12	0	1	54.1	Mitochondria IM
O96827	Probable elongation factor 1-beta	5	2.1	25	0	2	24.2	Ribosome
Q9U5L1	Signal recognition particle receptor subunit alpha homolog	12	1.8	17	0	1	67.8	ER
P23226	205 kDa microtubule-associated protein	10	0.8	11	0	1	126.7	Cytoskeleton
P46150	Moesin/ezrin/radixin homolog 1	11	1.6	16	0	1	68.1	PM/ cytoskeleton/ nucleus

8 LIST OF REFERENCES

1. Perera RM, Zoncu R. The Lysosome as a Regulatory Hub. Annual Review of Cell and Developmental Biology. 2016;32(1):223-53.
2. Lawrence RE, Zoncu R. The lysosome as a cellular centre for signalling, metabolism and quality control. Nature Cell Biology. 2019;21(2):133-42.
3. de Duve C, Pressman BC, Gianetto R, Wattiaux R, Appelmans F. Tissue fractionation studies. 6. Intracellular distribution patterns of enzymes in rat-liver tissue*. Biochemical Journal. 1955;60(4):604-17.
4. Inpanathan S, Botelho RJ. The Lysosome Signaling Platform: Adapting With the Times. Frontiers in Cell and Developmental Biology. 2019;7(113).
5. Doherty GJ, McMahon HT. Mechanisms of Endocytosis. Annual Review of Biochemistry. 2009;78(1):857-902.
6. Luzio JP, Pryor PR, Bright NA. Lysosomes: fusion and function. Nature Reviews Molecular Cell Biology. 2007;8:622.
7. Rink J, Ghigo E, Kalaidzidis Y, Zerial M. Rab Conversion as a Mechanism of Progression from Early to Late Endosomes. Cell. 2005;122(5):735-49.
8. Zoncu R, Perera RM, Balkin DM, Pirruccello M, Toomre D, De Camilli P. A Phosphoinositide Switch Controls the Maturation and Signaling Properties of APPL Endosomes. Cell. 2009;136(6):1110-21.
9. Christoforidis S, McBride HM, Burgoyne RD, Zerial M. The Rab5 effector EEA1 is a core component of endosome docking. Nature. 1999;397(6720):621-5.
10. Simonsen A, Lippe R, Christoforidis S, Gaullier J-M, Brech A, Callaghan J, et al. EEA1 links PI(3)K function to Rab5 regulation of endosome fusion. Nature. 1998;394(6692):494-8.
11. Horiuchi H, Lippé R, McBride HM, Rubino M, Woodman P, Stenmark H, et al. A Novel Rab5 GDP/GTP Exchange Factor Complexed to Rabaptin-5 Links Nucleotide Exchange to Effector Recruitment and Function. Cell. 1997;90(6):1149-59.
12. Schu P, Takegawa K, Fry M, Stack J, Waterfield M, Emr S. Phosphatidylinositol 3-kinase encoded by yeast VPS34 gene essential for protein sorting. Science. 1993;260(5104):88-91.
13. Söllner T, Whiteheart SW, Brunner M, Erdjument-Bromage H, Geromanos S, Tempst P, et al. SNAP receptors implicated in vesicle targeting and fusion. Nature. 1993;362(6418):318-24.
14. Rutherford AC, Traer C, Wassmer T, Pattni K, Bujny MV, Carlton JG, et al. The mammalian phosphatidylinositol 3-phosphate 5-kinase (PIKfyve) regulates endosome-to-TGN retrograde transport. Journal of Cell Science. 2006;119(19):3944-57.
15. Ishida Y, Nayak S, Mindell JA, Grabe M. A model of lysosomal pH regulation. The Journal of General Physiology. 2013;141(6):705-20.
16. Scott CC, Gruenberg J. Ion flux and the function of endosomes and lysosomes: pH is just the start. BioEssays. 2011;33(2):103-10.
17. Steinberg BE, Huynh KK, Brodovitch A, Jabs S, Stauber T, Jentsch TJ, et al. A cation counterflux supports lysosomal acidification. The Journal of Cell Biology. 2010;189(7):1171-86.

18. Hara-Chikuma M, Yang B, Sonawane ND, Sasaki S, Uchida S, Verkman AS. ClC-3 Chloride Channels Facilitate Endosomal Acidification and Chloride Accumulation. Journal of Biological Chemistry. 2005;280(2):1241-7.
19. Xu H, Ren D. Lysosomal Physiology. Annual Review of Physiology. 2015;77(1):57-80.
20. Rong Y, McPhee CK, Deng S, Huang L, Chen L, Liu M, et al. Spinster is required for autophagic lysosome reformation and mTOR reactivation following starvation. Proceedings of the National Academy of Sciences. 2011;108(19):7826-31.
21. Abu-Remaileh M, Wyant GA, Kim C, Laqtom NN, Abbasi M, Chan SH, et al. Lysosomal metabolomics reveals V-ATPase- and mTOR-dependent regulation of amino acid efflux from lysosomes. Science. 2017;358(6364):807-13.
22. Christoforidis S, Miaczynska M, Ashman K, Wilm M, Zhao L, Yip S-C, et al. Phosphatidylinositol-3-OH kinases are Rab5 effectors. Nature Cell Biology. 1999;1(4):249-52.
23. Raiborg C, Bremnes B, Mehlum A, Gillooly DJ, D'Arrigo A, Stang E, et al. FYVE and coiled-coil domains determine the specific localisation of Hrs to early endosomes. Journal of Cell Science. 2001;114(12):2255-63.
24. Teo H, Gill DJ, Sun J, Perisic O, Veprintsev DB, Vallis Y, et al. ESCRT-I Core and ESCRT-II GLUE Domain Structures Reveal Role for GLUE in Linking to ESCRT-I and Membranes. Cell. 2006;125(1):99-111.
25. Rojas R, van Vlijmen T, Mardones GA, Prabhu Y, Rojas AL, Mohammed S, et al. Regulation of retromer recruitment to endosomes by sequential action of Rab5 and Rab7. The Journal of Cell Biology. 2008;183(3):513-26.
26. Burda P, Padilla SM, Sarkar S, Emr SD. Retromer function in endosome-to-Golgi retrograde transport is regulated by the yeast Vps34 PtdIns 3-kinase. Journal of Cell Science. 2002;115(20):3889-900.
27. Dong X-p, Shen D, Wang X, Dawson T, Li X, Zhang Q, et al. PI(3,5)P_2 controls membrane trafficking by direct activation of mucolipin Ca^{2+} release channels in the endolysosome. Nature Communications. 2010;1:38.
28. Cao Q, Yang Y, Zhong XZ, Dong X-P. The lysosomal Ca^{2+} release channel TRPML1 regulates lysosome size by activating calmodulin. J Biol Chem. 2017;292(20):8424-35.
29. Duex JE, Nau JJ, Kauffman EJ, Weisman LS. Phosphoinositide 5-Phosphatase Fig4p Is Required for both Acute Rise and Subsequent Fall in Stress-Induced Phosphatidylinositol 3,5-Bisphosphate Levels. Eukaryotic Cell. 2006;5(4):723-31.
30. Dove SK, McEwen RK, Mayes A, Hughes DC, Beggs JD, Michell RH. Vac14 Controls PtdIns(3,5)P_2 Synthesis and Fab1-Dependent Protein Trafficking to the Multivesicular Body. Current Biology. 2002;12(11):885-93.
31. Botelho RJ, Efe JA, Teis D, Emr SD. Assembly of a Fab1 Phosphoinositide Kinase Signaling Complex Requires the Fig4 Phosphoinositide Phosphatase. Molecular Biology of the Cell. 2008;19(10):4273-86.
32. Chow CY, Zhang Y, Dowling JJ, Jin N, Adamska M, Shiga K, et al. Mutation of FIG4 causes neurodegeneration in the pale tremor mouse and patients with CMT4J. Nature. 2007;448:68.
33. Chow CY, Landers JE, Bergren SK, Sapp PC, Grant AE, Jones JM, et al. Deleterious Variants of *FIG4*, a Phosphoinositide Phosphatase, in Patients with ALS. The American Journal of Human Genetics. 2009;84(1):85-8.
34. Zhang Y, Zolov SN, Chow CY, Slutsky SG, Richardson SC, Piper RC, et al. Loss of Vac14, a regulator of the signaling lipid phosphatidylinositol 3,5-bisphosphate, results in

neurodegeneration in mice. Proceedings of the National Academy of Sciences. 2007;104(44):17518-23.
35. Schmidt O, Teis D. The ESCRT machinery. Current biology : CB. 2012;22(4):R116-R20.
36. Williams RL, Urbé S. The emerging shape of the ESCRT machinery. Nature Reviews Molecular Cell Biology. 2007;8:355.
37. Babst M, Katzmann DJ, Snyder WB, Wendland B, Emr SD. Endosome-Associated Complex, ESCRT-II, Recruits Transport Machinery for Protein Sorting at the Multivesicular Body. Developmental Cell. 2002;3(2):283-9.
38. Urbé S, Sachse M, Row PE, Preisinger C, Barr FA, Strous G, et al. The UIM domain of Hrs couples receptor sorting to vesicle formation. Journal of Cell Science. 2003;116(20):4169-79.
39. Katzmann DJ, Babst M, Emr SD. Ubiquitin-Dependent Sorting into the Multivesicular Body Pathway Requires the Function of a Conserved Endosomal Protein Sorting Complex, ESCRT-I. Cell. 2001;106(2):145-55.
40. Wollert T, Hurley JH. Molecular mechanism of multivesicular body biogenesis by ESCRT complexes. Nature. 2010;464:864.
41. Teis D, Saksena S, Judson BL, Emr SD. ESCRT-II coordinates the assembly of ESCRT-III filaments for cargo sorting and multivesicular body vesicle formation. The EMBO Journal. 2010;29(5):871-83.
42. Teis D, Saksena S, Emr SD. Ordered Assembly of the ESCRT-III Complex on Endosomes Is Required to Sequester Cargo during MVB Formation. Developmental Cell. 2008;15(4):578-89.
43. Whitley P, Reaves BJ, Hashimoto M, Riley AM, Potter BVL, Holman GD. Identification of Mammalian Vps24p as an Effector of Phosphatidylinositol 3,5-Bisphosphate-dependent Endosome Compartmentalization. Journal of Biological Chemistry. 2003;278(40):38786-95.
44. Saksena S, Wahlman J, Teis D, Johnson AE, Emr SD. Functional Reconstitution of ESCRT-III Assembly and Disassembly. Cell. 2009;136(1):97-109.
45. Babst M, Katzmann DJ, Estepa-Sabal EJ, Meerloo T, Emr SD. Escrt-III: An endosome-associated heterooligomeric protein complex required for mvb sorting. Developmental Cell. 2002;3(2):271-82.
46. Wollert T, Wunder C, Lippincott-Schwartz J, Hurley JH. Membrane scission by the ESCRT-III complex. Nature. 2009;458:172.
47. Mierzwa B, Gerlich Daniel W. Cytokinetic Abscission: Molecular Mechanisms and Temporal Control. Developmental Cell. 2014;31(5):525-38.
48. Jimenez AJ, Maiuri P, Lafaurie-Janvore J, Divoux S, Piel M, Perez F. ESCRT Machinery Is Required for Plasma Membrane Repair. Science. 2014;343(6174):1247136.
49. Scheffer LL, Sreetama SC, Sharma N, Medikayala S, Brown KJ, Defour A, et al. Mechanism of Ca2+-triggered ESCRT assembly and regulation of cell membrane repair. Nature Communications. 2014;5:5646.
50. Loncle N, Agromayor M, Martin-Serrano J, Williams DW. An ESCRT module is required for neuron pruning. Scientific Reports. 2015;5:8461.
51. Lee C-P, Liu P-T, Kung H-N, Su M-T, Chua H-H, Chang Y-H, et al. The ESCRT Machinery Is Recruited by the Viral BFRF1 Protein to the Nucleus-Associated Membrane for the Maturation of Epstein-Barr Virus. PLOS Pathogens. 2012;8(9):e1002904.

52. Martin-Serrano J, Zang T, Bieniasz PD. HIV-1 and Ebola virus encode small peptide motifs that recruit Tsg101 to sites of particle assembly to facilitate egress. Nature Medicine. 2001;7(12):1313-9.
53. Hermey G. The Vps10p-domain receptor family. Cellular and Molecular Life Sciences. 2009;66(16):2677-89.
54. Mari M, Bujny MV, Zeuschner D, Geerts WJC, Griffith J, Petersen CM, et al. SNX1 Defines an Early Endosomal Recycling Exit for Sortilin and Mannose 6-Phosphate Receptors. Traffic. 2008;9(3):380-93.
55. Ni X, Morales CR. The Lysosomal Trafficking of Acid Sphingomyelinase is Mediated by Sortilin and Mannose 6-phosphate Receptor. Traffic. 2006;7(7):889-902.
56. Canuel M, Korkidakis A, Konnyu K, Morales CR. Sortilin mediates the lysosomal targeting of cathepsins D and H. Biochemical and Biophysical Research Communications. 2008;373(2):292-7.
57. Lefrancois S, Zeng J, Hassan AJ, Canuel M, Morales CR. The lysosomal trafficking of sphingolipid activator proteins (SAPs) is mediated by sortilin. The EMBO Journal. 2003;22(24):6430-7.
58. Doray B, Ghosh P, Griffith J, Geuze HJ, Kornfeld S. Cooperation of GGAs and AP-1 in Packaging MPRs at the Trans-Golgi Network. Science. 2002;297(5587):1700-3.
59. Jacobsen L, Madsen P, Nielsen MS, Geraerts WPM, Gliemann J, Smit AB, et al. The sorLA cytoplasmic domain interacts with GGA1 and -2 and defines minimum requirements for GGA binding. FEBS Letters. 2002;511(1-3):155-8.
60. Nielsen MS, Madsen P, Christensen EI, Nykjær A, Gliemann J, Kasper D, et al. The sortilin cytoplasmic tail conveys Golgi–endosome transport and binds the VHS domain of the GGA2 sorting protein. The EMBO Journal. 2001;20(9):2180-90.
61. Mattera R, Arighi CN, Lodge R, Zerial M, Bonifacino JS. Divalent interaction of the GGAs with the Rabaptin-5–Rabex-5 complex. The EMBO Journal. 2003;22(1):78-88.
62. Bonifacino JS, Traub LM. Signals for Sorting of Transmembrane Proteins to Endosomes and Lysosomes. Annual Review of Biochemistry. 2003;72(1):395-447.
63. Ihrke G, Kyttälä A, Russell MRG, Rous BA, Luzio JP. Differential Use of Two AP-3-mediated Pathways by Lysosomal Membrane Proteins. Traffic. 2004;5(12):946-62.
64. Seaman MNJ. Identification of a novel conserved sorting motif required for retromer-mediated endosome-to-TGN retrieval. Journal of Cell Science. 2007;120(14):2378-89.
65. Briken V, Jackman RM, Dasgupta S, Hoening S, Porcelli SA. Intracellular trafficking pathway of newly synthesized CD1b molecules. The EMBO Journal. 2002;21(4):825-34.
66. Ihrke G, Bruns JR, Luzio JP, Weisz OA. Competing sorting signals guide endolyn along a novel route to lysosomes in MDCK cells. The EMBO Journal. 2001;20(22):6256-64.
67. Rous BA, Reaves BJ, Ihrke G, Briggs JAG, Gray SR, Stephens DJ, et al. Role of Adaptor Complex AP-3 in Targeting Wild-Type and Mutated CD63 to Lysosomes. Molecular Biology of the Cell. 2002;13(3):1071-82.
68. Janvier K, Bonifacino JS. Role of the Endocytic Machinery in the Sorting of Lysosome-associated Membrane Proteins. Molecular Biology of the Cell. 2005;16(9):4231-42.
69. Dell'Angelica EC, Shotelersuk V, Aguilar RC, Gahl WA, Bonifacino JS. Altered Trafficking of Lysosomal Proteins in Hermansky-Pudlak Syndrome Due to Mutations in the β3A Subunit of the AP-3 Adaptor. Molecular Cell. 1999;3(1):11-21.

70. Peden AA, Oorschot V, Hesser BA, Austin CD, Scheller RH, Klumperman J. Localization of the AP-3 adaptor complex defines a novel endosomal exit site for lysosomal membrane proteins. The Journal of Cell Biology. 2004;164(7):1065-76.
71. Saftig P, Klumperman J. Lysosome biogenesis and lysosomal membrane proteins: trafficking meets function. Nature Reviews Molecular Cell Biology. 2009;10:623.
72. Seaman MNJ. Recycle your receptors with retromer. Trends in Cell Biology. 2005;15(2):68-75.
73. Bonifacino JS, Rojas R. Retrograde transport from endosomes to the trans-Golgi network. Nature Reviews Molecular Cell Biology. 2006;7(8):568-79.
74. Seaman MNJ. Cargo-selective endosomal sorting for retrieval to the Golgi requires retromer. The Journal of Cell Biology. 2004;165(1):111-22.
75. Rojas R, Kametaka S, Haft CR, Bonifacino JS. Interchangeable but Essential Functions of SNX1 and SNX2 in the Association of Retromer with Endosomes and the Trafficking of Mannose 6-Phosphate Receptors. Molecular and Cellular Biology. 2007;27(3):1112-24.
76. Arighi CN, Hartnell LM, Aguilar RC, Haft CR, Bonifacino JS. Role of the mammalian retromer in sorting of the cation-independent mannose 6-phosphate receptor. The Journal of Cell Biology. 2004;165(1):123-33.
77. Ikonomov OC, Sbrissa D, Mlak K, Deeb R, Fligger J, Soans A, et al. Active PIKfyve Associates with and Promotes the Membrane Attachment of the Late Endosome-to-trans-Golgi Network Transport Factor Rab9 Effector p40. Journal of Biological Chemistry. 2003;278(51):50863-71.
78. Crump CM, Xiang Y, Thomas L, Gu F, Austin C, Tooze SA, et al. PACS-1 binding to adaptors is required for acidic cluster motif-mediated protein traffic. The EMBO Journal. 2001;20(9):2191-201.
79. Saint-Pol A, Yélamos B, Amessou M, Mills IG, Dugast M, Tenza D, et al. Clathrin Adaptor epsinR Is Required for Retrograde Sorting on Early Endosomal Membranes. Developmental Cell. 2004;6(4):525-38.
80. Díaz E, Pfeffer SR. TIP47: A Cargo Selection Device for Mannose 6-Phosphate Receptor Trafficking. Cell. 1998;93(3):433-43.
81. Díaz E, Schimmöller F, Pfeffer SR. A Novel Rab9 Effector Required for Endosome-to-TGN Transport. The Journal of Cell Biology. 1997;138(2):283-90.
82. Nakata T, Hirokawa N. Point mutation of adenosine triphosphate-binding motif generated rigor kinesin that selectively blocks anterograde lysosome membrane transport. The Journal of Cell Biology. 1995;131(4):1039-53.
83. Harada A, Takei Y, Kanai Y, Tanaka Y, Nonaka S, Hirokawa N. Golgi Vesiculation and Lysosome Dispersion in Cells Lacking Cytoplasmic Dynein. The Journal of Cell Biology. 1998;141(1):51-9.
84. Pu J, Schindler C, Jia R, Jarnik M, Backlund P, Bonifacino Juan S. BORC, a Multisubunit Complex that Regulates Lysosome Positioning. Developmental Cell. 2015;33(2):176-88.
85. Johansson M, Rocha N, Zwart W, Jordens I, Janssen L, Kuijl C, et al. Activation of endosomal dynein motors by stepwise assembly of Rab7–RILP–p150^{Glued}, ORP1L, and the receptor βIII spectrin. The Journal of Cell Biology. 2007;176(4):459-71.
86. Korolchuk VI, Saiki S, Lichtenberg M, Siddiqi FH, Roberts EA, Imarisio S, et al. Lysosomal positioning coordinates cellular nutrient responses. Nature Cell Biology. 2011;13:453.

87. Pu J, Keren-Kaplan T, Bonifacino JS. A Ragulator–BORC interaction controls lysosome positioning in response to amino acid availability. The Journal of Cell Biology. 2017;216(12):4183-97.
88. Filipek PA, de Araujo MEG, Vogel GF, De Smet CH, Eberharter D, Rebsamen M, et al. LAMTOR/Ragulator is a negative regulator of Arl8b- and BORC-dependent late endosomal positioning. The Journal of Cell Biology. 2017;216(12):4199-215.
89. Starling GP, Yip YY, Sanger A, Morton PE, Eden ER, Dodding MP. Folliculin directs the formation of a Rab34–RILP complex to control the nutrient-dependent dynamic distribution of lysosomes. EMBO reports. 2016;17(6):823-41.
90. Rocha N, Kuijl C, van der Kant R, Janssen L, Houben D, Janssen H, et al. Cholesterol sensor ORP1L contacts the ER protein VAP to control Rab7–RILP–p150^{Glued} and late endosome positioning. The Journal of Cell Biology. 2009;185(7):1209-25.
91. Li X, Rydzewski N, Hider A, Zhang X, Yang J, Wang W, et al. A molecular mechanism to regulate lysosome motility for lysosome positioning and tubulation. Nature Cell Biology. 2016;18:404.
92. Jaiswal JK, Andrews NW, Simon SM. Membrane proximal lysosomes are the major vesicles responsible for calcium-dependent exocytosis in nonsecretory cells. The Journal of Cell Biology. 2002;159(4):625-35.
93. Samie M, Wang X, Zhang X, Goschka A, Li X, Cheng X, et al. A TRP Channel in the Lysosome Regulates Large Particle Phagocytosis via Focal Exocytosis. Developmental Cell. 2013;26(5):511-24.
94. LaPlante JM, Sun M, Falardeau J, Dai D, Brown EM, Slaugenhaupt SA, et al. Lysosomal exocytosis is impaired in mucolipidosis type IV. Molecular Genetics and Metabolism. 2006;89(4):339-48.
95. Pevsner J, Hsu S-C, Braun JEA, Calakos N, Ting AE, Bennett MK, et al. Specificity and regulation of a synaptic vesicle docking complex. Neuron. 1994;13(2):353-61.
96. Rao SK, Huynh C, Proux-Gillardeaux V, Galli T, Andrews NW. Identification of SNAREs Involved in Synaptotagmin VII-regulated Lysosomal Exocytosis. Journal of Biological Chemistry. 2004;279(19):20471-9.
97. Verderio C, Cagnoli C, Bergami M, Francolini M, Schenk U, Colombo A, et al. TI-VAMP/VAMP7 is the SNARE of secretory lysosomes contributing to ATP secretion from astrocytes. Biology of the Cell. 2012;104(4):213-28.
98. Scales SJ, Chen YA, Yoo BY, Patel SM, Doung Y-C, Scheller RH. SNAREs Contribute to the Specificity of Membrane Fusion. Neuron. 2000;26(2):457-64.
99. Xu J, Toops KA, Diaz F, Carvajal-Gonzalez JM, Gravotta D, Mazzoni F, et al. Mechanism of polarized lysosome exocytosis in epithelial cells. Journal of Cell Science. 2012;125(24):5937-43.
100. Chapman ER. How Does Synaptotagmin Trigger Neurotransmitter Release? Annual Review of Biochemistry. 2008;77(1):615-41.
101. Czibener C, Sherer NM, Becker SM, Pypaert M, Hui E, Chapman ER, et al. Ca^{2+} and synaptotagmin VII–dependent delivery of lysosomal membrane to nascent phagosomes. The Journal of Cell Biology. 2006;174(7):997-1007.
102. Söllner T, Bennett MK, Whiteheart SW, Scheller RH, Rothman JE. A protein assembly-disassembly pathway in vitro that may correspond to sequential steps of synaptic vesicle docking, activation, and fusion. Cell. 1993;75(3):409-18.

103. Reddy A, Caler EV, Andrews NW. Plasma Membrane Repair Is Mediated by Ca^{2+}-Regulated Exocytosis of Lysosomes. Cell. 2001;106(2):157-69.
104. Arantes RME, Andrews NW. A Role for Synaptotagmin VII-Regulated Exocytosis of Lysosomes in Neurite Outgrowth from Primary Sympathetic Neurons. The Journal of Neuroscience. 2006;26(17):4630-7.
105. Medina Diego L, Fraldi A, Bouche V, Annunziata F, Mansueto G, Spampanato C, et al. Transcriptional Activation of Lysosomal Exocytosis Promotes Cellular Clearance. Developmental Cell. 2011;21(3):421-30.
106. Kaur J, Debnath J. Autophagy at the crossroads of catabolism and anabolism. Nature Reviews Molecular Cell Biology. 2015;16:461.
107. Settembre C, Fraldi A, Medina DL, Ballabio A. Signals from the lysosome: a control centre for cellular clearance and energy metabolism. Nature Reviews Molecular Cell Biology. 2013;14:283.
108. Zhang T, Wang R, Wang Z, Wang X, Wang F, Ding J. Structural basis for Ragulator functioning as a scaffold in membrane-anchoring of Rag GTPases and mTORC1. Nature Communications. 2017;8(1):1394.
109. Yonehara R, Nada S, Nakai T, Nakai M, Kitamura A, Ogawa A, et al. Structural basis for the assembly of the Ragulator-Rag GTPase complex. Nature Communications. 2017;8(1):1625.
110. Mu Z, Wang L, Deng W, Wang J, Wu G. Structural insight into the Ragulator complex which anchors mTORC1 to the lysosomal membrane. Cell Discovery. 2017;3(1):17049.
111. Nada S, Hondo A, Kasai A, Koike M, Saito K, Uchiyama Y, et al. The novel lipid raft adaptor p18 controls endosome dynamics by anchoring the MEK–ERK pathway to late endosomes. The EMBO Journal. 2009;28(5):477-89.
112. Gong R, Li L, Liu Y, Wang P, Yang H, Wang L, et al. Crystal structure of the Gtr1p–Gtr2p complex reveals new insights into the amino acid-induced TORC1 activation. Genes & Development. 2011;25(16):1668-73.
113. Sancak Y, Peterson TR, Shaul YD, Lindquist RA, Thoreen CC, Bar-Peled L, et al. The Rag GTPases Bind Raptor and Mediate Amino Acid Signaling to mTORC1. Science. 2008;320(5882):1496-501.
114. Dibble CC, Cantley LC. Regulation of mTORC1 by PI3K signaling. Trends in Cell Biology. 2015;25(9):545-55.
115. Menon S, Dibble Christian C, Talbott G, Hoxhaj G, Valvezan Alexander J, Takahashi H, et al. Spatial Control of the TSC Complex Integrates Insulin and Nutrient Regulation of mTORC1 at the Lysosome. Cell. 2014;156(4):771-85.
116. Inoki K, Li Y, Zhu T, Wu J, Guan K-L. TSC2 is phosphorylated and inhibited by Akt and suppresses mTOR signalling. Nature Cell Biology. 2002;4(9):648-57.
117. Manning BD, Tee AR, Logsdon MN, Blenis J, Cantley LC. Identification of the Tuberous Sclerosis Complex-2 Tumor Suppressor Gene Product Tuberin as a Target of the Phosphoinositide 3-Kinase/Akt Pathway. Molecular Cell. 2002;10(1):151-62.
118. Inoki K, Li Y, Xu T, Guan K-L. Rheb GTPase is a direct target of TSC2 GAP activity and regulates mTOR signaling. Genes & Development. 2003;17(15):1829-34.
119. Saucedo LJ, Gao X, Chiarelli DA, Li L, Pan D, Edgar BA. Rheb promotes cell growth as a component of the insulin/TOR signalling network. Nature Cell Biology. 2003;5(6):566-71.
120. Long X, Lin Y, Ortiz-Vega S, Yonezawa K, Avruch J. Rheb Binds and Regulates the mTOR Kinase. Current Biology. 2005;15(8):702-13.

121. Nojima H, Tokunaga C, Eguchi S, Oshiro N, Hidayat S, Yoshino K-i, et al. The Mammalian Target of Rapamycin (mTOR) Partner, Raptor, Binds the mTOR Substrates p70 S6 Kinase and 4E-BP1 through Their TOR Signaling (TOS) Motif. Journal of Biological Chemistry. 2003;278(18):15461-4.
122. Schalm SS, Fingar DC, Sabatini DM, Blenis J. TOS Motif-Mediated Raptor Binding Regulates 4E-BP1 Multisite Phosphorylation and Function. Current Biology. 2003;13(10):797-806.
123. Ruvinsky I, Sharon N, Lerer T, Cohen H, Stolovich-Rain M, Nir T, et al. Ribosomal protein S6 phosphorylation is a determinant of cell size and glucose homeostasis. Genes & Development. 2005;19(18):2199-211.
124. Chauvin C, Koka V, Nouschi A, Mieulet V, Hoareau-Aveilla C, Dreazen A, et al. Ribosomal protein S6 kinase activity controls the ribosome biogenesis transcriptional program. Oncogene. 2013;33:474.
125. Isotani S, Hara K, Tokunaga C, Inoue H, Avruch J, Yonezawa K. Immunopurified Mammalian Target of Rapamycin Phosphorylates and Activates p70 S6 Kinase α in Vitro. Journal of Biological Chemistry. 1999;274(48):34493-8.
126. Iadevaia V, Liu R, Proud CG. mTORC1 signaling controls multiple steps in ribosome biogenesis. Seminars in Cell & Developmental Biology. 2014;36:113-20.
127. Schalm SS, Blenis J. Identification of a Conserved Motif Required for mTOR Signaling. Current Biology. 2002;12(8):632-9.
128. Thoreen CC, Chantranupong L, Keys HR, Wang T, Gray NS, Sabatini DM. A unifying model for mTORC1-mediated regulation of mRNA translation. Nature. 2012;485(7396):109-13.
129. Porstmann T, Santos CR, Griffiths B, Cully M, Wu M, Leevers S, et al. SREBP Activity Is Regulated by mTORC1 and Contributes to Akt-Dependent Cell Growth. Cell Metabolism. 2008;8(3):224-36.
130. Peterson Timothy R, Sengupta Shomit S, Harris Thurl E, Carmack Anne E, Kang Seong A, Balderas E, et al. mTOR Complex 1 Regulates Lipin 1 Localization to Control the SREBP Pathway. Cell. 2011;146(3):408-20.
131. Düvel K, Yecies JL, Menon S, Raman P, Lipovsky AI, Souza AL, et al. Activation of a Metabolic Gene Regulatory Network Downstream of mTOR Complex 1. Molecular Cell. 2010;39(2):171-83.
132. Valvezan AJ, Turner M, Belaid A, Lam HC, Miller SK, McNamara MC, et al. mTORC1 Couples Nucleotide Synthesis to Nucleotide Demand Resulting in a Targetable Metabolic Vulnerability. Cancer Cell. 2017;32(5):624-38.e5.
133. Ben-Sahra I, Howell JJ, Asara JM, Manning BD. Stimulation of de Novo Pyrimidine Synthesis by Growth Signaling Through mTOR and S6K1. Science. 2013;339(6125):1323-8.
134. Ben-Sahra I, Hoxhaj G, Ricoult SJH, Asara JM, Manning BD. mTORC1 induces purine synthesis through control of the mitochondrial tetrahydrofolate cycle. Science. 2016;351(6274):728-33.
135. Robitaille AM, Christen S, Shimobayashi M, Cornu M, Fava LL, Moes S, et al. Quantitative Phosphoproteomics Reveal mTORC1 Activates de Novo Pyrimidine Synthesis. Science. 2013;339(6125):1320-3.

136. Hosokawa N, Hara T, Kaizuka T, Kishi C, Takamura A, Miura Y, et al. Nutrient-dependent mTORC1 Association with the ULK1–Atg13–FIP200 Complex Required for Autophagy. Molecular Biology of the Cell. 2009;20(7):1981-91.
137. Kim J, Kundu M, Viollet B, Guan K-L. AMPK and mTOR regulate autophagy through direct phosphorylation of Ulk1. Nature Cell Biology. 2011;13(2):132-41.
138. Sardiello M, Palmieri M, di Ronza A, Medina DL, Valenza M, Gennarino VA, et al. A Gene Network Regulating Lysosomal Biogenesis and Function. Science. 2009;325(5939):473-7.
139. Roczniak-Ferguson A, Petit CS, Froehlich F, Qian S, Ky J, Angarola B, et al. The Transcription Factor TFEB Links mTORC1 Signaling to Transcriptional Control of Lysosome Homeostasis. Science Signaling. 2012;5(228):ra42-ra.
140. Settembre C, Zoncu R, Medina DL, Vetrini F, Erdin S, Erdin S, et al. A lysosome-to-nucleus signalling mechanism senses and regulates the lysosome via mTOR and TFEB. The EMBO Journal. 2012;31(5):1095-108.
141. Martina JA, Puertollano R. Rag GTPases mediate amino acid–dependent recruitment of TFEB and MITF to lysosomes. The Journal of Cell Biology. 2013;200(4):475-91.
142. Saxton RA, Sabatini DM. mTOR Signaling in Growth, Metabolism, and Disease. Cell. 2017;168(6):960-76.
143. Rabanal-Ruiz Y, Korolchuk VI. mTORC1 and Nutrient Homeostasis: The Central Role of the Lysosome. Int J Mol Sci. 2018;19(3):818.
144. Bar-Peled L, Chantranupong L, Cherniack AD, Chen WW, Ottina KA, Grabiner BC, et al. A Tumor Suppressor Complex with GAP Activity for the Rag GTPases That Signal Amino Acid Sufficiency to mTORC1. Science. 2013;340(6136):1100-6.
145. Wolfson RL, Chantranupong L, Wyant GA, Gu X, Orozco JM, Shen K, et al. KICSTOR recruits GATOR1 to the lysosome and is necessary for nutrients to regulate mTORC1. Nature. 2017;543:438.
146. Parmigiani A, Nourbakhsh A, Ding B, Wang W, Kim Young C, Akopiants K, et al. Sestrins Inhibit mTORC1 Kinase Activation through the GATOR Complex. Cell Reports. 2014;9(4):1281-91.
147. Kimball SR, Gordon BS, Moyer JE, Dennis MD, Jefferson LS. Leucine induced dephosphorylation of Sestrin2 promotes mTORC1 activation. Cellular Signalling. 2016;28(8):896-906.
148. Wolfson RL, Chantranupong L, Saxton RA, Shen K, Scaria SM, Cantor JR, et al. Sestrin2 is a leucine sensor for the mTORC1 pathway. Science. 2016;351(6268):43-8.
149. Chantranupong L, Scaria SM, Saxton RA, Gygi MP, Shen K, Wyant GA, et al. The CASTOR Proteins Are Arginine Sensors for the mTORC1 Pathway. Cell. 2016;165(1):153-64.
150. Saxton RA, Chantranupong L, Knockenhauer KE, Schwartz TU, Sabatini DM. Mechanism of arginine sensing by CASTOR1 upstream of mTORC1. Nature. 2016;536:229.
151. Saxton RA, Knockenhauer KE, Wolfson RL, Chantranupong L, Pacold ME, Wang T, et al. Structural basis for leucine sensing by the Sestrin2-mTORC1 pathway. Science. 2016;351(6268):53-8.
152. Lee M, Kim JH, Yoon I, Lee C, Fallahi Sichani M, Kang JS, et al. Coordination of the leucine-sensing Rag GTPase cycle by leucyl-tRNA synthetase in the mTORC1 signaling pathway. Proceedings of the National Academy of Sciences. 2018;115(23):E5279-E88.

153. Han Jung M, Jeong Seung J, Park Min C, Kim G, Kwon Nam H, Kim Hoi K, et al. Leucyl-tRNA Synthetase Is an Intracellular Leucine Sensor for the mTORC1-Signaling Pathway. Cell. 2012;149(2):410-24.
154. Gu X, Orozco JM, Saxton RA, Condon KJ, Liu GY, Krawczyk PA, et al. SAMTOR is an *S*-adenosylmethionine sensor for the mTORC1 pathway. Science. 2017;358(6364):813-8.
155. Jewell JL, Kim YC, Russell RC, Yu F-X, Park HW, Plouffe SW, et al. Differential regulation of mTORC1 by leucine and glutamine. Science. 2015;347(6218):194-8.
156. Nicklin P, Bergman P, Zhang B, Triantafellow E, Wang H, Nyfeler B, et al. Bidirectional Transport of Amino Acids Regulates mTOR and Autophagy. Cell. 2009;136(3):521-34.
157. Durán Raúl V, Oppliger W, Robitaille Aaron M, Heiserich L, Skendaj R, Gottlieb E, et al. Glutaminolysis Activates Rag-mTORC1 Signaling. Molecular Cell. 2012;47(3):349-58.
158. Kim Sang G, Hoffman Gregory R, Poulogiannis G, Buel Gwen R, Jang Young J, Lee Ki W, et al. Metabolic Stress Controls mTORC1 Lysosomal Localization and Dimerization by Regulating the TTT-RUVBL1/2 Complex. Molecular Cell. 2013;49(1):172-85.
159. Shen K, Sabatini DM. Ragulator and SLC38A9 activate the Rag GTPases through noncanonical GEF mechanisms. Proceedings of the National Academy of Sciences. 2018;115(38):9545-50.
160. Bar-Peled L, Schweitzer Lawrence D, Zoncu R, Sabatini David M. Ragulator Is a GEF for the Rag GTPases that Signal Amino Acid Levels to mTORC1. Cell. 2012;150(6):1196-208.
161. Zoncu R, Bar-Peled L, Efeyan A, Wang S, Sancak Y, Sabatini DM. mTORC1 Senses Lysosomal Amino Acids Through an Inside-Out Mechanism That Requires the Vacuolar H^+-ATPase. Science. 2011;334(6056):678-83.
162. Jung J, Genau HM, Behrends C. Amino Acid-Dependent mTORC1 Regulation by the Lysosomal Membrane Protein SLC38A9. Molecular and Cellular Biology. 2015;35(14):2479-94.
163. Rebsamen M, Pochini L, Stasyk T, de Araújo MEG, Galluccio M, Kandasamy RK, et al. SLC38A9 is a component of the lysosomal amino acid sensing machinery that controls mTORC1. Nature. 2015;519:477.
164. Wang S, Tsun Z-Y, Wolfson RL, Shen K, Wyant GA, Plovanich ME, et al. Lysosomal amino acid transporter SLC38A9 signals arginine sufficiency to mTORC1. Science. 2015;347(6218):188-94.
165. Wyant GA, Abu-Remaileh M, Wolfson RL, Chen WW, Freinkman E, Danai LV, et al. mTORC1 Activator SLC38A9 Is Required to Efflux Essential Amino Acids from Lysosomes and Use Protein as a Nutrient. Cell. 2017;171(3):642-54.e12.
166. Lei H-T, Ma J, Sanchez Martinez S, Gonen T. Crystal structure of arginine-bound lysosomal transporter SLC38A9 in the cytosol-open state. Nature Structural & Molecular Biology. 2018;25(6):522-7.
167. Wu X, Zhao L, Chen Z, Ji X, Qiao X, Jin Y, et al. FLCN Maintains the Leucine Level in Lysosome to Stimulate mTORC1. PLOS ONE. 2016;11(6):e0157100.
168. Tsun Z-Y, Bar-Peled L, Chantranupong L, Zoncu R, Wang T, Kim C, et al. The Folliculin Tumor Suppressor Is a GAP for the RagC/D GTPases That Signal Amino Acid Levels to mTORC1. Molecular Cell. 2013;52(4):495-505.
169. Petit CS, Roczniak-Ferguson A, Ferguson SM. Recruitment of folliculin to lysosomes supports the amino acid–dependent activation of Rag GTPases. The Journal of Cell Biology. 2013;202(7):1107-22.

170. Lin S-C, Hardie DG. AMPK: Sensing Glucose as well as Cellular Energy Status. Cell Metabolism. 2018;27(2):299-313.
171. Zhang C-S, Hawley SA, Zong Y, Li M, Wang Z, Gray A, et al. Fructose-1,6-bisphosphate and aldolase mediate glucose sensing by AMPK. Nature. 2017;548:112.
172. Zhang C-S, Jiang B, Li M, Zhu M, Peng Y, Zhang Y-L, et al. The Lysosomal v-ATPase-Ragulator Complex Is a Common Activator for AMPK and mTORC1, Acting as a Switch between Catabolism and Anabolism. Cell Metabolism. 2014;20(3):526-40.
173. Zhang Y-L, Guo H, Zhang C-S, Lin S-Y, Yin Z, Peng Y, et al. AMP as a Low-Energy Charge Signal Autonomously Initiates Assembly of AXIN-AMPK-LKB1 Complex for AMPK Activation. Cell Metabolism. 2013;18(4):546-55.
174. Inoki K, Ouyang H, Zhu T, Lindvall C, Wang Y, Zhang X, et al. TSC2 Integrates Wnt and Energy Signals via a Coordinated Phosphorylation by AMPK and GSK3 to Regulate Cell Growth. Cell. 2006;126(5):955-68.
175. Inoki K, Zhu T, Guan K-L. TSC2 Mediates Cellular Energy Response to Control Cell Growth and Survival. Cell. 2003;115(5):577-90.
176. Palmieri M, Impey S, Kang H, di Ronza A, Pelz C, Sardiello M, et al. Characterization of the CLEAR network reveals an integrated control of cellular clearance pathways. Human Molecular Genetics. 2011;20(19):3852-66.
177. Martina JA, Chen Y, Gucek M, Puertollano R. MTORC1 functions as a transcriptional regulator of autophagy by preventing nuclear transport of TFEB. Autophagy. 2012;8(6):903-14.
178. Settembre C, Di Malta C, Polito VA, Arencibia MG, Vetrini F, Erdin S, et al. TFEB Links Autophagy to Lysosomal Biogenesis. Science. 2011;332(6036):1429-33.
179. Feng Y, He D, Yao Z, Klionsky DJ. The machinery of macroautophagy. Cell Research. 2014;24(1):24-41.
180. Zhao YG, Zhang H. Autophagosome maturation: An epic journey from the ER to lysosomes. The Journal of Cell Biology. 2019;218(3):757-70.
181. Oku M, Sakai Y. Three Distinct Types of Microautophagy Based on Membrane Dynamics and Molecular Machineries. BioEssays. 2018;40(6):1800008.
182. Kaushik S, Cuervo AM. Chaperone-mediated autophagy: a unique way to enter the lysosome world. Trends in Cell Biology. 2012;22(8):407-17.
183. Ndoye A, Weeraratna A. Autophagy- An emerging target for melanoma therapy [version 1; peer review: 2 approved]. F1000Research. 2016;5(1888).
184. Mizushima N, Yoshimori T, Ohsumi Y. The Role of Atg Proteins in Autophagosome Formation. Annual Review of Cell and Developmental Biology. 2011;27(1):107-32.
185. Hosokawa N, Sasaki T, Iemura S-i, Natsume T, Hara T, Mizushima N. Atg101, a novel mammalian autophagy protein interacting with Atg13. Autophagy. 2009;5(7):973-9.
186. Mercer CA, Kaliappan A, Dennis PB. A novel, human Atg13 binding protein, Atg101, interacts with ULK1 and is essential for macroautophagy. Autophagy. 2009;5(5):649-62.
187. Hara T, Takamura A, Kishi C, Iemura S-i, Natsume T, Guan J-L, et al. FIP200, a ULK-interacting protein, is required for autophagosome formation in mammalian cells. The Journal of Cell Biology. 2008;181(3):497-510.
188. Young ARJ, Chan EYW, Hu XW, Köchl R, Crawshaw SG, High S, et al. Starvation and ULK1-dependent cycling of mammalian Atg9 between the TGN and endosomes. Journal of Cell Science. 2006;119(18):3888-900.

189. Itakura E, Kishi C, Inoue K, Mizushima N. Beclin 1 Forms Two Distinct Phosphatidylinositol 3-Kinase Complexes with Mammalian Atg14 and UVRAG. Molecular Biology of the Cell. 2008;19(12):5360-72.
190. Tanida I, Tanida-Miyake E, Ueno T, Kominami E. The Human Homolog of Saccharomyces cerevisiae Apg7p Is a Protein-activating Enzyme for Multiple Substrates Including Human Apg12p, GATE-16, GABARAP, and MAP-LC3. Journal of Biological Chemistry. 2001;276(3):1701-6.
191. Weidberg H, Shvets E, Shpilka T, Shimron F, Shinder V, Elazar Z. LC3 and GATE-16/GABARAP subfamilies are both essential yet act differently in autophagosome biogenesis. The EMBO Journal. 2010;29(11):1792-802.
192. Kabeya Y, Mizushima N, Yamamoto A, Oshitani-Okamoto S, Ohsumi Y, Yoshimori T. LC3, GABARAP and GATE16 localize to autophagosomal membrane depending on form-II formation. Journal of Cell Science. 2004;117(13):2805-12.
193. Axe EL, Walker SA, Manifava M, Chandra P, Roderick HL, Habermann A, et al. Autophagosome formation from membrane compartments enriched in phosphatidylinositol 3-phosphate and dynamically connected to the endoplasmic reticulum. The Journal of Cell Biology. 2008;182(4):685-701.
194. Karanasios E, Stapleton E, Manifava M, Kaizuka T, Mizushima N, Walker SA, et al. Dynamic association of the ULK1 complex with omegasomes during autophagy induction. Journal of Cell Science. 2013;126(22):5224-38.
195. Hayashi-Nishino M, Fujita N, Noda T, Yamaguchi A, Yoshimori T, Yamamoto A. A subdomain of the endoplasmic reticulum forms a cradle for autophagosome formation. Nature Cell Biology. 2009;11(12):1433-7.
196. Karanasios E, Walker SA, Okkenhaug H, Manifava M, Hummel E, Zimmermann H, et al. Autophagy initiation by ULK complex assembly on ER tubulovesicular regions marked by ATG9 vesicles. Nature Communications. 2016;7(1):12420.
197. Hailey DW, Rambold AS, Satpute-Krishnan P, Mitra K, Sougrat R, Kim PK, et al. Mitochondria Supply Membranes for Autophagosome Biogenesis during Starvation. Cell. 2010;141(4):656-67.
198. Ravikumar B, Moreau K, Jahreiss L, Puri C, Rubinsztein DC. Plasma membrane contributes to the formation of pre-autophagosomal structures. Nature Cell Biology. 2010;12(8):747-57.
199. Moreau K, Ravikumar B, Renna M, Puri C, Rubinsztein David C. Autophagosome Precursor Maturation Requires Homotypic Fusion. Cell. 2011;146(2):303-17.
200. Puri C, Renna M, Bento Carla F, Moreau K, Rubinsztein David C. Diverse Autophagosome Membrane Sources Coalesce in Recycling Endosomes. Cell. 2013;154(6):1285-99.
201. Mari M, Griffith J, Rieter E, Krishnappa L, Klionsky DJ, Reggiori F. An Atg9-containing compartment that functions in the early steps of autophagosome biogenesis. The Journal of Cell Biology. 2010;190(6):1005-22.
202. Kaiser SE, Mao K, Taherbhoy AM, Yu S, Olszewski JL, Duda DM, et al. Noncanonical E2 recruitment by the autophagy E1 revealed by Atg7–Atg3 and Atg7–Atg10 structures. Nature Structural &Amp; Molecular Biology. 2012;19:1242.

203. Yamaguchi M, Matoba K, Sawada R, Fujioka Y, Nakatogawa H, Yamamoto H, et al. Noncanonical recognition and UBL loading of distinct E2s by autophagy-essential Atg7. Nature Structural &Amp; Molecular Biology. 2012;19:1250.
204. Bento CF, Renna M, Ghislat G, Puri C, Ashkenazi A, Vicinanza M, et al. Mammalian Autophagy: How Does It Work? Annual Review of Biochemistry. 2016;85(1):685-713.
205. Hanada T, Noda NN, Satomi Y, Ichimura Y, Fujioka Y, Takao T, et al. The Atg12-Atg5 Conjugate Has a Novel E3-like Activity for Protein Lipidation in Autophagy. Journal of Biological Chemistry. 2007;282(52):37298-302.
206. Noda NN, Fujioka Y, Hanada T, Ohsumi Y, Inagaki F. Structure of the Atg12–Atg5 conjugate reveals a platform for stimulating Atg8–PE conjugation. EMBO reports. 2013;14(2):206-11.
207. Nakatogawa H, Ichimura Y, Ohsumi Y. Atg8, a Ubiquitin-like Protein Required for Autophagosome Formation, Mediates Membrane Tethering and Hemifusion. Cell. 2007;130(1):165-78.
208. Takahashi Y, He H, Tang Z, Hattori T, Liu Y, Young MM, et al. An autophagy assay reveals the ESCRT-III component CHMP2A as a regulator of phagophore closure. Nature Communications. 2018;9(1):2855.
209. Zhou F, Wu Z, Zhao M, Murtazina R, Cai J, Zhang A, et al. Rab5-dependent autophagosome closure by ESCRT. The Journal of Cell Biology. 2019;218(6):1908-27.
210. Takahashi Y, Liang X, Hattori T, Tang Z, He H, Chen H, et al. VPS37A directs ESCRT recruitment for phagophore closure. The Journal of Cell Biology. 2019:jcb.201902170.
211. Stolz A, Ernst A, Dikic I. Cargo recognition and trafficking in selective autophagy. Nature Cell Biology. 2014;16:495.
212. Geisler S, Holmström KM, Skujat D, Fiesel FC, Rothfuss OC, Kahle PJ, et al. PINK1/Parkin-mediated mitophagy is dependent on VDAC1 and p62/SQSTM1. Nature Cell Biology. 2010;12(2):119-31.
213. Gegg ME, Cooper JM, Chau K-Y, Rojo M, Schapira AHV, Taanman J-W. Mitofusin 1 and mitofusin 2 are ubiquitinated in a PINK1/parkin-dependent manner upon induction of mitophagy. Human Molecular Genetics. 2010;19(24):4861-70.
214. Sarraf SA, Raman M, Guarani-Pereira V, Sowa ME, Huttlin EL, Gygi SP, et al. Landscape of the PARKIN-dependent ubiquitylome in response to mitochondrial depolarization. Nature. 2013;496:372.
215. Narendra D, Tanaka A, Suen D-F, Youle RJ. Parkin is recruited selectively to impaired mitochondria and promotes their autophagy. The Journal of Cell Biology. 2008;183(5):795-803.
216. Lazarou M, Sliter DA, Kane LA, Sarraf SA, Wang C, Burman JL, et al. The ubiquitin kinase PINK1 recruits autophagy receptors to induce mitophagy. Nature. 2015;524:309.
217. Narendra D, Kane LA, Hauser DN, Fearnley IM, Youle RJ. p62/SQSTM1 is required for Parkin-induced mitochondrial clustering but not mitophagy; VDAC1 is dispensable for both. Autophagy. 2010;6(8):1090-106.
218. Bjørkøy G, Lamark T, Brech A, Outzen H, Perander M, Øvervatn A, et al. p62/SQSTM1 forms protein aggregates degraded by autophagy and has a protective effect on huntingtin-induced cell death. The Journal of Cell Biology. 2005;171(4):603-14.

219. Pankiv S, Clausen TH, Lamark T, Brech A, Bruun J-A, Outzen H, et al. p62/SQSTM1 Binds Directly to Atg8/LC3 to Facilitate Degradation of Ubiquitinated Protein Aggregates by Autophagy. Journal of Biological Chemistry. 2007;282(33):24131-45.
220. McEwan David G, Popovic D, Gubas A, Terawaki S, Suzuki H, Stadel D, et al. PLEKHM1 Regulates Autophagosome-Lysosome Fusion through HOPS Complex and LC3/GABARAP Proteins. Molecular Cell. 2015;57(1):39-54.
221. Jiang P, Nishimura T, Sakamaki Y, Itakura E, Hatta T, Natsume T, et al. The HOPS complex mediates autophagosome–lysosome fusion through interaction with syntaxin 17. Molecular Biology of the Cell. 2014;25(8):1327-37.
222. Takáts S, Pircs K, Nagy P, Varga Á, Kárpáti M, Hegedűs K, et al. Interaction of the HOPS complex with Syntaxin 17 mediates autophagosome clearance in Drosophila. Molecular Biology of the Cell. 2014;25(8):1338-54.
223. Jung CH, Jun CB, Ro S-H, Kim Y-M, Otto NM, Cao J, et al. ULK-Atg13-FIP200 Complexes Mediate mTOR Signaling to the Autophagy Machinery. Molecular Biology of the Cell. 2009;20(7):1992-2003.
224. Kim Y-M, Jung Chang H, Seo M, Kim Eun K, Park J-M, Bae Sun S, et al. mTORC1 Phosphorylates UVRAG to Negatively Regulate Autophagosome and Endosome Maturation. Molecular Cell. 2015;57(2):207-18.
225. Jia R, Guardia CM, Pu J, Chen Y, Bonifacino JS. BORC coordinates encounter and fusion of lysosomes with autophagosomes. Autophagy. 2017;13(10):1648-63.
226. Saffi GT, Botelho RJ. Lysosome Fission: Planning for an Exit. Trends in Cell Biology. 2019;29(8):635-46.
227. Chen Y, Yu L. Recent progress in autophagic lysosome reformation. Traffic. 2017;18(6):358-61.
228. Yu L, McPhee CK, Zheng L, Mardones GA, Rong Y, Peng J, et al. Termination of autophagy and reformation of lysosomes regulated by mTOR. Nature. 2010;465:942.
229. Rong Y, Liu M, Ma L, Du W, Zhang H, Tian Y, et al. Clathrin and phosphatidylinositol-4,5-bisphosphate regulate autophagic lysosome reformation. Nature Cell Biology. 2012;14:924.
230. Du W, Su Qian P, Chen Y, Zhu Y, Jiang D, Rong Y, et al. Kinesin 1 Drives Autolysosome Tubulation. Developmental Cell. 2016;37(4):326-36.
231. Wong LH, Čopič A, Levine TP. Advances on the Transfer of Lipids by Lipid Transfer Proteins. Trends in Biochemical Sciences. 2017;42(7):516-30.
232. Hönscher C, Mari M, Auffarth K, Bohnert M, Griffith J, Geerts W, et al. Cellular Metabolism Regulates Contact Sites between Vacuoles and Mitochondria. Developmental Cell. 2014;30(1):86-94.
233. Jeong H, Park J, Kim H-I, Lee M, Ko Y-J, Lee S, et al. Mechanistic insight into the nucleus–vacuole junction based on the Vac8p–Nvj1p crystal structure. Proceedings of the National Academy of Sciences. 2017;114(23):E4539-E48.
234. Pan X, Roberts P, Chen Y, Kvam E, Shulga N, Huang K, et al. Nucleus–Vacuole Junctions in *Saccharomyces cerevisiae* Are Formed Through the Direct Interaction of Vac8p with Nvj1p. Molecular Biology of the Cell. 2000;11(7):2445-57.
235. Kvam E, Goldfarb D. Nucleus-Vacuole Junctions and Piecemeal Microautophagy of the Nucleus in *S. cerevisiae*. Autophagy. 2007;3(2):85-92.

236. Chen S, Tarsio M, Kane PM, Greenberg ML. Cardiolipin Mediates Cross-Talk between Mitochondria and the Vacuole. Molecular Biology of the Cell. 2008;19(12):5047-58.
237. Hughes AL, Gottschling DE. An early age increase in vacuolar pH limits mitochondrial function and lifespan in yeast. Nature. 2012;492:261.
238. Elbaz-Alon Y, Rosenfeld-Gur E, Shinder V, Futerman Anthony H, Geiger T, Schuldiner M. A Dynamic Interface between Vacuoles and Mitochondria in Yeast. Developmental Cell. 2014;30(1):95-102.
239. González Montoro A, Auffarth K, Hönscher C, Bohnert M, Becker T, Warscheid B, et al. Vps39 Interacts with Tom40 to Establish One of Two Functionally Distinct Vacuole-Mitochondria Contact Sites. Developmental Cell. 2018;45(5):621-36.e7.
240. Lang AB, Peter ATJ, Walter P, Kornmann B. ER–mitochondrial junctions can be bypassed by dominant mutations in the endosomal protein Vps13. The Journal of Cell Biology. 2015;210(6):883-90.
241. Park J-S, Thorsness MK, Policastro R, McGoldrick LL, Hollingsworth NM, Thorsness PE, et al. Yeast Vps13 promotes mitochondrial function and is localized at membrane contact sites. Molecular Biology of the Cell. 2016;27(15):2435-49.
242. Tan T, Özbalci C, Brügger B, Rapaport D, Dimmer KS. Mcp1 and Mcp2, two novel proteins involved in mitochondrial lipid homeostasis. Journal of Cell Science. 2013;126(16):3563-74.
243. John Peter AT, Herrmann B, Antunes D, Rapaport D, Dimmer KS, Kornmann B. Vps13-Mcp1 interact at vacuole–mitochondria interfaces and bypass ER–mitochondria contact sites. The Journal of Cell Biology. 2017;216(10):3219-29.
244. Velayos-Baeza A, Vettori A, Copley RR, Dobson-Stone C, Monaco AP. Analysis of the human VPS13 gene family. Genomics. 2004;84(3):536-49.
245. Rampoldi L, Dobson-Stone C, Rubio JP, Danek A, Chalmers RM, Wood NW, et al. A conserved sorting-associated protein is mutant in chorea-acanthocytosis. Nature Genetics. 2001;28(2):119-20.
246. Ueno S-i, Maruki Y, Nakamura M, Tomemori Y, Kamae K, Tanabe H, et al. The gene encoding a newly discovered protein, chorein, is mutated in chorea-acanthocytosis. Nature Genetics. 2001;28(2):121-2.
247. Kolehmainen J, Black GCM, Saarinen A, Chandler K, Clayton-Smith J, Träskelin A-L, et al. Cohen Syndrome Is Caused by Mutations in a Novel Gene, COH1, Encoding a Transmembrane Protein with a Presumed Role in Vesicle-Mediated Sorting and Intracellular Protein Transport. The American Journal of Human Genetics. 2003;72(6):1359-69.
248. Lesage S, Drouet V, Majounie E, Deramecourt V, Jacoupy M, Nicolas A, et al. Loss of VPS13C Function in Autosomal-Recessive Parkinsonism Causes Mitochondrial Dysfunction and Increases PINK1/Parkin-Dependent Mitophagy. The American Journal of Human Genetics. 2016;98(3):500-13.
249. Gauthier J, Meijer IA, Lessel D, Mencacci NE, Krainc D, Hempel M, et al. Recessive mutations in >VPS13D cause childhood onset movement disorders. Annals of Neurology. 2018;83(6):1089-95.
250. Seong E, Insolera R, Dulovic M, Kamsteeg E-J, Trinh J, Brüggemann N, et al. Mutations in VPS13D lead to a new recessive ataxia with spasticity and mitochondrial defects. Annals of Neurology. 2018;83(6):1075-88.

251. Lupo F, Tibaldi E, Matte A, Sharma AK, Brunati AM, Alper SL, et al. A new molecular link between defective autophagy and erythroid abnormalities in chorea-acanthocytosis. Blood. 2016;128(25):2976-87.
252. Anding AL, Wang C, Chang T-K, Sliter DA, Powers CM, Hofmann K, et al. Vps13D Encodes a Ubiquitin-Binding Protein that Is Required for the Regulation of Mitochondrial Size and Clearance. Current Biology. 2018;28(2):287-95.e6.
253. Kumar N, Leonzino M, Hancock-Cerutti W, Horenkamp FA, Li P, Lees JA, et al. VPS13A and VPS13C are lipid transport proteins differentially localized at ER contact sites. The Journal of Cell Biology. 2018;217(10):3625-39.
254. Seifert W, Kühnisch J, Maritzen T, Horn D, Haucke V, Hennies HC. Cohen Syndrome-associated Protein, COH1, Is a Novel, Giant Golgi Matrix Protein Required for Golgi Integrity. Journal of Biological Chemistry. 2011;286(43):37665-75.
255. Seifert W, Kühnisch J, Maritzen T, Lommatzsch S, Hennies HC, Bachmann S, et al. Cohen Syndrome-associated Protein COH1 Physically and Functionally Interacts with the Small GTPase RAB6 at the Golgi Complex and Directs Neurite Outgrowth. Journal of Biological Chemistry. 2015;290(6):3349-58.
256. Muñoz-Braceras S, Calvo R, Escalante R. TipC and the chorea-acanthocytosis protein VPS13A regulate autophagy in Dictyostelium and human HeLa cells. Autophagy. 2015;11(6):918-27.
257. Muñoz-Braceras S, Tornero-Écija AR, Vincent O, Escalante R. VPS13A is closely associated with mitochondria and is required for efficient lysosomal degradation. Disease Models & Mechanisms. 2019;12(2):dmm036681.
258. Weller J, Budson A. Current understanding of Alzheimer's disease diagnosis and treatment. F1000Research. 2018;7:F1000 Faculty Rev-161.
259. Mroczko B, Groblewska M, Litman-Zawadzka A, Kornhuber J, Lewczuk P. Amyloid β oligomers (AβOs) in Alzheimer’s disease. Journal of Neural Transmission. 2018;125(2):177-91.
260. Koo EH, Squazzo SL. Evidence that production and release of amyloid beta-protein involves the endocytic pathway. Journal of Biological Chemistry. 1994;269(26):17386-9.
261. Whyte LS, Lau AA, Hemsley KM, Hopwood JJ, Sargeant TJ. Endo-lysosomal and autophagic dysfunction: a driving factor in Alzheimer's disease? Journal of Neurochemistry. 2017;140(5):703-17.
262. Morel E, Chamoun Z, Lasiecka ZM, Chan RB, Williamson RL, Vetanovetz C, et al. Phosphatidylinositol-3-phosphate regulates sorting and processing of amyloid precursor protein through the endosomal system. Nature Communications. 2013;4(1):2250.
263. Kuhn P-H, Wang H, Dislich B, Colombo A, Zeitschel U, Ellwart JW, et al. ADAM10 is the physiologically relevant, constitutive α-secretase of the amyloid precursor protein in primary neurons. The EMBO Journal. 2010;29(17):3020-32.
264. Huse JT, Pijak DS, Leslie GJ, Lee VM-Y, Doms RW. Maturation and Endosomal Targeting of β-Site Amyloid Precursor Protein-cleaving Enzyme: THE ALZHEIMER'S DISEASE β-SECRETASE. Journal of Biological Chemistry. 2000;275(43):33729-37.
265. Vassar R, Bennett BD, Babu-Khan S, Kahn S, Mendiaz EA, Denis P, et al. β-Secretase Cleavage of Alzheimer's Amyloid Precursor Protein by the Transmembrane Aspartic Protease BACE. Science. 1999;286(5440):735-41.

266. Sannerud R, Esselens C, Ejsmont P, Mattera R, Rochin L, Tharkeshwar Arun K, et al. Restricted Location of PSEN2/γ-Secretase Determines Substrate Specificity and Generates an Intracellular Aβ Pool. Cell. 2016;166(1):193-208.
267. Takahashi RH, Milner TA, Li F, Nam EE, Edgar MA, Yamaguchi H, et al. Intraneuronal Alzheimer Aβ42 Accumulates in Multivesicular Bodies and Is Associated with Synaptic Pathology. The American Journal of Pathology. 2002;161(5):1869-79.
268. Edgar JR, Willén K, Gouras GK, Futter CE. ESCRTs regulate amyloid precursor protein sorting in multivesicular bodies and intracellular amyloid-β accumulation. Journal of Cell Science. 2015;128(14):2520-8.
269. Xiao Q, Yan P, Ma X, Liu H, Perez R, Zhu A, et al. Neuronal-Targeted TFEB Accelerates Lysosomal Degradation of APP, Reducing Aβ Generation and Amyloid Plaque Pathogenesis. The Journal of Neuroscience. 2015;35(35):12137-51.
270. Nixon RA. Niemann-Pick Type C Disease and Alzheimer's Disease: The APP-Endosome Connection Fattens Up. The American Journal of Pathology. 2004;164(3):757-61.
271. Cataldo AM, Peterhoff CM, Troncoso JC, Gomez-Isla T, Hyman BT, Nixon RA. Endocytic Pathway Abnormalities Precede Amyloid β; Deposition in Sporadic Alzheimer's Disease and Down Syndrome: Differential Effects of APOE Genotype and Presenilin Mutations. The American Journal of Pathology. 2000;157(1):277-86.
272. Cataldo AM, Petanceska S, Terio NB, Peterhoff CM, Durham R, Mercken M, et al. Aβ localization in abnormal endosomes: association with earliest Aβ elevations in AD and Down syndrome. Neurobiology of Aging. 2004;25(10):1263-72.
273. Cataldo AM, Barnett JL, Pieroni C, Nixon RA. Increased Neuronal Endocytosis and Protease Delivery to Early Endosomes in Sporadic Alzheimer's Disease: Neuropathologic Evidence for a Mechanism of Increased β-Amyloidogenesis. The Journal of Neuroscience. 1997;17(16):6142-51.
274. Emiliani C, Urbanelli L, Racanicchi L, Orlacchio A, Pelicci G, Sorbi S, et al. Up-regulation of Glycohydrolases in Alzheimer's Disease Fibroblasts Correlates with Ras Activation. Journal of Biological Chemistry. 2003;278(40):38453-60.
275. Pitto M, Raimondo F, Zoia C, Brighina L, Ferrarese C, Masserini M. Enhanced GM1 ganglioside catabolism in cultured fibroblasts from Alzheimer patients. Neurobiology of Aging. 2005;26(6):833-8.
276. Almeida CG, Takahashi RH, Gouras GK. β-Amyloid Accumulation Impairs Multivesicular Body Sorting by Inhibiting the Ubiquitin-Proteasome System. The Journal of Neuroscience. 2006;26(16):4277-88.
277. Yang D-S, Stavrides P, Mohan PS, Kaushik S, Kumar A, Ohno M, et al. Reversal of autophagy dysfunction in the TgCRND8 mouse model of Alzheimer's disease ameliorates amyloid pathologies and memory deficits. Brain. 2010;134(1):258-77.
278. Yang D-S, Stavrides P, Saito M, Kumar A, Rodriguez-Navarro JA, Pawlik M, et al. Defective macroautophagic turnover of brain lipids in the TgCRND8 Alzheimer mouse model: prevention by correcting lysosomal proteolytic deficits. Brain. 2014;137(12):3300-18.
279. Esbjörner Elin K, Chan F, Rees E, Erdelyi M, Luheshi Leila M, Bertoncini Carlos W, et al. Direct Observations of Amyloid β Self-Assembly in Live Cells Provide Insights into Differences in the Kinetics of Aβ(1–40) and Aβ(1–42) Aggregation. Chemistry & Biology. 2014;21(6):732-42.

280. Hu X, Crick SL, Bu G, Frieden C, Pappu RV, Lee J-M. Amyloid seeds formed by cellular uptake, concentration, and aggregation of the amyloid-beta peptide. Proceedings of the National Academy of Sciences. 2009;106(48):20324-9.
281. Kuperstein I, Broersen K, Benilova I, Rozenski J, Jonckheere W, Debulpaep M, et al. Neurotoxicity of Alzheimer's disease Aβ peptides is induced by small changes in the Aβ42 to Aβ40 ratio. The EMBO Journal. 2010;29(19):3408-20.
282. Kodam A, Maulik M, Peake K, Amritraj A, Vetrivel KS, Thinakaran G, et al. Altered levels and distribution of amyloid precursor protein and its processing enzymes in Niemann-Pick type C1-deficient mouse brains. Glia. 2010;58(11):1267-81.
283. Mattsson N, Zetterberg H, Bianconi S, Yanjanin NM, Fu R, Månsson J-E, et al. γ-Secretase-dependent amyloid-β is increased in Niemann-Pick type C. A cross-sectional study. 2011;76(4):366-72.
284. Tamboli IY, Hampel H, Tien NT, Tolksdorf K, Breiden B, Mathews PM, et al. Sphingolipid Storage Affects Autophagic Metabolism of the Amyloid Precursor Protein and Promotes Aβ Generation. The Journal of Neuroscience. 2011;31(5):1837-49.
285. Keilani S, Lun Y, Stevens AC, Williams HN, Sjoberg ER, Khanna R, et al. Lysosomal Dysfunction in a Mouse Model of Sandhoff Disease Leads to Accumulation of Ganglioside-Bound Amyloid-β Peptide. The Journal of Neuroscience. 2012;32(15):5223-36.
286. Auer IA, Schmidt ML, Lee VM-Y, Curry B, Suzuki K, Shin R-W, et al. Paired helical filament tau (PHFtau) in Niemann-Pick type C disease is similar to PHFtau in Alzheimer's disease. Acta Neuropathologica. 1995;90(6):547-51.
287. Distl R, Treiber-Held S, Albert F, Meske V, Harzer K, Ohm TG. Cholesterol storage and tau pathology in Niemann–Pick type C disease in the brain. The Journal of Pathology. 2003;200(1):104-11.
288. Jun G, Naj AC, Beecham GW, Wang L-S, Buros J, Gallins PJ, et al. Meta-analysis Confirms CR1, CLU, and PICALM as Alzheimer Disease Risk Loci and Reveals Interactions With APOE Genotypes. JAMA Neurology. 2010;67(12):1473-84.
289. Moreau K, Fleming A, Imarisio S, Lopez Ramirez A, Mercer JL, Jimenez-Sanchez M, et al. PICALM modulates autophagy activity and tau accumulation. Nature Communications. 2014;5(1):4998.
290. Ando K, Tomimura K, Sazdovitch V, Suain V, Yilmaz Z, Authelet M, et al. Level of PICALM, a key component of clathrin-mediated endocytosis, is correlated with levels of phosphotau and autophagy-related proteins and is associated with tau inclusions in AD, PSP and Pick disease. Neurobiol Dis. 2016;94:32-43.
291. Jin SC, Pastor P, Cooper B, Cervantes S, Benitez BA, Razquin C, et al. Pooled-DNA sequencing identifies novel causative variants in PSEN1, GRN and MAPT in a clinical early-onset and familial Alzheimer's disease Ibero-American cohort. Alzheimer's Research & Therapy. 2012;4(4):34.
292. Klein AD, Mazzulli JR. Is Parkinson's disease a lysosomal disorder? Brain. 2018;141(8):2255-62.
293. Deng H, Xiu X, Jankovic J. Genetic Convergence of Parkinson's Disease and Lysosomal Storage Disorders. Molecular Neurobiology. 2015;51(3):1554-68.
294. Cuervo AM, Stefanis L, Fredenburg R, Lansbury PT, Sulzer D. Impaired Degradation of Mutant α-Synuclein by Chaperone-Mediated Autophagy. Science. 2004;305(5688):1292-5.

295. Chu Y, Dodiya H, Aebischer P, Olanow CW, Kordower JH. Alterations in lysosomal and proteasomal markers in Parkinson's disease: Relationship to alpha-synuclein inclusions. Neurobiol Dis. 2009;35(3):385-98.
296. Wang C, Telpoukhovskaia MA, Bahr BA, Chen X, Gan L. Endo-lysosomal dysfunction: a converging mechanism in neurodegenerative diseases. Current Opinion in Neurobiology. 2018;48:52-8.
297. Saha S, Ash PEA, Gowda V, Liu L, Shirihai O, Wolozin B. Mutations in LRRK2 potentiate age-related impairment of autophagic flux. Molecular Neurodegeneration. 2015;10(1):26.
298. Schneider L, Zhang J. Lysosomal function in macromolecular homeostasis and bioenergetics in Parkinson's disease. Molecular Neurodegeneration. 2010;5(1):14.
299. Lavrov AY, Ilyna ES, Zakharova EY, Boukina AM, Tishkanina SV. The first three Russian cases of classical, late-infantile, neuronal ceroid lipofuscinosis. European Journal of Paediatric Neurology. 2002;6(3):161-4.
300. Cullen V, Lindfors M, Ng J, Paetau A, Swinton E, Kolodziej P, et al. Cathepsin D expression level affects alpha-synuclein processing, aggregation, and toxicity in vivo. Molecular Brain. 2009;2(1):5.
301. Suzuki K, Iseki E, Togo T, Yamaguchi A, Katsuse O, Katsuyama K, et al. Neuronal and glial accumulation of α- and β-synucleins in human lipidoses. Acta Neuropathologica. 2007;114(5):481-9.
302. Gitler AD, Chesi A, Geddie ML, Strathearn KE, Hamamichi S, Hill KJ, et al. α-Synuclein is part of a diverse and highly conserved interaction network that includes PARK9 and manganese toxicity. Nature Genetics. 2009;41(3):308-15.
303. Usenovic M, Tresse E, Mazzulli JR, Taylor JP, Krainc D. Deficiency of ATP13A2 Leads to Lysosomal Dysfunction, α-Synuclein Accumulation, and Neurotoxicity. The Journal of Neuroscience. 2012;32(12):4240-6.
304. Young JJ, Lavakumar M, Tampi D, Balachandran S, Tampi RR. Frontotemporal dementia: latest evidence and clinical implications. Ther Adv Psychopharmacol. 2018;8(1):33-48.
305. Almeida MR, Macário MC, Ramos L, Baldeiras I, Ribeiro MH, Santana I. Portuguese family with the co-occurrence of frontotemporal lobar degeneration and neuronal ceroid lipofuscinosis phenotypes due to progranulin gene mutation. Neurobiology of Aging. 2016;41:200.e1-.e5.
306. Ward ME, Chen R, Huang H-Y, Ludwig C, Telpoukhovskaia M, Taubes A, et al. Individuals with progranulin haploinsufficiency exhibit features of neuronal ceroid lipofuscinosis. Science Translational Medicine. 2017;9(385):eaah5642.
307. Baker M, Mackenzie IR, Pickering-Brown SM, Gass J, Rademakers R, Lindholm C, et al. Mutations in progranulin cause tau-negative frontotemporal dementia linked to chromosome 17. Nature. 2006;442(7105):916-9.
308. Geier EG, Bourdenx M, Storm NJ, Cochran JN, Sirkis DW, Hwang J-H, et al. Rare variants in the neuronal ceroid lipofuscinosis gene MFSD8 are candidate risk factors for frontotemporal dementia. Acta Neuropathologica. 2019;137(1):71-88.
309. van der Zee J, Mariën P, Crols R, Van Mossevelde S, Dillen L, Perrone F, et al. Mutated CTSF in adult-onset neuronal ceroid lipofuscinosis and FTD. Neurol Genet. 2016;2(5):e102-e.
310. Marques ARA, Saftig P. Lysosomal storage disorders – challenges, concepts and avenues for therapy: beyond rare diseases. Journal of Cell Science. 2019;132(2):jcs221739.

311. Platt FM, Boland B, van der Spoel AC. Lysosomal storage disorders: The cellular impact of lysosomal dysfunction. The Journal of Cell Biology. 2012;199(5):723-34.
312. Ward C, Martinez-Lopez N, Otten EG, Carroll B, Maetzel D, Singh R, et al. Autophagy, lipophagy and lysosomal lipid storage disorders. Biochimica et Biophysica Acta (BBA) - Molecular and Cell Biology of Lipids. 2016;1861(4):269-84.
313. Nascimbeni AC, Fanin M, Masiero E, Angelini C, Sandri M. The role of autophagy in the pathogenesis of glycogen storage disease type II (GSDII). Cell Death & Differentiation. 2012;19(10):1698-708.
314. Lieberman AP, Puertollano R, Raben N, Slaugenhaupt S, Walkley SU, Ballabio A. Autophagy in lysosomal storage disorders. Autophagy. 2012;8(5):719-30.
315. Seranova E, Connolly Kyle J, Zatyka M, Rosenstock Tatiana R, Barrett T, Tuxworth Richard I, et al. Dysregulation of autophagy as a common mechanism in lysosomal storage diseases. Essays In Biochemistry. 2017;61(6):733-49.
316. Mole SE, Cotman SL. Genetics of the neuronal ceroid lipofuscinoses (Batten disease). Biochimica et Biophysica Acta (BBA) - Molecular Basis of Disease. 2015;1852(10, Part B):2237-41.
317. Jabs S, Quitsch A, Käkelä R, Koch B, Tyynelä J, Brade H, et al. Accumulation of bis(monoacylglycero)phosphate and gangliosides in mouse models of neuronal ceroid lipofuscinosis. Journal of Neurochemistry. 2008;106(3):1415-25.
318. Cárcel-Trullols J, Kovács AD, Pearce DA. Cell biology of the NCL proteins: What they do and don't do. Biochimica et Biophysica Acta (BBA) - Molecular Basis of Disease. 2015;1852(10, Part B):2242-55.
319. Ahtiainen L, Van Diggelen OP, Jalanko A, Kopra O. Palmitoyl protein thioesterase 1 is targeted to the axons in neurons. Journal of Comparative Neurology. 2003;455(3):368-77.
320. Lehtovirta M, Kyttälä A, Eskelinen E-L, Hess M, Heinonen O, Jalanko A. Palmitoyl protein thioesterase (PPT) localizes into synaptosomes and synaptic vesicles in neurons: implications for infantile neuronal ceroid lipofuscinosis (INCL). Human Molecular Genetics. 2001;10(1):69-75.
321. Aby E, Gumps K, Roth A, Sigmon S, Jenkins SE, Kim JJ, et al. Mutations in palmitoyl-protein thioesterase 1 alter exocytosis and endocytosis at synapses in Drosophila larvae. Fly. 2013;7(4):267-79.
322. Kim S-J, Zhang Z, Sarkar C, Tsai P-C, Lee Y-C, Dye L, et al. Palmitoyl protein thioesterase-1 deficiency impairs synaptic vesicle recycling at nerve terminals, contributing to neuropathology in humans and mice. The Journal of Clinical Investigation. 2008;118(9):3075-86.
323. Sun Y, Almomani R, Breedveld GJ, Santen GWE, Aten E, Lefeber DJ, et al. Autosomal Recessive Spinocerebellar Ataxia 7 (SCAR7) is Caused by Variants in TPP1, The Gene Involved in Classic Late-Infantile Neuronal Ceroid Lipofuscinosis 2 Disease (CLN2 Disease). Human Mutation. 2013;34(5):706-13.
324. Micsenyi MC, Sikora J, Stephney G, Dobrenis K, Walkley SU. Lysosomal Membrane Permeability Stimulates Protein Aggregate Formation in Neurons of a Lysosomal Disease. The Journal of Neuroscience. 2013;33(26):10815-27.
325. Vidal-Donet JM, Cárcel-Trullols J, Casanova B, Aguado C, Knecht E. Alterations in ROS Activity and Lysosomal pH Account for Distinct Patterns of Macroautophagy in LINCL and JNCL Fibroblasts. PLOS ONE. 2013;8(2):e55526.

326. Lojewski X, Staropoli JF, Biswas-Legrand S, Simas AM, Haliw L, Selig MK, et al. Human iPSC models of neuronal ceroid lipofuscinosis capture distinct effects of TPP1 and CLN3 mutations on the endocytic pathway. Human Molecular Genetics. 2013;23(8):2005-22.
327. Moharir A, Peck SH, Budden T, Lee SY. The Role of N-Glycosylation in Folding, Trafficking, and Functionality of Lysosomal Protein CLN5. PLOS ONE. 2013;8(9):e74299.
328. Mamo A, Jules F, Dumaresq-Doiron K, Costantino S, Lefrancois S. The Role of Ceroid Lipofuscinosis Neuronal Protein 5 (CLN5) in Endosomal Sorting. Molecular and Cellular Biology. 2012;32(10):1855-66.
329. Siintola E, Partanen S, Strömme P, Haapanen A, Haltia M, Maehlen J, et al. Cathepsin D deficiency underlies congenital human neuronal ceroid-lipofuscinosis. Brain. 2006;129(6):1438-45.
330. Steinfeld R, Reinhardt K, Schreiber K, Hillebrand M, Kraetzner R, Brück W, et al. Cathepsin D Deficiency Is Associated with a Human Neurodegenerative Disorder. The American Journal of Human Genetics. 2006;78(6):988-98.
331. Metcalf P, Fusek M. Two crystal structures for cathepsin D: the lysosomal targeting signal and active site. The EMBO Journal. 1993;12(4):1293-302.
332. Koike M, Nakanishi H, Saftig P, Ezaki J, Isahara K, Ohsawa Y, et al. Cathepsin D Deficiency Induces Lysosomal Storage with Ceroid Lipofuscin in Mouse CNS Neurons. The Journal of Neuroscience. 2000;20(18):6898-906.
333. Shacka JJ, Klocke BJ, Young C, Shibata M, Olney JW, Uchiyama Y, et al. Cathepsin D Deficiency Induces Persistent Neurodegeneration in the Absence of Bax-Dependent Apoptosis. The Journal of Neuroscience. 2007;27(8):2081-90.
334. Tang C-H, Lee J-W, Galvez MG, Robillard L, Mole SE, Chapman HA. Murine Cathepsin F Deficiency Causes Neuronal Lipofuscinosis and Late-Onset Neurological Disease. Molecular and Cellular Biology. 2006;26(6):2309-16.
335. Smith KR, Dahl H-HM, Canafoglia L, Andermann E, Damiano J, Morbin M, et al. Cathepsin F mutations cause Type B Kufs disease, an adult-onset neuronal ceroid lipofuscinosis. Human Molecular Genetics. 2013;22(7):1417-23.
336. Kama R, Kanneganti V, Ungermann C, Gerst JE. The yeast Batten disease orthologue Btn1 controls endosome–Golgi retrograde transport via SNARE assembly. The Journal of Cell Biology. 2011;195(2):203-15.
337. Codlin S, Mole SE. *S. pombe btn1*, the orthologue of the Batten disease gene *CLN3*, is required for vacuole protein sorting of Cpy1p and Golgi exit of Vps10p. Journal of Cell Science. 2009;122(8):1163-73.
338. Metcalf DJ, Calvi AA, Seaman MN, Mitchison HM, Cutler DF. Loss of the Batten Disease Gene CLN3 Prevents Exit from the TGN of the Mannose 6-Phosphate Receptor. Traffic. 2008;9(11):1905-14.
339. Narayan SB, Rakheja D, Tan L, Pastor JV, Bennett MJ. CLN3P, the Batten's disease protein, is a novel palmitoyl-protein Δ-9 desaturase. Annals of Neurology. 2006;60(5):570-7.
340. Rusyn E, Mousallem T, Persaud-Sawin D-A, Miller S, Boustany R-MN. CLN3p Impacts Galactosylceramide Transport, Raft Morphology, and Lipid Content. Pediatric Research. 2008;63(6):625-31.
341. Kang S, Heo T-H, Kim S-J. Altered levels of α-synuclein and sphingolipids in Batten disease lymphoblast cells. Gene. 2014;539(2):181-5.

342. Tuxworth RI, Chen H, Vivancos V, Carvajal N, Huang X, Tear G. The Batten disease gene CLN3 is required for the response to oxidative stress. Human Molecular Genetics. 2011;20(10):2037-47.
343. Cao Y, Espinola JA, Fossale E, Massey AC, Cuervo AM, MacDonald ME, et al. Autophagy Is Disrupted in a Knock-in Mouse Model of Juvenile Neuronal Ceroid Lipofuscinosis. Journal of Biological Chemistry. 2006;281(29):20483-93.
344. Schmidt K, Wolfe DM, Stiller B, Pearce DA. Cd^{2+}, Mn^{2+}, Ni^{2+} and Se^{2+} toxicity to *Saccharomyces cerevisiae* lacking YPK9p the orthologue of human ATP13A2. Biochemical and Biophysical Research Communications. 2009;383(2):198-202.
345. Bras J, Verloes A, Schneider SA, Mole SE, Guerreiro RJ. Mutation of the parkinsonism gene ATP13A2 causes neuronal ceroid-lipofuscinosis. Human Molecular Genetics. 2012;21(12):2646-50.
346. Wöhlke A, Philipp U, Bock P, Beineke A, Lichtner P, Meitinger T, et al. A One Base Pair Deletion in the Canine ATP13A2 Gene Causes Exon Skipping and Late-Onset Neuronal Ceroid Lipofuscinosis in the Tibetan Terrier. PLOS Genetics. 2011;7(10):e1002304.
347. Dehay B, Ramirez A, Martinez-Vicente M, Perier C, Canron M-H, Doudnikoff E, et al. Loss of P-type ATPase ATP13A2/PARK9 function induces general lysosomal deficiency and leads to Parkinson disease neurodegeneration. Proceedings of the National Academy of Sciences. 2012;109(24):9611-6.
348. Benitez BA, Alvarado D, Cai Y, Mayo K, Chakraverty S, Norton J, et al. Exome-Sequencing Confirms DNAJC5 Mutations as Cause of Adult Neuronal Ceroid-Lipofuscinosis. PLOS ONE. 2011;6(11):e26741.
349. Tobaben S, Thakur P, Fernández-Chacón R, Südhof TC, Rettig J, Stahl B. A Trimeric Protein Complex Functions as a Synaptic Chaperone Machine. Neuron. 2001;31(6):987-99.
350. Zhang Y-Q, Henderson Michael X, Colangelo Christopher M, Ginsberg Stephen D, Bruce C, Wu T, et al. Identification of CSPα Clients Reveals a Role in Dynamin 1 Regulation. Neuron. 2012;74(1):136-50.
351. Sharma M, Burré J, Südhof TC. CSPα promotes SNARE-complex assembly by chaperoning SNAP-25 during synaptic activity. Nature Cell Biology. 2011;13(1):30-9.
352. Sharma M, Burré J, Bronk P, Zhang Y, Xu W, Südhof TC. CSPα knockout causes neurodegeneration by impairing SNAP-25 function. The EMBO Journal. 2012;31(4):829-41.
353. Thelen M, Dαμμe M, Schweizer M, Hagel C, Wong AMS, Cooper JD, et al. Disruption of the Autophagy-Lysosome Pathway Is Involved in Neuropathology of the nclf Mouse Model of Neuronal Ceroid Lipofuscinosis. PLOS ONE. 2012;7(4):e35493.
354. Lonka L, Kyttälä A, Ranta S, Jalanko A, Lehesjoki A-E. The neuronal ceroid lipofuscinosis CLN8 membrane protein is a resident of the endoplasmic reticulum. Human Molecular Genetics. 2000;9(11):1691-7.
355. Ranta S, Zhang Y, Ross B, Lonka L, Takkunen E, Messer A, et al. The neuronal ceroid lipofuscinoses in human EPMR and mnd mutant mice are associated with mutations in CLN8. Nature Genetics. 1999;23(2):233-6.
356. Winter E, Ponting CP. TRAM, LAG1 and CLN8: members of a novel family of lipid-sensing domains? Trends in Biochemical Sciences. 2002;27(8):381-3.
357. Haddad SE, Khoury M, Daoud M, Kantar R, Harati H, Mousallem T, et al. CLN5 and CLN8 protein association with ceramide synthase: Biochemical and proteomic approaches. ELECTROPHORESIS. 2012;33(24):3798-809.

358. Hermansson M, Käkelä R, Berghäll M, Lehesjoki A-E, Somerharju P, Lahtinen U. Mass spectrometric analysis reveals changes in phospholipid, neutral sphingolipid and sulfatide molecular species in progressive epilepsy with mental retardation, EPMR, brain: a case study. Journal of Neurochemistry. 2005;95(3):609-17.
359. Kuronen M, Hermansson M, Manninen O, Zech I, Talvitie M, Laitinen T, et al. Galactolipid deficiency in the early pathogenesis of neuronal ceroid lipofuscinosis model Cln8^{mnd}: implications to delayed myelination and oligodendrocyte maturation. Neuropathology and Applied Neurobiology. 2012;38(5):471-86.
360. Smith Katherine R, Damiano J, Franceschetti S, Carpenter S, Canafoglia L, Morbin M, et al. Strikingly Different Clinicopathological Phenotypes Determined by Progranulin-Mutation Dosage. The American Journal of Human Genetics. 2012;90(6):1102-7.
361. Daniel R, Daniels E, He Z, Bateman A. Progranulin (acrogranin/PC cell-derived growth factor/granulin-epithelin precursor) is expressed in the placenta, epidermis, microvasculature, and brain during murine development. Developmental Dynamics. 2003;227(4):593-9.
362. Zanocco-Marani T, Bateman A, Romano G, Valentinis B, He Z-H, Baserga R. Biological Activities and Signaling Pathways of the Granulin/Epithelin Precursor. Cancer Research. 1999;59(20):5331-40.
363. Bateman A, Bennett HPJ. The granulin gene family: from cancer to dementia. BioEssays. 2009;31(11):1245-54.
364. Staropoli John F, Karaa A, Lim Elaine T, Kirby A, Elbalalesy N, Romansky Stephen G, et al. A Homozygous Mutation in KCTD7 Links Neuronal Ceroid Lipofuscinosis to the Ubiquitin-Proteasome System. The American Journal of Human Genetics. 2012;91(1):202-8.
365. Van Bogaert P, Azizieh R, Désir J, Aeby A, De Meirleir L, Laes J-F, et al. Mutation of a potassium channel–related gene in progressive myoclonic epilepsy. Annals of Neurology. 2007;61(6):579-86.
366. Krabichler B, Rostasy K, Baumann M, Karall D, Scholl-Bürgi S, Schwarzer C, et al. Novel Mutation in Potassium Channel related Gene KCTD7 and Progressive Myoclonic Epilepsy. Annals of Human Genetics. 2012;76(4):326-31.
367. Farhan SMK, Murphy LM, Robinson JF, Wang J, Siu VM, Rupar CA, et al. Linkage analysis and exome sequencing identify a novel mutation in KCTD7 in patients with progressive myoclonus epilepsy with ataxia. Epilepsia. 2014;55(9):e106-e11.
368. Azizieh R, Orduz D, Van Bogaert P, Bouschet T, Rodriguez W, Schiffmann SN, et al. Progressive Myoclonic Epilepsy-Associated Gene KCTD7 is a Regulator of Potassium Conductance in Neurons. Molecular Neurobiology. 2011;44(1):111-21.
369. Siintola E, Topcu M, Aula N, Lohi H, Minassian BA, Paterson AD, et al. The Novel Neuronal Ceroid Lipofuscinosis Gene *MFSD8* Encodes a Putative Lysosomal Transporter. The American Journal of Human Genetics. 2007;81(1):136-46.
370. Kousi M, Siintola E, Dvorakova L, Vlaskova H, Turnbull J, Topcu M, et al. Mutations in CLN7/MFSD8 are a common cause of variant late-infantile neuronal ceroid lipofuscinosis. Brain. 2009;132(3):810-9.
371. Aiello C, Terracciano A, Simonati A, Discepoli G, Cannelli N, Claps D, et al. Mutations in MFSD8/CLN7 are a frequent cause of variant-late infantile neuronal ceroid lipofuscinosis. Human Mutation. 2009;30(3):E530-E40.

372. Zare-Abdollahi D, Bushehri A, Alavi A, Dehghani A, Mousavi-Mirkala M, Effati J, et al. MFSD8 gene mutations; evidence for phenotypic heterogeneity. Ophthalmic Genetics. 2019;40(2):141-5.
373. Khan KN, El-Asrag ME, Ku CA, Holder GE, McKibbin M, Arno G, et al. Specific Alleles of CLN7/MFSD8, a Protein That Localizes to Photoreceptor Synaptic Terminals, Cause a Spectrum of Nonsyndromic Retinal Dystrophy. Investigative Ophthalmology & Visual Science. 2017;58(7):2906-14.
374. Roosing S, van den Born LI, Sangermano R, Banfi S, Koenekoop RK, Zonneveld-Vrieling MN, et al. Mutations in *MFSD8*, Encoding a Lysosomal Membrane Protein, Are Associated with Nonsyndromic Autosomal Recessive Macular Dystrophy. Ophthalmology. 2015;122(1):170-9.
375. Craiu D, Dragostin O, Dica A, Hoffman-Zacharska D, Gos M, Bastian AE, et al. Rett-like onset in late-infantile neuronal ceroid lipofuscinosis (CLN7) caused by compound heterozygous mutation in the MFSD8 gene and review of the literature data on clinical onset signs. European Journal of Paediatric Neurology. 2015;19(1):78-86.
376. Mandel H, Katsanelson KC, Khayat M, Chervinsky I, Vladovski E, Iancu TC, et al. Clinico-pathological manifestations of variant late infantile neuronal ceroid lipofuscinosis (vLINCL) caused by a novel mutation in MFSD8 gene. European Journal of Medical Genetics. 2014;57(11):607-12.
377. Koulen P, Fletcher EL, Craven SE, Bredt DS, Wässle H. Immunocytochemical Localization of the Postsynaptic Density Protein PSD-95 in the Mammalian Retina. The Journal of Neuroscience. 1998;18(23):10136-49.
378. Hamanaka Y, Meinertzhagen IA. Immunocytochemical localization of synaptic proteins to photoreceptor synapses of Drosophila melanogaster. J Comp Neurol. 2010;518(7):1133-55.
379. Sharifi A, Kousi M, Sagné C, Bellenchi GC, Morel L, Darmon M, et al. Expression and lysosomal targeting of CLN7, a major facilitator superfamily transporter associated with variant late-infantile neuronal ceroid lipofuscinosis. Human Molecular Genetics. 2010;19(22):4497-514.
380. Damme M, Brandenstein L, Fehr S, Jankowiak W, Bartsch U, Schweizer M, et al. Gene disruption of Mfsd8 in mice provides the first animal model for CLN7 disease. Neurobiol Dis. 2014;65:12-24.
381. Brandenstein L, Storch S, Schweizer M, Sedlacik J, Fiehler J. Lysosomal dysfunction and impaired autophagy in a novel mouse model deficient for the lysosomal membrane protein Cln7. Human Molecular Genetics. 2015;25(4):777-91.
382. Jankowiak W, Brandenstein L, Dulz S, Hagel C, Storch S, Bartsch U. Retinal Degeneration in Mice Deficient in the Lysosomal Membrane Protein CLN7. Investigative Ophthalmology & Visual Science. 2016;57(11):4989-98.
383. Danyukova T, Ariunbat K, Thelen M, Brocke-Ahmadinejad N, Mole SE, Storch S. Loss of CLN7 results in depletion of soluble lysosomal proteins and impaired mTOR reactivation. Human Molecular Genetics. 2018;27(10):1711-22.
384. von Kleist L, Ariunbat K, Braren I, Stauber T, Storch S, Danyukova T. A newly generated neuronal cell model of CLN7 disease reveals aberrant lysosome motility and impaired cell survival. Molecular Genetics and Metabolism. 2019;126(2):196-205.
385. Guo J, O'Brien DP, Mhlanga-Mutangadura T, Olby NJ, Taylor JF, Schnabel RD, et al. A rare homozygous MFSD8 single-base-pair deletion and frameshift in the whole genome

sequence of a Chinese Crested dog with neuronal ceroid lipofuscinosis. BMC Veterinary Research. 2015;10(1):960.
386. Faller KME, Bras J, Sharpe SJ, Anderson GW, Darwent L, Kun-Rodrigues C, et al. The Chihuahua dog: A new animal model for neuronal ceroid lipofuscinosis CLN7 disease? Journal of Neuroscience Research. 2016;94(4):339-47.
387. Ashwini A, D'Angelo A, Yamato O, Giordano C, Cagnotti G, Harcourt-Brown T, et al. Neuronal ceroid lipofuscinosis associated with an MFSD8 mutation in Chihuahuas. Molecular Genetics and Metabolism. 2016;118(4):326-32.
388. Karli P, Oevermann A, Bauer A, Jagannathan V, Leeb T. MFSD8 single-base pair deletion in a Chihuahua with neuronal ceroid lipofuscinosis. Animal Genetics. 2016;47(5):631-.
389. McBride JL, Neuringer M, Ferguson B, Kohama SG, Tagge IJ, Zweig RC, et al. Discovery of a CLN7 model of Batten disease in non-human primates. Neurobiol Dis. 2018;119:65-78.
390. Steenhuis P, Herder S, Gelis S, Braulke T, Storch S. Lysosomal Targeting of the CLN7 Membrane Glycoprotein and Transport Via the Plasma Membrane Require a Dileucine Motif. Traffic. 2010;11(7):987-1000.
391. Steenhuis P, Froemming J, Reinheckel T, Storch S. Proteolytic cleavage of the disease-related lysosomal membrane glycoprotein CLN7. Biochimica et Biophysica Acta (BBA) - Molecular Basis of Disease. 2012;1822(10):1617-28.
392. Bond M, Holthaus S-Mk, Tammen I, Tear G, Russell C. Use of model organisms for the study of neuronal ceroid lipofuscinosis. Biochimica et Biophysica Acta (BBA) - Molecular Basis of Disease. 2013;1832(11):1842-65.
393. Faller KME, Gutierrez-Quintana R, Mohammed A, Rahim AA, Tuxworth RI, Wager K, et al. The neuronal ceroid lipofuscinoses: Opportunities from model systems. Biochimica et Biophysica Acta (BBA) - Molecular Basis of Disease. 2015;1852(10, Part B):2267-78.
394. Muzaffar NE, Pearce DA. Analysis of NCL Proteins from an Evolutionary Standpoint. Curr Genomics. 2008;9(2):115-36.
395. Imler E, Pyon JS, Kindelay S, Torvund M, Zhang Y-q, Chandra SS, et al. A *Drosophila* model of neuronal ceroid lipofuscinosis *CLN4* reveals a hypermorphic gain of function mechanism. eLife. 2019;8:e46607.
396. Hickey AJ, Chotkowski HL, Singh N, Ault JG, Korey CA, MacDonald ME, et al. Palmitoyl-protein thioesterase 1 deficiency in *Drosophila melanogaster* causes accumulation of abnormal storage material and reduced life span. Genetics. 2006;172(4):2379-90.
397. Pivtoraiko VN, Stone SL, Roth KA, Shacka JJ. Oxidative Stress and Autophagy in the Regulation of Lysosome-Dependent Neuron Death. Antioxidants & Redox Signaling. 2009;11(3):481-96.
398. Tuxworth RI, Vivancos V, O'Hare MB, Tear G. Interactions between the juvenile Batten disease gene, CLN3, and the Notch and JNK signalling pathways. Human Molecular Genetics. 2008;18(4):667-78.
399. Benedict JW, Sommers CA, Pearce DA. Progressive oxidative damage in the central nervous system of a murine model for juvenile Batten disease. Journal of Neuroscience Research. 2007;85(13):2882-91.
400. Connolly KJ, O'Hare MB, Mohammed A, Aitchison KM, Anthoney NC, Taylor MJ, et al. The neuronal ceroid lipofuscinosis protein Cln7 functions in the postsynaptic cell to regulate synapse development. Scientific Reports. 2019;9(1):15592.

401. Myllykangas L, Tyynelä J, Page-McCaw A, Rubin GM, Haltia MJ, Feany MB. Cathepsin D-deficient *Drosophila* recapitulate the key features of neuronal ceroid lipofuscinoses. Neurobiol Dis. 2005;19(1):194-9.
402. Mohammed A, O'Hare MB, Warley A, Tear G, Tuxworth RI. *In vivo* localization of the neuronal ceroid lipofuscinosis proteins, CLN3 and CLN7, at endogenous expression levels. Neurobiol Dis. 2017;103:123-32.
403. Sawin-McCormack EP, Sokolowski MB, Campos AR. Characterization and Genetic Analysis of *Drosophila Melanogaster* Photobehavior During Larval Development. Journal of Neurogenetics. 1995;10(2):119-35.
404. Kessner D, Agus D, Chambers M, Mallick P, Burke R. ProteoWizard: open source software for rapid proteomics tools development. Bioinformatics. 2008;24(21):2534-6.
405. Smith CA, Want EJ, O'Maille G, Abagyan R, Siuzdak G. XCMS: Processing Mass Spectrometry Data for Metabolite Profiling Using Nonlinear Peak Alignment, Matching, and Identification. Analytical Chemistry. 2006;78(3):779-87.
406. Brown M, Wedge DC, Goodacre R, Kell DB, Baker PN, Kenny LC, et al. Automated workflows for accurate mass-based putative metabolite identification in LC/MS-derived metabolomic datasets. Bioinformatics. 2011;27(8):1108-12.
407. Sumner LW, Amberg A, Barrett D, Beale MH, Beger R, Daykin CA, et al. Proposed minimum reporting standards for chemical analysis. Metabolomics. 2007;3(3):211-21.
408. Xia J, Han B, Sinelnikov IV, Wishart DS. MetaboAnalyst 3.0—making metabolomics more meaningful. Nucleic Acids Research. 2015;43(W1):W251-W7.
409. Fahy E, Subramaniam S, Brown HA, Glass CK, Merrill AH, Murphy RC, et al. A comprehensive classification system for lipids. Journal of Lipid Research. 2005;46(5):839-62.
410. Fahy E, Subramaniam S, Murphy RC, Nishijima M, Raetz CRH, Shimizu T, et al. Update of the LIPID MAPS comprehensive classification system for lipids. Journal of Lipid Research. 2009;50(Supplement):S9-S14.
411. Brent JR, Werner KM, McCabe BD. *Drosophila* larval NMJ dissection. J Vis Exp. 2009(24):1107.
412. Brent J, Werner K, McCabe BD. *Drosophila* larval NMJ immunohistochemistry. J Vis Exp. 2009(25):1108.
413. Feng Y, Ueda A, Wu C-F. A MODIFIED MINIMAL HEMOLYMPH-LIKE SOLUTION, HL3.1, FOR PHYSIOLOGICAL RECORDINGS AT THE NEUROMUSCULAR JUNCTIONS OF NORMAL AND MUTANT *DROSOPHILA* LARVAE. Journal of Neurogenetics. 2004;18(2):377-402.
414. Hung V, Udeshi ND, Lam SS, Loh KH, Cox KJ, Pedram K, et al. Spatially resolved proteomic mapping in living cells with the engineered peroxidase APEX2. Nature Protocols. 2016;11:456.
415. Roux KJ, Kim DI, Raida M, Burke B. A promiscuous biotin ligase fusion protein identifies proximal and interacting proteins in mammalian cells. The Journal of Cell Biology. 2012;196(6):801-10.
416. Davie K, Janssens J, Koldere D, De Waegeneer M, Pech U, Kreft Ł, et al. A Single-Cell Transcriptome Atlas of the Aging Drosophila Brain. Cell. 2018;174(4):982-98.e20.
417. Bass TM, Grandison RC, Wong R, Martinez P, Partridge L, Piper MDW. Optimization of dietary restriction protocols in *Drosophila*. J Gerontol A Biol Sci Med Sci. 2007;62(10):1071-81.
418. Thummel CS. Molecular Mechanisms of Developmental Timing in *C. elegans* and *Drosophila*. Developmental Cell. 2001;1(4):453-65.

419. NIJHOUT HF, WILLIAMS CM. Control of Moulting and Metamorphosis in the Tobacco Hornworm, *Manduca Sexta* (L.): Cessation of Juvenile Hormone Secretion as a Trigger for Pupation. Journal of Experimental Biology. 1974;61(2):493-501.
420. NIJHOUT HF. A THRESHOLD SIZE FOR METAMORPHOSIS IN THE TOBACCO HORNWORM, *MANDUCA SEXTA* (L.). The Biological Bulletin. 1975;149(1):214-25.
421. Tennessen JM, Thummel CS. Coordinating growth and maturation - insights from Drosophila. Current biology : CB. 2011;21(18):R750-R7.
422. Mirth C, Truman JW, Riddiford LM. The Role of the Prothoracic Gland in Determining Critical Weight for Metamorphosis in *Drosophila melanogaster*. Current Biology. 2005;15(20):1796-807.
423. Colombani J, Bianchini L, Layalle S, Pondeville E, Dauphin-Villemant C, Antoniewski C, et al. Antagonistic Actions of Ecdysone and Insulins Determine Final Size in *Drosophila*. Science. 2005;310(5748):667-70.
424. Caldwell PE, Walkiewicz M, Stern M. Ras Activity in the *Drosophila* Prothoracic Gland Regulates Body Size and Developmental Rate via Ecdysone Release. Current Biology. 2005;15(20):1785-95.
425. Robertson FW. The ecological genetics of growth in Drosophila 6. The genetic correlation between the duration of the larval period and body size in relation to larval diet. Genetical Research. 1963;4(1):74-92.
426. Shingleton AW, Das J, Vinicius L, Stern DL. The Temporal Requirements for Insulin Signaling During Development in Drosophila. PLOS Biology. 2005;3(9):e289.
427. Colombani J, Raisin S, Pantalacci S, Radimerski T, Montagne J, Léopold P. A Nutrient Sensor Mechanism Controls Drosophila Growth. Cell. 2003;114(6):739-49.
428. Géminard C, Rulifson EJ, Léopold P. Remote Control of Insulin Secretion by Fat Cells in *Drosophila*. Cell Metabolism. 2009;10(3):199-207.
429. Rajan A, Perrimon N. *Drosophila* Cytokine Unpaired 2 Regulates Physiological Homeostasis by Remotely Controlling Insulin Secretion. Cell. 2012;151(1):123-37.
430. Liu J, Yang L, Luan M, Wang Y, Zhang C, Zhang B, et al. A vacuolar phosphate transporter essential for phosphate homeostasis in *Arabidopsis*. Proceedings of the National Academy of Sciences. 2015;112(47):E6571-E8.
431. Lamming DW, Ye L, Katajisto P, Goncalves MD, Saitoh M, Stevens DM, et al. Rapamycin-Induced Insulin Resistance Is Mediated by mTORC2 Loss and Uncoupled from Longevity. Science. 2012;335(6076):1638-43.
432. Sarbassov DD, Ali SM, Sengupta S, Sheen J-H, Hsu PP, Bagley AF, et al. Prolonged Rapamycin Treatment Inhibits mTORC2 Assembly and Akt/PKB. Molecular Cell. 2006;22(2):159-68.
433. Ikeya T, Galic M, Belawat P, Nairz K, Hafen E. Nutrient-Dependent Expression of Insulin-like Peptides from Neuroendocrine Cells in the CNS Contributes to Growth Regulation in *Drosophila*. Current Biology. 2002;12(15):1293-300.
434. Goyal G, Zheng J, Adam E, Steffes G, Jain M, Klavins K, et al. Sphingolipid-dependent Dscam sorting regulates axon segregation. Nature Communications. 2019;10(1):813.
435. Huang Y, Huang S, Di Scala C, Wang Q, Wandall HH, Fantini J, et al. The glycosphingolipid MacCer promotes synaptic bouton formation in *Drosophila* by interacting with Wnt. eLife. 2018;7:e38183.

436. Ghosh A, Kling T, Snaidero N, Sampaio JL, Shevchenko A, Gras H, et al. A Global In Vivo Drosophila RNAi Screen Identifies a Key Role of Ceramide Phosphoethanolamine for Glial Ensheathment of Axons. PLOS Genetics. 2013;9(12):e1003980.
437. Atkinson D, Nikodinovic Glumac J, Asselbergh B, Ermanoska B, Blocquel D, Steiner R, et al. Sphingosine 1-phosphate lyase deficiency causes Charcot-Marie-Tooth neuropathy. Neurology. 2017;88(6):533-42.
438. Haines N, Stewart BA. Functional Roles for β1,4-*N*-Acetlygalactosaminyltransferase-A in *Drosophila* Larval Neurons and Muscles. Genetics. 2007;175(2):671-9.
439. Knowles TJ, Finka R, Smith C, Lin Y-P, Dafforn T, Overduin M. Membrane Proteins Solubilized Intact in Lipid Containing Nanoparticles Bounded by Styrene Maleic Acid Copolymer. Journal of the American Chemical Society. 2009;131(22):7484-5.
440. Lee SC, Knowles TJ, Postis VLG, Jamshad M, Parslow RA, Lin Y-p, et al. A method for detergent-free isolation of membrane proteins in their local lipid environment. Nature Protocols. 2016;11:1149.
441. SAGNÉ C, ISAMBERT M-F, HENRY J-P, GASNIER B. SDS-resistant aggregation of membrane proteins: application to the purification of the vesicular monoamine transporter. Biochemical Journal. 1996;316(3):825-31.
442. Kaur J, Bachhawat AK. A modified Western blot protocol for enhanced sensitivity in the detection of a membrane protein. Analytical Biochemistry. 2009;384(2):348-9.
443. Zhang Q, Ma X, Ward A, Hong W-X, Jaakola V-P, Stevens RC, et al. Designing Facial Amphiphiles for the Stabilization of Integral Membrane Proteins. Angewandte Chemie International Edition. 2007;46(37):7023-5.
444. Shen H-H, Lithgow T, Martin L. Reconstitution of membrane proteins into model membranes: seeking better ways to retain protein activities. Int J Mol Sci. 2013;14(1):1589-607.
445. Bayburt TH, Grinkova YV, Sligar SG. Self-Assembly of Discoidal Phospholipid Bilayer Nanoparticles with Membrane Scaffold Proteins. Nano Letters. 2002;2(8):853-6.
446. Orwick MC, Judge PJ, Procek J, Lindholm L, Graziadei A, Engel A, et al. Detergent-Free Formation and Physicochemical Characterization of Nanosized Lipid–Polymer Complexes: Lipodisq. Angewandte Chemie International Edition. 2012;51(19):4653-7.
447. Dörr JM, Scheidelaar S, Koorengevel MC, Dominguez JJ, Schäfer M, van Walree CA, et al. The styrene-maleic acid copolymer: a versatile tool in membrane research. Eur Biophys J. 2016;45(1):3-21.
448. Mehta V, Trinkle-Mulcahy L. Recent advances in large-scale protein interactome mapping [version 1; peer review: 3 approved]. F1000Research. 2016;5(782).
449. Beckett D, Kovaleva E, Schatz PJ. A minimal peptide substrate in biotin holoenzyme synthetase-catalyzed biotinylation. Protein Science. 1999;8(4):921-9.
450. Chapman-Smith A, Cronan Jr JE. Molecular Biology of Biotin Attachment to Proteins. The Journal of Nutrition. 1999;129(2):477S-84S.
451. Kwon K, Beckett D. Function of a conserved sequence motif in biotin holoenzyme synthetases. Protein Science. 2000;9(8):1530-9.
452. Choi-Rhee E, Schulman H, Cronan JE. Promiscuous protein biotinylation by *Escherichia coli* biotin protein ligase. Protein Science. 2004;13(11):3043-50.

453. Kim DI, KC B, Zhu W, Motamedchaboki K, Doye V, Roux KJ. Probing nuclear pore complex architecture with proximity-dependent biotinylation. Proceedings of the National Academy of Sciences. 2014;111(24):E2453-E61.
454. Hung V, Zou P, Rhee H-W, Udeshi Namrata D, Cracan V, Svinkina T, et al. Proteomic Mapping of the Human Mitochondrial Intermembrane Space in Live Cells via Ratiometric APEX Tagging. Molecular Cell. 2014;55(2):332-41.
455. Lam SS, Martell JD, Kamer KJ, Deerinck TJ, Ellisman MH, Mootha VK, et al. Directed evolution of APEX2 for electron microscopy and proximity labeling. Nature Methods. 2014;12:51.
456. Martell JD, Deerinck TJ, Sancak Y, Poulos TL, Mootha VK, Sosinsky GE, et al. Engineered ascorbate peroxidase as a genetically encoded reporter for electron microscopy. Nature Biotechnology. 2012;30:1143.
457. Knox S, Ge H, Dimitroff BD, Ren Y, Howe KA, Arsham AM, et al. Mechanisms of TSC-mediated Control of Synapse Assembly and Axon Guidance. PLOS ONE. 2007;2(4):e375.
458. Dollar G, Gombos R, Barnett AA, Sanchez Hernandez D, Maung SMT, Mihály J, et al. Unique and Overlapping Functions of Formins Frl and DAAM During Ommatidial Rotation and Neuronal Development in *Drosophila*. Genetics. 2016;202(3):1135-51.
459. O'Keefe DD, Edgar BA, Saucedo LJ. EndoGI modulates Notch signaling and axon guidance in *Drosophila*. Mechanisms of Development. 2011;128(1):59-70.
460. Bhattacharya S, Stewart BA, Niemeyer BA, Burgess RW, McCabe BD, Lin P, et al. Members of the synaptobrevin/vesicle-associated membrane protein (VAMP) family in *Drosophila* are functionally interchangeable *in vivo* for neurotransmitter release and cell viability. Proceedings of the National Academy of Sciences. 2002;99(21):13867-72.
461. Hu Y, Han Y, Shao Y, Wang X, Ma Y, Ling E, et al. Gr33a Modulates *Drosophila* Male Courtship Preference. Scientific Reports. 2015;5:7777.
462. Apostolopoulou AA, Köhn S, Stehle B, Lutz M, Wüst A, Mazija L, et al. Caffeine Taste Signaling in Drosophila Larvae. Frontiers in Cellular Neuroscience. 2016;10(193).
463. Scantlebury N, Zhao XL, Rodriguez Moncalvo VG, Camiletti A, Zahanova S, Dineen A, et al. The *Drosophila* Gene *RanBPM* Functions in the Mushroom Body to Regulate Larval Behavior. PLOS ONE. 2010;5(5):e10652.
464. Salemi LM, Loureiro SO, Schild-Poulter C. Characterization of RanBPM Molecular Determinants that Control Its Subcellular Localization. PLOS ONE. 2015;10(2):e0117655.
465. Watson JD, Wheeler SR, Stagg SB, Crews ST. *Drosophila hedgehog* signaling and *engrailed-runt* mutual repression direct midline glia to alternative ensheathing and non-ensheathing fates. Development. 2011;138(7):1285-95.
466. Ricolo D, Butí E, Araújo SJ. *Drosophila melanogaster* Hedgehog cooperates with Frazzled to guide axons through a non-canonical signalling pathway. Mechanisms of Development. 2015;137:11-22.
467. Brunner D, Oellers N, Szabad J, Biggs WH, Zipursky SL, Hafen E. A gain-of-function mutation in *Drosophila* MAP kinase activates multiple receptor tyrosine kinase signaling pathways. Cell. 1994;76(5):875-88.
468. Bergmann A, Tugentman M, Shilo B-Z, Steller H. Regulation of Cell Number by MAPK-Dependent Control of Apoptosis: A Mechanism for Trophic Survival Signaling. Developmental Cell. 2002;2(2):159-70.

469. Vanderheyden WM, Gerstner JR, Tanenhaus A, Yin JC, Shaw PJ. ERK Phosphorylation Regulates Sleep and Plasticity in *Drosophila*. PLOS ONE. 2013;8(11):e81554.
470. Wairkar YP, Toda H, Mochizuki H, Furukubo-Tokunaga K, Tomoda T, DiAntonio A. Unc-51 Controls Active Zone Density and Protein Composition by Downregulating ERK Signaling. The Journal of Neuroscience. 2009;29(2):517-28.
471. Koh Y-H, Ruiz-Canada C, Gorczyca M, Budnik V. The Ras1–Mitogen-Activated Protein Kinase Signal Transduction Pathway Regulates Synaptic Plasticity through Fasciclin II-Mediated Cell Adhesion. The Journal of Neuroscience. 2002;22(7):2496-504.
472. Spring AM, Brusich DJ, Frank CA. C-terminal Src Kinase Gates Homeostatic Synaptic Plasticity and Regulates Fasciclin II Expression at the *Drosophila* Neuromuscular Junction. PLOS Genetics. 2016;12(2):e1005886.
473. Nicolaï M, Lasbleiz C, Dura J-M. Gain-of-function screen identifies a role of the Src64 oncogene in *Drosophila* mushroom body development. Journal of Neurobiology. 2003;57(3):291-302.
474. Marchetti G, Reichardt I, Knoblich JA, Besse F. The TRIM-NHL Protein Brat Promotes Axon Maintenance by Repressing *src64B* Expression. The Journal of Neuroscience. 2014;34(41):13855-64.
475. Hoang B, Chiba A. Genetic Analysis on the Role of Integrin during Axon Guidance in *Drosophila*. The Journal of Neuroscience. 1998;18(19):7847-55.
476. Han C, Wang D, Soba P, Zhu S, Lin X, Jan Lily Y, et al. Integrins Regulate Repulsion-Mediated Dendritic Patterning of *Drosophila* Sensory Neurons by Restricting Dendrites in a 2D Space. Neuron. 2012;73(1):64-78.
477. Chambers DB, Androschuk A, Rosenfelt C, Langer S, Harding M, Bolduc FV. Insulin signaling is acutely required for long-term memory in *Drosophila*. Frontiers in Neural Circuits. 2015;9(8).
478. Naganos S, Horiuchi J, Saitoe M. Mutations in the *Drosophila* insulin receptor substrate, CHICO, impair olfactory associative learning. Neuroscience Research. 2012;73(1):49-55.
479. Moreira S, Osswald M, Ventura G, Gonçalves M, Sunkel CE, Morais-de-Sá E. PP1-Mediated Dephosphorylation of Lgl Controls Apical-basal Polarity. Cell Reports. 2019;26(2):293-301.e7.
480. Justice N, Roegiers F, Jan LY, Jan YN. Lethal Giant Larvae Acts Together with Numb in Notch Inhibition and Cell Fate Specification in the *Drosophila* Adult Sensory Organ Precursor Lineage. Current Biology. 2003;13(9):778-83.
481. Chen K, Merino C, Sigrist SJ, Featherstone DE. The 4.1 Protein Coracle Mediates Subunit-Selective Anchoring of *Drosophila* Glutamate Receptors to the Postsynaptic Actin Cytoskeleton. The Journal of Neuroscience. 2005;25(28):6667-75.
482. Bogdanik L, Framery B, Frölich A, Franco B, Mornet D, Bockaert J, et al. Muscle Dystroglycan Organizes the Postsynapse and Regulates Presynaptic Neurotransmitter Release at the *Drosophila* Neuromuscular Junction. PLOS ONE. 2008;3(4):e2084.
483. Wu C-L, Chang C-C, Wu J-K, Chiang M-H, Yang C-H, Chiang H-C. Mushroom body glycolysis is required for olfactory memory in Drosophila. Neurobiology of Learning and Memory. 2018;150:13-9.

484. Nahm M, Long AA, Paik SK, Kim S, Bae YC, Broadie K, et al. The Cdc42-selective GAP Rich regulates postsynaptic development and retrograde BMP transsynaptic signaling. The Journal of Cell Biology. 2010;191(3):661-75.
485. Bloomquist BT, Shortridge RD, Schneuwly S, Perdew M, Montell C, Steller H, et al. Isolation of a putative phospholipase c gene of *Drosophila*, norpA, and its role in phototransduction. Cell. 1988;54(5):723-33.
486. Hardie RC, Martin F, Chyb S, Raghu P. Rescue of Light Responses in the *Drosophila* "Null" Phospholipase C Mutant, norpAP24, by the Diacylglycerol Kinase Mutant, rdgA, and by Metabolic Inhibition. Journal of Biological Chemistry. 2003;278(21):18851-8.
487. Sepp KJ, Hong P, Lizarraga SB, Liu JS, Mejia LA, Walsh CA, et al. Identification of Neural Outgrowth Genes using Genome-Wide RNAi. PLOS Genetics. 2008;4(7):e1000111.
488. Pielage J, Bulat V, Zuchero JB, Fetter Richard D, Davis Graeme W. Hts/Adducin Controls Synaptic Elaboration and Elimination. Neuron. 2011;69(6):1114-31.
489. Wang S, Yang J, Tsai A, Kuca T, Sanny J, Lee J, et al. *Drosophila* adducin regulates Dlg phosphorylation and targeting of Dlg to the synapse and epithelial membrane. Developmental Biology. 2011;357(2):392-403.
490. Krieger C, Wang SJH, Yoo SH, Harden N. Adducin at the Neuromuscular Junction in Amyotrophic Lateral Sclerosis: Hanging on for Dear Life. Frontiers in Cellular Neuroscience. 2016;10(11).
491. O'Neill RS, Clark DV. Partial Functional Diversification of *Drosophila melanogaster* Septin Genes *Sep2* and *Sep5*. G3: Genes|Genomes|Genetics. 2016;6(7):1947-57.
492. Vanlandingham PA, Barmchi MP, Royer S, Green R, Bao H, Reist N, et al. AP180 Couples Protein Retrieval to Clathrin-Mediated Endocytosis of Synaptic Vesicles. Traffic. 2014;15(4):433-50.
493. Bao H, Daniels RW, MacLeod GT, Charlton MP, Atwood HL, Zhang B. AP180 Maintains the Distribution of Synaptic and Vesicle Proteins in the Nerve Terminal and Indirectly Regulates the Efficacy of Ca^{2+}-Triggered Exocytosis. Journal of Neurophysiology. 2005;94(3):1888-903.
494. Pielage J, Fetter RD, Davis GW. A postsynaptic Spectrin scaffold defines active zone size, spacing, and efficacy at the *Drosophila* neuromuscular junction. The Journal of Cell Biology. 2006;175(3):491-503.
495. Pielage J, Fetter RD, Davis GW. Presynaptic Spectrin Is Essential for Synapse Stabilization. Current Biology. 2005;15(10):918-28.
496. Billuart P, Winter CG, Maresh A, Zhao X, Luo L. Regulating Axon Branch Stability: The Role of p190 RhoGAP in Repressing a Retraction Signaling Pathway. Cell. 2001;107(2):195-207.
497. Goldbach P, Wong R, Beise N, Sarpal R, Trimble WS, Brill JA. Stabilization of the Actomyosin Ring Enables Spermatocyte Cytokinesis in *Drosophila*. Molecular Biology of the Cell. 2010;21(9):1482-93.
498. Rosby R, Cui Z, Rogers E, deLivron MA, Robinson VL, DiMario PJ. Knockdown of the *Drosophila* GTPase Nucleostemin 1 Impairs Large Ribosomal Subunit Biogenesis, Cell Growth, and Midgut Precursor Cell Maintenance. Molecular Biology of the Cell. 2009;20(20):4424-34.
499. Kim DI, Jensen SC, Noble KA, KC B, Roux KH, Motamedchaboki K, et al. An improved smaller biotin ligase for BioID proximity labeling. Molecular Biology of the Cell. 2016;27(8):1188-96.

500. Branon TC, Bosch JA, Sanchez AD, Udeshi ND, Svinkina T, Carr SA, et al. Efficient proximity labeling in living cells and organisms with TurboID. Nature Biotechnology. 2018;36:880.
501. Mizushima N, Yamamoto A, Matsui M, Yoshimori T, Ohsumi Y. In Vivo Analysis of Autophagy in Response to Nutrient Starvation Using Transgenic Mice Expressing a Fluorescent Autophagosome Marker. Molecular Biology of the Cell. 2004;15(3):1101-11.
502. Walkley SU. Secondary accumulation of gangliosides in lysosomal storage disorders. Seminars in Cell & Developmental Biology. 2004;15(4):433-44.
503. Shayman JA, Kelly R, Kollmeyer J, He Y, Abe A. Group XV phospholipase A2, a lysosomal phospholipase A2. Progress in Lipid Research. 2011;50(1):1-13.
504. Tsuboi K, Takezaki N, Ueda N. The N-Acylethanolamine-Hydrolyzing Acid Amidase (NAAA). Chemistry & Biodiversity. 2007;4(8):1914-25.
505. Perland E, Bagchi S, Klaesson A, Fredriksson R. Characteristics of 29 novel atypical solute carriers of major facilitator superfamily type: evolutionary conservation, predicted structure and neuronal co-expression. Open Biology. 2017;7(9):170142.
506. Seppo A, Moreland M, Schweingruber H, Tiemeyer M. Zwitterionic and acidic glycosphingolipids of the *Drosophila melanogaster* embryo. European Journal of Biochemistry. 2003;267(12):3549-58.